Imperial College London

Using porous boron nitride in adsorption-based processes: investigation of material challenges and opportunities

by

Anouk L'Hermitte

A thesis submitted in fulfilment of the requirements for the degree of Doctor of Philosophy and the Diploma of Imperial College London

CDT in the Advanced Characterisation of Materials

Department of Chemical Engineering & Department of Materials

Imperial College London, United Kingdom

March 2023

ABSTRACT

In 2016, industrial separation processes accounted for 10-15% of the global energy consumption. This striking figure has urged the scientific community to continue developing new materials and technologies to significantly reduce global emissions in industry, for example in the field of adsorption processes. In light of this, porous boron nitride (BN) has gradually appeared as a promising adsorbent owing to its tunable chemistry and porosity, which a priori make it adaptable for various applications. However, research on porous BN remains at laboratory scale due to a lack of understanding of its formation mechanism. Furthermore, the material has displayed hydrolytic instability, which is an issue due to the presence of moisture in most industrial settings. Finally, the use of porous BN has mainly been focusing on molecular separations, but little is known about its potential for other adsorption-based applications, such as thermal energy storage.

In this thesis, I first investigated the formation mechanism of porous BN to shed light on the critical steps of its synthesis. Considering a wide range of separations, I then searched new ways of enhancing its hydrolytic stability via surface functionalization. I developed two methods involving organosilane grafting, which produced porous BN adsorbents with enhanced moisture resistance and adequate CO_2/N_2 selectivity in the context of CO_2 capture. Finally, I expanded the range of possible applications using porous BN and researched its potential for thermochemical energy storage, which has recently emerged as a key technology to mitigate CO_2 emissions. I prepared BN-based adsorbents with various structural and thermal properties, allowing to understand how material properties affect the performance in thermochemical energy storage via adsorption.

Overall, this thesis presents new knowledge on porous BN and explores the opportunities and challenges associated with its unique properties in the context of adsorption-based applications, in particular CO_2/N_2 separation and thermochemical energy storage.

PUBLICATIONS

First-author publications:

1) **A. L'Hermitte**, H. Azzan, M. H. N. Yio, A. K. Rajagopalan, D. Danaci, T. Hirosawa, T. Isobe & C. Petit (2023) "Effect of Surface Functionalization on the Moisture Stability and Sorption Properties of Porous Boron Nitride", *Microporous and Mesoporous Materials*, **352**, 112478.

2) **A. L'Hermitte**,[¶] I. Itskou,[¶] S. Marchesini,[¶] T. Tian[¶] & C. Petit (2023) "How to tailor porous boron nitride properties for applications in interfacial processes", *Accounts of Materials Research*, **4**, 143-155 ([¶]: authors contributed equally).

3) **A. L'Hermitte**, D. M. Dawson, P. Ferrer, K. Roy, G. Held, T. Tian, S. E. Ashbrook & C. Petit (2021) "Formation Mechanism and Porosity Development in Porous Boron Nitride", *Journal of Physical Chemistry C,* **125**, 27429-27439.

Co-author publications:

4) H. Azzan,[¶] A. K. Rajagopalan,[¶] **A. L'Hermitte**, R. Pini & C. Petit (2022) "Simultaneous Estimation of Gas Adsorption Equilibria and Kinetics of Individual Shaped Adsorbents", *Chemistry of Materials*, **34**, 6671-6686 ([¶]: authors contributed equally).

5) Y. Xiong, T. Tian, **A. L'Hermitte**, A. S. J. Mendez, D. Danaci, A. E. Platero-Prats & C. Petit (2022) "Using silver exchange to achieve high uptake and selectivity for propylene/propane separation in zeolite Y", *Chemical Engineering Journal*, **446**, 137104.

6) T. Tian, J. Hou, H. Ansari, Y. Xiong, **A. L'Hermitte**, D. Danaci, R. Pini & C. Petit (2021) "Mechanically stable structured porous boron nitride with high volumetric adsorption capacity", *Journal of Materials Chemistry A*, **9**, 13366-13373.

7) J. Stafford, N. Uzo, U. Farooq, S. Favero, S. Wang, H.-H. Chen, **A. L'Hermitte**, C. Petit & O. K. Matar (2021) "Real-time monitoring and hydrodynamic scaling of shear exfoliated graphene", *2D Materials*, **8**, 025029.

8) Z. Ye, G. E. M. Schukraft, **A. L'Hermitte**, Y. Xiong, E. Brillas, C. Petit & I. Sires (2020) "Mechanism and stability of an Fe-based 2D MOF during the photoelectro-Fenton treatment of organic micropollutants under UVA and visible light irradiation", *Water Research*, **184**, 115986.

In preparation:

A. L'Hermitte, H. Ansari, S. Shervani, F. H. Tezel & C. Petit, "Evaluation of boron nitride-based materials for adsorption thermal energy storage", In preparation.

CONFERENCES

Oral presentations:

- International Zeolite Conference (IZC), Valencia, Spain (2022)

- AIChE annual meeting, Boston, USA (2021)

- Federation of European Zeolite Associations (FEZA) conference, online event (2021)

- bp-ICAM annual conference, online event (2020)

- AIChE annual meeting, online event (2020)

- bp-ICAM annual conference, Manchester, UK (2019)

Poster presentations:

- Imperial College ChemEng symposium, London, UK (2022), 2nd prize

- Fundamentals Of Adsorption conference, Broomfield, USA (2022), 3rd prize

- bp-ICAM annual conference, Manchester, UK (2018)

- Global Fellows Programme 'Climate Action', London, UK (2019)

- CDT-ACM summer retreat, Girona, Spain (2019)

- UK Porous Materials conference, Cardiff, UK (2019)

- bp-ICAM annual conference, Manchester, UK (2018)

STATEMENT OF ORIGINALITY

I hereby declare that the work presented in this thesis is my own and that all else is appropriately referenced.

COPYRIGHT DECLARATION

Signed: *Anouk L'Hermitte*

Date: 30/03/2023

ACKNOWLEDGMENTS

TABLE OF CONTENTS

LIST OF FIGURES

LIST OF TABLES

CHAPTER 1: INTRODUCTION

1.1. Background

Industrial separation processes account for 10-15% of the global energy consumption.[1] In particular, distillation, in which mixtures are separated based on the volatility of their species, is highly energy-intensive as it requires a large amount of energy for vaporization. Therefore, the development of energy-efficient separation technologies is critical to limit energy consumption and the associated CO_2 emissions driving climate change globally. One way to achieve this in the context of industrial separations is to move towards adsorption processes, i.e., using porous materials to separate molecules based on their size and/or chemistry.

An example of an inorganic adsorbent is porous boron nitride (BN): this material exhibits high surface area and porosity, and benefits from greater oxidative and thermal stability than common carbonaceous adsorbents.[2] Porous BN has already shown great potential in some gas and liquid separations due its tunable chemistry and pore structure.[3-5] However, research remains at laboratory scale due to a lack of understanding of its formation mechanism, which is largely a 'black box' and prevents scale-up. Partial reaction pathways have been unveiled, but they omit critical steps in the formation, including the porosity development, which is key to adsorption. In addition, the material has displayed hydrolytic instability, which further prevents scale-up.[6] Owing to the presence of moisture in most industrial settings, whether it is for storage or cyclic adsorption processes, ensuring the moisture stability of an adsorbent is crucial. While this topic has been researched for other adsorbents, little is known on controlling the hydrolytic stability of porous BN. Finally, the use of porous BN has mainly been focusing on molecular separations to date, but its material properties could potentially benefit other key adsorption-based applications to reduce energy consumption, such as thermal energy storage.

Thus, my thesis aims to explore further the potential of porous BN through a deeper understanding of its formation, its material properties, its hydrolytic stability, and its performance in adsorption-based applications, such as CO_2/N_2 separation and thermochemical energy storage.

1.2. Personal motivation

After my Master's degrees, I started working in R&D in the food industry. While the job was enjoyable and I learnt a lot about food science, I quickly realised that more fundamental science, especially chemistry, was lacking to fully satisfy me from a professional perspective. In parallel, I was reading more and more about climate science, and I felt that I should be doing more to contribute to the energy transition. With all of that in mind, I applied for this PhD project with Prof. Camille Petit at Imperial College London. This project was shared between the Department of Materials (through the CDT in the Advanced Characterisation of Materials) and the Department of Chemical Engineering (through the bp-International Centre for Advanced Materials), which promised to bring a great balance between fundamental science and energy-related applications, as well exemplified by my thesis content summarized in the following section.

1.3. Thesis content

This thesis consists of eight chapters, including this introductory Chapter 1. Chapter 2 presents the background and the state of the art related to my research, before covering in Chapter 3 the research gaps identified from the literature review, and my research objectives. Chapter 4 describes the materials and methods used during my PhD. Chapters 5 to 7 present the results and discussions originating from my PhD, each of these chapters being based on a sub-project

linked to porous BN. Finally, Chapter 8 brings this thesis to an end with a conclusion and a perspective on future work. Further results that are not crucial to the main messages of the results chapters, yet bring complementary information, are shared in Appendices.

CHAPTER 2: LITERATURE REVIEW

Some aspects of discussion described in this chapter have been published by the thesis author in the Journal of Physical Chemistry C,[7] in Microporous and Mesoporous Materials,[8] and in Accounts of Materials Research.[9]

2.1. Overview

This chapter begins with an introduction of boron nitride (BN) materials before focusing on porous BN, which is at the core of this thesis. After reviewing the features of BN materials, I explore the main synthesis routes to produce porous BN and I investigate past knowledge on its formation mechanism. This allows me to understand better how this material is synthesized and how successful scale-up can be achieved at industrial scale. I then look at the hydrolytic stability of porous BN and I carry out a literature review on methods used on other adsorbents to improve their moisture stability, to potentially apply these findings to porous BN. In the following section, I first cover fundamentals of adsorption theory and explain how adsorption is relevant for molecular separations. I then review the key properties of adsorbent materials and how they are assessed, before examining the properties of porous BN that could be relevant to adsorption-based applications. This leads me to look at separations that have been using porous BN as an adsorbent, in particular CO_2/N_2 separation in the context of CO_2 capture. Finally, I open up my thinking towards a different adsorption-based application, i.e., thermal energy storage using adsorption. After reviewing the different types of thermal energy storage with a particular focus on adsorption thermal energy storage, I survey which properties are sought when selecting an adequate adsorbent/adsorbate working pair. I then present an overview of adsorbates that could be paired with porous BN based on heat of adsorption and

energy storage density values reported for materials presenting similar structure or chemistry to porous BN.

Based on this literature review chapter, I have identified research gaps and subsequently drawn research objectives, which are presented in the next chapter of this thesis (Chapter 3: Research Gaps and Objectives).

2.2. Boron nitride (BN) materials

2.2.1. BN allotropes

Boron nitride is a chemical compound made of alternatively-bonded boron and nitrogen atoms with the chemical formula BN. It exists under different allotropic forms shown in **Figure 2.1**: cubic BN (c-BN), wurtzite BN (w-BN), rhombohedral BN (r-BN), turbostratic BN (t-BN), amorphous BN (a-BN) and hexagonal BN (h-BN).[9-11] c-BN and w-BN exhibit sp^3 bonds, whereas r-BN, t-BN and h-BN exhibit sp^2 in-plane bonding with different stacking arrangements.[9, 11] Different morphologies with the hexagonal lattice of h-BN exist, such as 2D BN nanosheets (BNNS), 1D BN nanotubes (BNNTs) and 0D fullerene (**Figure 2.1**). Finally, a-BN has a highly disordered structure formed from sp^2 hybridized atoms. BN is often compared to carbon-based compounds since the two families of materials share a similar crystallography. For example, h-BN can be linked to its carbon analogue graphite, owing to its regular stacked structure of BN nanosheets, leading sometimes to the name of 'white graphene' for a single or a few sheets of h-BN. Similarly, c-BN is analogous to diamond, the cubic form of carbon materials.
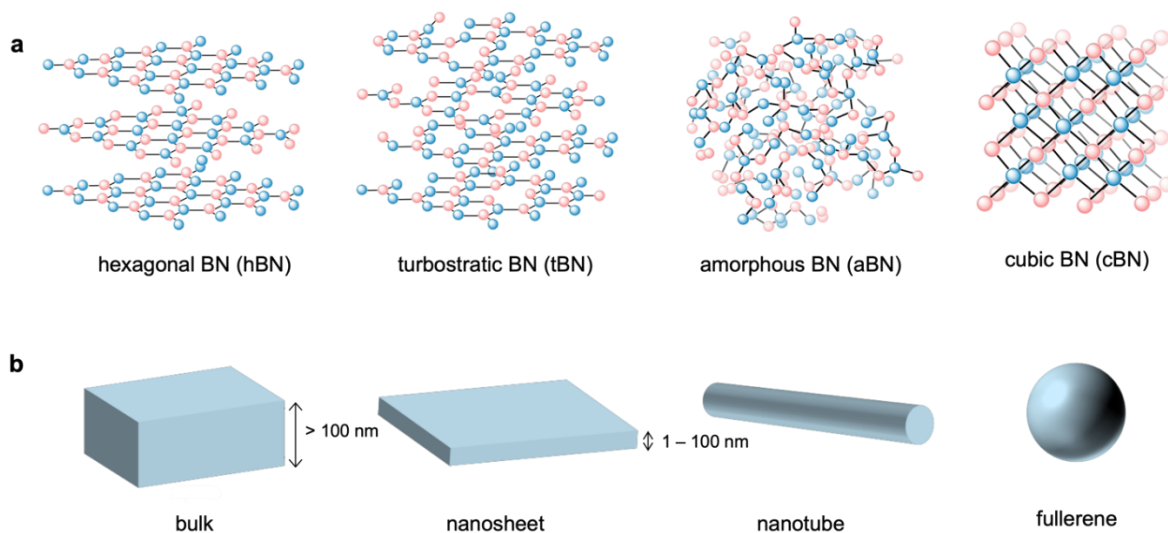
Figure 2.1 (a) Overview of some of the allotropic forms of boron nitride (BN) (not inclusive of all crystal structures); (b) Possible morphologies of BN materials. Reproduced with permission from reference [9]. Copyright 2023 American Chemical Society.

h-BN has attracted a lot of attention as it benefits from advantages over graphite thanks to the heteroatomic bond B-N. Indeed, h-BN exhibits high oxidative stability, alongside high thermal and mechanical resistance.[12, 13] Furthermore, the B-N bond is partially ionic contrary to the C-C bond.[2] This is due to the electron pair involved in the sp^2 hybridization mainly localized around the N atoms, which are more electronegative than B atoms. h-BN is non-porous, exhibiting a d-spacing between sheets of about 3.3 Å,[14, 15] which is very similar to graphite materials.[16] N_2 sorption measurements (see section 2.3.1.4) would not record any surface area between the sheets, since the kinetic diameter of N_2 is 3.6 Å. Any porosity observed in h-BN materials would arise from defects in the structure.[17] Among the BN forms previously mentioned, those relevant to adsorption (which is the focus of this thesis) are those exhibiting porosity, i.e., turbostratic and amorphous BN, forming what we call porous BN. t-BN is of great interest as far as adsorption is concerned due to the disordered stacking of BN nanosheets, leading to higher d-spacing between each sheet than h-BN.[18, 19] These properties are linked to higher specific surface area and porosity in t-BN than in h-BN. a-BN also displays high surface area due to a large number of stacking and vacancy defects, as well as impurities in the

structure, which will be discussed in section 2.2.2. Finally, like h-BN, t-BN and a-BN benefit from significant thermal and oxidative stability, and high mechanical resistance.[12, 13]

2.2.2. Porous BN

As mentioned previously, porous BN is mainly composed of disordered phases t-BN and a-BN, but it can also contain crystalline h-BN domains in its structure. Porous BN exhibits defects, which can be lattice vacancies, as well as O or C atoms in the structure, referred to as impurities. These impurities come from the precursors used to synthesize porous BN: B-containing precursors often contain O atoms, and N-containing precursors usually contain both C and O atoms. As shown in **Figure 2.2**, O impurities can replace N atoms (replacing B atoms would not be favoured due to structural deformations[20]), forming B-O, O-N or O-H bonds.[14] C impurities can replace B or N atoms, forming C-B, C-N or C-C bonds.[21]
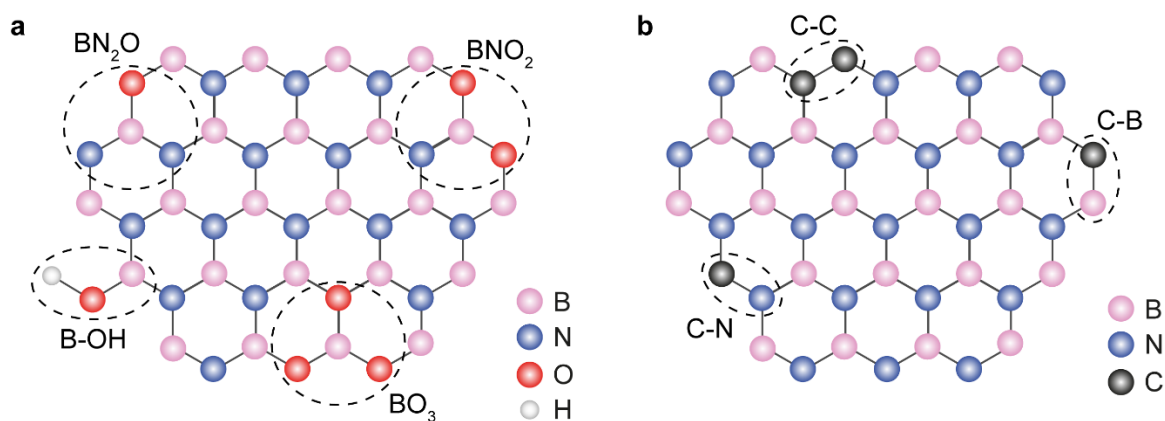
Figure 2.2 Schematic representation of the structure of a BN nanosheet showing the possible configurations for: (a) oxygen impurities and (b) carbon impurities.

In terms of atomic composition, porous BN materials typically contain 43-52% of B atoms, 31-49% of N atoms, 2-21% of O atoms and 2-20% of C atoms.[3-5, 7, 22-25] These contents depend on

the precursors and synthesis conditions (see section 2.2.3). It is worth noting that it is possible to obtain higher contents of C, making up what one could call boron carbon nitride (BCN),[26] but I made the choice not to consider such materials in this thesis since high amounts of C would influence the properties of BN. Higher O contents would lead to unstable structures.[27] The existence of all these defects in the structure of porous BN allows tuning the properties of the material based on the application targeted. For instance, changes in atomic contents will have an impact on the adsorptive and catalytic properties of porous BN.[3-5, 25] One can also look at using the O impurities present in the form of OH groups to functionalize the surface of the material. However, these O impurities have also been linked to moisture and water instability (see section 2.2.5).[6]

In section 2.3.2.1, I will discuss porous BN's sorption properties, but it is worth mentioning here that porous BN materials typically exhibit surface areas between ~100 and 2000 m^2 g^{-1} depending on the production method used and the reaction conditions.[28, 29]

2.2.3. Synthesis of porous BN

2.2.3.1. Review of the synthesis routes of porous BN

There are two different ways of producing porous BN: top-down synthesis and bottom-up synthesis. Top-down synthesis involves the exfoliation of crystal layers from a BN substrate. This can be done via mechanical exfoliation, such as ball milling,[30] or via chemical exfoliation.[31, 32] Bottom-up synthesis consists in producing BN from N-containing and B-containing precursors. Chemical blowing,[28, 33] chemical vapor deposition,[34, 35] solvothermal reaction[36] and high-temperature reaction[37] are among the bottom-up synthesis routes used to produce porous BN. Chemical blowing relies on blowing H$_2$ gas through a previously heated B-containing and N-containing precursor, creating B-N-H polymer structures with large

bubbles, which then collapse to form h-BN nanosheets with moderate surface areas of ~130 m^2 g^{-1}.[33] Chemical vapor deposition is preferred for applications requiring smaller amounts of material than for adsorption as it only produces a few layers of BN.[34, 35] In solvothermal synthesis, N- and B-containing precursors dispersed in a solvent, for instance benzene, are heated in an autoclave, usually below 500 °C.[36] The need for potentially toxic solvents followed by washing and separation steps makes this method less desirable. Finally, high-temperature reactions can be of various sorts, mainly template-based or template-free. Template-based synthesis employs a porous template, and BN is grown on its surface prior to the template removal. Templates can be solid mesoporous materials such as silica or carbon compounds, which mainly lead to the synthesis of mesoporous BN materials.[37, 38] Direct high-temperature synthesis without a template can be carried out under a controlled atmosphere. This method is practical and usually leads to high yields, high surface area and allows the tuning of the resulting product features.[3, 4, 39-41] In this PhD, I exclusively used a bottom-up synthesis via pyrolysis of B-containing and N-containing precursors under controlled atmosphere, and therefore I will focus on this for the rest of this thesis.

2.2.3.2. *High-temperature synthesis under controlled atmosphere*

In a typical high-temperature synthesis, B- and N-containing precursors, either solid or gaseous, are subjected to a high temperature treatment (> 800 °C) under a dynamic flow of a controlled atmosphere. Possible gases for the synthesis include N$_2$ and NH$_3$, which can also act as N-containing precursors in the reaction. The solid B- and N-containing precursors can be physically mixed, or first dissolved in a solvent and dried to form a solid intermediate that is then heated. The overall synthesis scheme is summarized in **Figure 2.3**.

1. Precursors selection		2. Mixing	3. Heat treatment
B-precursor	**N-precursor**	**Physical mixing**	**Atmosphere:** N_2, NH_3, Ar, H_2
Boric acid	Melamine	or	**Temperature:** 800-1800 °C
Boron trioxide	Urea	**Dissolution in solvent**	**Dynamic flow**
Ammonia borane	Biuret	**+ drying**	
HMTA			
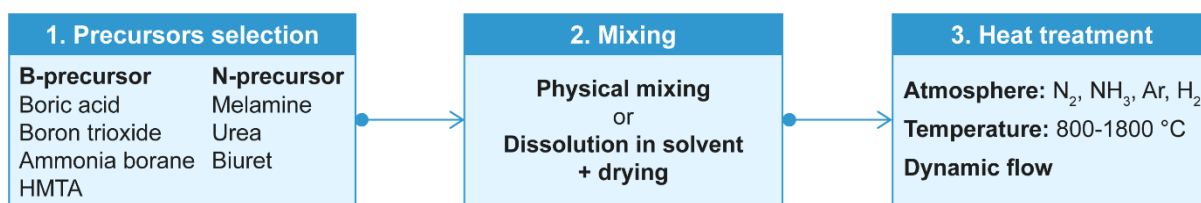
Figure 2.3 Schematic of the synthesis steps to produce porous BN with examples of precursors (HMTA = hexamethylenetetramine). Reproduced with permission from reference [9]. Copyright 2023 American Chemical Society.

Herein, we discuss the effect of synthesis parameters on porous BN and provide a summary later on in **Table 2.1**.

• *Mixing method:* Marchesini et al. investigated the preparation of a precursors mixture (boric acid and urea) to understand how to maximize surface area and porosity in porous BN.[4] The precursors mixture was first dissolved in water, before being dried for various times (between 0 and 200 h). A physical mixture without any solvent addition was also used for synthesis to compare the resulting porous BN materials. For each preparation, the synthesis was carried out at 1050 °C under N_2. This study showed that the drying time had a significant impact on the specific surface area of porous BN, which increased from ~400 to 1000 m^2 g^{-1} as drying time increased up to 200 h. Interestingly, the physical mixture of boric acid and urea led to a similar surface area as with the mixture drying for 200 h. Considering the experimental steps and time associated with both methods, the physical mixture was retained as standard preparation step in our laboratory.[3]

• *Choice and quantities of precursors:* Marchesini et al. and Shankar et al. showed that the nature and relative quantity of the precursors help tune the porosity of porous BN,[3] and the C and O contents.[25] In particular, using several N-containing precursors was shown to enhance the surface area and porosity of the final material.[3] The initial synthesis method in our laboratory was a high-temperature synthesis carried out under N_2 flow, using boric acid and a

N-containing precursor chosen among biuret, melamine and urea (**Figure 2.4**a).[4] This reaction led to porous BN as a white mixture of flakes and powder. In a follow-up study, Marchesini et al. investigated the impact of the choice of precursors and their relative quantities on the synthesis of porous BN.[3] This led to a novel method with optimized conditions to produce porous BN with tunable porosity and higher specific surface area, i.e., 1900 m^2 g^{-1}.[3] This synthesis involves the use of boric acid, melamine and urea in molar ratios of 1:1:5, which are physically ground and reacted under N_2 at 1050 °C (**Figure 2.4**b). The different thermal decomposition profiles of the three precursors lead to distinct release time frames of gases while the synthesis temperature is increasing, therefore creating different types of pores in the final product.[3] This creates a hierarchical pore structure in the material, increasing its surface area and porosity, desirable for sorption applications. This synthesis method was the one solely used in this thesis, therefore some of its mechanistical aspects will be further discussed in section 2.2.4. In terms of precursors, Weng et al. suggested that primary and secondary amine precursors should be preferred over tertiary amine precursors as they lead to a lower energy barrier for reaction with boric acid.[27]
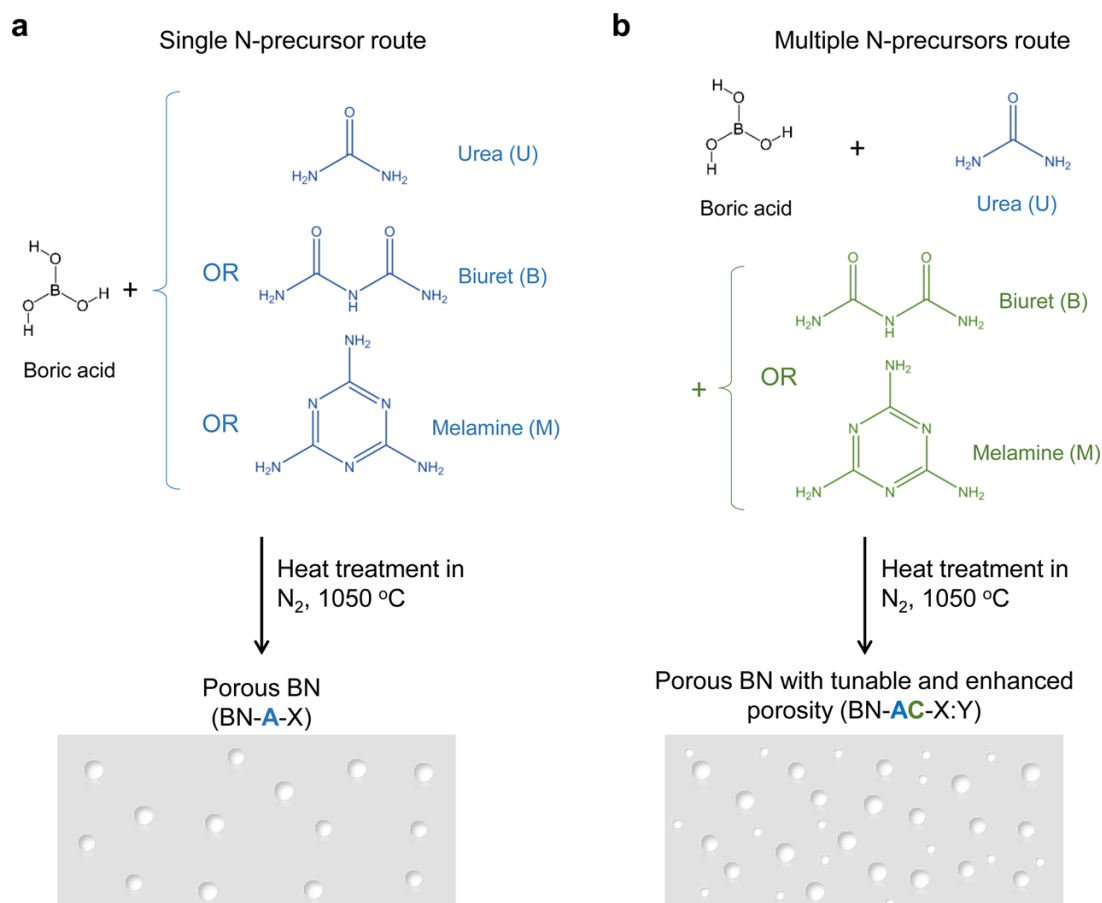
Figure 2.4 Schematics of: (a) single N-containing precursor route and (b) multiple N-containing precursor route for the synthesis of porous BN. Reproduced with permission from reference [3]. Copyright 2017 American Chemical Society.

• *Reaction atmosphere:* the nature of the reaction atmosphere influences both the porosity and composition of porous BN. Studies published in my laboratory during my PhD showed that, for instance, synthesis under NH_3 as opposed to N_2 provides more reactive N atoms, ensures the complete reaction of the B-containing precursors, and limits carbonization, thereby enhancing the porosity and limiting the presence of carbon impurities.[38, 42]

• *Flow rate:* the flow rate drives the reaction gas residence time and that of the gaseous intermediates formed. Hence, it can a priori impact how these species interact with the solid precursors and reaction intermediates, and thereby could have an effect on the composition of

the final porous BN. There is no proof of a strong correlation between flow rate and BN composition, though in some instances, a higher flow rate caused fewer C and O impurities.[25]

• *Temperature:* although not much is known about the optimal synthesis temperature range, a study published during my PhD showed that increasing the synthesis temperature tends to reduce O and C contents in the final porous BN materials.[25] This was expected as a higher temperature will drive the reaction further towards the formation of BN. It was also observed that crystallization occurs beyond a certain temperature, causing the surface area to decrease due to lower interplanar d-spacing and greater structural order in h-BN compared to porous BN.[25, 42] The exact temperature at which this transition happens remains unknown.

A summary of the previous findings is provided in **Table 2.1** below.

Table 2.1 Synthesis parameters and their impact on the resulting BN material (SSA = specific surface area). Adapted with permission from reference [9]. Copyright 2023 American Chemical Society.

Variable	Impact	Comments	Ref.
B-precursor	Purity	O content ↑: purity ↓	[3]
N-precursor	Reaction rate	Primary or secondary amines: reaction rate ↑	[25]
	Purity	Primary or secondary amines: purity ↑	[25]
	Porosity/surface area	> 1 N-precursor: porosity and SSA ↑	[3]
Mixing method	Porosity/surface area	Drying time ↑: porosity and SSA ↑	[4]
		Physical mixing: high porosity	[4]
Atmosphere	Purity	NH_3 vs. N_2: carbonization ↓ and purity ↑	[38, 42]
	Porosity/surface area	NH_3 vs. N_2: porosity ↑	[38, 42]
Flow rate	Purity	Flow rate ↑: O and C contents ↓	[25]
Temperature	Purity	T ↑: O and C contents ↓	[25]
	Porosity/surface area	1000-1500 °C: crystallization ↑, and porosity and SSA ↓	[25, 42]

2.2.4. Formation mechanism of porous BN

To date, few studies have investigated the mechanism of porous BN formation via bottom-up synthesis, from both a chemical and a textural perspective.[4, 14, 42-44] Most report the formation of hexagonal boron nitride (h-BN), the non-carbonaceous analogue of graphene with no or low surface area (< 100 m^2 g^{-1}) compared to porous BN.[17, 19] In all the studies of h-BN and porous BN, a few reactions have been suggested that account for the formation from B- and N-containing precursors, but there is no consensus to date for a comprehensive reaction scheme with respect to the thermal treatment. In addition, reported syntheses use different reagents, gas atmospheres and reaction conditions, which impact the formation process and resulting product. Herein, I will focus on mechanisms accounting for boric acid, urea and/or melamine or their direct intermediate products, such as boron oxide and ammonia, to remain within the scope of this thesis (see section 2.2.3.2). Literature review mostly covers h-BN, but the mechanisms underlying its formation are likely to be close to those for porous BN. I assume the differences will be mostly due to experimental conditions, such as final synthesis temperature for a given set of reagents.

In 1992, a mechanism for the formation of h-BN was proposed by Brožek and Hubáček based on the reaction between boric acid and ammonia up to 850 °C as shown in reaction (1):[14]

$$B_2O_3 + 2\,NH_3 \rightarrow 2\,BN + 3\,H_2O \quad (1)$$
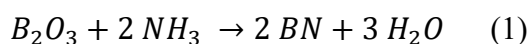
In more detail, Brožek and Hubáček suggested that boric acid and ammonia first formed a compound HNBOH and water, due to electronic displacement in the precursors leading to new bonds formation. Three molecules of HNOBH could then undergo a reorientation and form a trimer starting the BN structure with a six-atom ring (NH$_3$)(BOH)$_3$ composed of an alternance of B and N atoms (**Figure 2.5**a). From there, propagation started and gradually added BN rings

to form h-BN (**Figure 2.5**b). They also accounted for O impurities substituting N atoms in the

BN structure (**Figure 2.5**c).
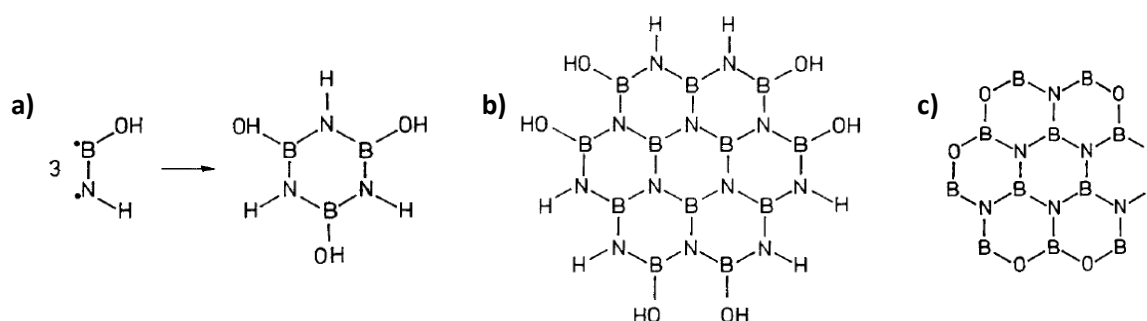
Figure 2.5 Suggested schematics of: (a) the formation of a BN trimer from an HNBOH compound; (b) the BN network following propagation; (c) the final h-BN structure with O impurities substituting N atoms. Reproduced with permission from reference [14]. Copyright 1992 Elsevier.

More recently in 2018, Ramirez Leyva et al. suggested a reaction scheme for the formation of

'h-BN' from a preparation of boric acid and melamine dissolved in water and dried before a

two-step heating treatment (500 °C in air, followed by 1200 °C under argon).[43] Although they

referred to their material as h-BN, they showed that it became highly porous as temperature

increased during its formation, which implies they in fact obtained porous BN. The overall

mechanism suggested that various intermediates were formed, in particular urea and boric

oxide, prior to the formation of BN, CO_2 and water between 500 °C and 750 °C. This seemed

to omit an important mechanistic event, considering that urea is sometimes used as a precursor

from the start, and that boric oxide starts forming around 130 °C, i.e., early in the reaction.[43] In

2020, Wu et al. proposed a mechanism for the formation of BN fibers from melamine

diborate.[44] Their thorough investigation of reaction intermediates gave insight into how those

fibers are formed, echoing the reaction suggested earlier by Brožek and Hubáček (reaction

(1)),[14] but porosity was not mentioned at all in this study. In 2021, Tian et al. suggested a

formation mechanism of structured porous BN obtained from the pyrolysis of a melamine-

formaldehyde resin in ammonia.[42] Although the experimental conditions vary significantly from the method used in this thesis, the findings can be relevant and also agree with reaction (1) presented above. A recent study by Gross and Höppe reported ammonium bis(biureto)borate as a crucial intermediate when using boric acid and urea under N_2 to form h-BN.[45] Their study could be valuable to understand better the steps of the formation of BN materials, but there was no mention of porosity as their material was crystalline and non-porous.

In 2014, Gong et al. offered a different perspective to the previous studies.[46] The authors demonstrated the chemical conversion of graphene into carbon nitride and h-BN upon heat treatment, using ammonia as a source of nitrogen and boric acid as a source of boron. This means that graphene could act as a template to form crystalline BN. Although this synthesis may still involve the reaction shown earlier in reaction (1) (no mention is made in the study), it also opened a new avenue into how one can form BN, since the other studies did not take into consideration the potential formation of a carbon nitride intermediate. In the same year, Hoffendahl et al. also indicated the formation of carbon nitride when synthesizing BN, this time from melamine and boric acid.[47] However, they still referred to the reaction of boron oxide with ammonia to form BN (reaction (1)), without mentioning carbon nitride.

In summary, although no detailed formation mechanism has been confirmed and the synthesis parameter space (i.e., precursors, atmosphere, temperature) varies from study to study, two possible mechanisms to form porous or non-porous BN seem to emerge. These two mechanisms were reported in a study by O'Connor[48]: (i) nitridation of boron oxide with ammonia either from the reaction atmosphere or from decomposition of N-containing precursors and (ii) annealing of carbon nitride with B atoms from boron oxide. The two mechanisms may not be mutually exclusive and may also depend on the synthesis parameter space. Under the former mechanism fall the studies by Brožek and Hubáček,[14] Ramirez Leyva

et al.,[43] Wu et al.,[44] Tian et al.[42] and Hoffendahl et al.[47] The second category includes the work by Gong et al.[46] As mentioned earlier, Hoffendahl et al.[47] indicated the formation of carbon nitride from melamine but referred to the reaction of boron oxide with ammonia to eventually form BN. Among all the above studies, only those of Ramirez Leyva et al.[43] and Tian et al.[42] cover the formation of porous BN specifically, and they link the porosity development to gases released during the reaction, as suggested by an earlier study in our research group.[4]

2.2.5. Hydrolytic stability of porous BN

2.2.5.1. State-of-the-art

Past studies have pointed towards the instability of porous BN in the presence of water or moisture.[6, 9, 15, 21, 49-54] However, studies reporting on adsorption with BN materials in aqueous media show that porous BN can be regenerated and reused several times without significantly losing adsorption performance, as seen for instance in a study by Feng et al.[55] After synthesizing porous BN via pyrolysis, they washed the material in water and dried it before any sorption measurement. Porous BN was added into acidic aqueous solutions and regenerated through calcination between each test. Although the BN material seemed to retain its sorption capacity, parameters such as specific surface area, micropore volume or elemental composition were not assessed between each cycle. A decrease in porosity may happen in certain circumstances without changing the overall adsorption performance for a small number of cycles. However, this may not be acceptable for some applications, depending on the scale and the environment involved. Indeed, several studies suggested reaction (2) to account for BN's hydrolysis:[6, 21, 52-54]

$$2\,BN_{(s)} + 3\,H_2O_{(l)} \rightarrow B_2O_{3\,(s)} + 2\,NH_{3\,(g)} \qquad (2)$$
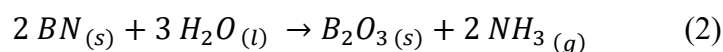
To date, the main factor identified as influencing the hydrolytic stability of porous BN materials is the synthesis temperature. For instance, research from 1982 investigated amorphous BN films deposited by chemical vapor deposition (CVD) at various temperatures.[49] Films deposited at 450 °C were unstable with respect to moisture and would gradually dissolve in water, whereas films deposited above 600 °C were highly stable. In 1989, Matsuda also deposited BN via CVD and observed that BN plates prepared under 1400 °C were unstable with moisture, and that the stability of BN decreased as the synthesis temperature was lowered.[50] Matsuda showed that in unstable samples, ammonium borate hydrates were formed after deposition from the reaction between BN and moisture in the atmosphere. Later in 1997, Alkoy et al. showed that t-BN materials exhibited degradation into an ammonium borate complex ($NH_4 \cdot B_5O_8 \cdot 4H_2O$) after prolonged storage in air.[19] They also showed that when synthesizing the material at higher temperature (> 1500 °C), higher crystallization was achieved and led to greater stability. However, a higher synthesis temperature was also linked to a decrease in surface area in the resulting BN material, which may be detrimental to adsorption applications. Recent work in our group further proved a significant degradation of porous BN under humid or wet conditions (**Figure 2.6**).[6] Porous BN materials were synthesized at two different temperatures: 1050 °C or 1500 °C. Nitrogen sorption isotherms were run at – 196 °C to characterize the specific surface area and the porosity of porous BN before and after water exposure via dye sorption testing in aqueous solutions. Firstly, all samples showed a significant decrease in specific surface area and pore volume after water exposure. However, the sample synthesized at 1050 °C demonstrated a sharper decrease in textural parameters. The sample synthesized at 1500 °C appeared to be more resistant and stable over time. It was observed that samples with higher micropore volume before water exposure were the most sensitive to water exposure. These results led to the assumption that micropores may constitute target sites during water degradation. Highly microporous BN materials are also assumed to

present more defect sites, leading to faster water degradation. Echoing these findings, Hojak et al. demonstrated that mesoporous BN exhibited greater water stability than microporous BN, thanks to a higher content of crystalline domains in the structure.[51]
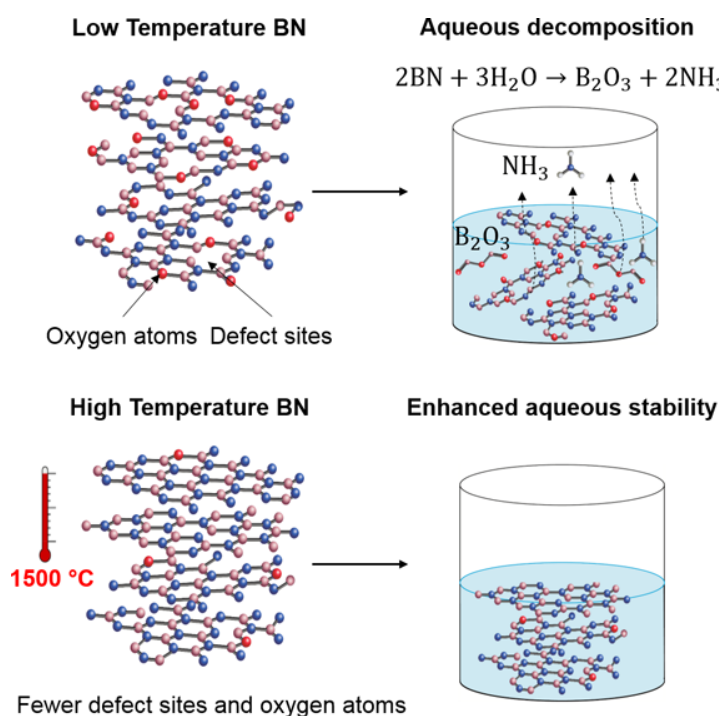
Figure 2.6 Effect of the synthesis temperature of porous BN on its water stability. Reproduced with permission from reference [6]. Copyright 2019 American Chemical Society.

In 1995, Cofer and Economy investigated the relationship between the crystalline structure of t-BN and its stability towards water and moisture,[15] bearing in mind that the crystalline structure is directly influenced by the synthesis temperature. Thermogravimetric analysis in air saturated with water was carried out at 700 °C to analyze the accelerated hydrolysis of BN samples with various interlayer d-spacing values (between 3.3 Å and 3.7 Å). BN samples with larger d-spacing were more sensitive to water and converted faster into boron oxide B_2O_3 compared to samples with d-spacing closer to h-BN's theoretical value, i.e., 3.3 Å. The same experiment carried out in pure N_2 (without O_2) saturated with water at 700 °C led to similar

results, confirming that the crystalline structure was the predominant factor in this experiment. The authors hypothesized that a larger d-spacing involved weaker bonds and interactions between the h-BN sheets, facilitating water attack.

In addition, our group identified that water instability in porous BN could be linked to the presence of oxygen in the material,[6] which is also correlated with the synthesis temperature. When synthesizing porous BN at higher temperature (1500 °C instead of 1050 °C), the resulting material exhibited fewer O impurities and fewer defect sites. This was regarded as, at least partially, responsible for increased stability in the presence of water. Lin et al. showed that it was possible to use sonication in water to hydrolyze BN nanosheets, relying on mechanical agitation to foster hydrolysis and segregate BN layers.[56] The authors then assumed that water molecules targeted primarily BN bonds near defect sites and the OH groups. A chain process could start with defects propagating, leading to bond cutting and smaller sheets of BN. On the other hand, Cao et al. assumed a predominant role of residual N-H bonds in the hydrolytic instability of BN.[52]

To summarize, increasing the synthesis temperature of porous BN is linked to higher crystallinity, lower porosity and fewer defects in the final porous BN samples,[57] leading to less intercalation of water molecules, and thus greater hydrolytic stability.

2.2.5.2. *Surface functionalization to enhance hydrophobicity*

Hydrolytic instability has already been highlighted extensively for other classes of inorganic and organic adsorbents, such as zeolites[58, 59] and metal organic frameworks (MOFs).[60-65] To tackle this issue, methods involving surface functionalization have been used to reduce the interaction of the adsorbent with water and prevent its degradation over time and repeated use. For instance, zeolites have been functionalized via the grafting of organosilanes onto their OH

groups,[66-68] whereas MOFs have been coated with a hydrophobic polymer, like polydopamine.[69] With the right experimental conditions and chemicals, such methods allow to make these adsorbents more hydrophobic and resistant to water, while retaining adequate surface area for adsorption applications.[66, 67, 69] Herein, I will review different functionalization methods that could potentially be applied to porous BN.

• *Organosilane grafting:* organosilanes have been used for years to tune the hydrophobicity of surfaces.[70-72] They contain an alkyl chain (usually hydrophobic) bonded via a silicon atom to one to three functional groups, which can interact with OH groups at the surface needing functionalization (**Figure 2.7**). These interactions can be via hydrogen bonding or covalent bonding. The alkylsilane molecules also react with each other depending on the number of functional groups available and can form a polymeric network leading to denser coverage of the material's surface (**Figure 2.7**). This way, grafted organosilanes create a hydrophobic barrier preventing water from interacting directly with the material structure.
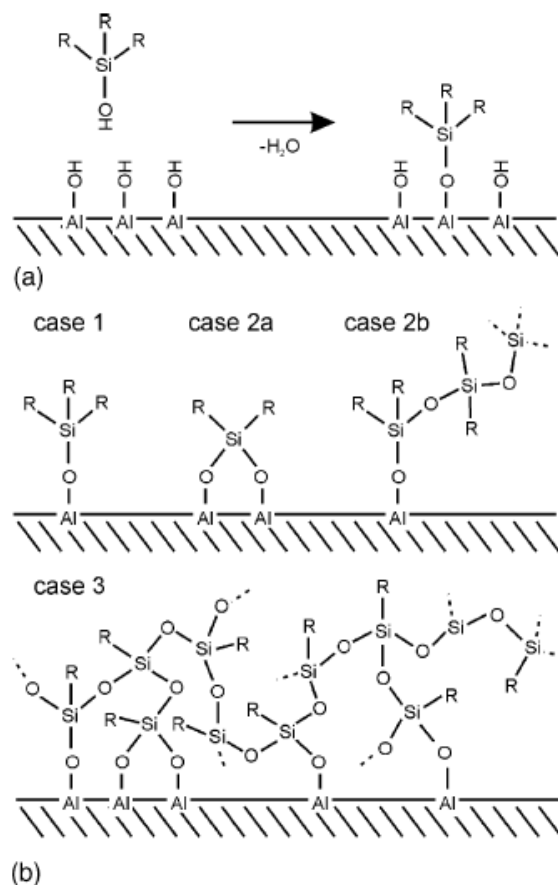
Figure 2.7 (a) Representation of the grafting of a surface containing OH sites using a mono-functional alkylsilane agent. (b) Representation of the possible grafted structures forming on a hydroxylated surface. Case 1: mono-functional alkylsilane anchoring to one OH site. Case 2a: bi-functional alkylsilane anchoring to two OH sites. Case 2b: bi-functional alkylsilane anchoring to one OH site and forming a polymerized chain with other alkylsilane molecules. Case 3: tri-functional alkylsilane forming a polymerized layer at the surface via numerous OH sites. Reproduced with permission from reference [72]. Copyright 2004 Elsevier.

Han et al. functionalized ZSM-5 zeolites with alkyl-trichlorosilanes ($CH_3(CH_2)_nSiCl_3$ with $n =$ 7; 9; 11 or 15) to tune their hydrophobicity.[66] The superficial layer of alkyl chains on the zeolites converted them from hydrophilic to hydrophobic, as shown by water contact angle measurements, even more so as the length of the alkyl chains increased. They showed that the functionalized ZSM-5 zeolites were stable for applications under 250-300 °C depending on the length of the alkyl chains chosen. Above this range of temperature, the hydrophobic layer was degraded, leading back to a hydrophilic zeolite. Some types of zeolites are also known for being highly unstable in hot liquid water.[58] In the presence of steam, some zeolites decompose

49

following a dealumination process (i.e., hydrolysis of Si-O-Al bonds), whereas a different mechanism has been suggested in hot liquid water: the hydrolysis of Si-O-Si bonds. To increase the hydrophobicity of HY zeolites and enhance their stability in water at 200 °C, Zapata et al. functionalized their surface with alkylchlorosilanes of various lengths ($CH_3(CH_2)_nSiCl_3$ with n = 2; 6 or 18).[68] In their earlier study, it was already shown that the hydrophobization process did not significantly modify the crystallinity, surface area, microporosity and density of acid sites in HY zeolites.[67] They also showed that heating the functionalized zeolites at 200 °C did not alter the grafted alkyl groups. To assess the stability of the zeolites, the authors exposed the untreated and functionalized zeolites to water vapor or liquid water, and they measured the crystallinity (with XRD), and surface area and pore volume (with N_2 sorption at –196 °C) before and after exposure. When using water vapor, they observed that the degradation of the zeolites was mainly due to condensed water.[68] Therefore, they focused their work on liquid water. The choice of alkylchlorosilane used for grafting depended on the environment considered.[68] The best stability results in pure liquid water were obtained with a high concentration of organosilanes with short alkyl chains, which may protect better small pores in the zeolite. In water/oil emulsions, long alkyl chains allowed a better stability of the zeolite by interacting more with the organic solvent and creating an efficient hydrophobic barrier. Sah et al. used different types of organochlorosilanes (R_x-Si-Cl_{4-x} with R an alkyl chain) to graft on inherently hydrophilic mesoporous γ-alumina membranes and investigated the resulting changes in hydrophobicity and adsorption properties.[72] They used either water-saturated toluene or ethanol as solvent depending on the solubility of the silylating agent. Instead of using a single-layer deposition via hydrolysis followed by condensation, they looked at directly grafting the pores with chlorosilanes by soaking the membrane. They used permporometry to investigate the active pores of their membranes before and after functionalization. To assess the hydrophobicity of their membranes, they carried out liquid permeation experiments with

50

hydrophobic and hydrophilic solvents (e.g., toluene and water). The use of chlorotrimethylsilane ($(CH_3)_3SiCl$) led to a reduced average pore size due to the formation of a monolayer inside the pores and did not lead to significantly enhanced hydrophobicity. On the other hand, trichloromethylsilane (CH_3SiCl_3) led to highly hydrophobic membranes thanks to a dense organosilane network that formed at the surface.

• *Surface coating:* another approach to make a surface hydrophobic consists of first coating it at the particle scale (rather than molecular scale as in the previous approach), and then covalently graft hydrophobic molecules onto this coating. Dopamine has been considered in many studies as a coating to functionalize surfaces, as it is known for its adhesive properties thanks to both catechol and amine functions, which mimic the properties of adhesive foot proteins used by mussels to adhere to wet surfaces.[73, 74] Lee et al. used a dip-coating method to coat various inorganic materials with an aqueous solution of dopamine at pH 8.5.[74] Indeed, the polymerization of dopamine requires a slightly alkaline aqueous environment, which is a limitation when the targeted material is known for being sensitive to water. Yang et al. slightly modified dopamine to tackle this issue.[69] They prepared deprotonated dopamine, which allowed to carry out the reaction under oxygen atmosphere rather than in an aqueous environment. Then, they reacted various MOFs with their polydopamine (PDA) coating followed by fluorination with *1H,1H,2H,2H*-perfluorodecanethiol (HSF), a highly hydrophobic compound (**Figure 2.8**). They first reported a decrease in surface area and porosity after surface modification, which they managed to limit by optimizing the quantity of coating. The greater water stability observed in these MOFs after functionalization was associated to both hydrophobicity and enhanced surface roughness. This coating method could be more widely applicable to porous materials than silylation since the coating can be applied to many types of surfaces. However, this is a highly sensitive protocol requiring anhydrous solvents and an inert atmosphere, making it more difficult to implement.
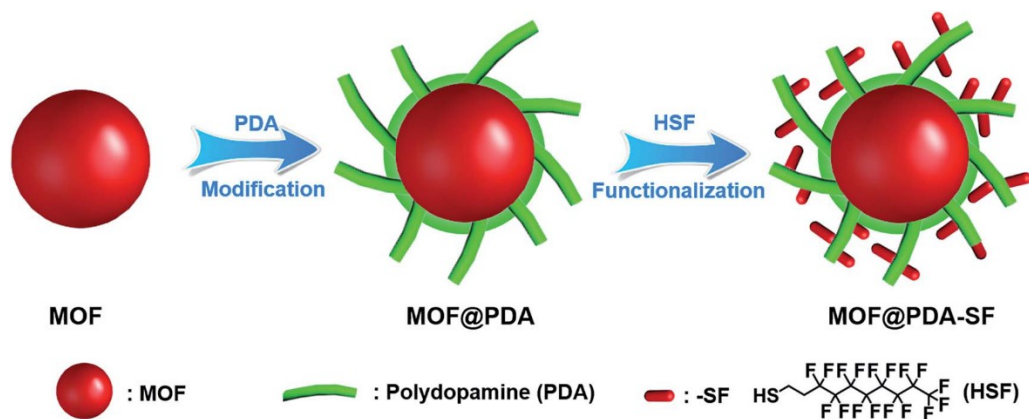
Figure 2.8 Schematic of the modification process used to make a hydrophobic MOF via coating with deprotonated dopamine followed by fluorination. Reproduced with permission from reference [69]. Copyright 2019 Royal Society of Chemistry.

2.3. Porous BN for gas separation via adsorption

2.3.1. Fundamentals of adsorption and adsorbents

2.3.1.1. Overview of adsorption

Since this thesis focuses on porous BN materials for adsorption-based applications, it is necessary to first review the fundamentals of adsorption theory. Adsorption is the interaction and adhesion of fluid molecules (adsorbates) to the surface of a material (adsorbent).[75] It is worth noting that it is a surface phenomenon and should not be confused with absorption, which involves the bulk of a material. It occurs even at the surface of non-porous materials, but it is more significant in the case of porous materials. Adsorption can happen following two mechanisms, namely physisorption and chemisorption.

• *Physisorption* relies on weak interactions, such as Van der Waals forces, making it a reversible phenomenon. Due to low activation energies required and the weak interactions involved, physisorption always occurs, but it is not highly chemically specific. Enthalpy of adsorption values range from 10 to 40 kJ mol^{-1} for physisorption phenomena.

• *Chemisorption* involves strong chemical bonding. Chemisorption is constrained by high activation energies and requires more energy to regenerate the adsorbent than in physisorption. Chemisorption requires specific affinity between the adsorbate molecules and the adsorbent surface, and therefore leads to more specific adsorption than physisorption.[75] Enthalpy of adsorption values range from 40 to 400 kJ mol^{-1} in the case of chemisorption.

2.3.1.2.   Measurement of adsorption

There are two main classes of techniques used to record adsorption: volumetric measurements and gravimetric measurements. Other techniques are possible, such as oscillometry,[76] but they are much less common.

• *Volumetric measurements* record changes in pressure between the manifold of the sorption analyzer and the sample chamber due to adsorption/desorption processes.[75] The number of moles of gas in the manifold volume can be calculated from the pressure and temperature measured at that moment. A valve then opens to let the gas flow into the sample chamber, and the reduction in pressure is measured. The adsorbed amount of gas can be determined from the difference in the number of moles in the manifold before and after the valve opens. To determine the free space (or dead volume), which is the volume of the chamber not occupied by the adsorbent, an inert gas such as helium is used. The assumptions are that helium does not interact with the adsorbent, that it behaves as an ideal gas and that it does not penetrate the pores of our materials.[75] Experimental aspects of volumetric measurements will be explained further in the Methods chapter of this thesis (section 4.3.2).

• *Gravimetric measurements* record the mass of a sample while a gas is introduced in a chamber, which is connected to a microbalance for accurate measurement. The balance measures the difference between the weight force and the buoyancy force of the sample, which

is constantly in contact with the adsorbate.[77] Prior to measurement, the free space is determined similarly to volumetric measurements.

In this thesis, volumetric measurements will be used to determine adsorption isotherms. The isotherms obtained after measurement can be classified into different types based on the IUPAC classification,[78] which gives information on the type of porous or non-porous material investigated. More information on the types of isotherms and their characteristics can be found in **Figure A1.1** in Appendix 1.

2.3.1.3.   Use of adsorption for molecular separations

Adsorption is a key technology to separate and/or store liquid or gaseous molecules as it is less energy-intensive than traditional distillation methods.[1, 79] Adsorbent materials used for molecular separations typically include silica,[80, 81] zeolites,[82-84] metal organic frameworks (MOFs),[85-87] covalent organic frameworks (COFs),[88, 89] porous polymers,[90-92] and activated carbons.[93-97] Adsorption-driven separation of a mixture of species can happen following three mechanisms, which are introduced below and represented in **Figure 2.9**.[98-100]

• *Equilibrium separation (or thermodynamic separation)* happens when the adsorbates are much smaller than the pores of the adsorbent, meaning that there is no diffusional limitation. The physical and chemical properties of the adsorbates are linked to different affinities with the adsorbent, which result in different adsorbate-adsorbent interactions, thus allowing separation. The affinity between an adsorbate and an adsorbent can be estimated by the heat of adsorption.[79] In particular, the adsorbate that displays the higher heat of adsorption is adsorbed the most, and is therefore removed from the mixture. The main disadvantage of equilibrium separation is that all species to separate will have some interactions with the adsorbent, even very small, meaning that no species can be fully removed from a mixture. This will be discussed in section 2.3.1.5 when considering purity and recovery.

• *Kinetic separation* happens when the adsorbates are of similar size to the pores of the adsorbent, and it relies on the different diffusional behaviors of the adsorbates through the pores. The species that diffuses faster is adsorbed the most and can be removed from the mixture. Equilibrium separation may start occurring over time as the slowly-diffusing species gradually reaches equilibrium. Therefore, the time during which the adsorbates are exposed to the adsorbent is key. In particular, a relatively short time would only separate the faster-diffusing component in the mixture.

• *Size-exclusion-based separation* (also known as molecular sieving) occurs when some of the molecules to separate, but not all, have a kinetic diameter larger than the pores of the adsorbent, meaning that they are prevented from diffusing through the pores. Contrary to equilibrium and kinetic separation mechanisms, size-exclusion-based separation can be fully selective if a species is sterically hindered, as it will not be adsorbed at all.
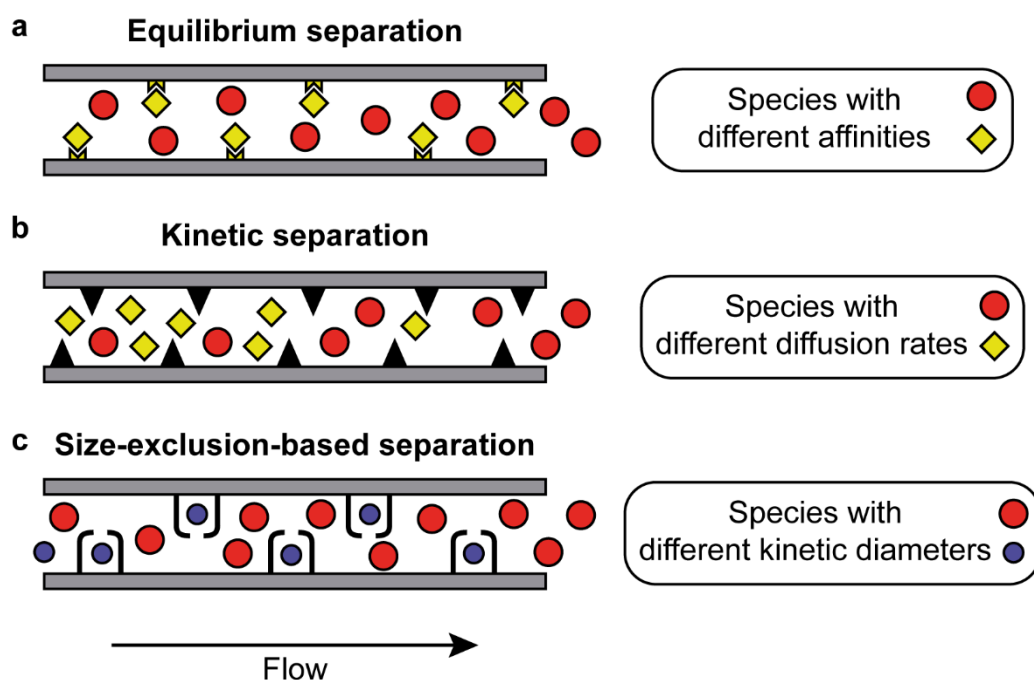
Figure 2.9 Schematic representation of the three separation mechanisms: (a) equilibrium (or thermodynamic) separation; (b) kinetic separation; (c) size-exclusion-based separation (or molecular sieving)

2.3.1.4. Adsorbent properties and their characterization

As seen previously, adsorption-based processes can happen following three mechanisms, which heavily rely on the physical, chemical and textural properties of the adsorbent materials. Depending on the application targeted, adsorbent materials should display a specific range of properties, such as surface area, pore size distribution and surface chemistry, to enhance adsorption uptake and selectivity of an adsorbate. Therefore, methods are required to assess textural and chemical properties.

• *Surface area* is a useful and common metric to compare adsorbents, although other parameters are relevant to determine the best adsorbents for a given application. For any adsorbate, a larger surface area will lead to an increased uptake. While this is desired to accommodate more of an adsorbate, it can also reduce the selectivity of a separation process since the other adsorbates will also be adsorbed more.[99] Among other applications, this is the case in CO_2/N_2 separation

where reducing N_2 adsorption has recently appeared more important than increasing that of CO_2 for a given adsorbent.[101-103]

Surface area is usually determined using nitrogen sorption at -196 °C ($= 77$ K). The adsorption isotherms are fitted to a model, which returns the volume of gas adsorbed in a single layer as a parameter. The equivalent number of molecules in this monolayer leads to the area occupied by one molecule, allowing the calculation of the total surface area of the monolayer.

• *Porosity and pore size distribution* are also key parameters for adsorption applications in terms of adsorbed quantity and specificity. Pores can exist in various shapes, in particular cylindrical or slit-shaped (i.e., parallel plates with spacing in between them). According to the IUPAC classification, pores can be classified into three main categories depending on their size:[78] micropores (≤ 2 nm), mesopores (≥ 2 nm and ≤ 50 nm), and macropores (≥ 50 nm). For pores larger than the kinetic diameter of a given adsorbate, a higher porosity will lead to an increased uptake of this adsorbate. The porosity of an adsorbent also impacts on the diffusion of the adsorbates, in particular the micropore diffusion. To allow better separation, the pore sizes are ideally discriminating between the different adsorbates, but this can be difficult when the adsorbates have very similar sizes.

Materials containing micropores and mesopores are often analyzed using N_2 sorption isotherms at -196 °C and the density functional theory (DFT) to obtain a continuous pore size distribution. However, if an adsorbent is also macroporous, N_2 sorption isotherms are not a reliable method anymore. Instead, one can use mercury intrusion porosimetry (MIP) to assess large pores.[104] In this absorption-based technique, the volume of mercury absorbed by a sample is obtained as a function of pressure, and then pore size. The derivative of this data leads to a pore size distribution.

• *Surface chemistry* is of particular importance to determine the attraction of an adsorbent with a given adsorbate. Tunable adsorbent materials are highly desirable to adjust their chemistry towards a particular separation. For instance, the presence of polar functional groups in an adsorbent can significantly increase the selectivity when separating a mixture of species with different polarities.[79]

The surface chemistry of an adsorbent can be assessed via spectroscopy measurements, such as Fourier-transform infrared spectroscopy (FTIR) and X-ray photoelectron spectroscopy (XPS). Such techniques allow the identification of chemical environments, which help choose an adsorbent to selectively separate an adsorbate.

In addition to the parameters described above, thermal and mechanical stability are desirable for prolonged use and recyclability of an adsorbent. For optimal use, one should also seek fast adsorption/desorption kinetics, low cost of production, mild regeneration conditions, and how to produce structured forms to allow easy handling.

2.3.1.5. Evaluation of separation processes

In this thesis, I have focused on CO_2/N_2 gas separation, which is relevant to the energy sector for post-combustion carbon capture. Post-combustion carbon capture can be applied to coal-fired power plants, gas-fired power plants or the petrochemical industry among other settings. It is often simplified to a CO_2/N_2 separation scenario, neglecting the presence of impurities such as SO_x, NO_x and moisture.[103] CO_2 is called the heavy product (preferentially adsorbed) and N_2 corresponds to the light product.

In separation processes involving two or more gaseous species, each of these components will have interactions with the adsorbent, even if these interactions are very small. In the case of CO_2/N_2 separation with an adsorbent material, this means that it will be impossible to separate

100% of the initial CO_2 content in the flue gas, and that the CO_2 product may still contain residual N_2. This leads to the definition of three main process performance parameters: purity, recovery and working capacity.[103, 105] For a flue gas made of CO_2 and N_2, these three parameters can be calculated using equations (3), (4) and (5):

$$Purity = \frac{n_{CO_2}^{product}}{n_{CO_2}^{product} + n_{N_2}^{product}} \quad (3)$$

$$Recovery = \frac{n_{CO_2}^{product}}{n_{CO_2}^{feed}} \quad (4)$$

$$Working\ capacity = q_{ads,CO_2}^* - q_{des,CO_2}^* \quad (5)$$

with:

$n_{CO_2}^{product}$	moles of CO_2 in the product (mol)
$n_{N_2}^{product}$	moles of N_2 in the product (mol)
$n_{CO_2}^{feed}$	moles of CO_2 in the feed (mol)
q_{ads,CO_2}^*	equilibrium loading of CO_2 at adsorption conditions (mol kg^{-1})
q_{des,CO_2}^*	equilibrium loading of CO_2 at desorption conditions (mol kg^{-1})

In the case of carbon capture and storage (CCS), a purity of at least 95% of CO_2 and a recovery of at least 90% of CO_2 are usually required, as advised by the US Department of Energy. The effluent, mainly composed of N_2, is released into the atmosphere, thus there are no purity and recovery requirements for N_2. Ideally, the adsorbent material does not degrade over repeated cycles, so that purity, recovery and working capacity remain constant. It is worth noting that the cost of a process is also crucial when looking at the viability of a separation process.

2.3.2. Porous BN: a promising adsorbent

Promising examples in the literature of gas sorption with porous BN relying on its great textural and chemical properties include CO_2 capture,[4, 106] CO_2/CH_4 separation,[107] paraffin/olefin

separation[108] for pollution reduction and H_2 storage[39, 109] for renewable energy production. Liquid separations tested with porous BN include water cleaning through removal of inorganic pollutants[39] and organic pollutants, such as organic solvents, dyes and oil.[110] In this thesis, the focus is on CO_2/N_2 gas separation in the context of post-combustion carbon capture.

2.3.2.1. Properties of porous BN for CO_2/N_2 separation

In this section, the properties of porous BN that are key to CO_2/N_2 separation applications are highlighted.

• *Surface area:* as mentioned in section 2.2.2, porous BN materials exhibit surface areas ranging between ~100 and 2000 m^2 g^{-1} depending on the production method used and the reaction conditions.[28, 29] The tunability of its surface area makes porous BN an attractive adsorbent, which can be adapted to a given CO_2/N_2 separation process depending on the cycle conditions (e.g., temperature, pressure) to optimize CO_2 and N_2 uptakes.[101].

• *Pore sizes and pore volume:* porous BN materials benefit from a wide pore size distribution including high micropore and mesopore volumes, which are tunable via the synthesis conditions.[3, 4] In the case of CO_2/N_2 separation, the kinetic diameters of CO_2 and N_2 are 3.3 Å and 3.6 Å, respectively.[111] This means that pores with sizes between these two values can selectively adsorb CO_2 via size-exclusion-based separation.[79] If pore sizes are slightly larger than 3.6 Å, the two gases can be separated considering a kinetic separation mechanism, since N_2 will diffuse more slowly than CO_2.[79]

• *Bond polarity:* another advantage of porous BN is linked to its rich chemistry owing to the B-N bond polarity, as opposed to carbon-based adsorbents.[2, 39] When considering equilibrium separation (or kinetic separation allowing equilibrium time), this feature would lead to

preferential adsorption of highly-quadrupolar CO_2 molecules (quadrupolar moment $= 4.3 \times 10^{-26}$ esu cm^{-2})[112] over N_2 molecules (1.4×10^{-26} esu cm^{-2})[112] via polarization interactions.

• *Impurities and functional groups:* C and O impurities present in porous BN (discussed in section 2.2.2)[14, 21] can affect local surface polarities, therefore modifying interactions with the adsorbates CO_2 and N_2 as discussed above. These impurities can also have an impact on the textural properties of porous BN by increasing the number of defects, and therefore increasing its surface area. Finally, the presence of OH groups in porous BN[14] opens the door to surface functionalization and tuning of its chemistry to enhance affinity towards CO_2 molecules.

• *Thermal stability:* porous BN has shown excellent thermal stability up to 1600 °C in inert atmospheres,[113, 114] and up to 1300 °C in oxidative conditions.[115] Although such extreme temperatures will not be necessary for industrial purpose, a certain level of thermal stability may be required for certain cycle conditions and storage, which is met with porous BN.

• *Other properties:* a few aspects such as adsorption kinetics and hydrolytic stability still need investigating as I will explain in Chapter 3 of this thesis. Both of these properties will be discussed extensively in Chapter 6.

2.3.2.2.   *Examples of CO_2 and N_2 adsorption using porous BN*

Herein, I have reviewed studies where porous BN materials synthesized via high-temperature reaction were tested for CO_2 adsorption and/or CO_2/N_2 separation (excluding functionalized and doped porous BN). We note that it can be challenging to compare the adsorption performance of different materials as they were tested under various conditions. **Table 2.2** presents an overview of the findings, before giving more details on each study.

Table 2.2 Examples of publications reporting CO_2 and/or N_2 adsorption using porous BN materials obtained via bottom-up synthesis with high-temperature treatment.

Year	Ref.	Surface area (m^2 g^{-1})	Temperature (°C)	Pressure (bar)	CO_2 and N_2 uptakes (mmol g^{-1})	Selectivity CO_2/N_2
1994	[107]	437-712	0	1	CO_2 ~0.4-5.6	-
2010	[40]	927	−78	0.9	CO_2 ~7.2	-
2016	[106]	236	25	1	CO_2 ~0.4; N_2 ~0.04	26
2017	[4]	1016	25	1	CO_2 ~0.6	-
2017	[3]	1924	25	1	CO_2 ~1.5; N_2 ~0.2	-
			25	20	CO_2 ~8.4; N_2 ~1.3	
2018	[116]	881-1132	0	1	CO_2 ~1.8-2.9	
			25	0.1	CO_2 ~0.2-0.3	
			25	0.15	CO_2 ~0.3-0.4	
			25	1	CO_2 ~1.2-1.7; N_2 ~0.1	18
2018	[117]	1114	0	1	CO_2 ~1.7	-
			25	1	CO_2 ~0.9	
2019	[24]	662-1042	25	1	CO_2 ~1.3-2.9	-
2019	[22]	1585	25	1	CO_2 ~1.3	-

Some studies in **Table 2.2** looked at the role of surface area and pore structure for CO_2 uptake.[3, 116, 117] Marchesini et al. and Nag et al. showed that CO_2 adsorption increases with surface area,[3, 40] and Chen et al. added that pore size is also an important factor, in particular that micropores enhance CO_2 uptake.[116] Yang et al. showed that mesopores also increase CO_2 uptake by facilitating access to the micropores, meaning that a hierarchical porosity is key to great CO_2 sorption properties.[117] The chemistry of porous BN is also cited as a crucial parameter in CO_2 adsorption, in particular with the presence of NH_2 and OH groups creating favorable interactions with the CO_2 adsorbate.[117]

Although most studies only looked at CO_2 adsorption, a few reported N_2 adsorption as well (**Table 2.2**). Marchesini et al. synthesized porous BN from melamine, urea and boric acid under N_2 at 1050 °C, and they showed its preferential adsorption of CO_2 over N_2 in both powder and

pellet forms.[3] Xiao et al. synthesized porous BN from MgB_2 and NH_4Cl under NH_3 at 1050 °C.[106] They calculated the CO_2/N_2 selectivity from single-component isotherms at 25 °C and 1 bar, in the scenario of a flue gas emitted by a coal-fired power plant (15% CO_2; 75% N_2; 10% other gases), and they obtained a value of 26.[106] Chen et al. also calculated the CO_2/N_2 selectivity at 25 °C and 1 bar for their BN materials obtained from different ratios of melamine and boric acid heated up to 800 °C under Ar, then at 800 °C under NH_3. They used the ideal adsorption solution theory (IAST)[118] for a typical flue gas composition (15% CO_2; 85% N_2), which led to a value of 18.[116] As a comparison, a past study showed that MOF ZIF-8 and zeolite 13X had a CO_2/N_2 selectivity of 12 and 120, respectively, both for a composition of 15% CO_2 and 85% N_2 at 25 °C and 1 bar.[119]

Although porous BN materials present relevant features that make them desirable for CO_2/N_2 separation, other adsorbent materials introduced earlier (e.g., MOFs, activated carbons) have also shown great performance results for this separation.

2.3.2.3.   *Shaping of porous BN*

Since porous BN obtained via bottom-up high-temperature synthesis (see section 2.2.3.2) is usually powdery or flake-like, it is also key to develop ways of forming robust forms of BN for easier use and storage in industrial applications. Looking at the literature, this has already been researched to foster scaling-up. Bottom-up methods forming such materials involve reactions forming a shaped intermediate, such as a foam or an aerogel. For instance, Zhao et al. used ammonia borane and thiourea at 1200 °C to produce a BN foam via the gradual release of gases during the synthesis.[120] The BN foam was able to adsorb various organics, but it had a low surface area of 32 $m^2\ g^{-1}$. Pham et al. produced a BN aerogel via the carbothermal conversion of a graphene aerogel, leading to a surface area of about 400 $m^2\ g^{-1}$, but with mainly mesopores when micropores would also be desirable for various applications.[121] More recently,

mechanically-robust structured porous BN was obtained by Tian et al. in our group.[42] First, formaldehyde, NaOH, melamine, dicyandiamide and boric acid were used to prepare a melamine-formaldehyde resin. This B- and N-containing resin acting as a polymer precursor was then heated up under ammonia up to 1000 °C to form structured porous BN with a surface area of 1523 m^2 g^{-1}.

2.4. Porous BN for thermal energy storage (TES) via adsorption

2.4.1. TES theory and classification

To expand the knowledge on porous BN, I looked at a different adsorption-based application that had not been researched with porous BN to date. I selected thermal energy storage (TES), which has become a key application to increase the efficiency of energy systems and reduce their environmental impact.[122, 123] TES contributes to reducing the share of fossil fuels and enables their partial replacement with cost-efficient renewable energies, such as solar heat, in industrial or residential settings. TES allows to collect and store energy (charge), which can then be used when needed (discharge), thereby tackling the issue of intermittent energy demand (e.g., day and night) and supply (e.g., solar energy).

Three main technologies are used in TES: sensible heat, latent heat and thermo-chemical heat storage (**Figure 2.10**). These three categories are at different stages in terms of development and industrial use, and each comes with specific advantages and limitations. Herein, I will start by giving a brief overview of each technology, and I will then focus on thermo-chemical heat storage using adsorption.
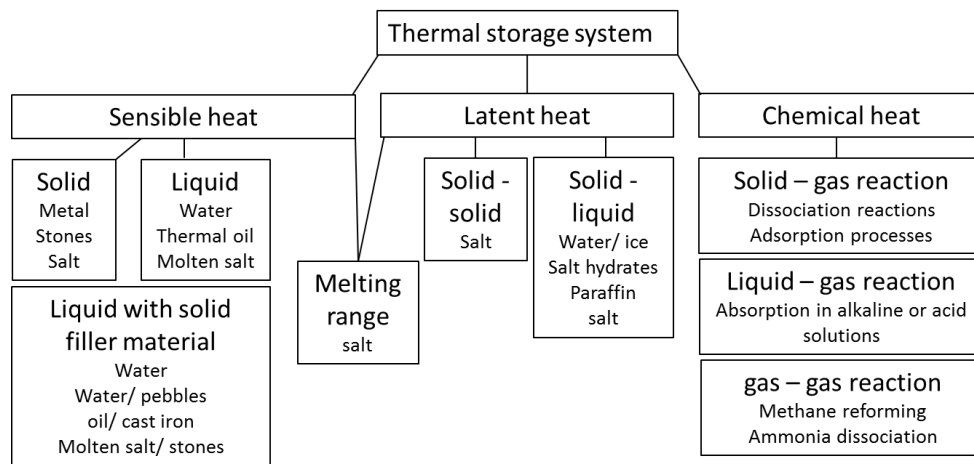
Figure 2.10 Classification of thermal energy storage technologies. Reproduced with permission from reference [123]. Copyright 2015 Beilstein Institute for the Advancement of Chemical Sciences.

2.4.1.1. Sensible heat storage

Sensible heat storage relies on a temperature gradient in a material, which constitutes the charging medium. The amount of energy stored in this material will depend on the temperature difference, as well as on its specific heat capacity.[122] It is expressed as follows in equation (6):

$$E = m \int_{T_1}^{T_2} C_p(T) \, dT \qquad (6)$$

with:

E energy stored during the temperature change (J)

m mass of the material (kg)

$C_p(T)$ specific heat capacity of the material (J kg^{-1} K^{-1})

T_1 initial temperature of the material (K)

T_2 final temperature of the material with $T_2 > T_1$ (K)

The storing medium used in sensible heat storage can be either solid or liquid, but the most common medium remains liquid water due to its abundance, low cost and high specific heat

capacity.[122] For example, sensible heat storage is widely used for domestic hot water storage. However, despite being a cost-effective and non-polluting technology, it is limited by the temperature range at which it can operate, i.e., up to 100 °C when water is used. For higher temperatures, molten salts are a good alternative due to their high thermal stability, high specific heat capacity and low vapor pressure.[123] However, sensible heat storage systems often lead to low energy density values (amount of energy stored/released per unit volume of adsorbent) between 40-60 kWh m^{-3}, which means large volumes of material are needed for storage.[124] Kiyabu et al. screened various materials used in TES and predicted energy density values up to ~140 kWh m^{-3} in sensible heat storage.[125]

2.4.1.2. Latent heat storage

Latent heat storage relies on the latent heat of a phase transition happening in the heat storage medium at a constant temperature.[122, 123] The phase change can be a solid-liquid transition (melting or solidification) or a solid-solid transition (crystal transition). The energy associated with a given phase transition can be expressed as shown in equation (7):

$$E = mL \qquad (7)$$

with:

E energy stored during the phase transition (J)

m mass of the material (kg)

L latent heat of the phase transition (J kg^{-1})

In latent heat storage processes, the charging and the release of energy occur during a phase change, whereas energy is stored when maintaining a given phase of the material considered.[126] The most common materials used in latent heat storage are salts, water and paraffins

undergoing a solid/liquid transition.[122] This technology presents higher heat storage density values than sensible heat storage, which can reach up to ~550 kWh m^{-3} in theory,[125] but this technology is also linked to slow kinetics, energy dissipation and a change of volume during phase transition, which all remain significant drawbacks.[122]

2.4.1.3. Thermo-chemical heat storage

Thermo-chemical heat storage is based on a reversible reaction taking place between two components and the associated enthalpy of reaction ΔH.[122, 123] Energy can be stored during an endothermic reaction ($\Delta H > 0$) and released during an exothermic reaction ($\Delta H < 0$). One advantage of this technology is it can be operated over a large range of temperatures depending on the reaction considered, making it a versatile technology.[127] During thermo-chemical heat storage, heat is stored in the form of chemical potential, meaning that thermal losses are minimal and that this technology is adapted for long-term storage.[128, 129]

Thermo-chemical energy storage often requires a smaller storage volume than sensible and latent TES, which leads to higher energy density in theory.[130] Examples of experimental values of energy density could be found in studies by Shervani et al. (139 kWh m^{-3}),[131] Dicaire and Tezel (200 kWh m^{-3}),[132] Strong et al. (200 kWh m^{-3}),[133] Aidoun and Ternan (235 kWh m^{-3}),[134] and Donkers et al. (up to 556 kWh m^{-3})[135] among others. Theoretical predictions have displayed values up to ~1250 kWh m^{-3} using hydration/dehydration of salts.[125] It is worth noting that thermo-chemical energy storage remains under research with novel materials being trialed, as opposed to sensible and latent heat storage, which are more established technologies. Therefore, achievable energy densities may vary in the future.

Thermo-chemical energy storage includes solid-liquid or solid-gas reactions, such as those involved in adsorption processes.[123] During thermo-chemical energy storage via adsorption,

the charging/storage phase corresponds to the endothermic desorption (or regeneration) and the discharging/release phase equates to the exothermic adsorption (**Figure 2.11**). The energy released during adsorption can be assessed via equation (8):[131, 136]

$$E_{ads} = \int_0^{t_f} \dot{m} \, C_p(T) \, (T_{out} - T_{in}) \, dt \qquad (8)$$

with:

E_{ads} energy released during adsorption (J)

t_f time corresponding to the end of adsorption (s)

$\dot{m}$ mass flow rate of the adsorbate (kg min^{-1})

$C_p(T)$ specific heat capacity of the adsorbate (J kg^{-1} K^{-1})

T_{out} temperature at the column outlet (K)

T_{in} temperature at the column inlet (K)
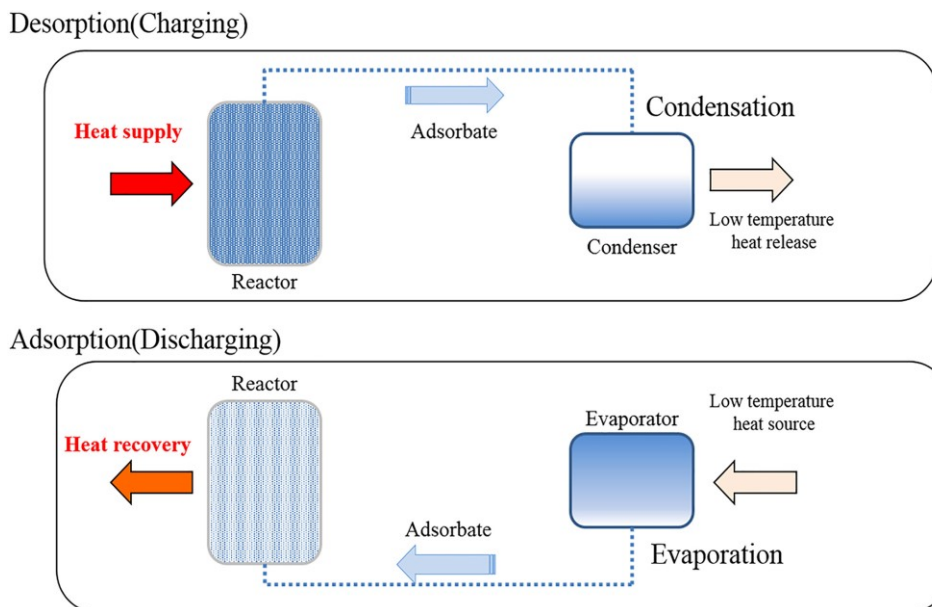
Figure 2.11 Schematic representing the principle of thermo-chemical heat storage via adsorption. Reproduced with permission from reference [136]. Copyright 2019 John Wiley & Sons, Ltd.

2.4.2. Determination of a working pair for TES via adsorption

2.4.2.1. State-of-the-art of adsorbent/adsorbate working pairs

Adsorption heat storage usually involves a liquid or gaseous adsorbate with a solid adsorbent, constituting an adsorbent/adsorbate working pair. The liquid adsorbate is often water[126] or ammonia, and CO_2 can be used as a gas adsorbate.[126] Various adsorbents have already been trialed for adsorption heat storage, such as zeolites, silica gels and activated carbons.[122, 136] Zeolites are often used with water vapor adsorption due to their high hydrophilicity.[127] However, relatively high temperatures are required for their regeneration (> 150 °C). Silica gels are also often used with water vapor due to their hygroscopic and adsorptive properties,[137] but their use is limited due to low energy density.[122] If not directly suitable for a TES application, they can however be used as host matrices for composites.[122] Finally, activated carbons could be used for ammonia or alcohols adsorption due their high affinity towards those adsorbates. To date, there has not been much research on their direct use in TES systems, apart from their role as host matrices, like silica gels.[122]

2.4.2.2. Adsorbent properties for TES via adsorption

To select suitable adsorbents for TES via adsorption, it is crucial to look at their properties. I have reviewed below the key material properties one should assess, bearing in mind that most of them will also depend on the paired adsorbate in a TES process.

• *Chemical properties:* the chemistry of an adsorbent material will partly determine the affinity with an adsorbate, thereby influencing the adsorption uptake (see section 2.3.2.1), and it will influence the heat of adsorption. The adsorbent has to be carefully selected depending on the adsorbate, and vice-versa.[122, 138] In the case of TES via adsorption, reversible processes are

required during the adsorption/desorption cycles, therefore physisorption should be the primary adsorption phenomenon occurring.[139]

• *Textural properties:* an adsorbent with high surface area and porosity is desired to obtain high uptake of the sorbate.[140] The ideal pore structure will depend on the adsorbate selected to maximize its adsorption.

• *Thermal properties:* definitions of relevant thermal parameters for TES via adsorption are first introduced. The specific heat capacity C_p of a material corresponds to the amount of heat needed to increase its temperature by 1 °C; the thermal conductivity λ is the ability of a material to transfer heat; finally, the thermal diffusivity κ corresponds to the rate at which heat transfer occurs. All these parameters are linked as per equation (9):

$$\kappa = \frac{\lambda}{\rho C_p} \qquad (9)$$

with:

κ thermal diffusivity ($m^2\ s^{-1}$)

λ thermal conductivity ($W\ m^{-1}\ K^{-1}$)

ρ density ($kg\ m^{-3}$)

C_p specific heat capacity ($J\ kg^{-1}\ K^{-1}$)

In TES via adsorption, it is desirable to have an adsorbent with high thermal conductivity, high thermal diffusivity and low specific heat capacity to enhance the temperature lift and heat transfer during the adsorption/desorption cycles.[122, 126, 139, 141] As explained in a study by Bird et al., all these thermal properties can be difficult to measure reliably, and discrepancies have been found in the literature depending on the measurement method and the sample composition.[141]

Before looking at other material properties, it is important to highlight the link between textural and thermal properties in solids. Phonons, which correspond to a unit of vibrational energy

coming from oscillating atoms within a crystal structure, interact via scattering. Due to these interactions, the thermal conductivity of a solid varies along the crystallographic axes.[141] The presence of defects (e.g., vacancies, substituted atoms) in the crystal structure leads to increased phonon scattering, which results in a decrease in thermal conductivity.[141, 142] This implies that more amorphous materials, which typically have a significant amount of defects and/or impurities, would tend to have lower thermal conductivity. However, such materials often exhibit high surface areas, which are key to obtain high adsorption uptake. This means that a compromise between textural and thermal properties may be required when looking for an adsorbent in TES via adsorption.

• *Thermodynamic properties:* the heat of adsorption indicates how strong is the interaction between an adsorbent and an adsorbate. It can be calculated by measuring adsorption isotherms at several temperatures, and it is dependent on both the adsorbent and the adsorbate. In TES via adsorption, it is preferable to have high heats of adsorption so that more energy is available to the system,[138] but this is also linked to higher regeneration temperatures during desorption, which can be a disadvantage.[132]

• *Stability:* since TES via adsorption involves the cyclic use of an adsorbent/adsorbate pair, the adsorbent material needs to be stable towards the selected adsorbate. This will be further discussed in 2.4.2.3 when looking at which sorbates could be paired with BN-based materials.

2.4.2.3. *Potential adsorbates for porous BN*

To date, there has not been any study on porous BN for thermo-chemical energy storage. Herein, I review some studies linked to thermo-chemical energy storage or thermal properties in general that have mentioned materials presenting similarities to porous BN: activated carbon (similar crystalline structure, i.e., highly amorphous) and hexagonal BN (similar chemistry). In terms of thermal properties, activated carbon materials typically display heat capacities of

$\sim 0.7\text{-}1.3 \text{ J kg}^{-1} \text{ K}^{-1}$,[143-145] and thermal conductivity values of $\sim 0.2\text{-}0.6 \text{ W m}^{-1} \text{ K}^{-1}$.[146-148] h-BN

materials have similar heat capacities, ranging from $\sim 0.7\text{-}1.9 \text{ J kg}^{-1} \text{ K}^{-1}$,[149, 150] and significantly

higher thermal conductivity values than activated carbon, up to $\sim 420 \text{ W m}^{-1} \text{ K}^{-1}$.[149, 151] The

difference in thermal conductivity between activated carbon and h-BN can be explained by

phonon scattering, as explained previously in section 2.4.2.2.

To understand further which families of adsorbates could be considered with porous BN in

TES via adsorption, **Table 2.3** presents measured or estimated values of heat of adsorption

with activated carbon and h-BN materials. All values from the literature were converted in kJ

mol^{-1} for clarity purposes. As seen earlier, the heat of adsorption represents the affinity between

an adsorbent and an adsorbate, and its value should be high enough to generate a high amount

of energy during adsorption.[132, 138] Although activated carbon has been regarded as a promising

adsorbent for TES in some reviews, only a few studies have reported energy density values.[122]

Srivastava and Eames reviewed adsorbent/adsorbate working pairs for TES via adsorption and

presented the estimated heats of adsorption generated by models.[152] In the case of activated

carbon, they reported values for water, ammonia, methanol and ethanol as adsorbates. Saha et

al. calculated the heat of adsorption based on measured isotherms when using activated carbon

fibers with ethanol.[153] In a later study, they also investigated the adsorption of n-butane on

activated carbon.[154] Following this work, Madero-Castro et al. looked at the adsorption of

various alcohols (methanol, ethanol, n-propanol and n-butanol) on activated carbon and

estimated the corresponding heats of adsorption.[155] They observed an increase in heat of

adsorption with a longer alkyl chain due to greater interactions with activated carbon. In this

study, energy storage density values were also estimated for each alcohol. The trend was

reversed compared to the heats of adsorption, with higher energy storage density achieved

when adsorbing an alcohol with a shorter alkyl chain. This was assumed to be linked to higher

adsorption uptakes with the shorter alcohols, in particular methanol. This study highlighted that

a combination of factors must be considered when assessing an adsorbent/adsorbate working pair, such as adsorbate uptake and heat of adsorption. A study by Kohler and Müller also looked at activated carbon paired with different alcohols and estimated energy storage density values with a model.[156] Echoing the findings of Madero-Castro et al., the highest energy storage density was obtained using methanol, followed by n-propanol, ethanol and n-butanol sharing similar values.

Table 2.3 Examples of heats of adsorption and energy storage density values obtained for solvents paired with activated carbon and hexagonal BN (h-BN) materials. *: the last column used the density of one type of activated carbon, i.e., NORIT RB3 (ρ = 2 g cm^{-3}),[157] to convert the energy storage density in relevant units for comparison purposes. <u>Note</u>: the question marks indicate that no values were found in the literature to the best of our knowledge.

Ref.	Material	Adsorbate	Boiling point (°C)	Heat of adsorption (kJ mol^{-1})	Energy storage density (kJ kg^{-1})	Energy storage density (kWh m^{-3})*
152, 155, 156, 158	Activated carbon	Methanol	64.7	36-52	402-600	224-334
152, 153, 155, 156	Activated carbon	Ethanol	78.4	40-55	310-475	172-264
155, 156	Activated carbon	n-propanol	97.2	45-60	320-375	178-209
155, 156	Activated carbon	n-butanol	117.7	49-65	316-325	176-181
152	Activated carbon	Ammonia	−33.3	24-32	?	?
152	Activated carbon	Ethane	−89	30-36	?	?
154	Activated carbon	n-butane	−1	5-12	?	?
152, 159	Activated carbon	Water	100	41-47	295	181
160	h-BN	Isopentane	27.8	39	?	?
160	h-BN	Cyclohexane	80.8	43	?	?
160	h-BN	n-pentane	36.1	44	?	?
160	h-BN	Benzene	80.1	47	?	?
160	h-BN	n-hexane	69	52	?	?
160	h-BN	n-heptane	98.4	57	?	?
160	h-BN	n-octane	125.6	65	?	?

Considering its lack of porosity, h-BN would not be considered as an adsorbent in TES, but the review of its thermal characteristics could be relevant due to its similar chemistry to porous BN. This explains why no energy storage density values were reported in **Table 2.3** with h-BN. Finally, Curthoys and Elkington obtained experimental heats of adsorption from gas chromatography with h-BN and various alkanes or alkenes.[160] They observed that, when considering linear alkanes, the heat of adsorption increases as the number of carbons increases, implying greater interactions with h-BN.

When considering an adsorbate, it can also be worth considering its boiling point (**Table 2.3**) to facilitate the TES experiments, for instance during desorption steps to avoid energy waste. One should also consider the toxicity of the adsorbate. For instance, benzene and methanol should not be considered due to their high toxicity. Finally, some of the adsorbates described in **Table 2.3** could present stability issues with porous BN. For instance, depending on the experimental conditions, it is possible that water would degrade porous BN as explained previously in section 2.2.5. When testing a new adsorbate, it will be key to carry out stability testing to assess the recyclability of the adsorbent.

CHAPTER 3: RESEARCH GAPS AND OBJECTIVES

Some aspects of discussion and figures described in this chapter have been published by the thesis author in the Journal of Physical Chemistry C,[7] and in Microporous and Mesoporous Materials.[8]

3.1. Research gaps from the literature

The literature review chapter presented up-to-date knowledge on porous BN materials, with a focus on their synthesis, their properties and their potential use for gas adsorption and thermal energy storage using adsorption. In this paragraph, I have assessed knowledge gaps relating to porous BN, which will lead to the formulation of research objectives in section 3.2.

To ensure the deployment of porous BN at large scale, one must be able to tune its properties for a given application, which clearly necessitates an understanding of its formation process. In the literature review, I saw that two formation mechanisms have been suggested for the formation of porous BN. There is no consensus on which one was relevant (if not both) or on a comprehensive reaction scheme with respect to the thermal treatment. In particular, I identified the following areas lacking knowledge:

• What is the minimal temperature required to form porous BN?

• Which chemical intermediates are formed before obtaining porous BN?

• What is the influence of the precursors on the chemical and structural features of porous BN?

• Could the two mechanisms mentioned earlier take place concurrently in the reaction medium?

• How can inherent oxygen and carbon impurities be eliminated from the BN structure?

Looking at the nature of most separations, it also appears crucial to have adsorbents that sustain water or moisture exposure during storage, transport and adsorption. Past studies have reported the cyclic use of porous BN as adsorbent in potentially mild or extreme humidity conditions, but the impact on surface area, porosity and sorption performance upon moisture exposure was not assessed. This is all the more important since studies have pointed towards the instability of porous BN in the presence of water or moisture. Since porous BN can contain OH groups at its surface, surface functionalization could be used to increase its hydrophobicity and resistance to moisture. Considering the potential of porous BN as an adsorbent, it is key to answer the following questions:

• Can surface functionalization be used on porous BN to enhance its hydrophobicity?

• Which molecules could be used to graft onto porous BN?

• Can a compromise be reached between enhanced hydrophobicity and porosity in porous BN?

Finally, there has been extensive research in the field of gas adsorption using porous BN, with links being drawn between BN's structural properties and adsorptive capacity. While the literature review showed results on the performance of porous BN regarding CO_2 adsorption, there has been little research on the separation of CO_2 from other gases, for instance N_2. However, this is key in the context of CO_2 capture and the overall aim of reducing greenhouse gases emissions, as CO_2 is emitted in a mixture of gases. It also appeared that adsorption kinetics in porous BN have not been studied, although this is crucial for the development and scaling-up of an adsorbent. Looking at other industrial applications, I noticed that there was no research on porous BN for use in thermal energy storage, despite being a booming technology to reduce energy consumption. Porous BN already benefits from some of the required

properties for TES adsorbents, but more research needs to be done on its suitability with various adsorbates and its thermal properties. Therefore, the following areas of research have been identified:

• What is the performance of porous BN for CO_2/N_2 separation, from both an equilibrium and kinetics perspective?

• If surface functionalization is used to enhance the hydrophobicity of porous BN, what would be the impact on CO_2/N_2 separation?

• Does porous BN have potential for use in thermal energy storage via adsorption?

• Can we reliably measure some thermal properties of porous BN?

• Which adsorbates could be paired with porous BN for thermal energy storage?

3.2. Research objectives

3.2.1. Research objective 1: investigate the formation mechanism of porous BN

The first research objective is to obtain a clear reaction mechanism for the formation of porous BN to foster scaling-up of the synthesis of the material. To do this, I have focused on our in-house method using boric acid, melamine and urea heated up to 1050 °C under N_2 atmosphere (**Figure 3.1**), which consistently yields porous BN with high surface area, high pore volume and promising sorption performance.
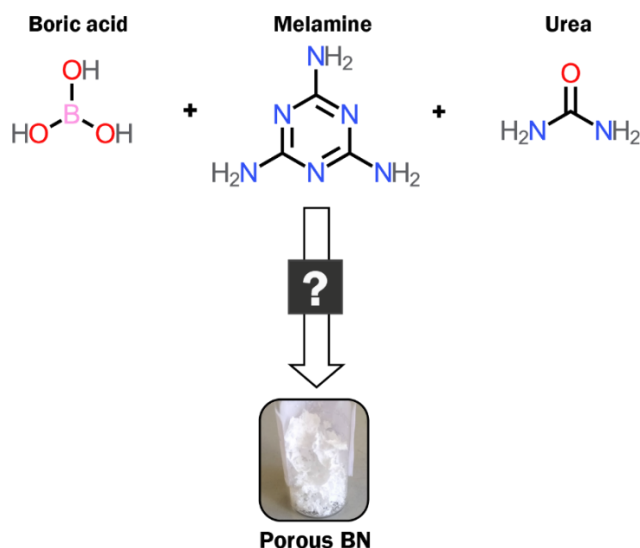
Figure 3.1 Schematic of the precursors used for the high-temperature synthesis of porous BN and picture of the final product. Reproduced with permission from reference [7]. Copyright 2021 American Chemical Society.

3.2.2. Research objective 2: enhance the hydrolytic stability of porous BN

The second research objective is to enhance the hydrolytic stability of porous BN to make it a more reliable adsorbent for a various range of molecular separations. To this aim, I will consider surface functionalization to tune the hydrophobicity of the material, potentially finding a compromise between high surface area and enhanced hydrophobicity (**Figure 3.2**).
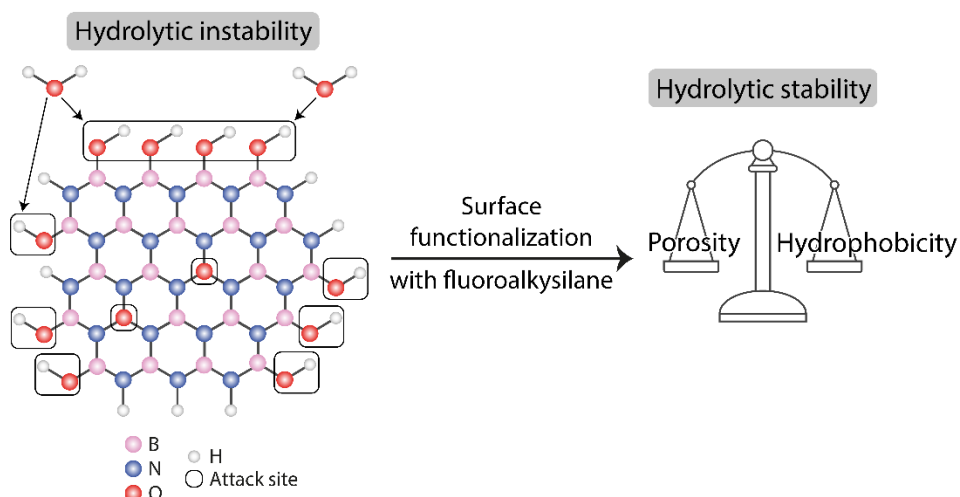
Figure 3.2 Schematic showing the targeted sites in porous BN for water attack and the method used to enhance its hydrolytic stability. Reproduced with permission from reference [8]. Copyright 2023 Elsevier.

3.2.3. Research objective 3: assess the potential of porous BN for adsorption-based processes, namely CO_2/N_2 separation and thermochemical energy storage

The third research objective is two-fold: i) to assess further the use of porous BN for CO_2/N_2 separation, including with functionalized materials (see research objective 2), by carrying out both equilibrium and kinetics sorption measurements; ii) to look into the potential of porous BN for a new area, i.e., adsorption thermal energy storage (TES), by investigating its compatibility with various adsorbates and testing it for TES applications (**Figure 3.3**).
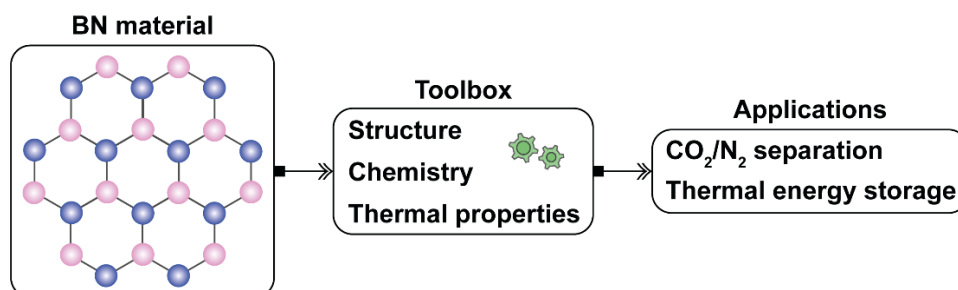
Figure 3.3 Schematic showing the properties of BN materials that can be tuned for applications in CO_2/N_2 separation and thermal energy storage.

CHAPTER 4: MATERIALS AND METHODS

Some aspects described in this chapter have been published by the thesis author as part of other Methods sections in the Journal of Physical Chemistry C,[7] and in Microporous and Mesoporous Materials.[8]

This chapter describes how porous BN-based materials were synthesized during this PhD, and how their properties were evaluated using analytical and spectroscopic tools.

4.1. Preparation of porous BN materials

4.1.1. Synthesis of porous BN powder

In each Results chapter of this thesis, porous BN was synthesized via a bottom-up synthesis using one boron-containing precursor and two nitrogen-containing precursors. The reagents boric acid (ACS reagent, Sigma Aldrich), melamine (99%, Sigma Aldrich) and urea (molecular biology grade, Sigma Aldrich) were used with molar ratios of 1:1:5 following the multiple N-containing precursor synthesis previously developed in our research group.[3] The three precursors were physically ground and mixed for 3 min until homogeneous, before being placed in an alumina crucible with the lid partially open (~2 cm) to allow for any gas flow (**Figure 4.1**). The crucible was placed inside a quartz tube (Ø = 80 mm, length = 1050 cm), which was set up inside a horizontal tubular furnace (HST 12/600, Carbolite) in N_2 flow (99.998%, zero grade, BOC). The tube was thermally insulated with ceramic plugs at both ends, sealed with flanges and connected with inlet and outlet tubing for the gas flow. A mass flow controller (FMA-2619A-V2, Omega) was used to control accurately the N_2 gas flow entering the furnace. At the exit of the furnace, a trap was connected to prevent any air from entering the furnace, followed by a bubbler filled with water to dissolve any gas produced

during the synthesis, such as ammonia. Each synthesis started with a 2 h purge at room temperature under N_2 with a flow rate of 250 cm^3 min^{-1}. After this step, the flow rate was lowered to 50 cm^3 min^{-1} and the temperature ramped up to 1050 °C at a rate of 10 °C min^{-1}. The complete synthesis of the porous BN material was obtained after a dwell time of 3 to 3.5 h at 1050 °C before cooling down, still under flowing N_2. Samples were stored in a desiccator at room temperature without vacuum until characterization to prevent degradation from ambient moisture.
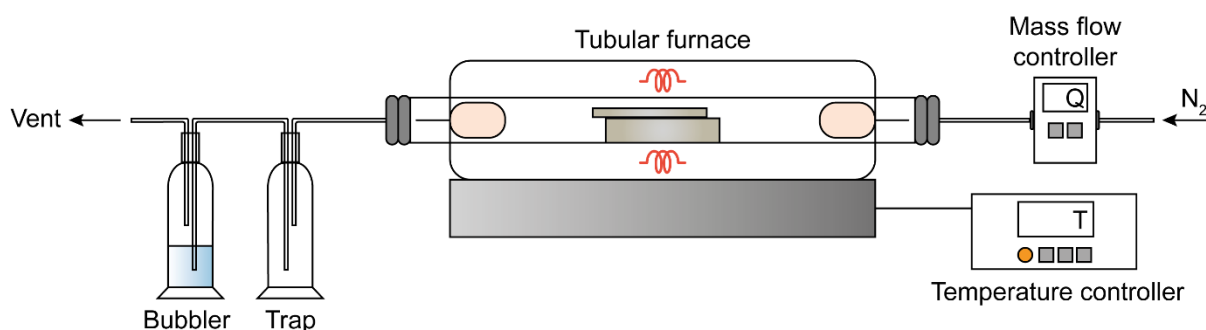
Figure 4.1 Tubular furnace set-up used to produce porous BN under controlled N_2 atmosphere and temperature.

4.1.2. Pelletization of porous BN

To prepare porous BN-based pellets, 40 mg of porous BN powder were ground with a mortar and pestle, and placed into a pellet die (5-mm evacuable stainless steel, Specac). The die was positioned into a manual hydraulic press (Atlas^{TM} Manual 15T, Specac) fitted with a low tonnage gauge conversion kit (0-1 t, Specac). A load of 0.2 t was applied and maintained for 20 s to form a pellet. The pellet was then ejected with a small load applied to an extractor ring placed onto the base of the pellet die.

In Chapter 6 of this thesis, I determined that 0.2 t was the optimal load for successful pelletization of 40 mg of porous BN while maintaining high surface area compared to porous BN powder (more details in Chapter 6).

4.2.   Characterization of chemical features

4.2.1.   Fourier-transform infrared spectroscopy (FTIR)

Fourier transform infrared spectroscopy (FTIR) is a characterization technique analyzing which radiation wavelengths are absorbed by a sample, giving information on the chemical bonds it contains. In attenuated total reflectance FTIR (ATR-FTIR), a solid or liquid sample can be directly analyzed without further treatment. During a measurement, an IR beam is focused onto a crystal to generate an evanescent wave, which penetrates through a sample in contact with the top surface of the crystal (**Figure 4.2**). The measurement pathlength does not depend on the thickness of the sample, but on the penetration depth of the IR beam, which itself depends on the wavenumber, the incident angle of the beam, and the refractive index of the crystal. In ATR-FTIR, the penetration depth is typically of ~0.5-2 µm.[161] Once in contact with the sample, the IR wave is attenuated in the energy regions where the sample absorbs, and the resulting attenuated energy is guided back to the other side of the crystal and goes into a detector. This results into an infrared spectrum showing different molecular vibrational modes, which represent specific chemical bonds in the sample.
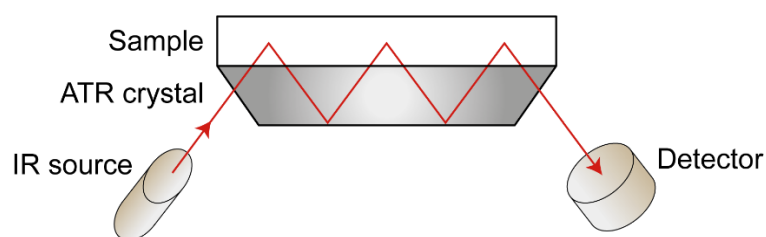
Figure 4.2 Principle of attenuated total reflectance FTIR with the infrared (IR) source, the attenuated total reflectance (ATR) crystal and the detector.

In Chapters 5, 6 and 7, ATR-FTIR was used to verify whether the characteristic B-N and B-N-B bonds of porous BN were detected in samples, and to assess the presence of oxygen through the observation of B-O bonds.

Prior to measurement, each powder sample was ground finely in an agate mortar, and spectra were collected using an Agilent Cary 630 FTIR spectrometer equipped with an ATR accessory. Pelletized samples were analyzed without prior treatment. A background spectrum was first recorded without any sample to be subsequently subtracted from each spectrum. Sixteen spectra were collected per sample to obtain an averaged spectrum over a wavenumber range of 450-4000 cm^{-1} with a resolution of 2 cm^{-1}.

4.2.2. X-ray photoelectron spectroscopy (XPS)

X-ray photoelectron spectroscopy (XPS) is a surface-sensitive technique that allows the identification of atomic environments in a sample, as well as the chemical state and electronic structure of these atoms.[162] A sample submitted to ultra-high vacuum ($P < 10^{-7}$ Pa) is irradiated with an X-ray beam, which ejects electrons from atoms: this is known as the photoelectric effect (**Figure 4.3**). The measurement of the number of ejected electrons and their associated kinetic energy gives information on the atomic chemical states. This allows the calculation of the electron binding energy E_b following equations (10) and (11) illustrating the photoelectric effect:

$$E_{kin} = E_{ph} - E_b - W_f \qquad (10)$$

$$E_{ph} = h\nu \qquad (11)$$

with:

E_{kin} kinetic energy of the detected electron (eV)

E_{ph} photon energy of the X-ray beam (eV)

E_b binding energy of the emitted electron (eV)

W_f work function of the spectrometer (eV)

h Planck's constant ($\approx 6.62607 \times 10^{-34}$ J s^{-1})

ν frequency of the X-ray beam (s^{-1})
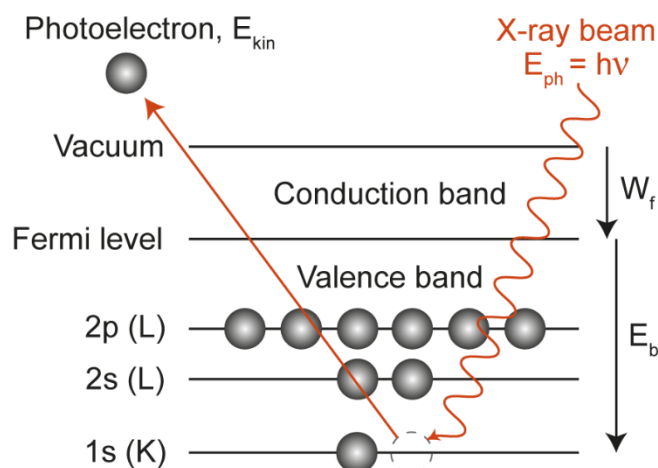
Figure 4.3 Principle of XPS with the photoelectric effect.

A spectrum of intensity vs. binding energy is plotted based on the number of electrons measured at specific binding energies. Binding energies are dependent on the chemical environment of a given element, so they can be associated with characteristic atomic environments.[163] Specific peak shapes (e.g., single peak or doublet) can give information on the chemical state of an element.

In Chapters 5, 6 and 7, XPS analyses were used to evaluate the elemental composition of porous BN-based samples (containing B, N, O and C elements) and the chemical environments for each of these elements. In Chapter 6, Si and F atoms were also probed in samples after functionalizing the surface of porous BN.

XPS analyses were performed using a Thermo Scientific K-Alpha X-ray photoelectron spectrometer equipped with an MXR3 Al Kα monochromatic X-ray source (hν = 1486.6 eV) set to 72 W (6 mA and 12 kV). Powder samples were ground in an agate mortar prior to analysis and mounted onto conductive carbon tape. Pelletized samples were directly mounted onto

carbon tape. The data was processed with Thermo Scientific Avantage^{TM} software for B 1s, N 1s, O 1s, C 1s, Si 2s, Si 2p and F 1s spectra. The adventitious carbon (C-C) peak set at 284.8 eV was used for binding energy calibration. The recommended Smart background, based on the Shirley background, and the Powell peak fitting algorithm were used for all peak fitting in this thesis.

4.2.3. Solid-state nuclear magnetic resonance (NMR)

Nuclear magnetic resonance (NMR) spectroscopy is a non-destructive technique based on the phenomenon of nuclear magnetic resonance, also used in magnetic resonance imaging (MRI). The nuclei of many elemental isotopes have a characteristic spin, which generates a specific magnetic field when charged in the presence of an external magnetic field.[164] Depending on their electron density, neighboring atoms influence the magnetic fields around atomic nuclei. Based on this property, NMR spectroscopy studies local magnetic fields around specific atomic nuclei (e.g., ^{1}H, ^{13}C and ^{15}N are the main isotopes used in NMR) and gives information on the electronic structure of a molecule and the functional groups composing it. In practice, NMR spectroscopy involves three main steps: i) polarization of the magnetic nuclear spins in a constant magnetic field; ii) perturbation of the polarization by a weak oscillating magnetic field; iii) detection and analysis of the electromagnetic waves emitted by the atomic nuclei following the perturbation. Due to the low content of magnetic isotopes in some samples, magic angle spinning (MAS) is often used to enhance the NMR signals and increase the resolution of the spectra. This method involves the fast rotation of the sample around a fixed angle, called the magic angle.[165]

In Chapter 5, ^{11}B MAS NMR analyses were used to investigate the chemical environments and the configuration of B atoms in intermediate molecules formed during the synthesis of porous BN. ^{13}C solid-state NMR was used to evaluate the potential formation of carbon nitride during

this synthesis. ^{11}B and ^{13}C solid-state NMR spectra were recorded by Dr. Daniel M. Dawson with the support of Prof. Sharon E. Ashbrook at the University of St Andrews, UK.

Solid-state ^{11}B NMR spectra were recorded using a Bruker Avance III spectrometer equipped with a wide-bore 14.1 T superconducting magnet ([11]B Larmor frequency of 192.6 MHz) and a Bruker 4-mm BN-free magic angle spinning (MAS) probe head. Samples were ground and packed into zirconia rotors, which were rotated about an axis inclined at the magic angle at a rate of 10 kHz. Spectra were acquired using a single soft pulse (ν_1 ~20 kHz) of short flip angle (β ~7°) to enable quantitation of signals with widely different magnitudes of the quadrupolar coupling constant (C_Q). Signal averaging was carried out for either 128 transients with a recycle interval of 2 s or 64 transients with a recycle interval of 30 s when T_1 relaxation was observed to be slower. All spectra were recorded with high-power (ν_1 ~90 kHz) continuous wave decoupling of ^{1}H during acquisition, to improve the resolution of signals for any protonated species. Chemical shifts were reported relative to $BF_3.Et_2O$ using BPO_4 (δ = −3.3 ppm) as a secondary solid reference. The [11]B multiple-quantum (MQ) MAS spectra of selected samples were recorded using a z-filtered amplitude-modulated pulse sequence, with signal averaging for 24 or 120 transients for each of 90 t_1 increments of 50 μs. Spectra were shown after shearing and referencing in δ_1 according to the formalism of Pike et al.[26]

Density functional theory (DFT) calculations were carried out at the B3LYP/6-311+G(2d,p) theory level using GAUSSIAN 09 revision D.01.[27] Calculations were performed on an individual 32-core Intel Broadwell nodes of the University of St Andrews computing cluster. Computed magnetic shieldings (σ_{iso}) were converted to computed chemical shifts (δ_{iso}) using $\delta_{iso} = \sigma_{ref} - \sigma_{iso}$, with a value of σ_{ref} = 100.0038 ppm determined using $BF_3.Et_2O$ (calculated at the same theory level).

Solid-state ^{13}C NMR spectra were recorded using a Bruker Avance III spectrometer equipped with a wide-bore 9.4 T superconducting magnet ([13]C Larmor frequency of 100.9 MHz).

Samples were packed into standard 4 mm ZrO_2 rotors and rotated about an axis inclined at the magic angle at a rate of 12.5 kHz. Spectra were recorded with direct polarization using a rotor-synchronized spin-echo pulse sequence ($\tau = 80$ μs) to eliminate the probe background. Signal averaging was carried out for either 640 transients or 1024 transients with a recycle interval of 90 s. Spectra were processed with 20 Hz exponential broadening. Chemical shifts were reported in ppm relative to TMS using the CH_3 signal of L-alanine ($\delta = 20.5$ ppm) as a secondary solid reference.

4.2.4. Micro X-ray fluorescence (μXRF)

μXRF is a non-destructive technique used to determine qualitatively and quantitatively the elemental composition of a sample. The sample is exposed to an X-ray beam and the XRF spectrometer measures the fluorescent X-ray radiation emitted back by the sample (**Figure 4.4**). Different atoms emit fluorescent light with characteristic wavelengths, allowing the measurement of a spectrum with different wavelengths emitted by the sample and the identification of the corresponding atoms.
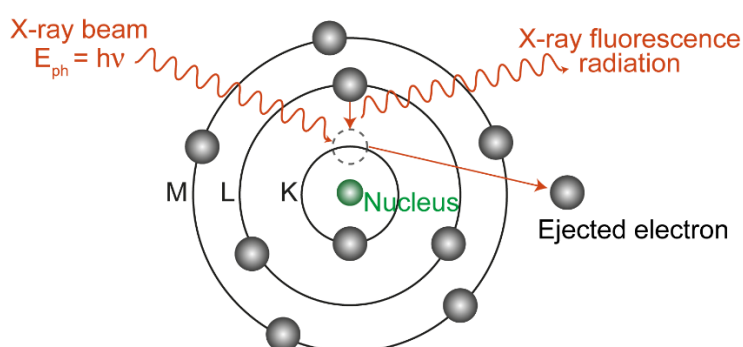
Figure 4.4 Principle of μXRF based on the generation of characteristic X-ray fluorescence radiations.

In Chapter 6, μXRF was carried out to map the distribution of silicon in BN pellets that were functionalized with a grafting agent containing silicon. This allowed to understand where the silane molecules were grafted depending on the functionalization method used. μXRF was carried out by Dr. Marcus H. N. Yio at Imperial College London.

Prior to the measurements, pelletized samples were encased in Struers EpoFix resin and then dry-ground on 500 grit SiC paper to expose the internal surface for analysis. After grinding, the samples were cleaned by ultrasonication in acetone for 10 min and then air-dried for 15 min. An EDAX Orbis PC μXRF spectrometer equipped with a 50 kV Rh anode X-ray tube and an 80 mm^2 Si(Li) energy-dispersive detector was used to map the distribution of Si in the samples. The beam voltage, beam spot size and dwell time were set to 30 kV, 30 μm and 100 ms respectively to ensure high spatial resolution and high contrast mapping.[166] The scan format was set to 256 × 200 to achieve a pixel size of around 18.6 μm.

4.2.5. Near edge X-ray absorption fine structure (NEXAFS)

Near edge X-ray absorption fine structure (NEXAFS) spectroscopy is a characterization technique that provides information on the chemical and electronic structure of a sample. When the X-ray beam passes through the sample, absorption phenomena attenuate its intensity. The photoabsorption cross-section is a measure of the probability of an absorption process occurring. It corresponds to the number of electrons excited per unit time divided by the number of incident photons per unit time and unit area.[167] This means that high energy photons can penetrate further into a sample as they are less likely to be absorbed. When the incident photon energy ($E = h\nu$) is higher than the binding energy of a core electron, the X-ray absorption cross-section increases sharply (this is called an absorption edge) and then decreases slowly beyond this core edge. Absorption edges are classified based on the origin of the core excited electron. For instance, 1s electrons lead to K-edge absorption, whereas 2s or 2p electrons lead

to L-edge absorption.[167] Changes in atomic environments can be detected via the position of absorption edges as well as their shape and intensity. It is important to note that, contrary to XPS where spectra are acquired over a kinetic energy range (see section 4.2.2), NEXAFS records spectra over photon energies.[168]

In Chapter 5, B K-edge and O K-edge NEXAFS spectroscopy was used to help identify varying chemical states and environments for B and O atoms in porous BN and intermediates formed during its synthesis. NEXAFS spectroscopy experiments were carried out at the B07 beam line of Diamond Light Source, UK with the support of Dr. Kanak Roy, Dr. Pilar Ferrer and Prof. Georg Held.[169]

Prior to measurement, samples were ground as powders and were mounted onto carbon tape. I used 400 lines per mm Pt gratings of the beamline's plane grating monochromator with an exit slit width of 50 μm, which led to an energy resolution of 50 meV and 200 meV at the B and O K-edges, respectively. B K-edge and O K-edge spectra were recorded at room temperature under ultra-high vacuum (UHV, typically 10^{-8} mbar).

4.2.6. Thermogravimetric analysis coupled with mass spectrometry (TG-MS)

Thermogravimetric analysis (TGA) is used to determine the thermal stability of a sample and which range of temperature can be used to activate a material without degrading it. TGA records the mass loss of a sample over a given temperature range and profile under controlled atmosphere with a high-precision balance ($\pm$0.0001 mg accuracy). Thermogravimetric analysis coupled with mass spectrometry (TG-MS) is used to simultaneously determine the thermal stability of a sample and which gaseous species are released during its heat treatment. Recorded signals in MS need to be associated with potential molecules and ions corresponding to the m/z values detected (where m is the mass of the compound and z the charge number).

In Chapter 5, TG-MS was used to monitor the gas release during the formation of porous BN and understand the porosity development in BN. In Chapter 6, TG-MS helped confirm the functionalization of porous BN with an organosilane through the analysis of the mass loss profile and the associated gaseous species released. The thermal decomposition analysis also allowed quantifying the amount of silane grafted upon functionalization.

TGA was carried out with a Netzsch TG 209 F1 Libra thermal analyzer and MS was carried out with a Netzsch QMS 403 D Aëolos spectrometer. Powder samples were ground prior to measurement and pelletized samples were directly placed in an alumina crucible. The heat treatment first consisted of heating from room temperature to 120 °C and maintaining this temperature for 30 min to remove any moisture. The temperature was then increased to 800 °C with a ramp rate of 10 °C min^{-1} under a mixture of air flow (80 mL min^{-1}; zero grade, 99.998%, BOC) and protective N$_2$ flow (20 mL min^{-1}; 99.998%, zero grade, BOC). Prior to the measurements, a correction run was performed with the empty crucible under the same conditions as used during analysis.

4.3. Characterization of structural and textural features

4.3.1. X-ray diffraction (XRD)

X-ray diffraction (XRD) in reflection mode is a non-destructive technique used to determine the crystal structure of samples.[170] An X-ray beam of wavelength λ is directed towards a sample consisting of different lattice planes separated by a distance d (**Figure 4.5**).
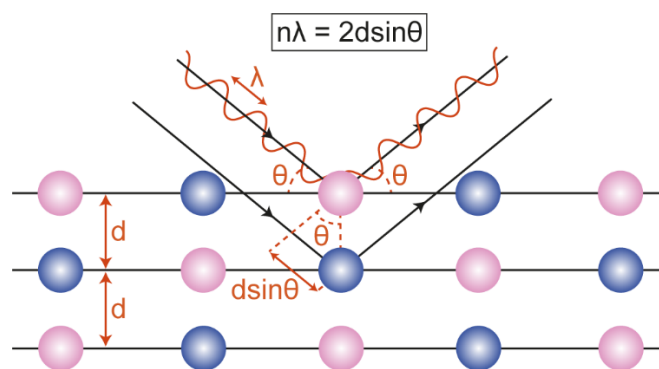
Figure 4.5 Principle of X-ray diffraction illustrated with Bragg's law.

As the angle θ of the beam varies during a measurement, different lattice plans will diffract it, leading to different diffraction patterns that can be associated with certain crystalline structures. This is illustrated by Bragg's law shown in equation (12):

$$n\lambda = 2dsin(\theta) \qquad (12)$$

with:

n diffraction order $\in \mathbb{N}$ (-)

λ wavelength (nm)

d spacing between successive layers of atoms (nm)

θ scattering angle (°)

In Chapters 5, 6 and 7, XRD was used to analyze the crystalline structure of powder and pelletized samples. In Chapter 6 specifically, XRD also allowed to survey the evolution of the amorphous/crystalline character of porous BN upon moisture exposure.

XRD was carried out using a PANalytical X'Pert Pro X-ray diffractometer with an anode voltage of 40 kV and an emission current of 20 mA using a monochromatic Cu Kα radiation ($\lambda = 1.54178$ Å). The XRD detector used was an X'Celerator silicon strip detector. We recorded 1646 points over a 2θ angle range of 5-60° with a step size of 0.033°. Powder samples were ground prior to measurement and pelletized samples were analyzed directly.

4.3.2. Nitrogen sorption isotherms at –196 °C

Nitrogen sorption at –196 °C is a volumetric technique measuring pressure changes between the manifold of the sorption analyzer and the sample chamber due to adsorption/desorption processes.[75] These pressure changes are linked to the quantity of N_2 gas adsorbed at the surface of the adsorbent material tested. N_2 is gradually added in the sample chamber as soon as equilibrium is reached with the adsorbent. This is repeated until the saturation pressure is reached. To determine the free space (or dead volume), which is the volume of the chamber not occupied by the adsorbent, an inert gas such as helium (not interacting with the adsorbent) is used. This technique enables the determination of specific surface area and pore volume.

In this thesis, specific surface area was first evaluated using the Brunauer-Emmett-Teller (BET) theory,[171] which relies on several assumptions:

• the adsorption sites of the adsorbent are energetically equivalent;

• the interactions between neighboring adsorbates are negligible;

• multi-layer adsorption occurs after the formation of a monolayer at the surface of the adsorbent (**Figure 4.6**), this first layer corresponding to Langmuir adsorption;[172]

• the number of adsorbed layers is infinite at the saturation pressure;

• the heat of adsorption in the first layer is higher than in the following layers;

• the heat of adsorption in the second and further layers corresponds to the enthalpy of condensation between neighboring adsorbates.
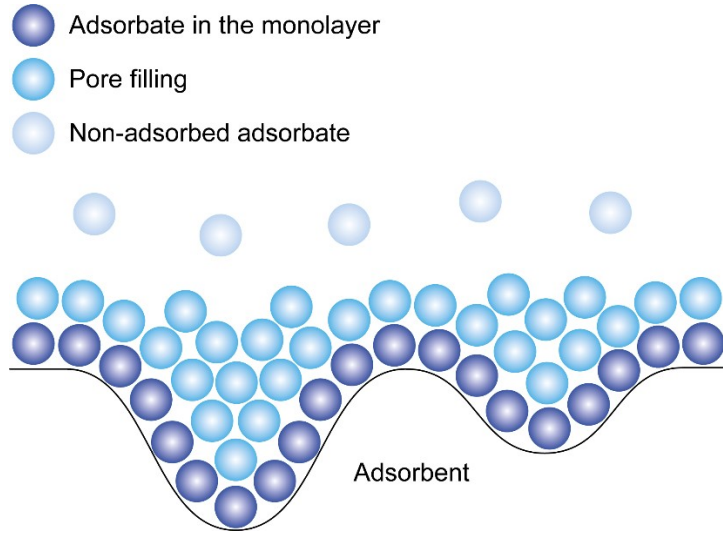
Figure 4.6 Schematic representing the adsorption process with the formation of a monolayer prior to pore filling.

The monolayer capacity and the diameter of the adsorbate, herein N_2, allow the determination of the BET surface area following equation (13):

$$\frac{P}{V(P_0 - P)} = \frac{1}{CV_{mono}} + \frac{C-1}{CV_{mono}}\frac{P}{P_0} \qquad (13)$$

with:

P equilibrium pressure (Pa)

P_0 saturated vapor pressure of N_2 at the measurement temperature (Pa)

V volume of N_2 adsorbed at P (cm^3)

V_{mono} volume of N_2 adsorbed in the monolayer (cm^3)

C BET constant (-)

We note that the constant C can be expressed as shown in equation (14):

$$C = \exp\left(\frac{E_{mono} - E_L}{RT}\right) \qquad (14)$$

with:

E_{mono} adsorption energy of the monolayer (J mol^{-1})

E_L heat of liquefaction (J mol^{-1})

R universal gas constant (≈ 8.314 J K^{-1} mol^{-1})

T temperature (K)

After rearranging equation (13), one can plot the following function shown in equation (15):

$$\frac{1}{V\left(\frac{P_0}{P} - 1\right)} = f\left(\frac{P}{P_0}\right) \qquad (15)$$

C and V_{mono} are obtained using the slope and the intercept values. One can then apply the Rouquerol criteria,[173] which can be used with microporous adsorbents,[174] such as porous BN. Ideally, five data points following a linear fit in the P/P_0 range 0.025-0.30 are used to determine the BET surface area. At partial pressures lower than 0.025, only the monolayer is forming and at partial pressures above ~0.5, capillary condensation may be occurring. Then, the BET surface area can be obtained following equation (16), using V_{mono} that was determined previously:

$$S_{BET} = \frac{V_{mono} S_{ads} N_A}{V_M m} \qquad (16)$$

with:

S_{BET} BET surface area ($m^2\ g^{-1}$)

V_{mono} volume of N_2 adsorbed in the monolayer (cm^3)

S_{ads} cross-sectional area of N_2 ($\approx 0.162\ nm^2$)

N_A Avogadro's constant ($\approx 6.022 \times 10^{23}\ mol^{-1}$)

V_M molar volume of N_2 at standard temperature and pressure ($\approx 22.41\ dm^3\ mol^{-1}$)

m mass of the adsorbent sample (g)

Since the BET surface identification method involves significant manual input, the BETSI method has recently been suggested to overcome the issue of reliability.[175] It is still based on the original Rouquerol criteria, but it does not rely on manual analysis and selection of the isotherm data anymore, which removes error and bias. The BETSI algorithm operates linear regressions on the BET analyses and checks compliance with linearity and fitting criteria iteratively.

The 'total pore volume' (as obtained through N_2 sorption only, which will be discussed later) can be estimated from the volume of N_2 adsorbed at a relative pressure P/P_0 of 0.97, which is obtained from the isotherm using equation (17):

$$V_{tot} = \frac{P_s V_{N_2} V_{M'}}{RT_s} \quad (17)$$

with:

V_{tot} total pore volume ($cm^3\ g^{-1}$)

P_s standard pressure ($=10^5$ Pa)

V_{N_2} quantity of N_2 adsorbed at $P/P_0 = 0.97$ ($cm^3\ g^{-1}$)

$V_{M'}$ molar volume of N_2 at $-196\ °C$ ($\approx 34.7\ cm^3\ mol^{-1}$)

R universal gas constant ($\approx 8.314\ J\ K^{-1}\ mol^{-1}$)

T_s standard temperature ($=273.15$ K)

The micropore volume is determined using the Dubinin-Radushkevich method[176] available on the software. The calculation is based on equations (18) and (19):

$$\log(q) = \log(q_{micro}) - D\left(\log\left(\frac{P_0}{P}\right)\right)^2 \quad (18)$$

with:

q total N_2 adsorption capacity at P ($cm^3\ g^{-1}$)

q_{micro} N_2 adsorption capacity from micropores at P ($cm^3\ g^{-1}$)

D empirical constant (-)

P equilibrium pressure (Pa)

P_0 saturation pressure (Pa)

We can then plot the following function (19):

$$\log(q) = f\left(\log\left(\frac{P_0}{P}\right)\right)^2 \quad (19)$$

This allows the determination of q_{micro} via the calculation of the intercept. The micropore can then be calculated following equation (20):

$$V_{micro} = \frac{q_{micro} M_{N_2}}{\rho} \quad (20)$$

with:

V_{micro} volume of micropores (cm^3 g^{-1})

q_{micro} N$_2$ adsorption capacity from micropores (mol g^{-1})

M_{N_2} molar mass of N$_2$ (=28.02 g mol^{-1})

ρ density of N$_2$ at 77 K (=0.808 g cm^{-3})

Finally, the mesopore volume can be calculated by subtracting the micropore volume V_{micro} from the total pore volume V_{tot}.

In Chapters 5, 6 and 7, I used N$_2$ sorption isotherms at –196 °C to estimate the BET area and the pore volume, in particular of micropores, for all samples studied. The recent BETSI method was used in Chapters 6 and 7 as an improvement to determine BET areas.[175]

N$_2$ sorption isotherms were collected using a Micromeritics 3Flex porosity analyzer at –196 °C. All samples were first degassed ex-situ overnight at 140 °C and 0.2 mbar and then degassed in-situ at 120 °C for 4 h at 0.0030 mbar. At the end of the measurement, the free space was measured with helium. The total pore volume for pore sizes up to 12 nm was estimated from the volume of N$_2$ adsorbed at a relative pressure P/P$_0$ of 0.97. We obtained pore size distributions in the pore width range 0.5-10 nm from the adsorption branch of the N$_2$ isotherms using non-local density functional theory (NLDFT) with a carbon slit-shaped pore geometry kernel. This was sometimes used to determine the micropore volume instead of using the Dubinin-Radushkevich method, considering pores with a width below 2 nm.

4.3.3. Mercury intrusion porosimetry (MIP)

N$_2$ sorption at –196 °C presented above does not enable to probe macropores. Previously, what was referred to as 'total pore volume' could thus be misleading as the maximum pore size being probed was ~50 nm. To tackle this issue, mercury intrusion porosimetry (MIP) can be used to survey larger pores.[104] This technique relies on the concept of wetting: when a drop of liquid is placed on a surface, a contact angle (or wetting angle) forms depending on the surface tension

of the liquid and its attraction to the surface (**Figure 4.7**). A contact angle smaller than 90° is characteristic of a wetting fluid, whereas a contact angle equal to or greater than 90° corresponds to a non-wetting fluid. Since mercury is a non-wetting fluid, an external pressure needs to be applied to make it enter pores.[177] In MIP, the change in volume of mercury is measured as pressure is varied. The applied pressure and the corresponding pore size can be linked through the Washburn equation shown in equation (21):

$$P = \frac{-2\gamma\cos(\theta)}{r} \quad (21)$$

where:

P applied pressure (psi or N m^{-2})

γ surface tension (N m^{-1})

θ contact angle (°)

r pore radius (m)

After obtaining the volume of mercury absorbed by the sample as a function of pressure, and then pore size, the derivative of this data can lead to a pore size distribution. In chapter 6, I will discuss in depth how I combined pore size distributions obtained from both N$_2$ sorption at $-$196 °C and MIP to represent the full pore structure of a hierarchically porous material such as porous BN.
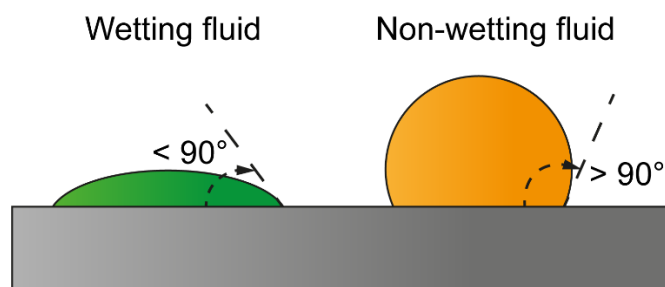
Figure 4.7 Schematic representing a wetting fluid and a non-wetting fluid on a given surface.

In Chapters 6 and 7, MIP was carried out to survey macropores in all the adsorbent materials used. The pore size distributions obtained from both N_2 sorption at –196 °C and MIP were combined to obtain an overall distribution as explained later in Chapter 6.

MIP was carried out using a Micromeritics AutoPore IV instrument. Prior to measurements, pelletized samples were dried under vacuum at 120 °C overnight to remove any moisture. For each sample, five pellets were added to a mercury penetrometer with a capillary intrusion stem volume of 1.1 cm^3. For the low-pressure step, an evacuation pressure of 50 µmHg was applied for 5 min and mercury was then filled at a pressure of 37 mbar and left to equilibrate for 10 s. For the high-pressure measurement, a maximum pressure of 2275 bar with an equilibration time of 10 s was used. The AutoPore IV software (version 9500) was used to obtain a pore size distribution in the range of 2 nm - 325 µm.

4.4. Characterization of thermal properties

Differential scanning calorimetry (DSC)

In this thesis, only differential scanning calorimetry (DSC) was used to characterize the thermal properties of samples. DSC is a technique measuring the difference in the amount of heat needed to increase the temperature of a sample and a reference material. The resulting heat flow is measured as a function of temperature. During a measurement, both the sample and the reference are maintained at the same temperature. DSC is often used to measure the heat flow resulting from a phase change, or to calculate the specific heat capacity of a material, which corresponds to the amount of heat needed to increase its temperature by 1 °C.

In Chapter 7, DSC was used to calculate the specific heat capacity of BN-based materials and activated carbon when considering thermal energy storage applications.

DSC was carried out with a PerkinElmer DSC 8000 instrument under N_2 flow (40 mL min^{-1}; 99.998%, zero grade, BOC). An empty standard pan with a lid was placed in the right side of the furnace, and the left side was used for the measurement of the baseline, the reference and all samples. First, the baseline was measured with an empty pan with a lid, then the reference run used a pan loaded with a sapphire disc of known heat capacity and a lid on top. Finally, each sample was placed as a powder in a pan with a lid on top, without sealing it to allow any residual moisture to escape during the first heat treatment. Each day started with three runs of the baseline and three runs with the sapphire disc to check that the measurements were repeatible. Each sample was also measured three times to remove errors (e.g., due to thermal history, or adsorbed species) and check repeatability. The last runs of the baseline, the reference and a given sample were used for the calculation of the specific heat capacity using the DSC software. The heat treatment first consisted of maintaining a temperature of 15 °C for 5 min to stabilize the heat flow. The temperature was then increased to 130 °C with a ramp rate of 10 °C min^{-1} and maintained for 15 min. The furnace then cooled down to 15 °C before starting the next temperature programme.

4.5. Gas and vapor uptake

4.5.1. CO_2 and N_2 sorption

In Chapter 6, CO_2 and N_2 sorption measurements were carried out to quantify the gas uptake of our porous BN-based materials at 25 °C up to 1 bar and to assess their CO_2/N_2 selectivity. CO_2 sorption measurements were also measured to assess the kinetics of CO_2 adsorption. More information on how adsorption takes place during a measurement can be found in section 4.3.2 on N_2 sorption at –196 °C.

CO_2 (99.9990%, N5.0 research grade, BOC) and N_2 (99.99990%, N6.0 grade, BOC) sorption isotherms were recorded at 25 °C using a Micromeritics 3Flex porosity analyzer and an oil bath to control the temperature. All samples were first degassed ex-situ overnight at 140 °C and 0.2 mbar, and then degassed in-situ at 120 °C for 4 h at 0.0030 mbar prior to analysis.

CO_2 (99.9990%, N5.0 research grade, BOC) sorption isotherms were also collected using a Quantachrome Autosorb iQ3 porosity analyzer at 20, 30 and 40 °C as part of the kinetics study. All samples were degassed ex-situ at 50 °C for 1 h, at 100 °C for 2 h, and finally at 120 °C for 12 h at 0.0053 mbar following our previous method.[178] Details of the set-up used to quantify kinetics are outlined in section 6.3.3 of Chapter 6.

4.5.2. Water vapor sorption

In Chapter 6, water vapor sorption was used to quantify the water uptake of unmodified and functionalized porous BN pellets, and assess their stability towards water vapor.

Water vapor sorption isotherms were collected using a Micromeritics 3Flex porosity analyzer at 22 °C and an oil bath to control the temperature. Deionized water (18 MΩ cm) was placed in a container fitted to the instrument and purified with four freeze-pump-thaw cycles prior to the measurement to remove any air and dissolved gases. All samples were first degassed ex-situ overnight at 140 °C and 0.2 mbar and then degassed in-situ at 120 °C for 4 h at 0.0030 mbar.

4.5.3. Heptane and n-propanol sorption

In Chapter 7, heptane and n-propanol sorption isotherms were individually measured to quantify the uptake of BN-based materials and activated carbon. These measurements were

also used for the determination of heats of adsorption, and the modeling of breakthrough curves and temperature profiles during adsorption.

Heptane (anhydrous 99%, Sigma-Aldrich, CAS 142-82-5) and n-propanol ($\geq$ 99.9%, Sigma-Aldrich, CAS 71-23-8) sorption isotherms were collected using a Micromeritics 3Flex porosity analyzer at 15, 25 and 35 °C, with an oil bath to control the temperature. Heptane or n-propanol was placed in a container fitted to the instrument and purified with four freeze-pump-thaw cycles prior to the measurement to remove any air and dissolved gases. All samples were first degassed ex-situ overnight at 140 °C and 0.2 mbar and then degassed in-situ at 120 °C for 4 h at 0.0030 mbar.

CHAPTER 5: FORMATION MECHANISM AND POROSITY DEVELOPMENT IN POROUS BORON NITRIDE

The work and the discussion described in this chapter (apart from the pilot plant study) have been previously published by the thesis author in the Journal of Physical Chemistry C.[7] All measurements were performed by the thesis author, except the nuclear magnetic resonance (NMR) measurements, which were carried out by Dr. Daniel M. Dawson at the University of St Andrews, UK. The NEXAFS spectroscopy experiments were carried out by the thesis author at the B07 beam line of Diamond Light Source, UK with the support of Dr. Kanak Roy, Dr. Pilar Ferrer and Prof. Georg Held.

5.1. Introduction

As seen earlier in this thesis, various studies in the literature provide preliminary insights into the potential of porous BN for molecular separations,[4, 24, 39, 106-110] and more recently for photocatalysis.[22, 27] This encourages researchers to produce porous BN in larger quantities than those obtained at laboratory scale. At the start of my PhD, I received porous BN materials that had been produced by a third-party manufacturer following the synthesis process used in our laboratory.[3] Stark differences were observed in the pilot plant samples, both between each other and compared to lab-made porous BN. This will be discussed in this chapter to draw insights on what may have been missing during scaling-up. In particular, to ensure the reliable deployment of porous BN at larger scale and a repeatable synthesis process, an understanding of its formation process is required.

Few studies investigated the mechanism of porous BN formation via bottom-up synthesis.[4, 14, 42-44] Most report the formation of hexagonal boron nitride (h-BN), the non-carbonaceous analogue of graphene with no surface area (or low surface area < 100 m^2 g^{-1} when defects are present) as opposed to porous BN.[17, 19] In all the studies of porous BN, a few reactions have been suggested that account for the formation from boron- and nitrogen-containing precursors, but there is no consensus to date for a comprehensive reaction scheme with respect to the thermal treatment. In addition, reported syntheses use different reagents, gas atmospheres and reaction conditions, which impact the formation process and resulting product. Finally, different levels of purity are required, depending on the industrial application. Therefore, understanding how inherent oxygen and carbon impurities can be eliminated from the BN structure is critical.

Although no detailed formation mechanism has been confirmed and the synthesis parameter space (i.e., precursors, atmosphere, temperature) varies from study to study, two possible mechanisms to form porous or non-porous BN seem to emerge and were reported in a previous study by O'Connor:[48] (i) nitridation of boron oxide with ammonia either from the reaction atmosphere or from decomposition of N-containing precursors, and (ii) annealing of carbon nitride with boron from boron oxide. The two mechanisms may not be mutually exclusive and may also depend on the synthesis parameter space. Under the former mechanism fall, for instance, the studies by Brožek and Hubáček,[14] Ramirez Leyva et al.,[43] Wu et al.,[44] Tian et al.,[42] Hoffendahl et al.[47] and Jahnichen et al.[179] The second category includes the work by Gong et al.,[46] who used graphene as a precursor. Hoffendahl et al.[47] indicated the formation of carbon nitride from melamine but referred to the reaction of boron oxide with ammonia to eventually form BN. Among all the above studies, only those of Ramirez Leyva et al.[43] and Tian et al.[42] cover the formation of porous BN and they link the porosity to gases released during the reaction, as also suggested by our earlier study.[4] A recent study by Höppe and Gross reports

ammonium bis(biureto)borate as an intermediate in boron nitride formation using boric acid and urea under N_2.[45] In short, the formation mechanism of porous BN remains largely a 'black box'. Herein, I aim to address this knowledge gap by answering the following questions: What is the minimal temperature required to form porous BN? Which chemical intermediates are formed before obtaining porous BN? What is the influence of the precursors on the chemical and structural features of porous BN? I will also consider whether the two mechanisms mentioned earlier could take place concurrently in the reaction medium. To answer these questions, I focus on the formation mechanism based on the reaction of boric acid, melamine and urea heated up to 1050 °C under N_2 atmosphere, which consistently yields porous BN with high surface area, high pore volume and promising sorption performance.[3] To this end, I synthesized reaction intermediates at different temperatures up to 1050 °C. I investigated these intermediates with a variety of analytical and spectroscopic tools to propose a comprehensive formation mechanism of porous BN, paving the way for scale-up towards industrial applications.

5.2. Materials

5.2.1. Pilot plant production of porous BN by a third-party manufacturer

Based on the synthesis of porous BN previously developed in our group,[3] a third-party manufacturer was asked to synthesize the material at larger scale in a pilot plant. As a comparison, a typical synthesis in our laboratory would yield approximately 200 mg of porous BN, whereas their theoretical yield could reach 20 g (**Table 5.1**). Despite using the same precursors as in our laboratory process (i.e., boric acid, melamine and urea) and N_2 gas atmosphere with a flow rate of 250 cm^3 min^{-1}, the manufacturer's set-up presented some differences to ours previously shown in **Figure 4.1**: their tubular furnace was vertical as opposed to horizontal, and the maximum temperature they could reach was 950 °C as opposed

to 1050 °C in our synthesis. They produced four batches of material, named BN-1 to BN-4, based on the run number. **Table 5.1** summarizes the temperature conditions and the yields for each run. The manufacturer observed that the target temperature of 950 °C was not reached for runs 1, 2 and 3. The higher experimental yields than the theoretical values, especially for BN-3, imply that impurities were present in the materials obtained. The composition of these impurities will be explained later on.

Table 5.1 Synthesis conditions and yields for each pilot plant run from BN-1 to BN-4.

Sample	BN-1	BN-2	BN-3	BN-4
Furnace temperature (°C)	930	930	800	950
Theoretical yield (g)	10	10	20	20
Experimental yield (g)	10.7	10.7	36	18

5.2.2. Synthesis of porous BN and its reaction intermediates

In our laboratory, porous BN was synthesized following the multiple N-containing precursor synthesis previously developed in our group[3] and described in the Methods chapter of this thesis (section 4.1.1). To investigate the nature of the reaction intermediates in the formation of porous BN, I carried out multiple syntheses based on the same initial mixture by programming the final temperature at: 100, 200, 300, 400, 600, 700, 800 and 900 °C. In the case of the intermediates, the furnace was allowed to cool down naturally as soon as the final temperature was reached to analyze the compounds present at this exact temperature during porous BN synthesis - neglecting any effect of the cooling down step. As a reference, the initial mixture was also analyzed and referred to as the room temperature (RT) intermediate. Intermediate samples are referred to as 'INT-X' where X corresponds to RT or the final temperature reached for each intermediate between 100 and 900 °C. Finally, I evaluated the

impact of the 3.5-h dwell time at 1050 °C and synthesized an intermediate at 1050 °C with no dwell time before cooling. This sample is referred to as 'BN-1050-t_0' as opposed to 'BN-1050-$t_{3.5}$', which corresponds to our final product, porous BN. Note that when 1050 °C is mentioned in results without time indication, this corresponds to the sample 'BN-1050-$t_{3.5}$'. After synthesis, all samples were stored in a desiccator at room temperature to enhance shelf-life and prevent any degradation from moisture.[6]

5.2.3. Synthesis of carbon nitride

To compare the composition of relevant intermediates, carbon nitride (C_3N_4) was synthesized from melamine powder. Melamine was placed in an alumina crucible with the lid on, which was then placed inside a muffle furnace heated up to 560 °C with a heating rate of 5 °C min^{-1}. The final temperature was maintained for 4 h before the furnace was allowed to cool down naturally.

5.3. Results & discussion

A range of analytical and spectroscopic techniques that I have used extensively in this PhD (described in the Methods chapter) were used to characterize the intermediates materials and porous BN. In particular, FTIR and XPS were used to investigate chemical features, and XRD and N_2 sorption isotherms at –196 °C were used to look at structural features. Solid-state NMR and NEXAFS provided further knowledge on the chemical features. TG-MS helped shed light on the porosity development and the species released during the synthesis of porous BN.

5.3.1. The challenge of scaling-up the synthesis of porous BN

As mentioned previously, we received pilot-plant-scale porous BN samples at Imperial College London. All samples were composed of hard aggregates instead of flakes or powder obtained in our laboratory, called BN-lab (**Figure 5.1**). BN-1, BN-2 and BN-4, all synthesized between 930 and 950 °C (**Table 5.1**), contained a heterogeneous mix of colors, whereas BN-3 had a uniform beige color. In comparison, BN-lab always has a white color. It is worth noting that BN-3 was only synthesized at 800 °C, which may imply an incomplete formation of porous BN, linked to the much higher yield for this synthesis. The black color can be characteristic of carbon impurities, whereas yellow color can correspond to oxygen impurities.
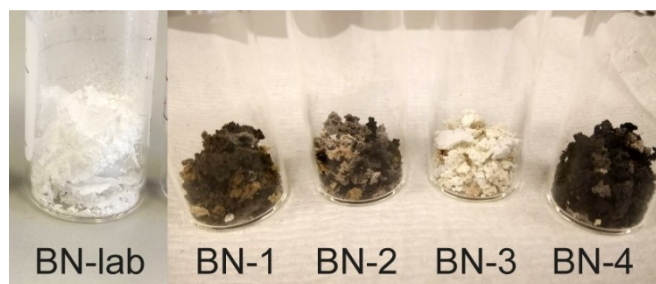
Figure 5.1 Visual aspect of porous BN as synthesized in our laboratory ('BN-lab') and the four BN materials synthesized at multi-gram scale ('BN-1' to 'BN-4').

To confirm that porous BN was obtained and to assess the nature of the potential impurities, I characterized the chemical and structural properties of each sample. In terms of chemistry, FTIR analyses showed the characteristic B-N and B-N-B bands around 1354 cm^{-1} and 812 cm^{-1}, respectively,[180] confirming that BN was effectively obtained in each pilot plant run (**Figure 5.2**a), but the atomic composition derived from XPS analyses showed varying proportions of B and N atoms depending on the run (**Figure 5.2**b; XPS spectra shown in **Figure A2.1** in Appendix 2). BN-1, BN-2 and BN-3 contained relatively high amounts of O and C impurities, whereas BN-4 had an atomic composition close to that of BN-lab. However, this did not explain

the difference in visual aspect of BN-4, which was made of gray and black aggregates (**Figure 5.1**). Furthermore, I had hypothesized that the yellow color of BN-3 could be linked to a high content of oxygen, but the B-O bands observed around 1120 cm^{-1} in FTIR do not appear stronger in BN-3 than in other samples. This is also not shown in the XPS results (**Figure 5.2**b). One hypothesis could be the presence of carbon nitride or other compounds with triazine rings (6-membered ring with 3 C and 3 N atoms), which are characteristically yellow.[47] The higher content of C and lower content of B in BN-3 could reinforce this hypothesis (**Figure 5.2**b), as well as the lower synthesis temperature recorded for this sample (**Table 5.1**). This hypothesis will be checked in the rest of this chapter.
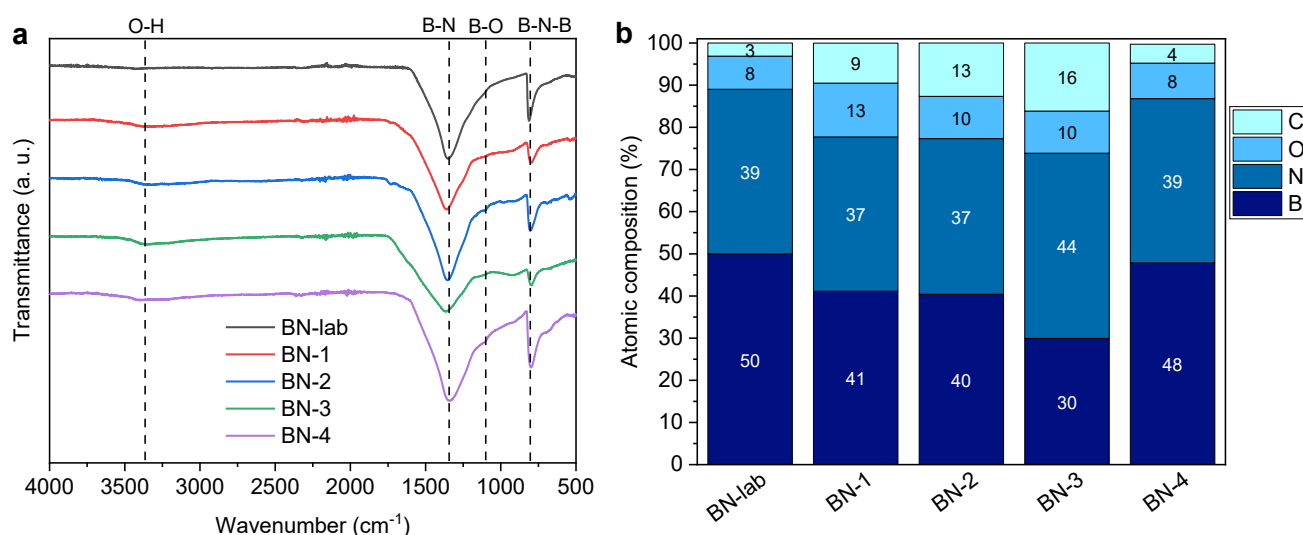
Figure 5.2 (a) FTIR spectra for porous BN obtained in the laboratory and in the pilot plant. (b) Estimated atomic composition derived from XPS analyses.

When looking at the XRD profiles for the pilot plant samples, broad humps around 24° and 44° were observed in all samples (**Figure 5.3**a). Features at these angles typically correspond to the (002) and (100) planes in graphitic-like structures such as BN and C$_3$N$_4$,[181-183] but their wide shape implies that the materials are highly amorphous, similarly to BN-lab. BN-1 and BN-2 presented peaks around 11° and 28° that could correspond to boron oxide B$_2$O$_3$.[184] To

assess textural properties, N_2 sorption isotherms were measured at –196 °C (**Figure 5.3**b). Textural parameters were then extracted from these measurements (**Figure 5.3**c). All samples had lower BET areas and pore volumes than BN-lab. In particular, BN-3 had a BET area of 332 m^2 g^{-1} compared to 1664 m^2 g^{-1} in the case of BN-lab. This reinforced the hypothesis of the presence of carbon nitride compounds, which would be non-porous.[185] BN-1 and BN-2 had different BET areas (968 m^2 g^{-1} and 580 m^2 g^{-1}, respectively) and total pore volumes assessed via N_2 sorption (0.748 cm^3 g^{-1} and 0.475 cm^3 g^{-1}, respectively) despite being synthesized at the same temperature, 930 °C (**Table 5.1**). We note that BN-4, which presented the most similar chemistry as BN-lab (**Figure 5.2**), had the highest BET area (1232 m^2 g^{-1}) and pore volume (1.341 cm^3 g^{-1}) among the pilot plant BN materials. These textural properties were the closest to those of BN-lab.
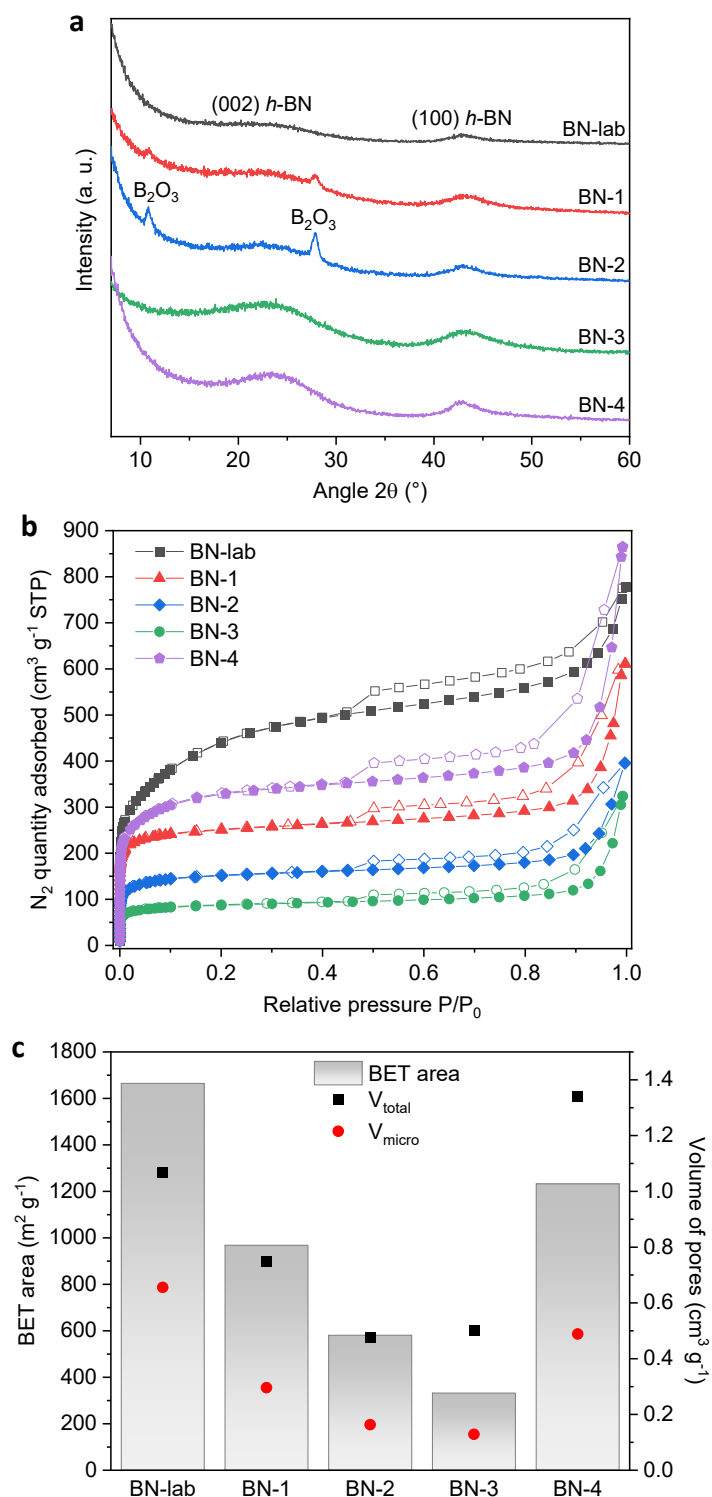
Figure 5.3 (a) XRD profiles; (b) N_2 sorption isotherms at –196 °C (full symbols = adsorption; open symbols = desorption) and (c) Associated textural parameters for porous BN synthesized in the lab and at the third-party manufacturer.

In conclusion, this preliminary work showed that porous BN could be synthesized using a multi-gram-scale set-up, but it was difficult to get a repeatable process despite using the same

initial conditions between different runs (i.e., precursors, targeted temperature). All samples were heterogeneous in color and varied in chemical compositions. A high amount of O and C impurities was usually observed, which is not desired over a certain extent in the final porous BN product, as it would impact on its sorption properties. One sample performed relatively well in N_2 sorption at –196 °C with high BET area and pore volume (BN-4). However, two materials produced at the same temperature exhibited different textural properties (BN-1 and BN-2). All of these observations pointed to the complexity of the synthesis process of porous BN, which is not straightforward to scale-up even at an intermediate scale, i.e., from multigram- to gram-scale herein.

5.3.2. Chemical aspects of the formation of porous BN

From now on, I will be focusing on materials made in our laboratory and will use the sample naming system introduced in section 5.2.2.

Upon synthesis, consistent results were obtained for the final porous BN product in terms of macroscopic appearance (**Figure 5.4**a) compared to porous BN synthesized following the same methodology.[3, 6] All the intermediates were collected after synthesis in the furnace and were analyzed to investigate their composition and understand the chemical formation of porous BN. INT-RT and INT-100 were powders whereas the samples prepared at 200 °C and above appeared as flakes (**Figure 5.4**a). Two intermediates were distinct by their yellow color: INT-600 and INT-700 (**Figure 5.4**a). This unique characteristic suggests important implications and will be discussed later alongside the characterization results.
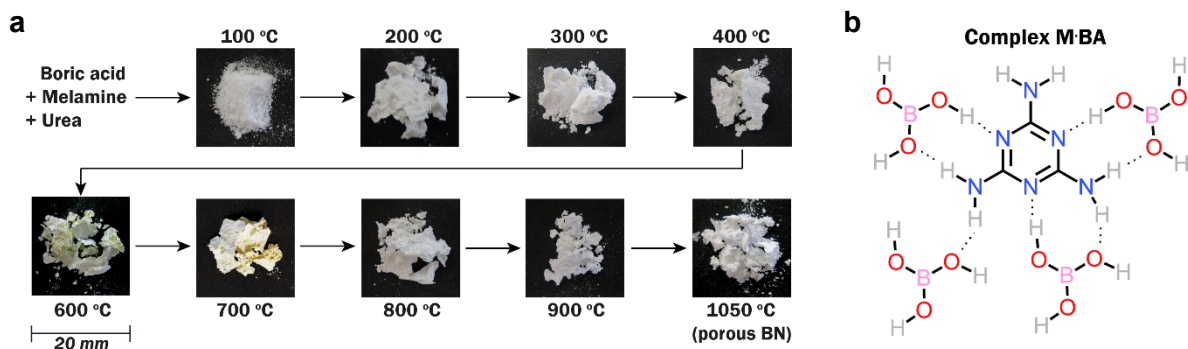
Figure 5.4 (a) Macroscopic aspect of the reaction intermediates and final product porous BN. (b) Chemical structure of the adduct M.BA formed by melamine and boric acid via hydrogen bonding.

Starting intermediate, room temperature – I now focus on the chemical features of the intermediates. I first recorded the FTIR spectra for each reagent individually (**Figure A2.2**a in Appendix 2) to calculate the expected spectrum of the mixture without any interaction by considering the relative amounts of reagents. To identify IR bands and assess the interaction between the initial reagents upon mixing, I compared the experimental FTIR spectrum with the calculated spectrum of the initial mixture of reagents, INT-RT (**Figure 5.5**a and **Figure A2.2**b in Appendix 2). The theoretical FTIR spectrum for INT-RT was calculated using the molar quantities of each reagent used in the synthesis (molar ratios BA:M:U = 1:1:5) and neglecting any interaction between them. Boric acid was not traced at RT due to its low quantity in the initial mixture compared to the N-containing precursors. This was confirmed by the calculated FTIR spectrum based on the initial composition. However, I observed differences between the expected FTIR spectrum and the one obtained, especially in the $3100 - 3470$ cm^{-1} region corresponding to OH and NH$_2$ groups. INT-RT exhibited bands at 3469, 3426, 3326 cm^{-1} accounting for NH$_2$ groups of melamine and urea, whereas the calculated spectrum only showed bands at 3418 and 3323 cm^{-1} (**Figure A2.2**b in Appendix 2). The presence of an additional band at higher frequency, 3469 cm^{-1}, and the redshift of the two other bands could be linked to hydrogen bonding (H bonding) between melamine and boric acid.[186] I attributed

the 3256 cm^{-1} band observed in both INT-RT and the calculated spectrum to NH$_2$ groups from urea, which appeared unaffected by hydrogen bonding. From this observation, I hypothesized that boric acid and melamine formed a melamine-boric acid adduct (M·BA) via H bonding after mechanical mixing at RT (**Figure 5.4**b). The proportion of this adduct in the sample is not known and pristine reagents are likely to still be present in significant quantity, which might be the reason why no signs of this intermediate are observed in the XRD patterns (**Figure 5.5**c). Previous studies showed that M·BA adducts adopt a specific configuration with only two amino groups from melamine involved in H bonding with three to four boric acid molecules.[186, 187] This adduct explains the additional IR band observed at 3469 cm^{-1} in INT-RT corresponding to the different N-H bond length when NH$_2$ groups from melamine molecules are involved in H bonding. The two red-shifted bands at 3418 and 3323 cm^{-1} correspond to NH$_2$ groups not contributing to H bonding but affected by a different chemical environment.
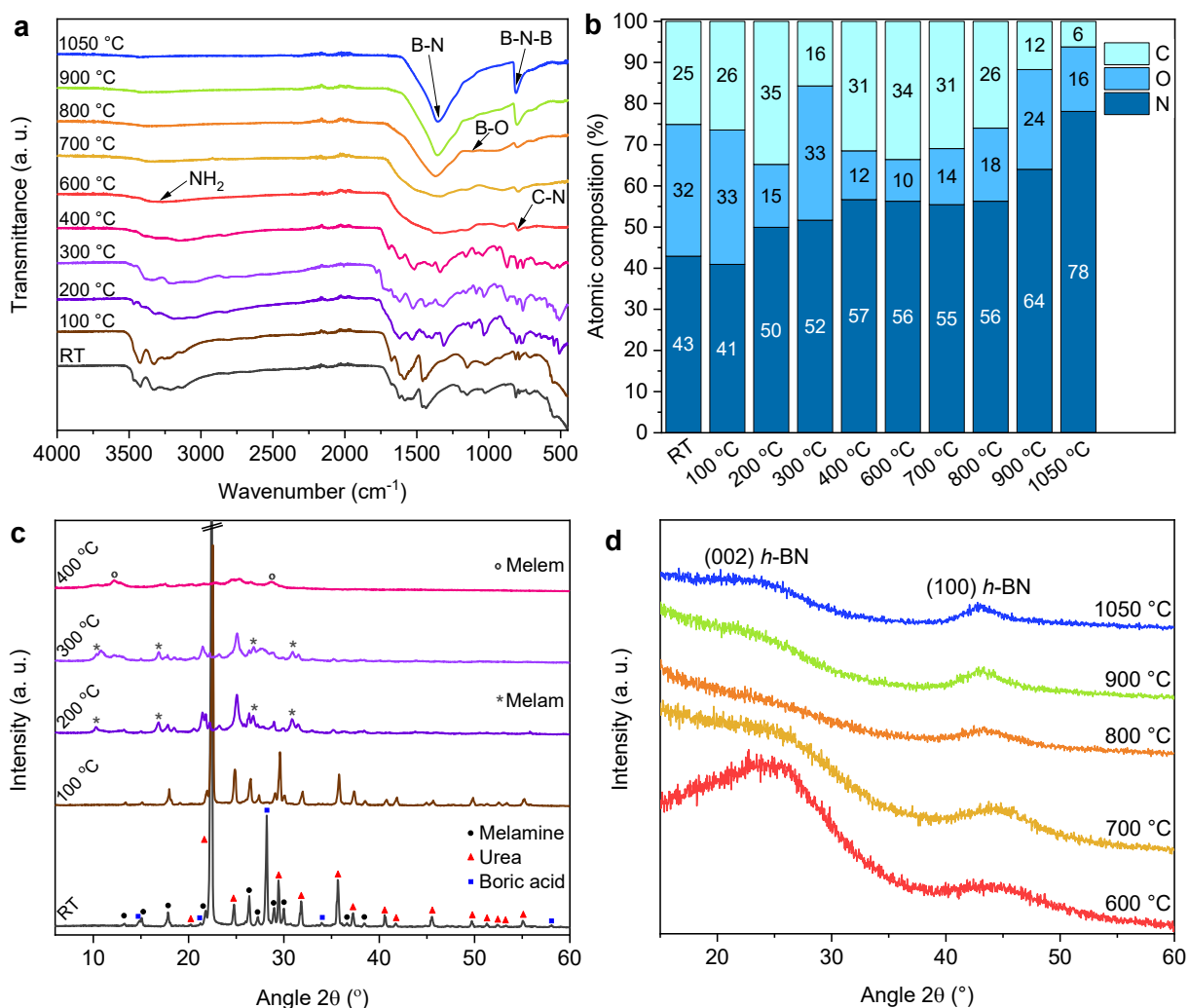
Figure 5.5 (a) FTIR spectra for all the intermediates. (b) Estimated atomic composition derived from XPS. The data were normalised based on the constant boron content. (c) XRD profiles for the intermediates obtained between 100 and 400 °C. (d) XRD profiles for the intermediates obtained between 600 and 1050 °C. Note: a different vertical scale was used in (c) and (d) for clarity.

Between room temperature and 100 °C – Here, I observed a minor change in composition based on the FTIR and XPS analyses (**Figure 5.5**a-b and **Figure 5.6**). We note that the atomic composition derived from XPS measurements in **Figure 5.5**b is normalized to the boron content, which remains constant during the synthesis due to its thermal stability (boron's melting point is 2077 °C). The initial composition exhibited lower %N and higher %O than expected from a theoretical calculation based on the amounts of precursors (**Table A2.1** in Appendix 2). This variation appears as XPS, a surface-sensitive technique, provided only the

surface composition. The formation of the M·BA adduct can likely modify the surface composition after grinding at RT. In the XRD patterns, I observed the three precursors at RT (**Figure 5.5**c, see reagents XRD patterns in **Figure A2.2**c in Appendix 2). INT-100 exhibited the same XRD peaks as INT-RT corresponding to urea (e.g., 22, 25, 29, 32 and 36°) and melamine (e.g., 18, 22, 26, 29 and 30°), but with lower intensities, and the boric acid peaks were not present (**Figure 5.5**c). These changes could indicate the conversion of boric acid into boron oxide (B_2O_3) with the release of water,[188] and/or the formation of another B-containing species. Indeed, quantitative ^{11}B NMR spectra confirm that a large portion (~72%) of the B is trigonal in INT-100, as expected for either $B(OH)_3$ or B_2O_3 (**Figure 5.7**a). However, the remaining 28% of the B spectral intensity corresponds to tetrahedral species with isotropic shifts of 1.5 and 0.5 ppm. We hypothesize that these tetrahedral species correspond to adducts formed between boric acid and the amine groups present in urea and melamine. This is supported by the Lewis acid nature of boron and the Lewis basic nature of the amines.
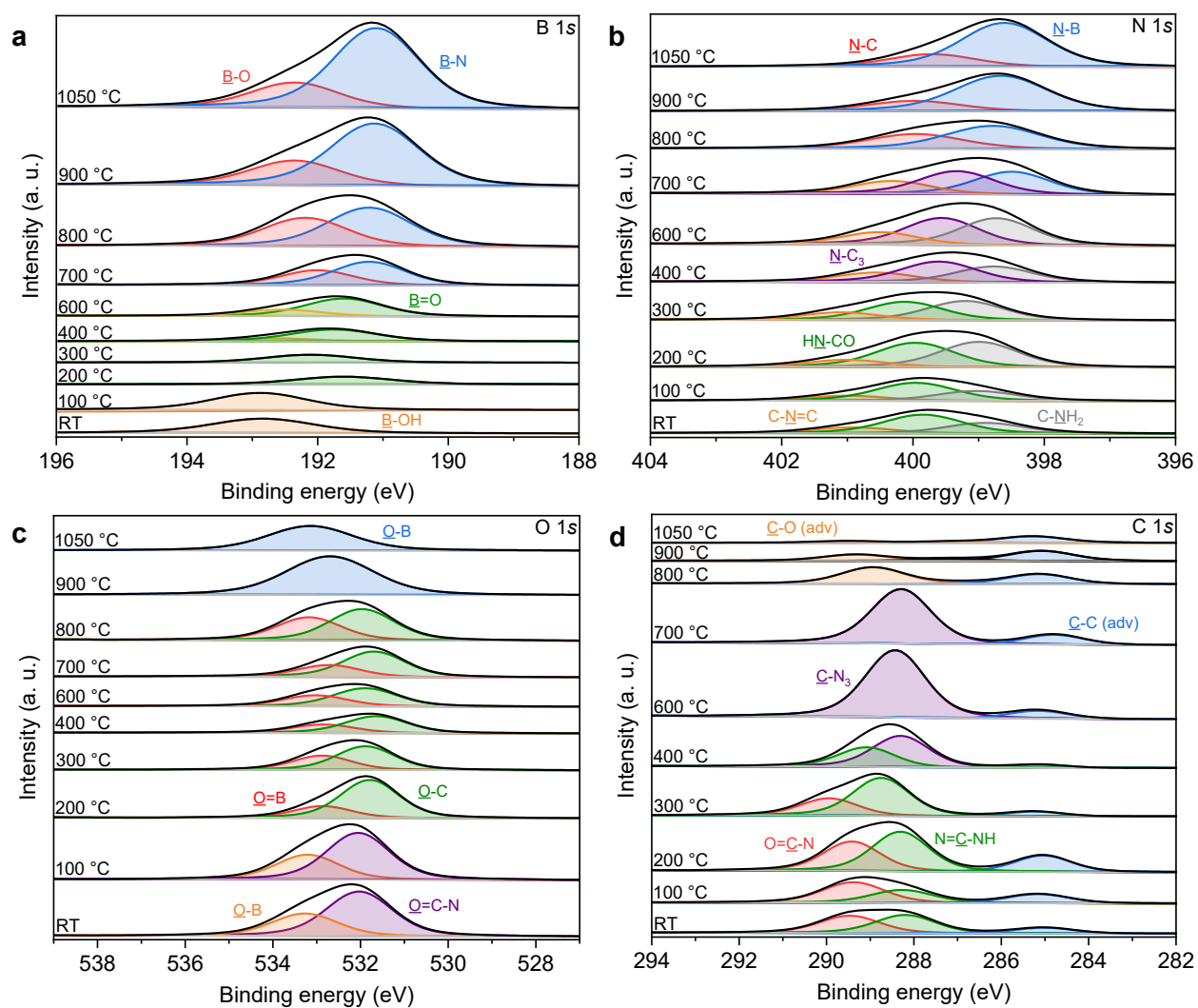
Figure 5.6 High-resolution XPS and peak fitting of the (a) B 1*s* (b) N 1*s* (c) O 1*s* and (d) C 1*s* core levels for all the intermediates.
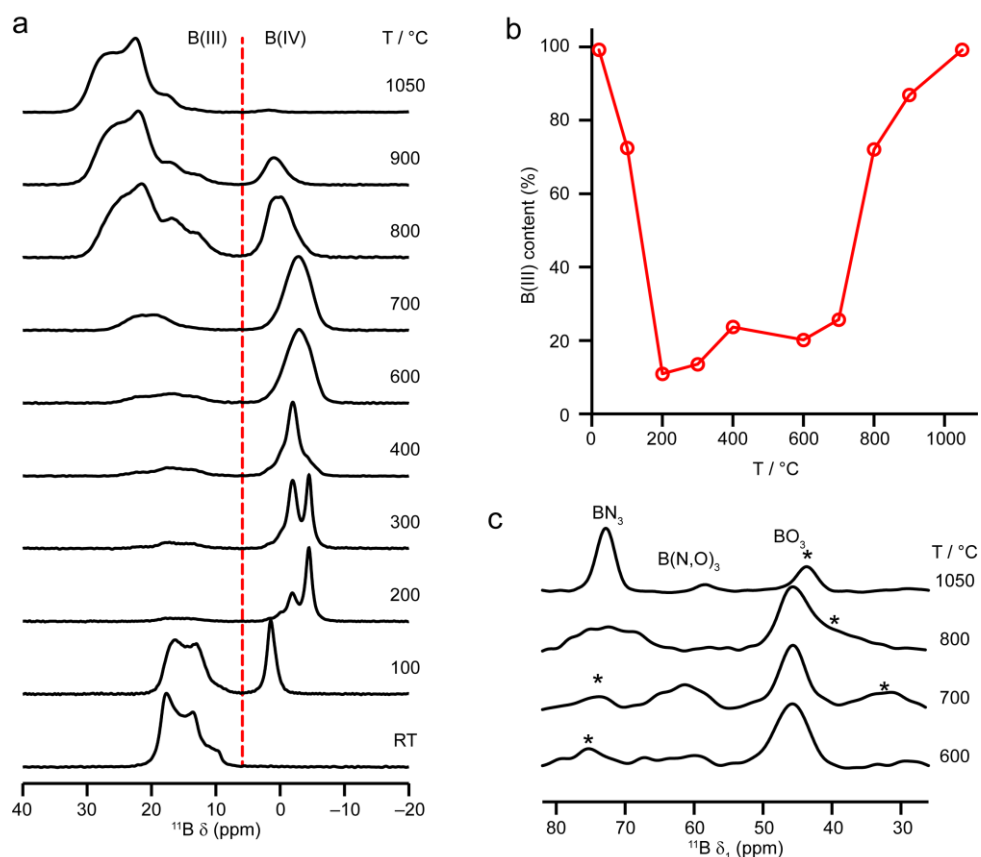
Figure 5.7 (a) $^{11}B(^{1}H)$ (14.1 T, 10 kHz MAS) NMR spectra of all of the intermediates. The dotted line at 6 ppm shows the border between trigonal (> 6 ppm) and tetrahedral (< 6 ppm) B signals. (b) The proportion of trigonal B signal determined from integrated intensities from the spectra in (a). (c) δ_1 projections of the trigonal B signals observed in ^{11}B MQMAS spectra for selected intermediates. Spinning sidebands are marked * (see later in Figure 5.10).

Between 100 and 200 °C – The B 1*s* XPS peak corresponding to B-O bonds (192.9 eV) was replaced by a peak corresponding to B=O bonds (191.6 eV), showing that a significant quantity of boric acid disappeared as it formed boron oxide (**Figure 5.6**a). Urea was mostly degraded at 200 °C, as shown by the disappearance of the corresponding signals in FTIR (e.g., C=O, 1677 cm^{-1} and C-N, 1457 cm^{-1} in **Figure 5.5**a) and XRD (e.g., 22, 29, 36° in **Figure 5.5**c). Urea decomposed into sub-products such as biuret, cyanuric acid and ammelide, which can coexist over a wide range of temperatures.[179, 189, 190]

Between 200 and 400 °C – At 200 °C, a new FTIR band was observed at 1311 cm^{-1}, which shifted towards higher wavenumbers at 300 °C and 400 °C. I identified this band as melam, which is one of the condensates of melamine with two bonded triazine rings.[191] I attributed the gradual shift to 1343 cm^{-1} at 400 °C to a further condensation into melem, containing a tri-s-triazine ring.[191, 192] Additionally, the band at 809 cm^{-1} in INT-200 is characteristic of the triazine ring of melamine and melam whereas the band at 798 cm^{-1} in INT-300 and INT-400 is characteristic of the tri-s-triazine ring of melem.[181, 182, 193] The sharp band appearing at 874 cm^{-1} in INT-300 and INT-400 is also characteristic of the tri-s-triazine ring of melem.[182] In XRD, I observed peaks at 10°, 17°, 27° and 31° in INT-200 (**Figure 5.5**c). These four peaks remained at 300 °C with equal intensities but were not observed at 400 °C, which suggests the condensation of melamine and melam into melem at 400 °C. I attributed the new peaks at 12° and 28° in INT-400 to melem.[192] This was consistent with the XPS of INT-400 showing a new C 1s peak at a binding energy of 288.3 eV, corresponding to CN$_3$ environments present in melem. In parallel, the evolution of boric acid and urea likely contributed to an amorphous transition of the mixture, and no clear peaks were observed in XRD beyond 400 °C.

Over the 200-400 °C temperature range, the quantitative ^{11}B NMR spectra show that the vast majority of B is present in tetrahedral environments, giving rise to isotropic shifts of 0, –1.9 and –4.5 ppm (**Figure 5.7**a). Around 11-23% of B is trigonal, with peak positions consistent with BO$_3$ and, at 400 °C, BN$_2$O local environments (**Figure A2.3** in Appendix 2). The tetrahedral species could correspond to B atoms being coordinated to carbon/nitrogen-based structures evolving in the reaction medium.

Between 400 and 700 °C – 600 °C marked a crucial transition in the synthesis process: the product appeared yellow to the naked eye and was completely amorphous based on the broad XRD features (**Figure 5.4**a and **Figure 5.5**d). INT-700 was also yellow and amorphous. The

yellow color of these samples suggested the presence of carbon nitride.[47, 192] We note that some IR bands of carbon nitride and BN compounds can overlap, e.g., bands at 812 cm^{-1}, 891 cm^{-1} and between 1200 and 1600 cm^{-1}.[183] This effect complicates the interpretation of the FTIR spectra for INT-600 and INT-700 (**Figure 5.5**a). Bearing that in mind, I did not clearly see the characteristic IR band for B-N bonds (~1354 cm^{-1}) in INT-600 and INT-700 (**Figure 5.5**a), suggesting that significant porous BN did not form at 600 °C nor 700 °C. The XRD patterns of INT-600 and INT-700 showed broad humps around 24° and 44°, which typically correspond to the (002) and (100) planes in graphitic-like structures, such as BN and C_3N_4.[181-183] Although matching with the profile of porous BN, the hump around 44° could also correspond to the tri-s-triazine ring observed in melem and carbon nitride.[182, 194] This suggestion is further supported for INT-600 by the rest of the pattern below 24° that differed from BN (**Figure 5.5**d). However, the XRD profile of INT-700 seemed to be intermediate between those of INT-600 and INT-800. I did not observe the characteristic B 1s peak for B-N bonds (191.2 eV) in the XPS of INT-600 whereas it started appearing in INT-700 (**Figure 5.6**a). The carbon content was still high in INT-700 but decreased significantly in INT-800, as observed in the estimated composition in XPS (**Figure 5.5**b). Based on the yellow color of both INT-600 and INT-700 and the previous analyses, I propose the formation of carbon nitride prior to the formation of porous BN. INT-600 and INT-700 appeared amorphous and non-porous as discussed below. These observations supported the hypothesis that carbon nitride formed, since this material has low porosity.[185] Some BN was observed in INT-700, but in too little proportion to observe porosity. I discuss this aspect further in section 5.3.3. ^{13}C NMR confirmed further the formation of carbon nitride in INT-600, comparing to the spectrum of pure C_3N_4 (**Figure 5.8**). Condensation towards carbon nitride-like species, such as melam and melem, starts at relatively low temperature (~200 °C) but is not complete even by 600 °C (**Figure 5.8**).
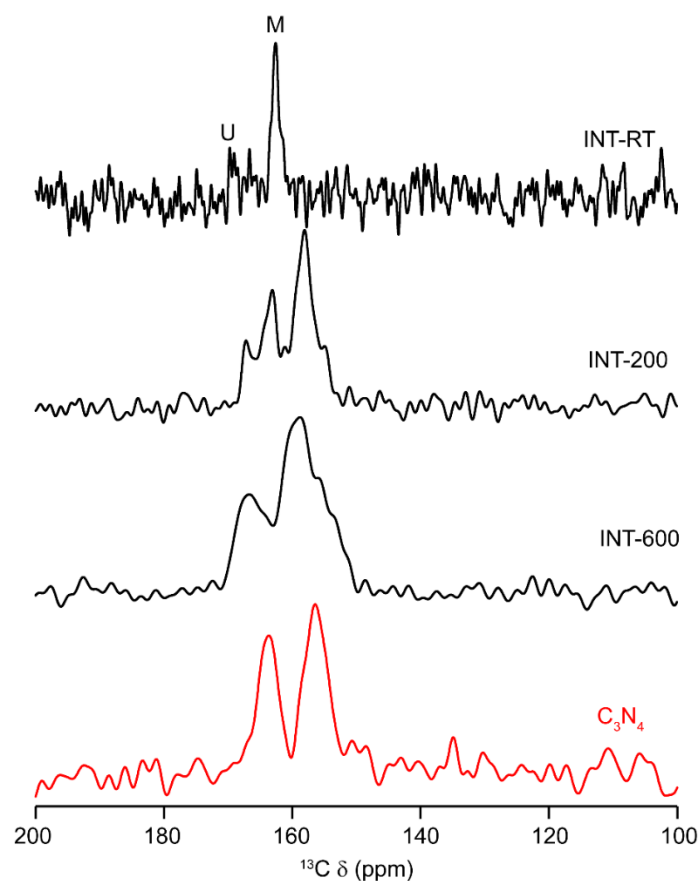
Figure 5.8 ^{13}C (9.4 T, 12.5 kHz MAS) NMR spectra of the indicated intermediates (black) and carbon nitride C_3N_4 (red). Owing to the very slow longitudinal relaxation for urea, the signal (marked U) is much lower in intensity, relative to the melamine (M) signal, than might be expected.

The quantitative ^{11}B MAS NMR spectra of INT-600 and INT-700 (**Figure 5.7**a) show that the majority of B remains tetrahedral at this stage in the reaction (80% for INT-600, 75% for INT-700). However, in contrast to the sharp signals for the samples formed at 200-400 °C, the resonances at 600 and 700 °C are much broader, indicative of a loss of longer-range order (consistent with the XRD data, **Figure 5.5**c-d). While the signal for the tetrahedral B is essentially unchanged between 600 and 700 °C, what little trigonal B is present does change in environment, with the peak positions consistent with predominantly BO_3 and a smaller amount of BN_2O at 600 °C and almost exclusively BN_2O at 700 °C.

Between 700 and 1050 °C – BN formed between 700 and 800 °C, as supported by the B-N bonds identified in FTIR (1354 cm^{-1} for B-N and 812 cm^{-1} for B-N-B; Figure 2a)[180], in XPS (191.2 eV for B 1s and 398.6 eV for N 1s; **Figure 5.6**a-b)[195] and ^{11}B MAS NMR (for BN$_3$ environments; **Figure 5.7**a-c), as well as the (002) and (100) XRD humps (respectively 24° and 44°; **Figure 5.5**d) expected for amorphous BN.[19] On the FTIR spectra, B-O bands (~1120 cm^{-1}) gradually disappeared between 800 °C and 1050 °C (**Figure 5.5**a). In parallel, the content of carbon decreased as seen in XPS (**Figure 5.5**b). The dwell time of 3.5 h at 1050 °C did not significantly change the structure of porous BN as I obtained identical results for BN-1050-t$_0$ and BN-1050-t$_{3.5}$, but it contributed to further overall conversion into porous BN with a decrease in O and C impurities (**Figure 5.9**a-c). The ^{11}B MAS NMR spectra of the samples formed above 700 °C show a loss of tetrahedral B, with only ~1% B in a tetrahedral environment by 1050 °C (**Figure 5.7**a-b). For INT-800 and INT-900, some BO$_3$ signals are observed, although by 1050 °C, the trigonal B is almost exclusively in a BN$_3$ environment, as would be expected in hexagonal BN, and only a trace (~7%) of BN$_2$O is observed for this sample.
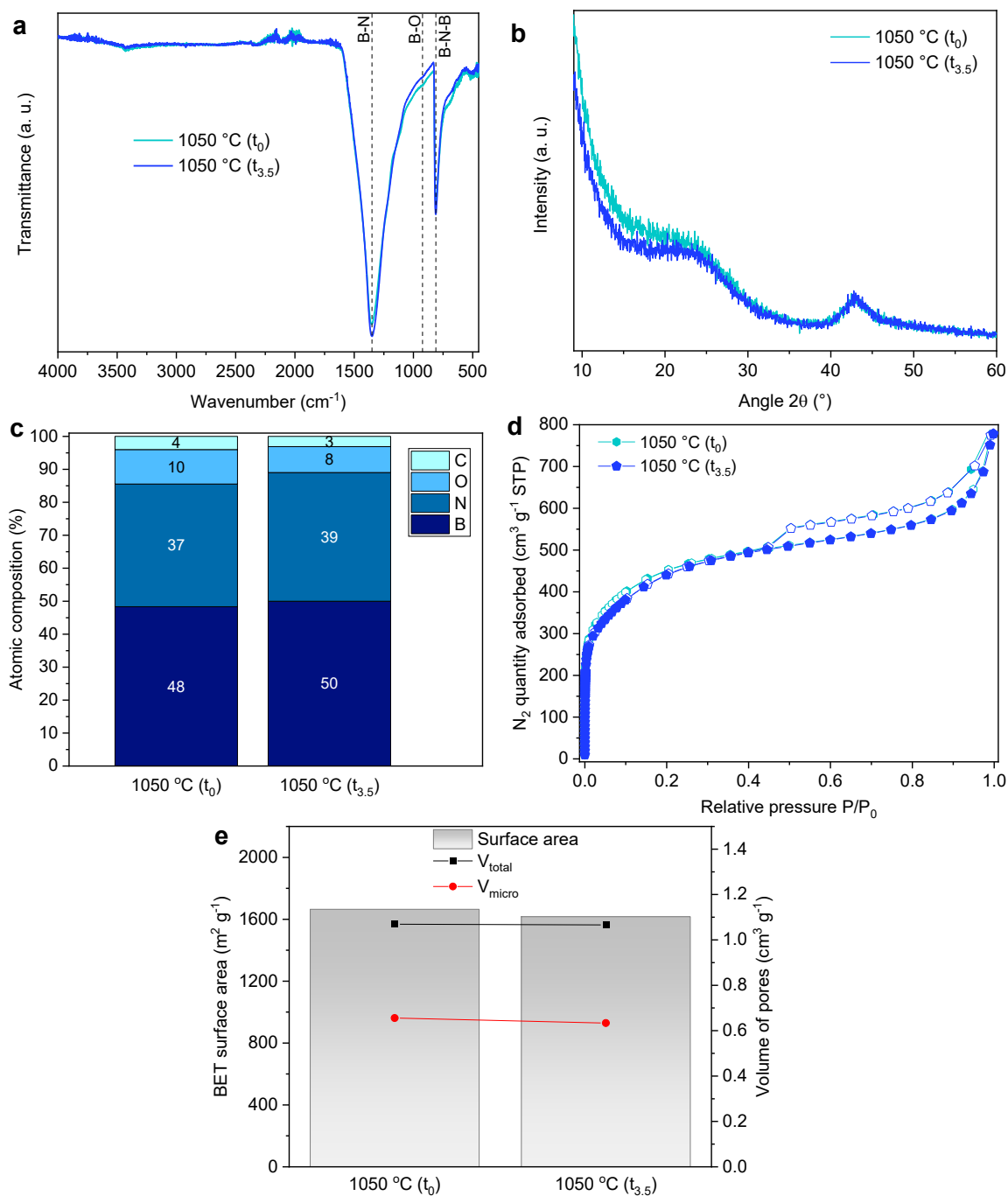
Figure 5.9 (a) FTIR spectra, (b) XRD patterns, (c) atomic composition derived from XPS, (d) N_2 sorption isotherms at –196 °C (full symbols = adsorption; open symbols = desorption) and (e) associated textural parameters for porous BN obtained at 1050 °C before and after 3.5 h dwell time.

Figure 5.10 shows the ^{11}B MQMAS NMR spectra (after shearing and referencing δ_1 as described in 4.2.3) of INT-600, INT-700, INT-800 and INT-1050-t_0. Note that, to reduce

spectral acquisition time, a narrow F_1 sweep width was chosen, such that the signals for tetrahedral B species are folded and should appear at much lower δ_1 values.
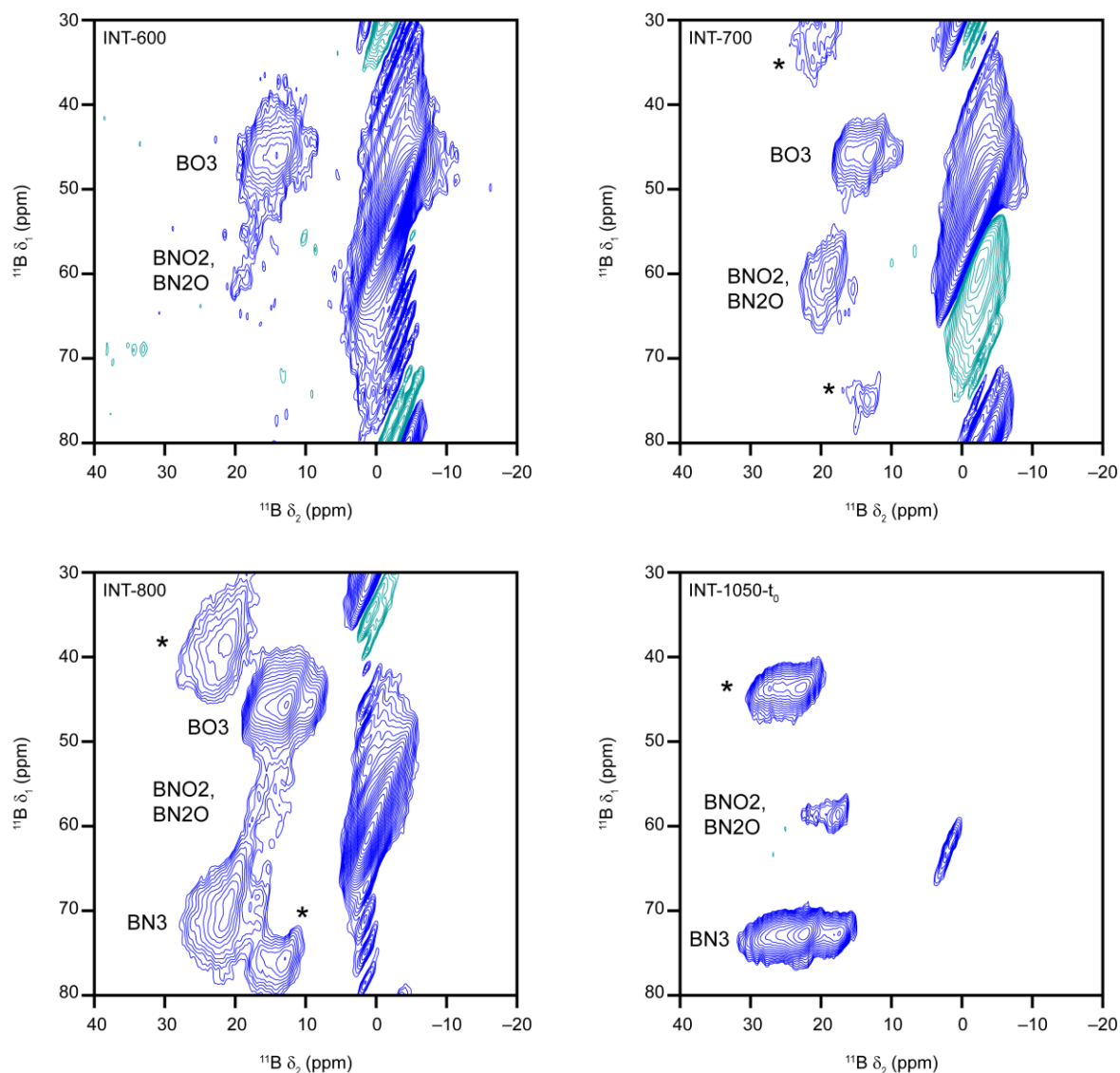
Figure 5.10 ^{11}B (14.1 T, 10 kHz MAS) MQMAS NMR spectra of selected intermediates. The resonances for trigonal B species are assigned and spinning sidebands are marked * (see Figure 5.7). Contours are colored with blue = positive, teal = negative.

I then used NEXAFS to complement XPS and NMR and help identify varying chemical states and environments for B atoms. NEXAFS detects signals from π and σ^* orbitals in the samples, where π bonding involving B atoms would indicate the presence of compounds containing B-

O-N or B-N environments. The absence of π bonding would point towards boron oxide only, prior to the formation of porous BN. In the case of π bonding, the identification of B-O or B-N bonds would indicate the chemical environments of B atoms, shedding light on the advancement of the formation of porous BN. I tested three samples with B K-edge measurements to follow the formation of porous BN: INT-600, INT-800 and BN-1050-$t_{3.5}$ (**Figure 5.11**). Based on our previous results, I did not expect to observe BN patterns below 700 °C (**Figure 5.5**, **Figure 5.6** and **Figure 5.7**). Indeed, no π signal was observed for boron in INT-600, which confirmed that BN had not formed at 600 °C as carbon nitride would still be predominant (**Figure 5.11**). INT-800 exhibited four peaks, each corresponding to a different atomic environment for B atoms: BN_3, BN_2O, BNO_2 and BO_3 (see **Figure 5.11** for visualisation). The BN_3 peak at 191.3 eV corresponds to the only peak that would be observed in pure hexagonal BN.[196] The doublet peak (198; 199 eV) is linked to the corresponding σ^* transition.[197, 198] The three other π peaks represent defects where B atoms are bonded to one, two or three O atoms, confirming that the formation of porous BN is still ongoing at 800 °C. INT-1050-$t_{3.5}$ exhibited the same four π peaks but in different proportions: BN_3 was predominant compared to BN_2O, BNO_2 and BO_3, which we expect in porous BN where a lower content of O was measured in XPS (**Figure 5.5**b). The XPS results are corroborated by the ^{11}B MQMAS spectra of INT-600, INT-700, INT-800 and BN-1050-$t_{3.5}$ (δ_1 projections shown in **Figure 5.7**c, full spectra shown in **Figure 5.10**), which show that the majority of trigonal B is present in BN_3 environments (δ_1 = 69-79 ppm), but some BN_2O and BNO_2 (δ_1 = 60-65 ppm), and BO_3 (δ_1 = 44-46 ppm) are also present (see Appendix 2 and **Figure A2.3** for further details of the assignments).
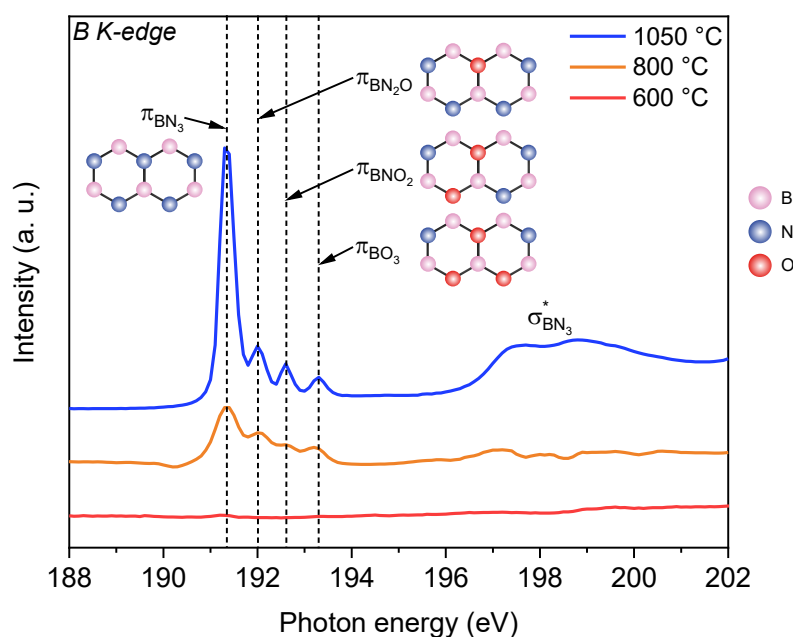
Figure 5.11 B K-edge NEXAFS for the intermediates at 600 °C, 800 °C and the final product BN-1050-t$_{3.5}$, with schematics of the different chemical environments for B atoms.

5.3.3. Porosity development during the formation of porous BN

Alongside the chemical formation of porous BN, I investigated its porosity development to understand how to tune the porosity depending on the targeted application. The final product, porous BN, typically shows a type IV isotherm (**Figure A1.1** in Appendix 1) with a type H3/H4 hysteresis loop, indicating the presence of slit-shaped micropores and mesopores.[78]

Based on the XRD patterns, I observed that the amorphous transition started from around 400 °C, with INT-600 and INT-700 being completely amorphous (**Figure 5.5**d). However, neither INT-600 nor INT-700 exhibited surface area or porosity using N$_2$ sorption at -196 °C (**Figure 5.12**). This aligns with the hypothesis that INT-600 and INT-700, despite being amorphous, were composed of carbon nitride whose porosity is typically under 100 m^2 g^{-1}.[185] At 800 °C, the surface area dramatically increased to 1539 m^2 g^{-1} and the total pore volume reached 0.869 cm^3 g^{-1} with both micropores and mesopores derived from the type IV isotherm (**Figure 5.12**). The intermediate at 900 °C exhibited a slight decrease in surface area and micropore volume, whereas the total pore volume slightly increased, implying higher macropore and mesopore

volumes. The final temperature 1050 °C with dwell time (BN-1050-$t_{3.5}$) led to a surface area of 1616 m^2 g^{-1} and a total pore volume of 1.066 cm^3 g^{-1}. This 3.5 h dwell period did not significantly change the surface area nor the pore volume as BN-1050-t_0 had a surface area of 1664 m^2 g^{-1} and a total pore volume of 1.066 cm^3 g^{-1} (**Figure 5.9**e). However, XPS data suggests that the dwell period allowed further conversion into BN with a decrease in C and O content (**Figure 5.9**c). Choosing between a slightly higher purity or higher surface area would depend on the specific application that is required.
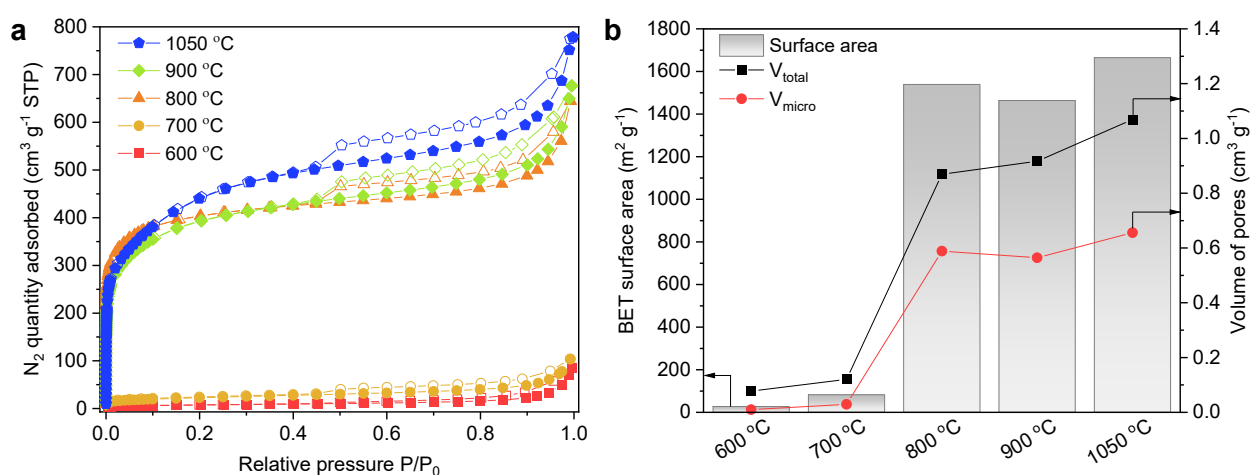
Figure 5.12 (a) N$_2$ sorption isotherms at –196 °C (full symbols = adsorption; open symbols = desorption) and (b) associated textural parameters for the intermediates synthesized at 600 °C and above.

Next, I conducted TG-MS analyses to assess the role of gas release in the formation of BN and the development of its porosity. Between 700-800 °C where porosity and surface area increased (**Figure 5.12**), the main gases released were CO$_2$ and HCN (**Figure 5.13**). This corresponds to the conversion to boron nitride via the reaction between carbon nitride and boron-containing species. This was corroborated by the significant decrease in C observed in XPS analyses (**Figure 5.5**b). Therefore, CO$_2$ and HCN are the main porogens in the formation of porous BN.
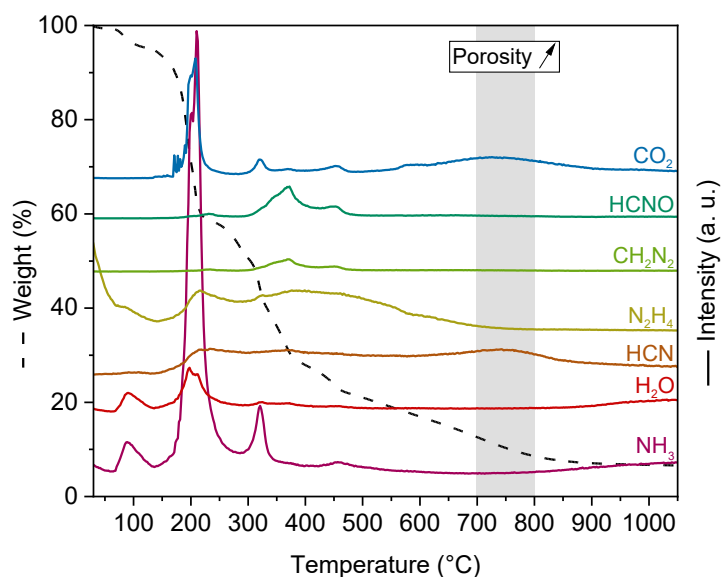
Figure 5.13 TG-MS in N_2 for the initial mixture of boric acid, melamine and urea. MS signals include: NH_3 (m/z = 17), H_2O (m/z = 18), HCN (m/z = 27), N_2H_4 (m/z = 32), CH_2N_2 (m/z = 42), HCNO (m/z = 43) and CO_2 (m/z = 44).

Below 700-800 °C, I identified four steps of significant weight loss. After moisture removal and NH_3 release (60-140 °C), I observed NH_3 and CO_2 release from urea degradation (160-230 °C) as well as N_2H_4 and HCN (**Figure 5.13**). Subsequently, NH_3, CH_2N_2, HCNO and CO_2 release (250-400 °C) occurred due to the decomposition of the urea sub-products, such as biuret, cyanuric acid, ammeline and ammelide,[190] and the condensation of melamine into melam and melem.[191, 192] Finally, I observed further release of NH_3 and CO_2 (450 °C to 625 °C) owing to similar decomposition and condensation reactions that lead to non-porous carbon nitride formation.[183] Above 800 °C, a quasi-plateau was observed in TGA, corresponding to the condensation of BN with minor release of O as shown in FTIR (**Figure 5.5**a), XPS (**Figure 5.5**b and **Figure 5.6**c) and NEXAFS analyses (**Figure 5.11**).

5.3.4. Roles of urea and melamine as N-precursors

The choice of precursors is of paramount importance to form porous BN, based on the gaseous species being released. Although using either melamine or urea allows to produce porous BN

with boric acid, a previous study showed that high hierarchical porosity in porous BN derives from complex thermal degradation patterns of precursors.[4] Herein, I will investigate whether melamine and urea play critical roles in the chemistry or/and porosity development of porous BN. I carried out TG analyses in N_2 for each reagent individually, as well as mixtures of boric acid (BA) with either urea (U) or melamine (M), or both at a time. The boric acid to N-precursor molar ratios were kept constant: BA:M = 1:1 and BA:U = 1:5. TG-MS was done in parallel to survey the gases released by each combination of precursors and identify the source of porogens mentioned earlier. After these experiments, I analyzed the residues using FTIR spectroscopy to assess whether BN formed with each combination of reagents (**Figure 5.14**). I obtained BN in all cases, but with traces of B-O and O-H when using urea and melamine, and with significant boron oxide B_2O_3 and other B-O compounds when using melamine only. This is most likely due to the lower B:N ratio in the case of melamine-based synthesis.
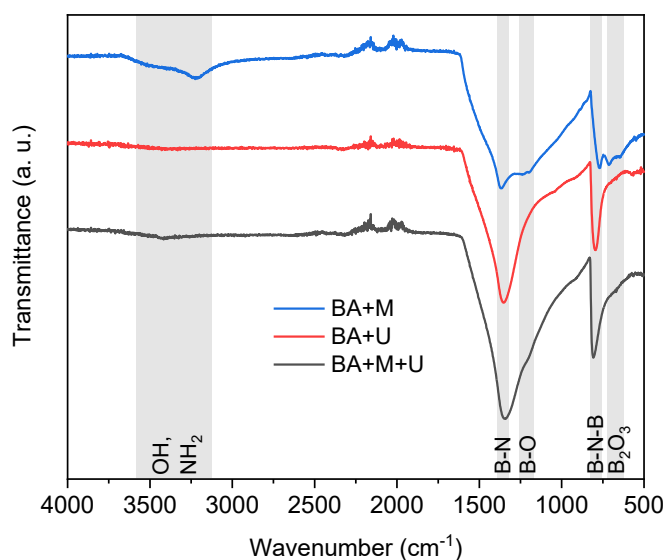
Figure 5.14 FTIR spectra of residual products obtained after TG-MS with mixtures of boric acid (BA), urea (U) or/and melamine (M) with molar ratios of: BA:M = 1:1; BA:U = 1:5; and BA:M:U = 1:1:5.

TGA showed that the degradation profiles of the mixtures of reagents did not strictly follow the combination of each reagent's weight loss since additional reactions occurred (**Figure**

5.15a). Thanks to TG-MS, I reported the main species released during the synthesis: ammonia NH_3, water H_2O, hydrogen cyanide HCN, fulminic acid HCNO and carbon dioxide CO_2 (**Figure 5.15**b-f). Firstly, I observed that the gas release profiles were more complex when both N-containing precursors were used, with additional release peaks that would lead to enhanced porosity.[4] Ammonia release with both N-containing precursors roughly corresponded to the releases observed with either melamine or urea alone with boric acid (**Figure 5.15**b). While water release also followed the pattern for each N-containing precursor, an additional peak was observed above 900 °C (**Figure 5.15**c), corresponding to the removal of O impurities and the formation of purer BN, as observed in XPS earlier (**Figure 5.5**b). When both melamine and urea were used, I observed a continuous HCN release from 150 °C, which corresponded to the degradation of urea followed by the condensation of melamine into melem, leading to the formation of carbon nitride before 600 °C (**Figure 5.15**d). In the temperature range 700-800 °C corresponding to the porosity development with porogens HCN and CO_2, HCN was mainly released when melamine was used, either with or without urea. In parallel, a significant release of CO_2 was observed only when both N-precursors were used (**Figure 5.15**f). This confirms that both melamine and urea are needed to enhance surface area and porosity in porous BN via the formation of intermediates (e.g., melem, carbon nitride) releasing HCN and CO_2, the main porogen agents.
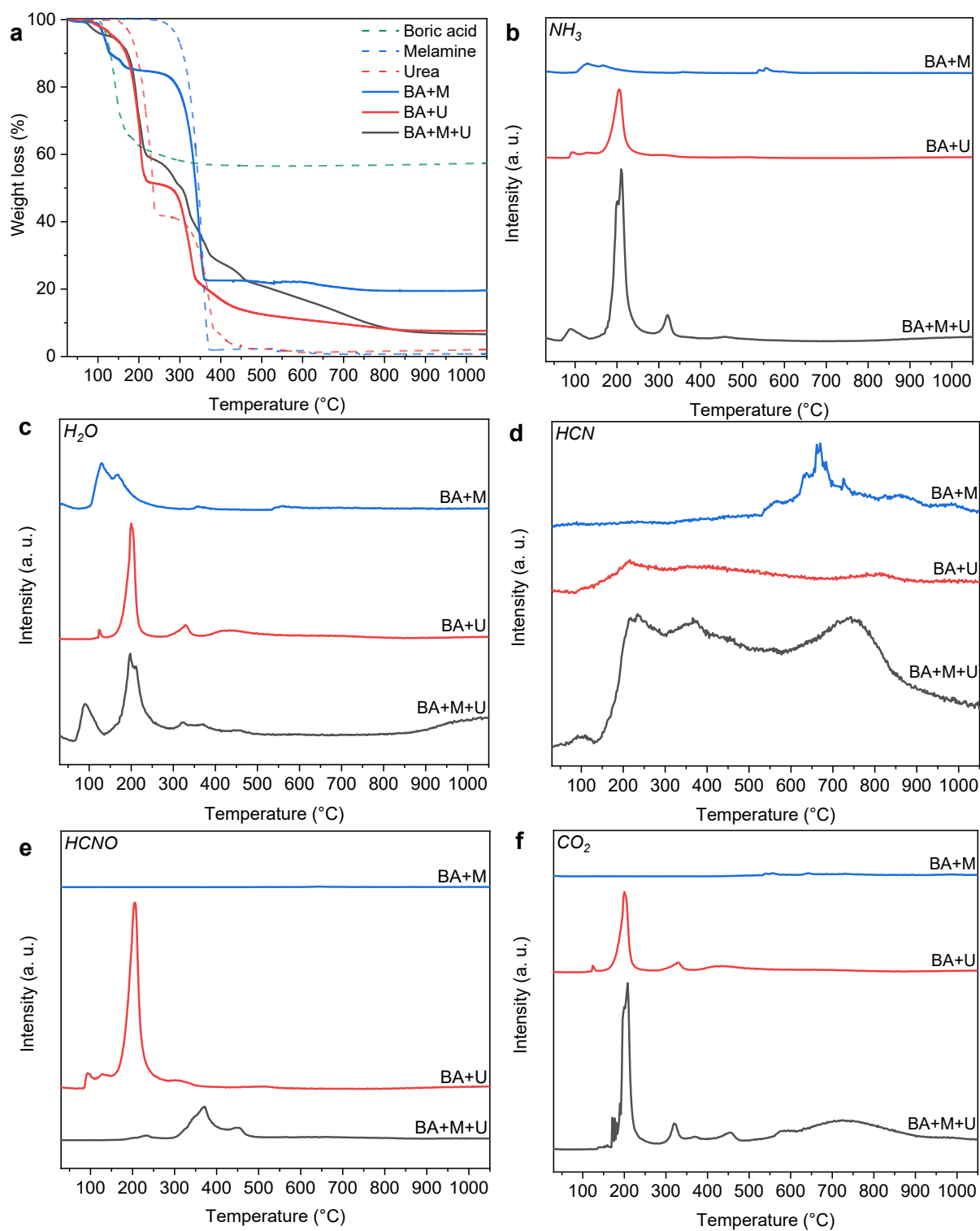
Figure 5.15 (a) TGA in N_2 for each reagent individually and the mixtures of reagents. (c-g) Mass spectra obtained in TG-MS for the different mixtures of reagents with the gaseous species: (b) ammonia NH_3 (m/z = 17); (c) water H_2O (m/z = 18); (d) hydrogen cyanide HCN (m/z = 27); (e) fulminic acid HCNO (m/z = 43) (f) carbon dioxide CO_2 (m/z = 44).

5.3.5. Formation mechanism of porous BN

Based on the interpretation of the characterization analyses, I propose a formation mechanism of porous BN with boric acid, melamine and urea reacting under N_2 atmosphere up to 1050 °C (**Figure 5.16**). From RT to around 500 °C, the degradation of urea into biuret, cyanuric acid, ammelide, ammeline and eventually melamine took place. These decompositions led to significant weight loss and gas release (e.g., water and ammonia). Concurrently, I observed the condensation of melamine into melam and melem with the formation of tri-s-triazine rings. In parallel, boric acid was converted into B-containing species displaying either trigonal B (i.e., B_2O_3, $B(OH)_3$) or tetrahedral B (adducts formed between boric acid and the amine groups). Around 500 °C, melem evolved further to form carbon nitride clearly identified in the two yellow intermediates INT-600 and INT-700. Although the samples were amorphous at these temperatures, no porosity had developed. Thanks to the reaction of carbon nitride with boron-containing species, such as B_2O_3, X_2B-OH, $X_2B{=}O$, $X_2B{=}N$ (where X = C or N) depending on the temperature, boron oxynitride BON was formed via the release of HCN and CO_2, identified as porogens in the synthesis. Porosity then developed between 700 and 800 °C via further release of HCN and CO_2 forming pores in the BON structure. As the temperature increased over 800 °C, O and C atoms evolved as CO_2 and H_2O to form porous BN. Some O impurities remained even at 1050 °C but in small quantities.

The mechanism above relates to the synthesis conditions I have explored in this study. Yet, I speculate that if using melamine and urea, a similar carbon nitride intermediate would form since heating melamine or urea eventually leads to carbon nitride. Overall, I assume the type of chemistry involved in the reactions would not change significantly, but the temperatures at which intermediates form could vary depending on the precursors (e.g., temperature at which NH_3 is generated, formation of carbon nitride, etc.).
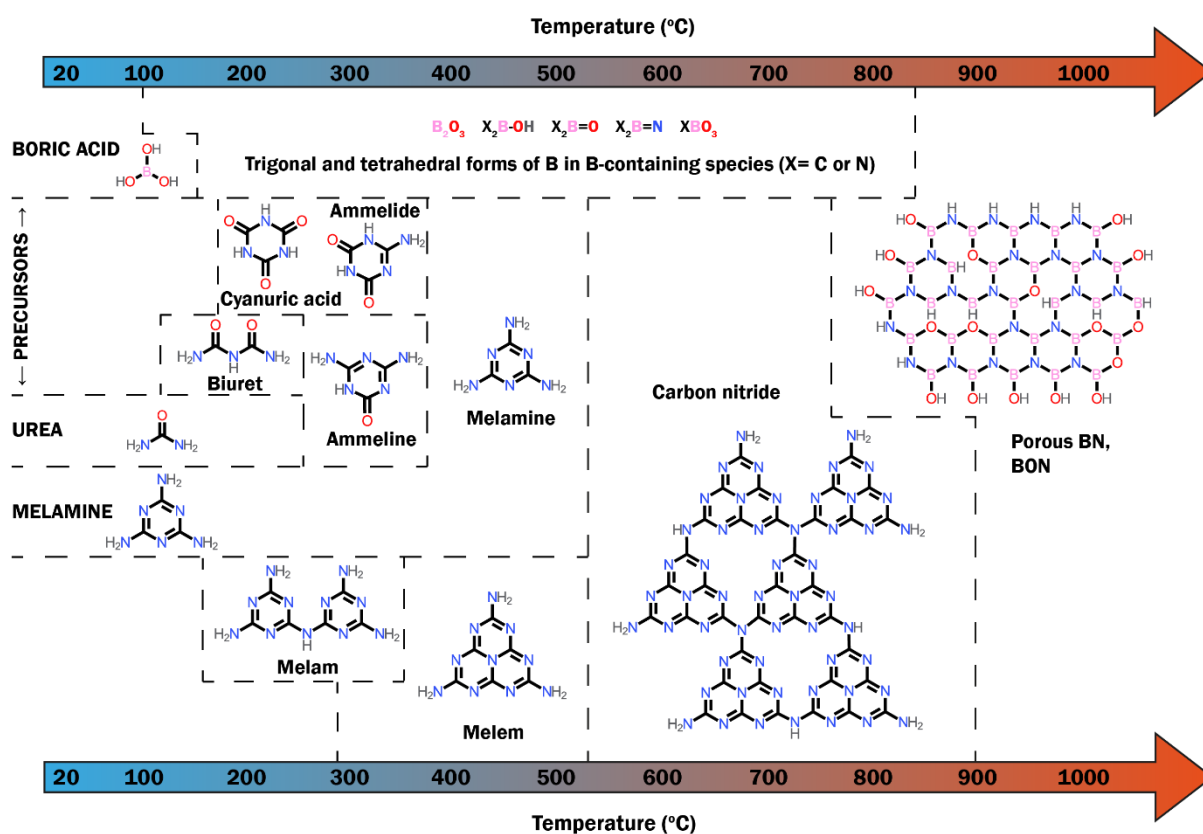
Figure 5.16 Proposed species evolution during the formation of porous BN from boric acid, melamine and urea under N_2 atmosphere up to 1050 °C.

5.4.   Conclusions

In this chapter, I investigated the chemical formation and the porosity development of porous BN under a N_2 atmosphere with analytical and spectroscopic techniques. This allowed to propose a formation mechanism highlighting the most critical stages of the synthesis for this specific synthesis parameter space. In particular, I found the following answers to my research questions highlighted in Chapter 3 and related to research objective 1:

• Porous BN forms only above 700 °C, with a dramatic increase in surface area between 700 and 800 °C.

• Up to 700 °C, various reaction intermediates were identified, including non-porous carbon nitride, which eventually reacted with a tetrahedral form of boron to form boron nitride.

• Both urea and melamine are crucial in the formation of porous BN, since they act as chemical precursors and form some intermediates releasing porogens.

• After the porosity onset, as temperature increases during the synthesis, the contents of oxygen and carbon in the intermediates and final product decrease.

These results bring further understanding on how porous BN is formed and shed light on how and when porosity develops, which is critical for industrial scale-up towards adsorption-based applications.

CHAPTER 6: EFFECT OF SURFACE FUNCTIONALIZATION ON THE HYDROLYTIC STABILITY AND SORPTION PROPERTIES OF POROUS BN

The work and the discussion described in this chapter have been published by the thesis author in Microporous and Mesoporous Materials.[8] All measurements were performed by the thesis author, except the kinetic testing, which was carried out by Hassan Azzan at Imperial College London, and the micro-XRF measurements, which were carried out by Dr. Marcus H. N. Yio at Imperial College London.

6.1. Introduction

Due to the nature of most adsorption-driven separations, it is crucial to have adsorbents that sustain water or moisture exposure during storage, transport and use. Following the investigation of the formation mechanism of porous BN in Chapter 5, it appeared that knowledge on its hydrolytic stability was also required prior to industrial scale-up. Past studies have reported the cyclic use of porous BN as adsorbent in potentially mild or extreme humidity conditions, but the impact on surface area, porosity and sorption performance upon moisture exposure was not assessed.[108] This is all the more important since studies have pointed towards the instability of porous BN in the presence of water or moisture.[6, 15, 21, 49-51, 199] Considering the potential of porous BN as an adsorbent, it is key to enhance its hydrolytic stability.

Hydrolytic instability has already been highlighted for classes of inorganic and organic adsorbents, such as zeolites[58, 59] and metal organic frameworks (MOFs).[60-65] To tackle this limitation, methods involving surface functionalization have been used to reduce the

interaction of the adsorbent with water and prevent its degradation over time and repeated use. For instance, zeolites have been functionalized via the grafting of alkylsilanes onto their OH groups,[66-68] whereas MOFs have been coated with a hydrophobic polymer, like polydopamine.[69] With the right experimental conditions and chemicals, such methods allow to make these adsorbents more hydrophobic and resistant to water, while retaining adequate surface area for adsorption applications.[66, 67, 69]

Past studies have looked at making porous BN materials more crystalline or with fewer micropores to enhance their resistance to moisture,[6, 51] thus reducing their surface area and sorption properties. Herein, I have looked at an alternative way to achieve a compromise between high surface area and enhanced hydrolytic stability in porous BN. Using the findings of past studies, our group and others have hypothesized that the origin of the hydrolytic instability in porous BN materials derives from a combination of a lack of crystalline structure[51] and the presence of oxygen atoms, both in the bulk and at the edges of the BN sheets.[6, 7] These oxygen impurities, which account for 8-9% of the atomic composition of porous BN,[7] constitute hydrophilic sites in the structure that promote interaction with water, and can lead to subsequent degradation of the material following reaction (2) introduced in Chapter 2:

$$2\ BN_{(s)} + 3\ H_2O_{(l)} \rightarrow B_2O_{3\ (s)} + 2\ NH_{3\ (g)} \qquad (2)$$
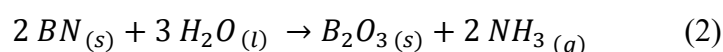
To address this, I have functionalized the surface of porous BN similarly to other materials, such as zeolites.[67, 68] I have used an alkylsilane to graft onto the OH groups present at the edges of porous BN. I have selected a fluoroalkylsilane with a short alkyl chain to benefit from the hydrophobicity of the fluorine atoms, while avoiding bulky chains that would block pores and hinder the adsorption capacity of porous BN after functionalization. Two different functionalization routes were trialed using the same silane: route 1 relies on the silylation of porous BN powder, followed by pelletization; route 2 starts with porous BN pellets, which are then subjected to chemical vapor deposition (CVD). To monitor the changes in hydrophobicity,

I have subjected samples to different levels of humidity, relevant to storage and post-combustion CO_2 capture sorption testing conditions. I have then used a range of spectroscopic and analytical tools to probe the impact of moisture on the chemical and textural properties, before and after surface functionalization. Finally, I have tested the potential of my functionalized adsorbents for CO_2/N_2 separation by carrying out both equilibrium and kinetics sorption measurements.

6.2. Materials

6.2.1. Synthesis and pelletization of porous BN

Porous BN powder was synthesized following the multiple N-precursor synthesis previously developed in our group[3] and described in the Methods chapter of this thesis (section 4.1.1). To form pellets, 40 mg of porous BN powder were ground with a mortar and pestle, and placed into a pellet die (5-mm evacuable stainless steel, Specac). The die was positioned into a manual hydraulic press (Atlas^{TM} Manual 15T, Specac) fitted with a low tonnage gauge conversion kit (0-1 t, Specac). I tested various weights and loads to prepare porous BN pellets while retaining adequate BET area and porosity compared to porous BN powder. Using too high tonnage could lead to a significant degradation of the pore structure of porous BN. After observing such an impact with tonnages above 0.25 t, I tried using 0.1 t and 0.2 t with 40 mg of porous BN powder (**Figure 6.1**). Both loads led to mechanically-stable pellets for basic manual handling, such as performing characterization techniques on full pellets. Considering the BET areas and porosities were almost identical, I kept 0.2 t to provide more mechanical strength to our pellets. From here onwards, a load of 0.2 t was applied and maintained for 20 s on the pellet press to form a porous BN pellet. The pellet was then ejected with a small load applied to an extractor ring placed onto the base of the pellet die.
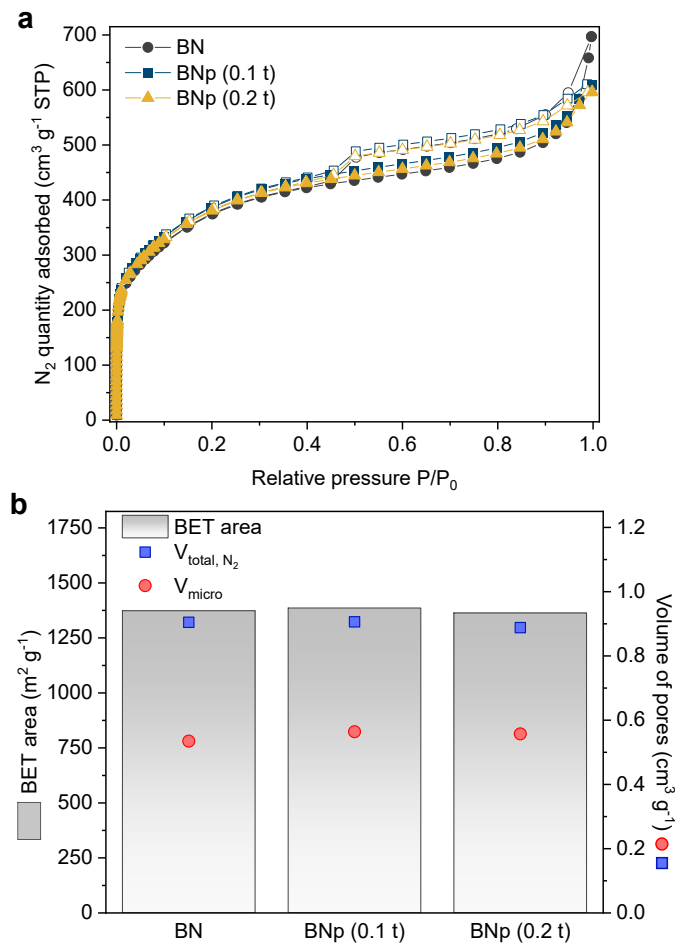
Figure 6.1 (a) N_2 sorption isotherms at $-196\,^{\circ}C$ and (b) Derived textural parameters for porous BN powder and porous BN pellets made with loads of 0.1 t and 0.2 t. <u>Note</u>: total pore volumes $V_{tot,\,N_2}$ correspond to pore sizes up to 12 nm as obtained from N_2 sorption.

6.2.2. Surface functionalization of porous BN

6.2.2.1. *Preliminary work: selection of an alkylsilane grafting agent*

Initially, I used two alkylsilanes to functionalize porous BN powder: n-propyltrichlorosilane (PTS; > 95%, Fisher Scientific, CAS 141-57-1) and n-octadecyltrichlorosilane (OTS; Sigma-Aldrich, CAS 112-04-9). The aim was to trial two very different grafting agents based on the number of carbon atoms in their alkyl chains, in this case, 3 in PTS versus 18 in OTS. Functionalization of porous BN powder was carried out in toluene to avoid any contact with water due to BN's hydrolytic instability. A concentration of 10 mmol of silane per gram of BN was used, following the functionalization work carried out on zeolites.[67, 68] The protocol was

retained later on and is explained in section 6.2.2.2. Characterization results showed that surface area was mostly retained after functionalization with PTS, whereas a sharp decrease was observed after functionalization with OTS, as expected (**Figure A3.1** in Appendix 3). The loss of surface area in the case of OTS can be explained by the bulky 18-carbon alkyl chains that could block a significant amount of pores in porous BN. Water sorption adsorption isotherms showed that porous BN functionalized with PTS was highly hydrophilic while porous BN functionalized with OTS was more hydrophobic (**Figure A3.2** in Appendix 3). This meant that a compromise between porosity and hydrophobicity may need to be achieved when using such alkylsilanes.

In 2019, I carried out a one-month research visit at the Tokyo Institute of Technology, Japan, where researchers were using fluoroalkylsilanes to modify the surface of their materials, such as porous glass and alumina, to make them hydrophobic.[200, 201] This led me to focus on finding another grafting agent that would combine hydrophobic properties thanks to F atoms, while having a short alkyl chain to avoid blocking pores in porous BN.

To make porous BN more hydrophobic, its surface was then functionalized via two experimental routes using trimethoxy(3,3,3-trifluoropropyl)silane (97%, Sigma-Aldrich, CAS 429-60-7), abbreviated as FAS for fluoroalkylsilane (**Figure 6.2**).
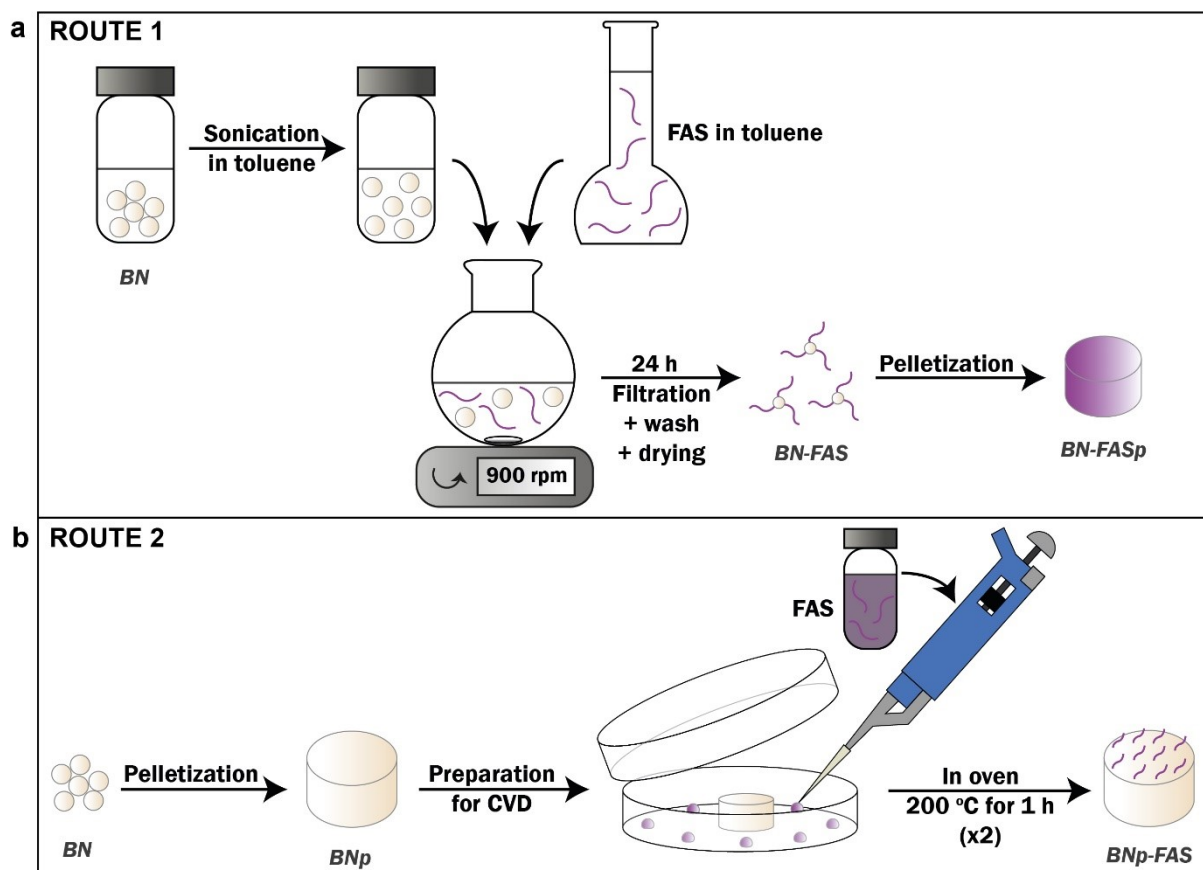
Figure 6.2 Schematics representing the two experimental routes used to functionalize the surface of porous BN. (a) Experimental route 1 consisting of silylation using trimethoxy(3,3,3-trifluoropropyl)silane (FAS) followed by pelletization. (b) Experimental route 2 consisting of pelletization followed by chemical vapor deposition (CVD) using FAS.

6.2.2.2.   Route 1: silylation of porous BN powder followed by pelletization

I first dispersed 200 mg of porous BN powder in 4 mL of toluene (100%, ACS reagent, VWR) for 20 min in a sonicator (Clifton). In parallel, I prepared a solution of FAS in 10 mL of toluene with a concentration of 10 mmol of FAS per g of BN, hence a volume of 384 μL of FAS. The dispersed porous BN and the FAS solution were both added inside a 50-mL round-bottom flask with a magnetic stirrer. The mixture was stirred at 900 rpm at room temperature for 24 h. The resulting material was filtered and washed with ethanol (99.95%, ACS reagent, VWR) before being dried in an oven at 120 °C overnight, as shown in **Figure 6.2a**. A control sample was prepared using the same method without FAS to check the impact of filtration, washing and

drying in route 1. In a second stage, pellets were prepared with the functionalized powder following the pelletization method explained in section 6.2.1.

6.2.2.3. Route 2: chemical vapor deposition (CVD) on porous BN pellets

A pellet was prepared from 40 mg of porous BN powder following the pelletization method outlined in section 6.2.1. This pellet was then placed on one of its flat surfaces in the centre of a Petri dish, as shown in **Figure 6.2**b.[202] To target 10 mmol per g of BN as in route 1 and bearing in mind I wanted to functionalize both sides of the pellet equally, 38.2 µL of pure FAS (not diluted in any solvent) were first added in several droplets around the 40-mg pellet with a volume-adjustable pipette. The lid was then placed on top of the bottom part of the Petri dish and placed in an oven at 200 °C for 1 h to carry out chemical vapor deposition (CVD). The CVD process was repeated once after delicately turning the pellet upside down in the Petri dish and adding another 38.2 µL of FAS around the pellet.

6.2.3. Glossary

To facilitate understanding of the results, I introduced a naming system for all samples (**Figure 6.3**). This system considers the order of experimental steps carried out, such as pelletization ('p') and functionalization with FAS ('-FAS'). A control sample ('-control') was added to check the potential impact of solvents used in route 1, without using FAS. This control sample underwent each step used in route 1, but no FAS was added in the toluene solution (**Figure 6.2**a).
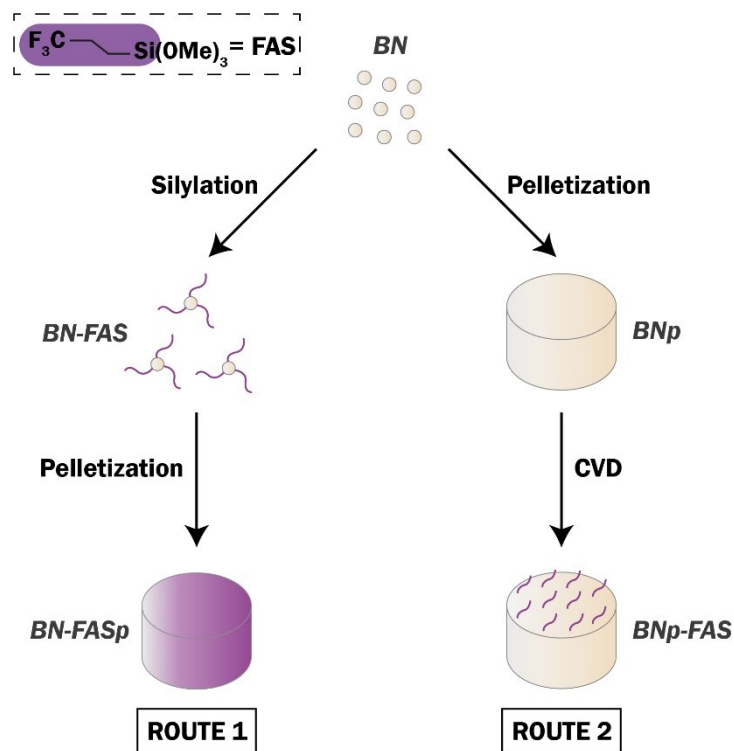
Figure 6.3 Summary of experimental routes 1 and 2 used to functionalize porous BN with FAS and associated samples names.

6.3. Methods

All materials were characterized using a range of spectroscopic and analytical tools. Fourier transform infrared spectroscopy (FTIR), X-ray photoelectron spectroscopy (XPS), thermogravimetric analysis coupled with mass spectrometry (TG-MS) and micro X-ray fluorescence (μXRF) were used to analyze chemical features. X-ray diffraction (XRD), scanning electron microscopy (SEM), N_2 sorption at –196 °C and mercury intrusion porosimetry (MIP) were used to investigate structural and textural features. CO_2 and N_2 sorption isotherms were recorded to quantify the gas uptake of our porous BN-based materials and to assess their CO_2/N_2 selectivity. All of these techniques are detailed in Chapter 4 of this thesis, whereas specific methods used in the current chapter are explained below.

6.3.1. Moisture exposure testing

To quickly assess hydrophobicity of the unmodified and functionalized pellets, water contact angles were carried out using a Krüss Drop Shape Analyzer (DSA 25) instrument by means of sessile drop method. A pellet was placed on the sample platform and a 2-mL droplet of deionized water (18 MΩ cm) was formed using a syringe controlled by the software Krüss Advance. The platform was moved up manually to bring the top surface of the pellet towards the droplet. Once the droplet was in contact with the pellet, the platform was slowly lowered down. Contact angles were then measured over 10 s with a frequency of 10 s^{-1} on two different spots of each flat surface of the pellet, hence four measurements per pellet. Short videos were also recorded with the software when the surfaces were too hydrophilic to measure static contact angles.

To investigate the impact of humidity exposure on the samples in more depth, I set up a closed environment with a plastic box and its lid sealed with vacuum grease (**Figure 6.4**). A beaker was filled with a saturated salt solution and placed inside the sealed box. A sample was then placed inside the box and subjected to a given relative humidity (RH) level for 24 h in a temperature-controlled environment. 24 h was selected as the exposure time for two reasons: this is a relatively short time for industrial purpose, and significant impact had been observed on a similar material in a past study for exposure at relative humidity above 90% for 8 h.[6] Relative humidity can be fixed with a given saturated salt solution at a set temperature.[203] I used two different salts to prepare saturated solutions: magnesium nitrate and potassium nitrate. At 22 °C, these two saturated solutions produce RH levels of 54% and 92% respectively. These RH values could correspond to two industrial scenarios: 54% represents a RH level that can be found in storage conditions, whereas 92% represents more extreme conditions that can be seen in some adsorption processes, such as CO_2 capture with high moisture content.[204] After humidity exposure, samples were dried in a vacuum oven overnight at 110 °C.
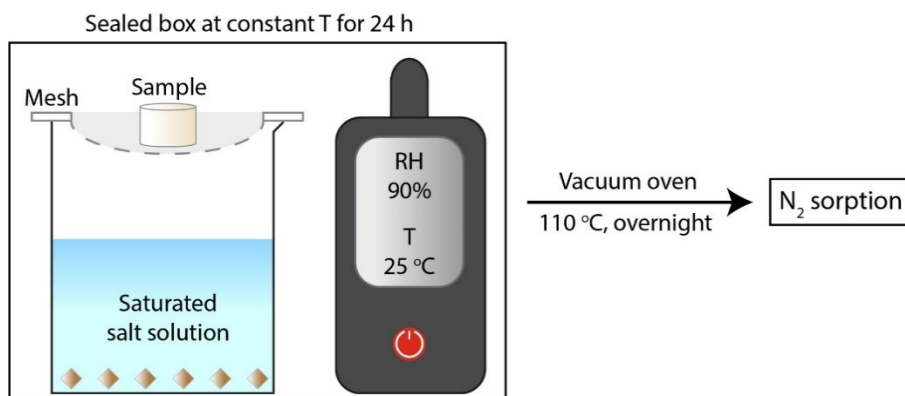
Figure 6.4 Schematic of the experimental set-up used for humidity exposure testing of unmodified and functionalized porous BN pellets.

To obtain additional insight into the behavior of unmodified and functionalized porous BN upon moisture exposure, water vapor sorption isotherms were collected using a Micromeritics 3Flex porosity analyzer at 22 °C. This method is explained in Chapter 4 of this thesis.

6.3.2. Combination of pore size distributions

In this chapter, the overall pore size distribution (~0.5 nm - 325 µm) was obtained by combining the results from both N_2 sorption isotherms at –196 °C (~0.5-10 nm), and mercury intrusion porosimetry measurements (~2 nm - 325 µm).[178] To do so, we assume continuity between both pore size distributions obtained via low pressure N_2 adsorption and MIP.[205] To select the transition point in the overlapping region of each pore size distribution, I favored pore sizes obtained via N_2 sorption over MIP. As the mercury pressure increases towards smaller pore sizes during the measurement, the results would be less accurate at higher pressures due to possible compression of the pellet.

6.3.3. Kinetic testing for CO_2 adsorption

We carried out CO_2 sorption kinetic testing to extract the kinetic rate constant in the three pellet samples BNp, BN-FASp and BNp-FAS following the method described in Azzan et al.[178] For

each measurement, about 100 mg of sample was needed (~2-3 pellets). Dynamic sorption experiments were carried out at two different helium flow rates: 10 $cm^3\,min^{-1}$ and 60 $cm^3\,min^{-1}$ (99.9990%, N5.0 CP grade, BOC). The adsorbent was saturated at CO_2 partial pressures of 0.12 and 0.94 bar, and 0.11 and 0.73 bar for experiments at 10 $cm^3\,min^{-1}$ and 60 $cm^3\,min^{-1}$, respectively. All these experiments were conducted at a total pressure of 1.01 bar. The desorption of CO_2 from each adsorbent was tracked by switching to pure helium (inert gas) flow at the aforementioned flow rates, which facilitates extraction of the kinetics through a mathematical model. To determine the temperature dependence of the adsorption kinetics, time-resolved desorption curves were obtained at three different temperatures: 33, 52 and 72 °C for BNp, and 10, 20 and 30 °C for BN-FASp and BNp-FAS. The samples were first degassed ex-situ prior to the CO_2 isotherm measurements, using the procedure described in section 4.5.1 of the Methods chapter. They were then degassed in-situ within the dynamic sorption cell at 100 °C for 2 hours prior to the desorption experiments.

A derivative-free optimizer was used to fit mathematical models that describe the mass transport within the system to the experimental desorption curves, as described in Azzan et al.[178] Using the approach, both equilibrium and kinetic parameters can be extracted. However, in this work, the CO_2 adsorption capacity on BN-FASp and BNp-FAS was deemed to be too low, even at reduced temperatures, for the experimental desorption curves to be resolved sufficiently to accurately estimate adsorption equilibria and kinetics simultaneously. Therefore, the CO_2 volumetric adsorption isotherms were provided as an input to the mathematical model, and the kinetic parameters (k_{1,CO_2} and k_{2,CO_2}) were varied to fit the time-resolved experimental desorption curves to the mathematical model described in the previous work. The details of the validation of this approach can be found in Appendix 3. The experimental desorption curves along with the corresponding model fits are shown in **Figure A3.12** in Appendix 3. A single-site Langmuir (SSL) model was used to describe the adsorption equilibrium of CO_2 on BNp

and BNp-FAS, and a dual-site Langmuir (DSL) model was used for BN-FASp. The kinetics of adsorption was modeled using a two-parameter lumped kinetic rate constant that incorporates contributions analogous to macropore and micropore resistance within the adsorbent pellet. The equations that describe the equilibrium and kinetics of CO_2 sorption in these experiments are described in Appendix 3.

We note that to carry out experiments at sub-ambient temperatures, the set-up described in our previous study[178] was modified as follows. A thermo-electric cooler (Laird ETX25-12-F1-6262-TA-W6, Laird Thermal Systems GmbH, Germany) along with an OEM Precision Temperature Controller (TEC-1090-HV, Meerstetter Engineering GmbH, Switzerland) was used to ensure isothermal operation between 5 and 100 °C. The ambient-side temperature of the thermo-electric cooler was maintained at 20 °C using a 6-pass liquid cold plate heat-sink (Aavid, U.S.A.). The heat-sink was supplied with water at 20 °C from a circulating chiller (Huber Minichiller 300, Huber, Germany). The adsorption cell was also rebuilt in-house to allow for good thermal contact between the cell and the thermoelectric cooler. The adsorption cell was insulated using a foam cover that is placed on the exposed surface. The modifications to the experimental set-up are shown in **Figure A3.11** in Appendix 3.

6.4. Results & discussion

6.4.1. Confirming functionalization and composition

I first confirmed the functionalization of porous BN for both routes 1 and 2 using FTIR and XPS (**Figure 6.5**, **Figure 6.6**). FTIR was carried out on powder samples (BN, BN-control and BN-FAS) and FAS for comparison (**Figure 6.5**a; zoomed-in spectrum in **Figure A3.3**a in Appendix 3). Results showed B-N and B-N-B bands at 1353 cm^{-1} and 801 cm^{-1} respectively, in all powder samples.[206] I observed in the BN-control sample a band at 1104 cm^{-1} indicating

the presence of B-O bonds, likely due to partial degradation of porous BN during the washing step with ethanol. This was confirmed by a higher O content than in porous BN in the atomic composition derived from XPS (**Figure 6.5**b). Looking at BN-FAS, I observed new bands in the region 1290-865 cm^{-1}. These bands corresponded to Si-O-Si, Si-C and -CF$_3$ observed in FAS.[206] Bands in the region 3065-2793 cm^{-1} corresponded to the -CH$_2$ groups in FAS.[206] These bands showed low intensity in BN-FAS, potentially due to the low content of FAS, which will be discussed later in this section. XPS analyses for C 1s and F 1s showed C-F and C-H peaks corresponding to FAS in all functionalized samples (**Figure 6.6**), whereas only noise was observed in the F 1s spectrum of unmodified BN (**Figure A3.4** in Appendix 3). We should note that the C-C peaks can be attributed to both adventitious carbon (also observed in BN and BNp) and FAS. The estimated atomic composition confirmed that pelletization did not significantly impact the chemistry of the samples when comparing BN vs. BNp, and BN-FAS vs. BN-FASp (**Figure 6.5**b). I noted that the contents of Si and F were higher in BNp-FAS (route 2) compared to BN-FASp (route 1). This may be partly due to XPS being a surface-sensitive technique, and FAS is expected to be mainly present at the surface of BNp-FAS pellets after the CVD treatment (**Figure 6.2**b).
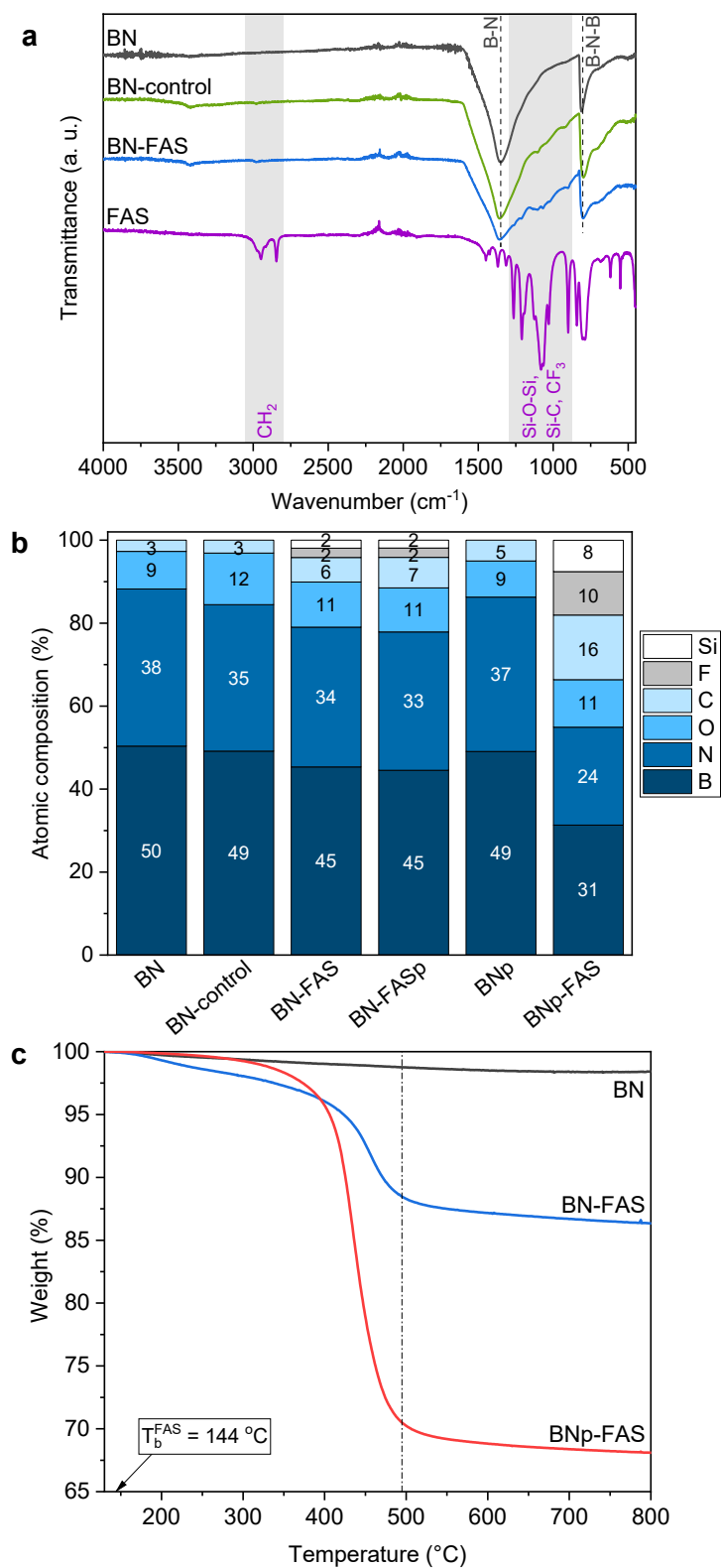
Figure 6.5 Chemical analyses of unmodified and functionalized porous BN. (a) FTIR spectra for route 1 samples. (b) Atomic composition derived from XPS for routes 1 and 2 samples. (c) TG curves in air for routes 1 and 2 samples. T_b^{FAS} refers to the boiling point of trimethoxy(3,3,3-trifluoropropyl)silane (FAS), i.e., 144 °C.
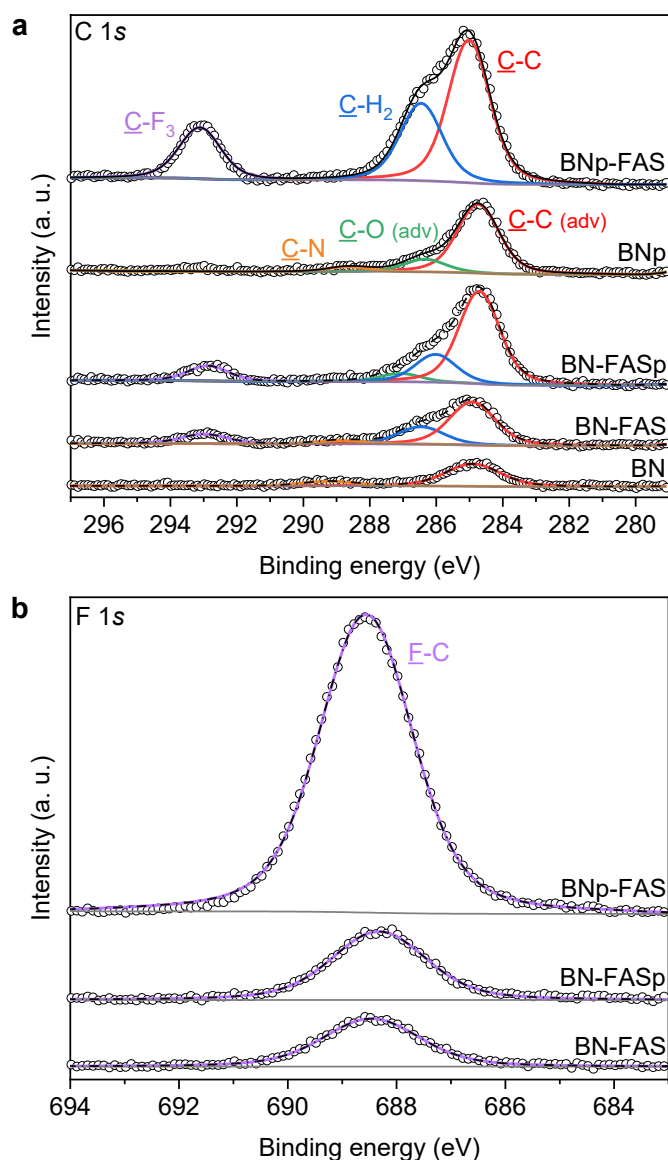
Figure 6.6 High-resolution XPS and peak fitting of the (a) C 1*s* and (b) F 1*s* core levels of the unmodified and functionalized porous BN samples.

I used TGA and TG-MS to further confirm functionalization qualitatively and quantitatively. The sharp weight loss observed in TGA between 350 and 495 °C in BN-FAS and BNp-FAS, but not in BN, corresponded to the removal of FAS molecules or fragments. In TG-MS, I observed that H_2O and CH_3OH were the main species decomposing up to 350 °C in BN-FAS (**Figure 6.7**), implying that non-grafted CH_3O^- groups from FAS were removed.[207] Between 350 and 800 °C, CF_2 and CF_3 signals showed that the alkyl chains $F_3C-(CH_2)_2$ were removed.[207] As the boiling point of FAS is 144 °C, these results show that FAS was strongly attached to

porous BN, i.e., via covalent bonding. The bonds are most likely formed with the OH groups present in porous BN as per reaction (22),[208] with R representing the BN structure with hydrophilic OH groups, and R' the hydrophobic alkyl chain of FAS:

$$R - OH_{(s/l)} + (CH_3O)_3 - Si - R'_{(l)} \rightleftharpoons R - O - Si(OCH_3)_2R'_{(s/l)} + CH_3OH_{(l)} \quad (22)$$
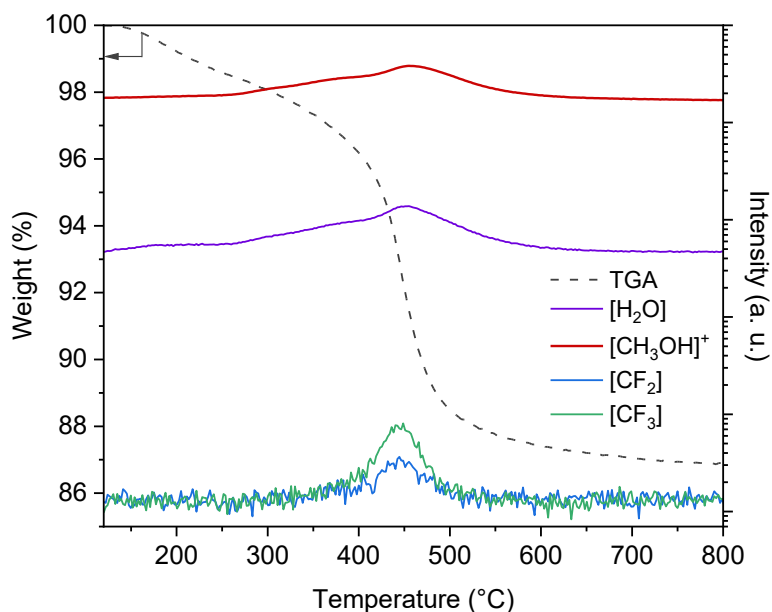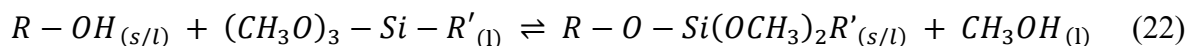
Figure 6.7 TG-MS in air for BN-FAS. MS signals include: H_2O (m/z = 18); CH_3OH (m/z = 32); CF_2 (m/z = 50); CF_3 (m/z = 69).

6.4.2. Calculation of the amount of FAS grafted via routes 1 and 2

To calculate the amount of FAS grafted via both functionalization routes, I used the TGA results carried out in air up to 800 °C (**Figure 6.5**c). Firstly, I assumed that residual water was removed after the 30-min plateau at 120 °C. Based on the weight loss profile, I hypothesized that dangling CH_3O^- groups not grafted via the OH groups of porous BN were removed between 120 and 350 °C.[207] This gives an estimate of the ratio of CH_3O^- groups that were grafted and those that remained dangling. Between 350 and 800 °C, alkyl chains $F_3C\text{-}(CH_2)_2$ were removed.

Below are the definitions of the different terms present in the equations used to explain the calculation process of the grafted amount of FAS:

m_{dry} is the total mass of dry sample after the plateau at 120 °C to desorb residual water

m_{CH_3O} is the mass of CH_3O^- groups dangling from silane molecules

m_{alkyl} is the mass of alkyl chains $F_3C-(CH_2)_2$ from silane molecules

m_{350} is the remaining mass of sample in TGA at 350 °C

m_{800} is the remaining mass of sample in TGA at 800 °C

$m_{grafting}$ is the mass of silane grafted on porous BN

r is the ratio of CH_3O^- groups and $F_3C-(CH_2)_2$ alkyl chains

r' is the percentage of dangling CH_3O^- groups, as opposed to grafted CH_3O^- groups

Between 120 and 350 °C, the dangling CH_3O^- groups are removed following equation (23):

$$m_{CH_3O} = m_{dry} - m_{350} \qquad (23)$$

Between 350 and 800 °C, the alkyl chains $F_3C-(CH_2)_2$ are removed following equation (24):

$$m_{alkyl} = m_{350} - m_{800} \qquad (24)$$

We can derive the molar quantities of CH_3O^- groups and $F_3C-(CH_2)_2$ using equations (25) and (26):

$$n_{CH_3O} = \frac{m_{CH_3O}}{M_{CH_3O}} \qquad (25) \quad \text{with} \quad M_{CH_3O} = 31 \text{ g mol}^{-1}$$

$$n_{alkyl} = \frac{m_{alkyl}}{M_{alkyl}} \qquad (26) \quad \text{with} \quad M_{alkyl} = 97 \text{ g mol}^{-1}$$

We can then calculate the molar ratio r of CH_3O^- groups and $F_3C-(CH_2)_2$ alkyl chains using equation (27):

$$r = \frac{n_{CH_3O}}{n_{alkyl}} \qquad (27)$$

Considering some O atoms are shared between several anchor points (OH groups) on porous BN, therefore creating a siloxane network, we can calculate an average molar mass of grafted silane. To determine the possible chemical configurations, we first need to calculate the ratios r for our functionalized samples, BN-FAS and BNp-FAS. We then derive the percentage of

FAS, r'. To do this, I reported the relevant masses extracted from TGA and calculated the associated masses and molar quantities (**Table 6.1**).

Table 6.1 Masses of samples in TGA at 120, 350 and 800 °C, and relevant masses and molar quantities for the calculation of the ratio of CH_3O^- groups and $F_3C\text{-}(CH_2)_2$ alkyl chains.

	BN-FAS	**BNp-FAS**
m_{dry}	17.200 mg	66.460 mg
m_{350}	16.733 mg	65.358 mg
m_{800}	14.851 mg	45.260 mg
m_{CH_3O}	0.467 mg	1.102 mg
m_{alkyl}	1.882 mg	20.098 mg
n_{CH_3O}	0.015 mmol	0.0355 mmol
n_{alkyl}	0.0194 mmol	0.207 mmol
r	0.77	0.17
r'	25.7%	5.7%

I obtained $r = 0.77$ in BN-FAS, so on average there are 0.77 CH_3O^- group dangling and 2.23 CH_3O^- groups grafted to the surface of porous BN (25.7% vs. 74.3%). In BNp-FAS, $r = 0.17$, so on average there are 0.17 CH_3O^- group dangling and 2.83 CH_3O^- groups grafted to the surface of porous BN (5.7% vs. 94.3%). The two possible configurations are represented in **Figure 6.8**, bearing in mind that one or two O atoms are shared with one or two other silane molecules.

$r'*(M_{alkyl}+M_{Si}+M_{OCH3}+1.5*M_O)$ $(1-r')*(M_{alkyl}+M_{Si}+2*M_O)$
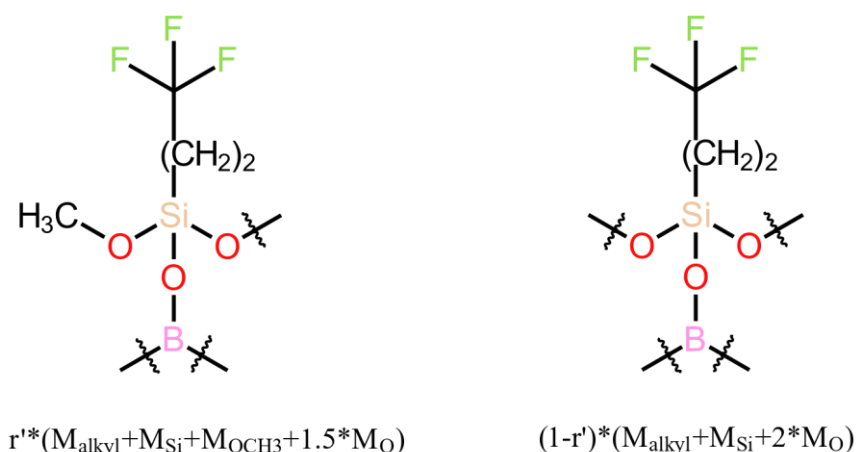
Figure 6.8 Schematics of the two configurations of grafting with trimethoxy(3,3,3-trifluoropropyl)silane (FAS), and the associated molar masses of grafted silane.

We can now calculate the average molar mass of grafted silane using equation (28):

$$M_{grafting} = r' * (M_{alkyl} + M_{Si} + M_{OCH_3} + 1.5 * M_O) + (1 - r') * (M_{alkyl} + M_{Si} + 2 * M_O)$$

$$M_{grafting} = r' * 180 + (1 - r') * 157 = 23 * r' + 157 \quad (28)$$

The weight of grafted silane is given by equation (29):

$$m_{grafting} = n_{alkyl} * M_{grafting} \quad (29)$$

Finally, we can get the weight percentages of FAS and BN in each sample as shown in equations (30) and (31). Before sorption analysis, I degassed samples at 120 °C, so we consider the dry sample as our starting material to calculate the percentages:

$$\%FAS = \frac{m_{grafting}}{m_{dry}} * 100 \quad (30)$$

$$\%BN = 100 - \%FAS \quad (31)$$

Molar quantities of FAS can be given per gram of BN, by simply converting molar quantities obtained per mass of dry sample. All results for both routes are given in **Table 6.2** below. In summary, the estimated content of FAS grafted in each functionalized sample is 18.4wt% in BN-FAS and BN-FASp (1.13 mmol per g of BN) and 49.3wt% in BNp-FAS (3.11 mmol per g of BN). A possible hypothesis explaining the different loadings between both routes is that FAS molecules could react with each other during the silylation process, without grafting to

153

porous BN. Therefore, these molecules would be removed during the filtration of the functionalized BN powder in route 1. In the rest of this chapter, I have used the calculated FAS concentrations to report gas sorption results (i.e., N_2, CO_2 and H_2O in this study) per gram of porous BN (as opposed to per gram of sample). These results are indicated with an asterisk '*' after the corresponding samples names.

Table 6.2 Average molar masses and associated masses of grafted silane, weight percentage of FAS and BN, and molar quantity of grafted FAS per gram of porous BN.

	BN-FAS	**BNp-FAS**
$M_{grafting}$	162.9 g mol^{-1}	158.3 g mol^{-1}
$m_{grafting}$	3.160 mg	32.768 mg
%**FAS**	18.4wt%	49.3wt%
%**BN**	81.6wt%	50.7wt%
$n_{grafting}$	1.13 mmol per g of BN	3.11 mmol per g of BN

6.4.3. Assessing pore structure and porosity

To survey the impact of functionalization on BET area and porosity, I used N_2 sorption at -196 °C (**Figure 6.9**). Relevant results are expressed after weight adjustment (annotated with '*'). BNp and porous BN powder had similar BET areas (1455 m^2 g^{-1} and 1521 m^2 g^{-1} respectively), as well as BN-FASp* and BN-FAS* but with lower values (827 m^2 g^{-1} and 816 m^2 g^{-1} respectively). I attribute the decrease in BET area and porosity to the synthesis process employed for route 1, i.e., use of toluene and/or ethanol, as opposed to the silylation reaction itself. This interpretation arises from the study of the BN-control sample (**Figure A3.5** in Appendix 3). After route 2, BNp-FAS* had a BET area of 575 m^2 g^{-1}, which may indicate pore blockage.
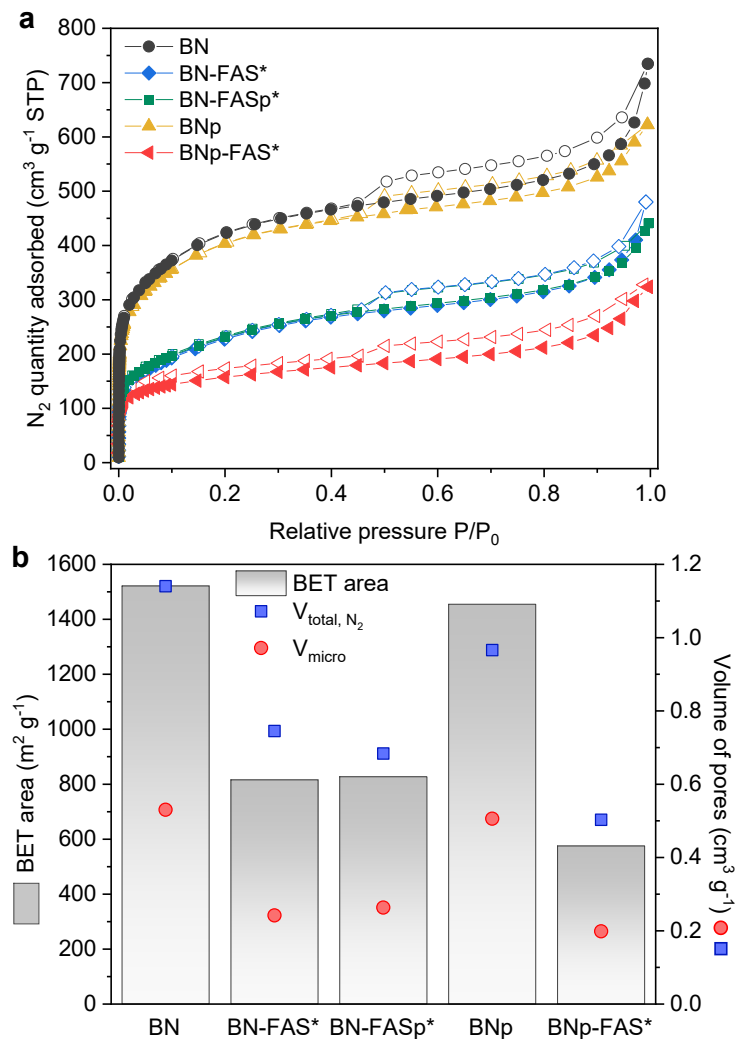
Figure 6.9 (a) N$_2$ sorption isotherms at –196 °C for unmodified and functionalized porous BN. (b) Associated textural parameters extracted from N$_2$ sorption measurements. <u>Note:</u> total pore volumes $V_{\text{tot, N}_2}$ correspond to pore sizes up to 12 nm as obtained from N$_2$ sorption.

I combined pore size distributions from N$_2$ sorption analyses at –196 °C and mercury intrusion porosimetry (**Figure 6.10**) to obtain the overall pore size distribution over the range 0.5 nm - 325 μm (**Figure 6.11**).[205] As expected, the total volumes of pores in **Figure 6.9** and **Figure 6.10** differ. As MIP can survey larger pores than N$_2$ sorption at –196 °C (**Figure 6.10**), both techniques are required to get an accurate indication of the total pore volume in samples that have a very wide pore size distribution (i.e., also containing meso- and macropores). The volumes of micropores (< 2nm) are identical in both **Figure 6.9** and **Figure 6.10** as only the contribution from N$_2$ sorption is considered for this size range.
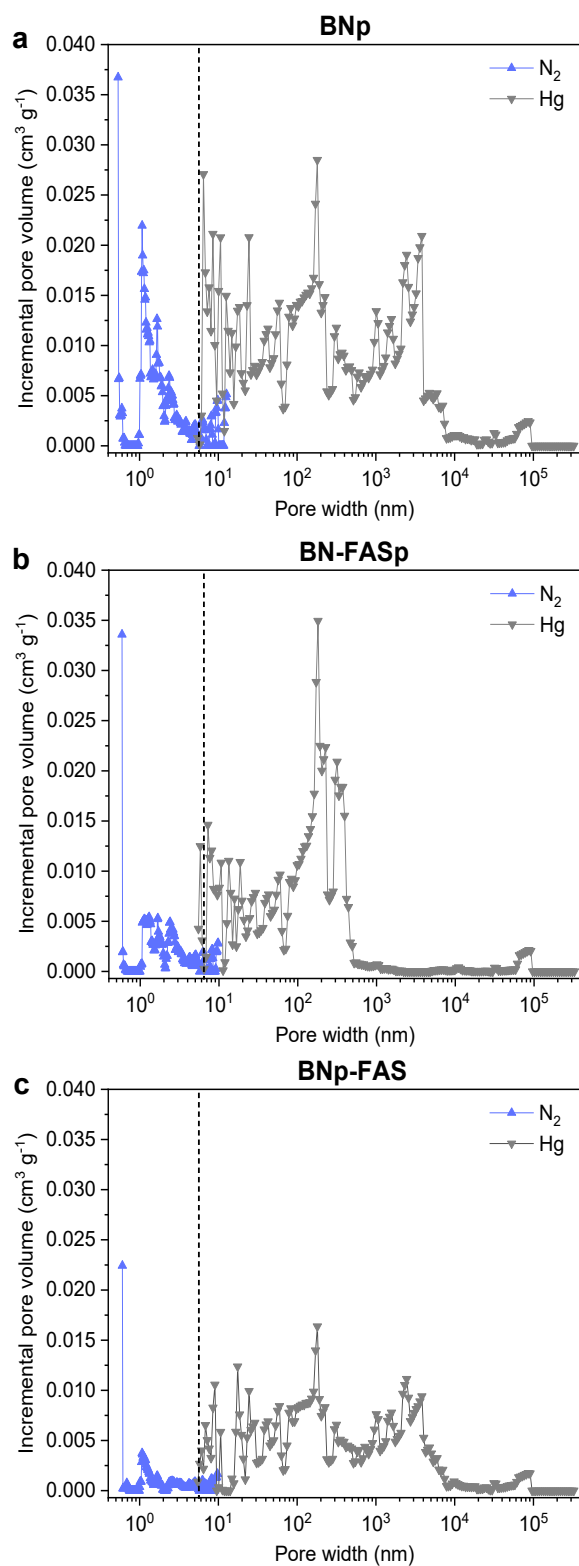
Figure 6.10 Pore size distributions derived from N_2 sorption isotherms at –196 °C and mercury intrusion porosimetry for: (a) BNp, (b) BN-FASp, (c) BNp-FAS. Dotted lines represent the cut-off points used to combine the two pore size distributions.
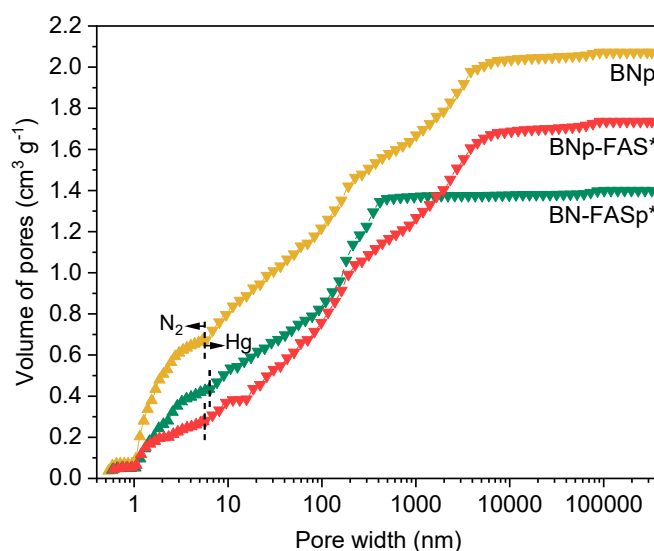
Figure 6.11 Pore size distribution based on the combination of N_2 sorption at -196 °C and mercury intrusion porosimetry. <u>Note:</u> the dotted lines represent the cut-off points used to combine the pore size distributions obtained from N_2 sorption isotherms and MIP (see Figure 6.10).

BNp exhibited micropores, mesopores and macropores. BNp-FAS obtained via CVD showed a similar profile, but with lower pore volume at every scale, particularly in the region of pores smaller than 100 nm. This observation suggests that FAS blocked these smaller pores. BN-FASp had a distinct profile with hardly any pores larger than 465 nm but a significant amount of small pores.

Then, µXRF shed light on the location of FAS molecules in the functionalized samples (**Figure 6.12**). We performed cross-sectional mapping of silicon in BNp as a control. In both functionalized pellets, Si atoms can be clearly observed. BN-FASp displayed a uniform distribution of Si apart from the top and bottom surfaces of the pellet, which appeared slightly less concentrated. This could be due to the pelletization process, leading to non-uniform structure between the surface and the bulk. In BNp-FAS, the distribution of Si was even less uniform, as expected due to the CVD process. A less concentrated amount of Si appears at the centre of the pellet. This is likely related to the diffusion process of FAS during which molecules may not have reached the centre of the pellet. We excluded any impact from the

157

grinding process during sample preparation, as the μXRF instrument performs auto-focusing on each point to ensure that the sample surface is in plane before analysis. The μXRF images support the MIP analyses (**Figure 6.10** and **Figure 6.11**): the higher proportion of large pores for BNp-FAS as opposed to BN-FASp could point to a deeper diffusion of FAS molecules inside the BNp-FAS pellet.
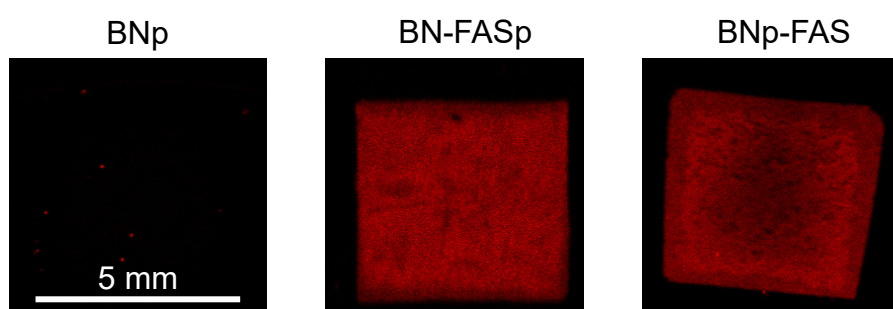
Figure 6.12 Cross-section silicon elemental mapping (in red) using μXRF for BNp, BN-FASp and BNp-FAS. White line corresponds to 5 mm and all three images are at the same scale.

6.4.4. Probing the hydrophobicity

I first measured water contact angles to quickly probe hydrophobicity of the pellets. Both BNp and BN-FASp absorbed water within 1-2 s of deposition, which made the recording of contact angles inaccurate. Corresponding contact angles would be smaller than 90°, indicating hydrophilic surfaces. Videos were recorded to show this hydrophilic behavior (screenshots in **Figure 6.13**). On the contrary, BNp-FAS displayed a static contact angle of 133.2°, corresponding to a hydrophobic surface (**Figure 6.14**). Hydrophobic contact angles can depend on the chemistry of the samples but also on their surface roughness, which may have an impact here since sample surfaces underwent various treatments with pelletization and CVD steps (**Figure 6.3**). Therefore, it was difficult to draw definite conclusions from water contact angle measurements and I proceeded with complementary analyses.
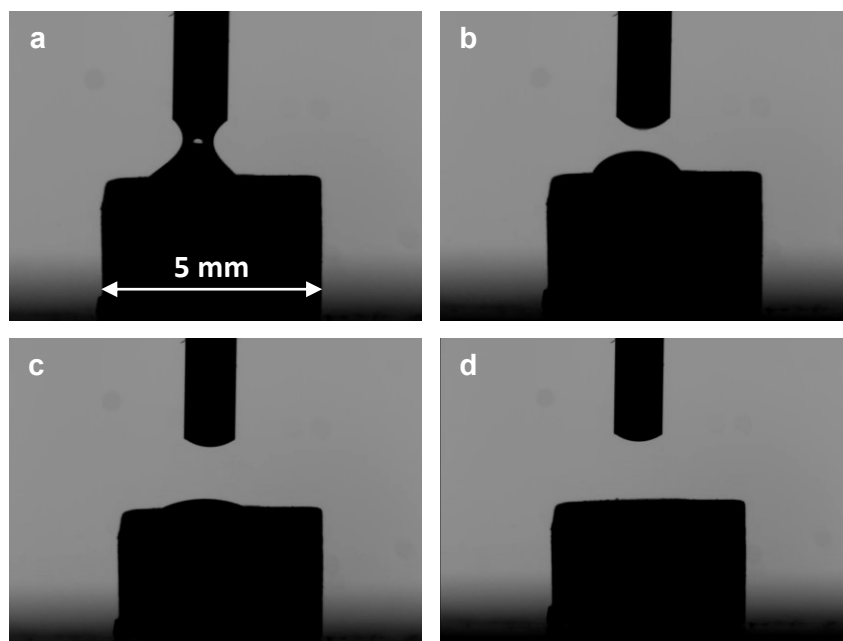
Figure 6.13 Consecutive screenshots, from (a) to (d), of the water contact angle video for BN-FASp showing hydrophilic behavior.
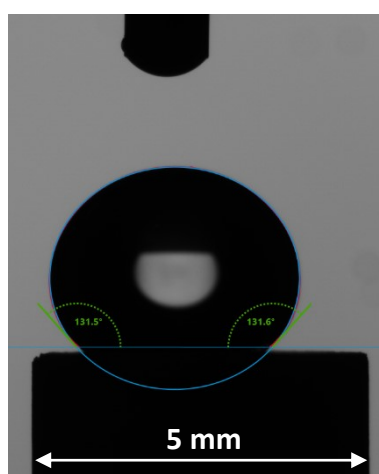
Figure 6.14 Static water contact angle measurement for BNp-FAS showing hydrophobic behavior with contact angles of 131.5 and 131.6 °.

I carried out water sorption isotherms at 22 °C to probe the behavior of pelletized samples upon water vapor exposure (**Figure 6.15**a). I observed for BNp a step around $P/P_0 = 0.25$ indicating condensation and/or degradation of porous BN at this humidity level. Therefore, I repeated the measurements on fresh samples and stopped the measurement at this humidity level to compare the stability of our pellets (**Figure 6.15**b). I observed a large gap between desorption and

adsorption in BNp, indicating that the structure of porous BN was damaged, and its chemistry would have changed upon prolonged moisture exposure. These chemical and structural changes will be discussed in greater detail in sections 6.4.5 and 6.4.6. In the case of BN-FASp, a significant amount of water was adsorbed, confirming the contact angle analysis. Interestingly, this sample adsorbed more water than BNp per gram of boron nitride after weight adjustment. At this time, I cannot provide a verified explanation for this behavior. However, I speculate that since these sorption experiments are long, the structure of the sample may change during the analysis if it is not fully water stable. This change might lead to an increased water sorption. Finally, BNp-FAS adsorbed less water than BNp and BN-FASp up to a relative pressure of 0.6, suggesting improved hydrophobicity thanks to the silane protection, and supporting the previous contact angle findings. We note that BNp-FAS has lower BET area than BNp and BN-FASp (**Figure 6.9**a), which could potentially translate to lower water adsorption. However, we should note that although N_2 molecules may not be able to access partially blocked pores at –196 °C, water molecules could still do so. In summary, water sorption isotherms have provided an insight into the hydrophobicity of our materials, but this needs further investigation as shown in the following section.
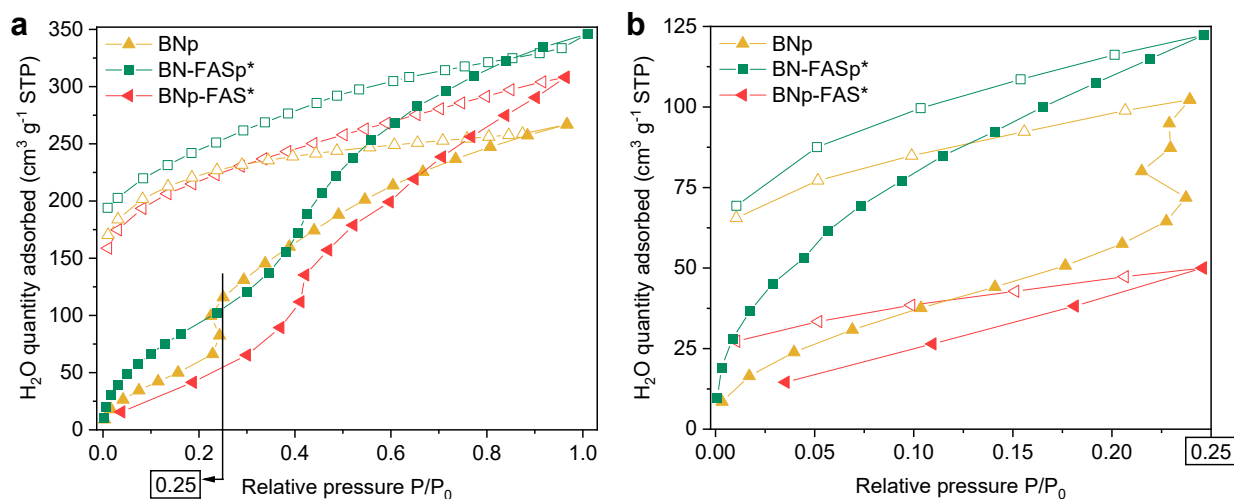
Figure 6.15 Water vapor sorption isotherms at 22 °C for BNp, BN-FASp and BNp-FAS: (a) Up to 1 bar; (b) Up to $P/P_0 = 0.25$. The black arrow in (a) indicates where the second measurement, in (b), was stopped.

6.4.5. Assessing the moisture impact on chemistry

To probe the impact of moisture on the chemistry of the unmodified and functionalized pelletized samples, I used FTIR and XPS prior to and after moisture exposure at 54% and 92% RH for 24 h (**Figure 6.16**). All samples exhibited B-O bonds after exposure to moisture, which was even more pronounced at 92% RH (**Figure 6.16**a-c), indicating partial degradation of the BN-based materials. The B-N bands at 1355 and 776 cm^{-1} were still visible after moisture exposure, meaning some BN had been preserved. XPS analyses for B $1s$ confirmed the FTIR results with appearance of B-O chemical environments in all samples (**Figure 6.16**d-f). B $1s$ XPS peaks corresponding to B-N bands were still predominant in the functionalized pellets compared to unmodified BNp, confirming that BN was still present despite water exposure.
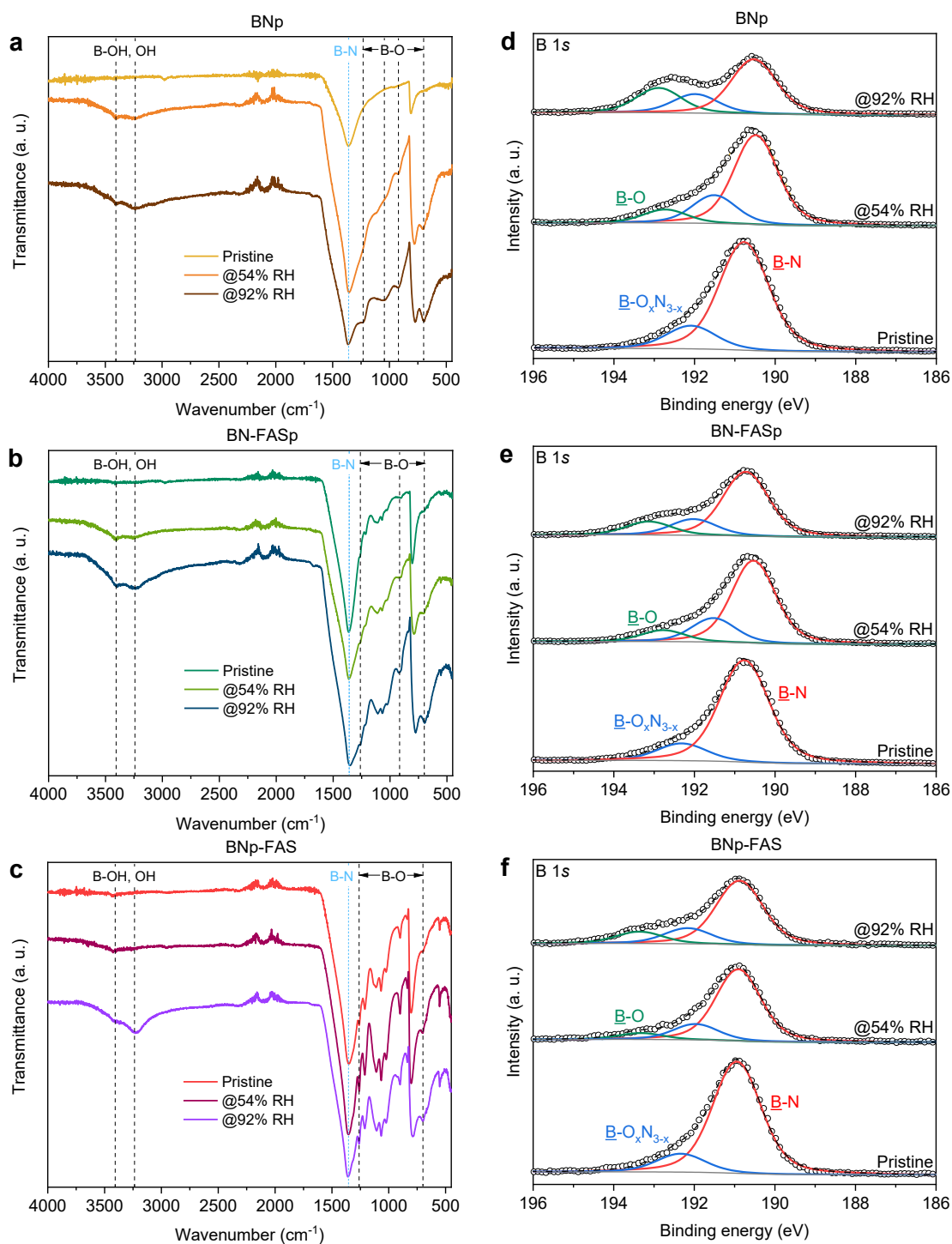
Figure 6.16 FTIR before and after humidity testing for: (a) BNp; (b) BN-FASp; (c) BNp-FAS. High-resolution XPS and peak fitting of the B 1*s* core level before and after humidity testing for: (d) BNp; (e) BN-FASp; (f) BNp-FAS.

To get a better quantification of the moisture impact and the stability of the samples, I estimated the atomic composition based on XPS results (**Figure 6.17**). I then calculated the B-N/B-O

ratios, since porous BN reacts with water and degrades into boron oxide via the release of

ammonia, leading to a decrease in N atoms after moisture exposure.[6] I obtained B-N/B-O ratios

of 6.7 in BNp, 7.2 in BN-FASp and 11.2 in BNp-FAS after exposure to 54% RH (**Table 6.3**).

These ratios decreased after exposure to 92% RH, reaching 2.2 in BNp, 4.8 in BN-FASp and

5.4 in BNp-FAS. This implied that more significant degradation took place in unmodified BNp

compared to the functionalized pellets, corresponding to better protection of the chemistry of

BN thanks to functionalization. The Si 2*s* spectra did not show shifts in binding energy upon

moisture exposure (**Figure A3.8** in Appendix 3), suggesting that the siloxane network at the

surface of porous BN was not impacted. Corroborating the contact angle measurements and

the water sorption analyses, XPS data pointed to the better moisture stability of BNp-FAS

compared to BN-FASp.
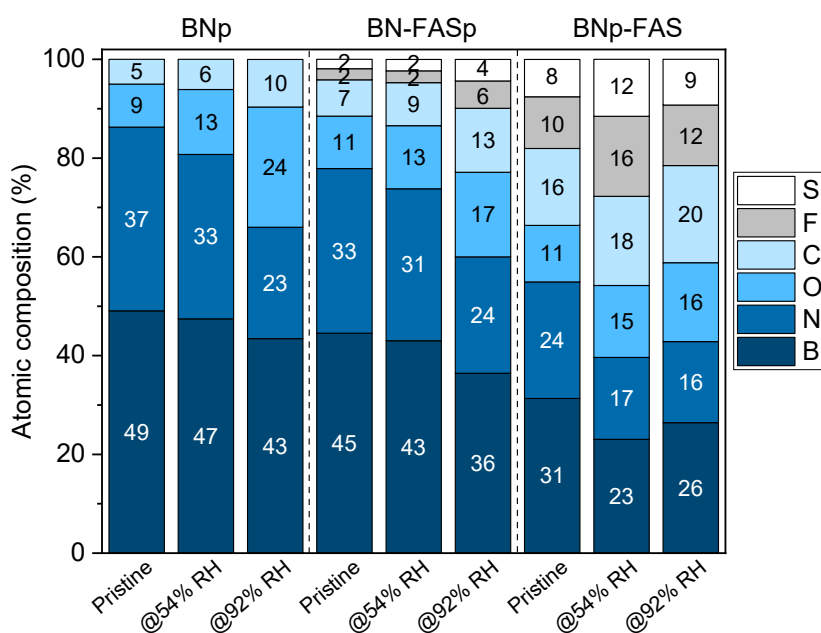
Figure 6.17 Atomic composition derived from XPS for the pelletized samples before and after moisture exposure.

Table 6.3 Ratios of B-N/B-O bonds (excluding B-O-N) derived from XPS after moisture exposure at 54% RH and 92% RH.

Sample	After 54% RH	After 92% RH
BNp	6.7	2.2
BN-FASp	7.2	4.8
BNp-FAS	11.2	5.4

6.4.6. Assessing the moisture impact on structure and porosity

To probe the impact of moisture on the structure of the unmodified and functionalized pelletized samples, I used XRD prior to and after moisture exposure at 54% and 92% RH for 24 h (**Figure 6.18**a-c). Results for powder samples can be found in **Figure A3.9** in Appendix 3. Prior to moisture exposure, unmodified BNp exhibited two broad humps around 24° and 44° (**Figure 6.18**a), which typically correspond to the (002) and (100) planes in graphitic-like structures, such as crystalline hexagonal BN.[4, 209] These two features appeared narrower and more defined after moisture exposure at 54% RH, and even narrower after 92% RH. This implies that the structure of BNp became more crystalline overall upon moisture exposure due to the reaction with water. I hypothesize that water primarily reacts with the amorphous phases in porous BN and decomposes them, while leaving more crystalline phases in the samples intact, therefore exhibiting higher crystallinity on average after moisture exposure.[6] In BN-FASp, I observed a similar effect after moisture exposure with more defined peaks, but with no significant difference between 54% and 92% RH exposure. On the contrary, the signals were still very broad in BNp-FAS, implying that the sample remained highly amorphous. These observations align with the XPS analyses presented above.

I probed the impact of moisture on the porosity of the samples via N_2 sorption isotherms and the derivation of textural parameters (**Figure 6.18**d-i). When looking at unmodified BNp, I observed that exposure at 54% and 92% RH dramatically reduced BET area and porosity (**Figure 6.18**d and g). BET area decreased from 1455 m^2 g^{-1} to 177 m^2 g^{-1} after 54% RH

exposure (87% reduction), and to 40 m^2 g^{-1} after 92% RH exposure (99% reduction). In comparison, BN-FASp* had its BET area decrease from 827 m^2 g^{-1} to 239 m^2 g^{-1} after 54% RH exposure (71% reduction), and to 78 m^2 g^{-1} after 92% RH exposure (91% reduction) (**Figure 6.18**e and h). Finally, BNp-FAS* had its BET area decrease from 575 m^2 g^{-1} to 319 m^2 g^{-1} after 54% RH exposure (45% reduction), and to 112 m^2 g^{-1} after 92% RH exposure (81% reduction) (**Figure 6.18**f and i). Accessible BET area remained after exposure at 92% RH in the functionalized pellets BN-FASp and particularly BNp-FAS, whereas unmodified BN hardly had any porosity left. Another interesting observation is the apparent advantage of pelletization after high humidity exposure, as observed by the higher BET area in BNp and BN-FASp*, compared to BN and BN-FAS respectively (**Figure A3.9**f in Appendix 3).
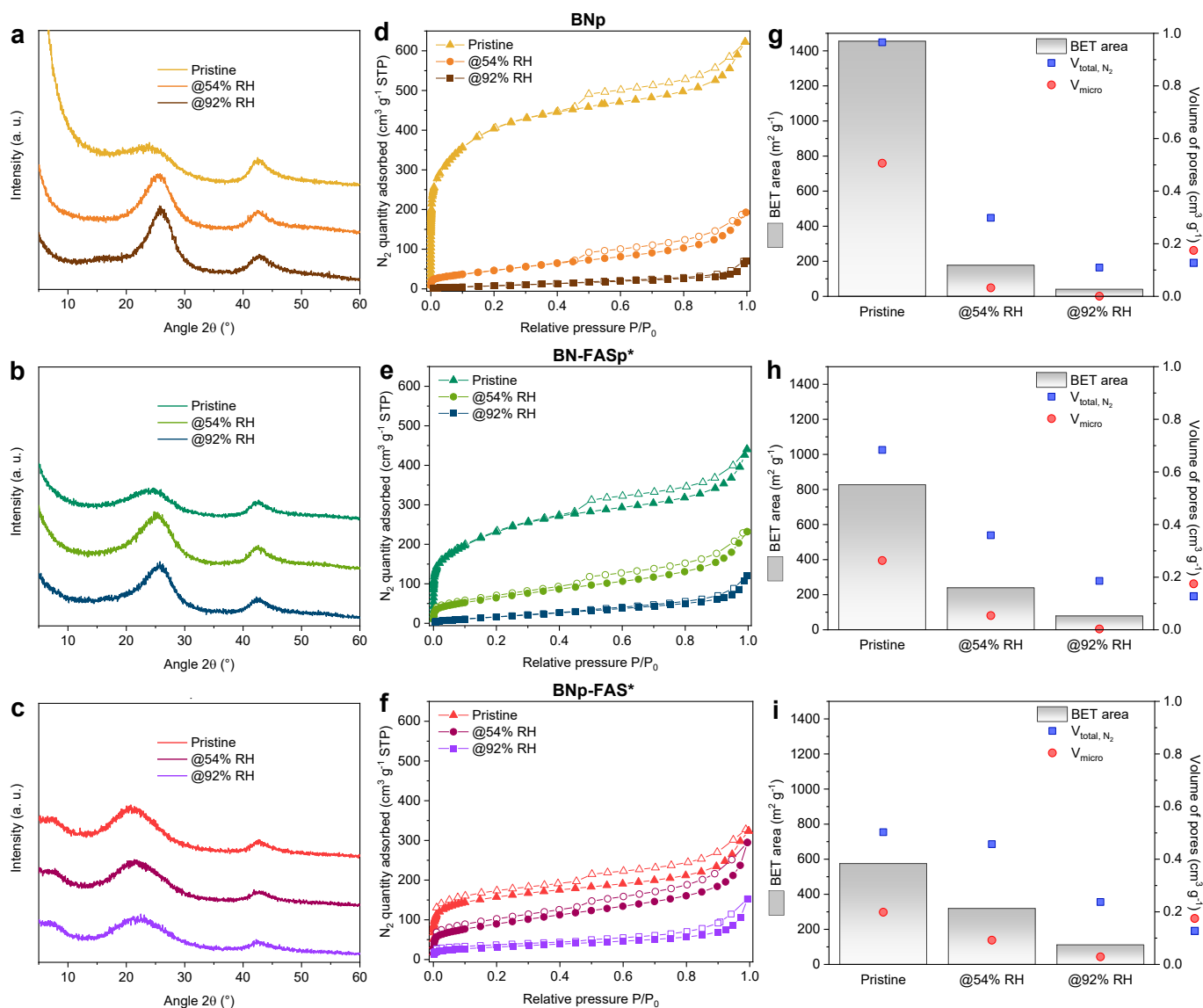
Figure 6.18 XRD patterns before and after humidity exposure for: (a) BNp; (b) BN-FASp*; (c) BNp-FAS*. N_2 sorption isotherms at –196 °C before and after humidity exposure for: (d) BNp; (e) BN-FASp*; (f) BNp-FAS*. Textural parameters obtained from N_2 sorption isotherms before and after humidity exposure for: (g) BNp; (h) BN-FASp*; (i) BNp-FAS*. <u>Note:</u> total pore volumes V_{tot, N_2} correspond to pore sizes up to 12 nm as obtained from N_2 sorption.

6.4.7. Probing equilibrium separation properties

To understand the practical efficiency of our functionalization methods and progress towards scale-up, I measured CO_2 and N_2 sorption isotherms at 25 °C on the three pellets for all three scenarios: pristine, after 54% RH moisture exposure and after 92% RH moisture exposure (**Figure 6.19**). In the case of BNp, CO_2 adsorption capacity significantly decreased after

moisture exposure at 54% RH, and further at 92% RH where hardly any CO_2 adsorbed over the pressure range surveyed (**Figure 6.19**a). N_2 adsorption capacity at 25 °C also decreased after water exposure. These results were expected based on the previous porosity analyses (**Figure 6.18**d and g). Looking at both BN-FASp and BNp-FAS, CO_2 adsorption capacity slightly decreased after moisture exposure but was less impacted compared to BNp (**Figure 6.19**b-c).
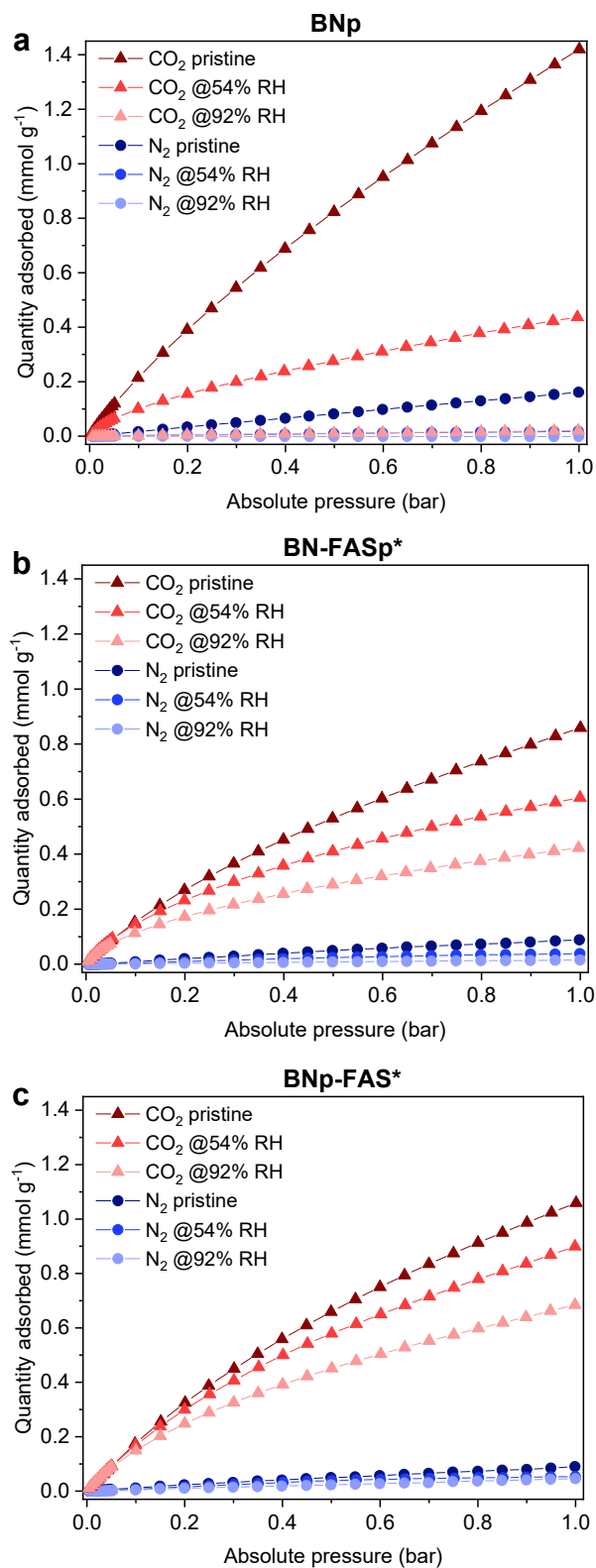
Figure 6.19 CO_2 and N_2 sorption isotherms at 25 °C before and after moisture exposure at 54% and 92% RH for: (a) BNp; (b) BN-FASp*; (c) BNp-FAS* (* indicates that quantities adsorbed were adjusted per g of BN; see section 6.4.2).

To estimate the CO_2/N_2 selectivity, I extracted the capacities at given pressures corresponding to a common composition in post-combustion carbon capture scenarios: $CO_2/N_2 = 0.15/0.85$ (**Figure 6.20**). I then calculated the pure component selectivity using equation (32), with q_{CO2} and q_{N2} being the CO_2 capacity at 0.15 partial pressure and the N_2 capacity 0.85 partial pressure, respectively:

$$S = \frac{q_{CO2}}{q_{N2}} \frac{0.85}{0.15} \qquad (32)$$

I report the capacity values and the calculated selectivities for all pellets in **Figure 6.20**. The selectivity for BNp after moisture exposure at 92% RH was not determined due to the extremely low N_2 capacity. In summary, prior to moisture exposure, functionalization very slightly enhances selectivity while maintaining reasonable uptake for both BN-FASp and BNp-FAS compared to unmodified BNp. After exposure to high RH, functionalization helps maintain a reasonable balance between selectivity and uptake, which can be desirable for industrial applications. Exposure to moisture enhances selectivity owing to the marked decrease in N_2 uptake caused by the loss in porosity.
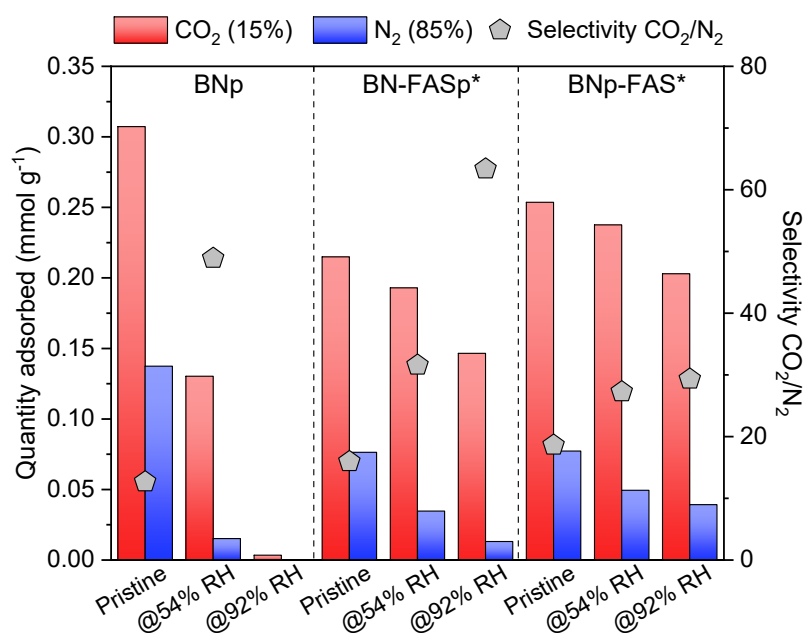
Figure 6.20 CO_2 and N_2 uptakes at 25 °C for a composition of CO_2/N_2 = 0.15:0.85 before and after moisture exposure, and associated selectivity values (not defined for BNp @92% RH due to very low value for N_2 adsorption).

6.4.8. Estimating kinetics of adsorption

The experimental CO_2 adsorption isotherms obtained using the methodology described in Azzan et al.[178], along with the fitted isotherm models, are shown in **Figure 6.21**a-c. The lumped kinetic constants for CO_2 (k_{CO_2}) obtained by carrying out dynamic sorption tests are shown in **Figure 6.21**d-f. The equations that describe the equilibrium and kinetics of CO_2 sorption in these experiments are described in Appendix 3, and the resulting model parameters are shown in **Table 6.4**. The kinetic model used in the parameter estimation for the dynamic sorption experiments can be used to infer dominant resistances to mass transfer, namely, resistance in the micropores and resistance in the macropores of the adsorbent.[210] In the case of BNp, the dominant resistance to mass transfer is in the micropores, as inferred from experimental observations reported previously. This results in a constant value for the lumped kinetic rate constant k_{CO_2} over the entire range of pressures and temperatures.[178] As for the functionalized BN samples, the parameter estimation on the dynamic sorption experiments results in much

170

higher values of the kinetic rate constant k, indicating a faster mass transfer. Looking at the magnitudes of the two contributions k_1 and k_2, which are analogous to resistances in micropores and macropores, respectively, we can conclude that there is negligible resistance to mass transfer in both the macro- and micropores for the case of BN-FASp. However, for BNp-FAS, although k_1 is large, k_2 is significantly smaller compared to both BNp and BN-FASp. From this, we can infer that there is a greater resistance to mass transfer in the macropores for the case of BNp-FAS, when compared to BNp and BN-FASp. BNp-FAS has a notably higher bulk density (770.5 kg m^{-3} as derived from MIP measurement) compared to BNp and BN-FASp (413.2 kg m^{-3} and 448.7 kg m^{-3}, respectively), which indicates that the functionalization has caused changes in the porosity of the pellets, leading to changes in the mass transfer process. As seen in **Figure 6.9**b and **Figure 6.11**, BNp has a greater proportion of smaller micropores than the functionalized samples, which might explain the enhanced micropore resistance for this sample. To conclude, it is worth emphasizing that the k_1 and k_2 values are fitted to one set of experiments and only allow to infer mass transfer resistance in the different samples. These values do not have physical meaning, and the theoretical determination of controlling mechanisms would require another set of experiments, which constitutes future work.
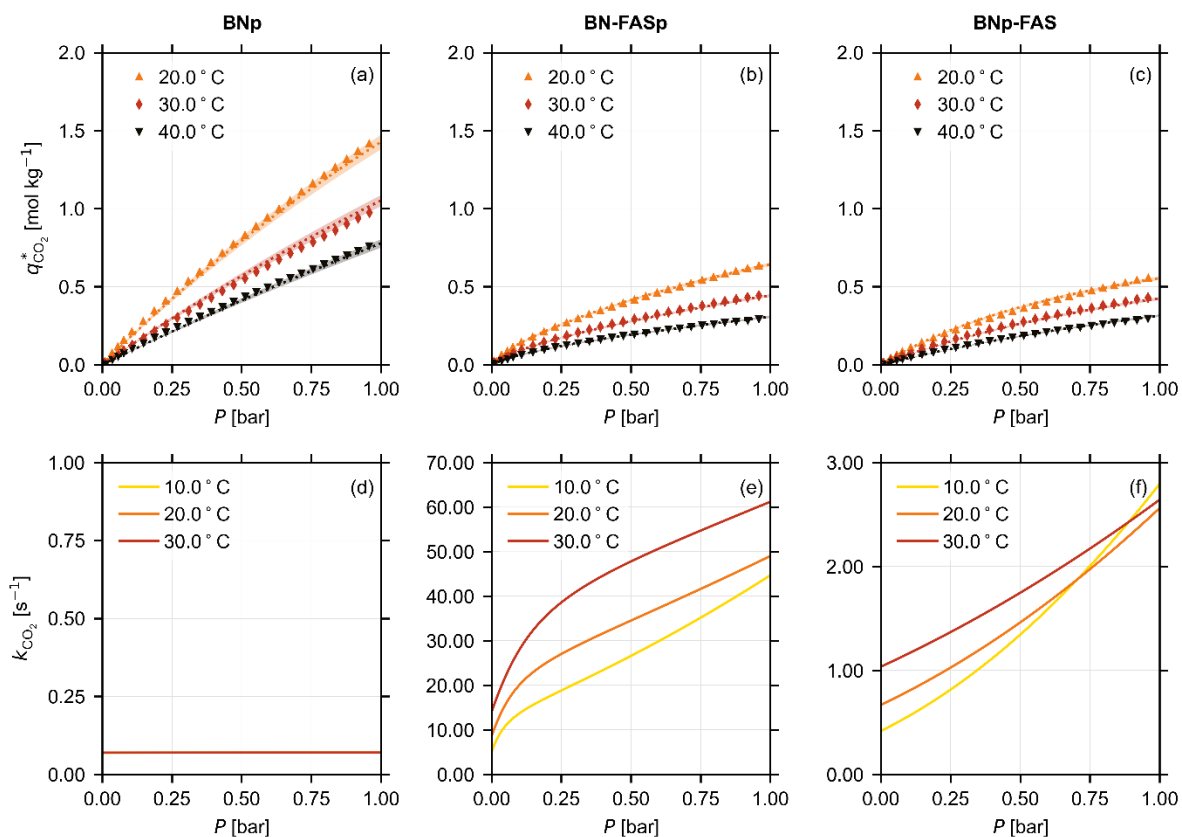
Figure 6.21 CO_2 sorption isotherms $q_{CO_2}^*(P, T)$ at 20, 30 and 40 °C with isotherm model fits for: (a) BNp (single-site Langmuir model); (b) BN-FASp (dual-site Langmuir model); (c) BNp-FAS (single-site Langmuir model). The shaded region (very narrow) corresponds to the 95% confidence bounds for the model fits with respect to the experimental data. Corresponding lumped kinetic rate constant k_{CO_2} for: (d) BNp; (e) BN-FASp and (f) BNp-FAS. <u>Note:</u> for BNp, k_{CO_2} was obtained using experiments carried out at 33, 52 and 72 °C as described in reference [178].

Table 6.4 Parameters for the CO_2 equilibrium isotherms obtained from fitting the relevant isotherm model to the data from Figure 6.21, and the corresponding parameters for the CO_2 adsorption kinetics for BNp, BN-FASp and BNp-FAS (more information on the equations and parameters can be found in Appendix 3). For perspective, kinetics parameters for CO_2 sorption in zeolite 13X pellets measured using the same technique as the one used here are reported in the table too (taken from reference [178]).

Parameters	Unit	BNp	BN-FASp	BNp-FAS	Zeolite 13X pellet
Isotherm parameters					
q_{sb,CO_2}	mol kg^{-1}	7.01 ± 0.09	1.74 ± 0.31	1.13 ± 0.17	-
b_{0,CO_2}	$(\times 10^{-7})$ m^3 mol^{-1}	2.30 ± 0.03	$5.61 \times 10^{-3} \pm 9.59 \times 10^{-4}$	0.39 ± 0.06	-
$-\Delta U_{b,CO_2}$	kJ mol^{-1}	24.87 ± 0.04	41.00 ± 0.08	32.40 ± 0.08	-
q_{sd,CO_2}	mol kg^{-1}	-	0.09 ± 0.03	-	-
d_{0,CO_2}	$(\times 10^{-7})$ m^3 mol^{-1}	-	2.94 ± 0.56	-	-
$-\Delta U_{d,CO_2}$	kJ mol^{-1}	-	34.30 ± 0.501	-	-
Kinetic parameters					
k_{1,CO_2}	s^{-1}	0.07 ± 0.00	920.00 ± 117.00	867.00 ± 118.00	779.18 ± 49.36
k_{2,CO_2}	s^{-1}	831.77 ± 69.51	631.00 ± 105.00	40.80 ± 4.68	75.34 ± 4.22

6.5.   Conclusions

In this chapter, I explored ways of enhancing the hydrolytic stability of porous BN via surface functionalization using a fluoroalkylsilane, i.e., trimethoxy(3,3,3-trifluoropropyl)silane. I trialed two functionalization methods: i) silylation of porous BN powder followed by pelletization (route 1); ii) chemical vapor deposition of alkylsilane on pre-formed porous BN pellets (route 2). These two routes led to shaped adsorbents with distinct chemical and textural features. This in turn caused changes in their hydrophobic/hydrophilic nature, as well as sorption equilibrium and kinetic properties. The summary below provides answers to my research questions highlighted in Chapter 3 and related to research objectives 2 and 3:

• By capping the OH groups present at the surface of porous BN, functionalization partially protected the chemistry and structure of porous BN against moisture attack compared to pristine porous BN.

• The use of an alkylsilane with a short alkyl chain and F atoms appeared promising to incur hydrophobicity without blocking all the pores of porous BN.

• Route 2 led to a higher silane grafting yield and produced a hydrophobic sample more structurally resistant to moisture compared to the sample obtained via route 1. This enhanced feature can be linked to the overall higher silane content in this sample and/or the greater silane concentration on the surface of the pellets.

• From an equilibrium sorption point of view, for both routes, functionalization very slightly enhanced selectivity towards CO_2 in CO_2/N_2 separation while maintaining reasonable CO_2 and N_2 uptakes. Upon exposure to moisture, the gas uptakes of all the samples decreased, but significantly less for the functionalized samples owing to their greater structural stability.

• CO_2 sorption kinetics analyses pointed to different mass transfer mechanisms for the three samples, i.e., pristine porous BN and the two functionalized samples.

These findings highlight the critical aspect of formulation to control dynamic sorption processes. Overall, this work paves the way for a better understanding of the hydrolytic instability of porous BN, and for the development of further methods to functionalize porous BN to tailor its hydrophobicity.

CHAPTER 7: ASSESSING THE POTENTIAL OF POROUS BN FOR THERMOCHEMICAL ENERGY STORAGE

The work described in this chapter was carried out by the thesis author, apart from the modeling component described in section 7.3.4.2, which was done by Dr. Humera Ansari. The thermal energy storage experiments using water were performed by the thesis author on a set-up at the University of Ottawa, Canada under the supervision of Prof. F. Handan Tezel and Dr. Suboohi Shervani. The heat of adsorption calculations were carried out by the thesis author with useful advice from Dr. David Danaci at Imperial College London.

7.1.   Introduction

As explained earlier in this thesis, porous BN has proven promising as an adsorbent material for gas adsorption, mainly due to its rich chemistry, its high surface area and its high porosity.[4, 24, 39, 106-109] In particular, the tunability of its surface area is a key attribute making it a versatile adsorbent depending on the targeted molecules to separate. The chemistry of porous BN is also tunable, as shown in Chapter 6 when using surface functionalization to enhance the hydrolytic stability of the material.[8] All these attributes led me to probe further the potential of porous BN in another key adsorption-based application to reduce energy consumption, namely thermal energy storage (TES) via adsorption.[122, 123] This type of TES remains under research with novel adsorbent materials being trialed, as opposed to sensible and latent heat storage, which are more established technologies.[126]

The most common adsorbents used for TES via adsorption are zeolites, silica gels and activated carbons.[122, 127, 136, 137] To date, no research has been carried out on porous BN in this context. In Chapter 2, I surveyed which material properties were sought after in an adsorbent for TES

via adsorption. Findings showed that the ideal adsorbent should exhibit high surface area and porosity to enhance the uptake of the adsorbate,[140] in parallel with high thermal conductivity and low specific heat capacity to increase the temperature lift and heat transfer during adsorption/desorption cycles.[122, 126, 139, 141] From a chemistry perspective, the choice of the adsorbent would depend on the paired adsorbate (or vice-versa), as this will influence the adsorption uptake and the heat of adsorption, which are both key parameters in a TES system.[122, 138] Porous BN presents attractive textural and chemical features for TES via adsorption, similarly to activated carbon materials, but little is known about its thermal properties. Its amorphous character and high porosity may imply poor thermal properties, in particular low thermal conductivity due to the presence of defects in its crystal structure.[141, 142] Since porous BN benefits from some of the required properties for TES adsorbents, more research needs to be carried out on its potential suitability with various adsorbates in the context of TES via adsorption.

Contrary to porous BN, hexagonal BN (h-BN) is known for its great thermal properties, such as high thermal conductivity,[149] but it is non-porous. Therefore, mixtures of porous and hexagonal BN could be a way to achieve a compromise between textural and thermal properties, while benefiting from the rich chemistry of BN materials. In terms of adsorbates, it is worth considering common adsorbates already researched in TES via adsorption with other materials, namely water, alkanes and alcohols.[122] Indeed, water is the most common fluid used in this application, displaying high values of heat of adsorption and energy storage densities with various porous materials, such as zeolites and metal organic frameworks (MOFs).[122, 152] However, stability issues may arise with porous BN, depending on the conditions used.[6, 8] Alcohols have shown promising results with other amorphous adsorbents, such as activated carbon, displaying high uptake and heat of adsorption.[122, 153] Finally, alkanes can also be potential candidates due to their high affinity with h-BN.[160]

Herein, I have considered various samples, namely porous BN, h-BN, mixtures of these two compounds, and activated carbon. h-BN is used as a reference with no porosity yet great thermal properties, whereas activated carbon is considered as a benchmark as it has been the main amorphous adsorbent researched for TES via adsorption to date. I have first characterized the chemical, textural and thermal properties of all the samples considered using a range of spectroscopic and analytical tools. I have then looked at the stability of these adsorbents towards the three adsorbates selected: water, heptane and n-propanol. In particular, one would expect high stability with heptane, whereas n-propanol may degrade porous BN over time due to the affinity with OH groups present in porous BN,[8] but this needed verification. I showed in Chapter 6 that porous BN is unstable in the presence of water vapor, but this depended on the humidity conditions.[8] Therefore, mild conditions could be used in the case of water to get a comprehensive understanding of the performance of porous BN in TES via adsorption, as water remains the most common adsorbate used in the literature. TES experiments with water were carried out on a fit-for-purpose set-up at the University of Ottawa, Canada, which provided breakthrough curves and temperature profiles to calculate energy storage density values. In the case of heptane and n-propanol, which could not directly be used with the set-up, an indirect method was devised to estimate energy storage density. Adsorption isotherms were first measured at different temperatures to determine the heats of adsorption, hinting which pairs would generate more energy during TES experiments. These isotherms were then used to model breakthrough and temperature profiles for each working pair,[211] allowing the calculation of energy storage density.

This pioneering work provided a better understanding of the feasibility of using porous BN materials in TES via adsorption, and it proposed a screening tool to determine the suitability of an adsorbate for a given adsorbent using adsorption isotherms.

7.2. Materials and solvents

7.2.1. BN-based materials

Porous boron nitride (p-BN) powder was synthesized following the multiple N-precursor synthesis previously developed in our group[3] and described in the Methods chapter of this thesis (section 4.1.1). Hexagonal boron nitride (h-BN) was purchased as a powder (98%, Sigma-Aldrich, CAS 10043-11-5). Two physical mixtures of p-BN and h-BN were prepared to look for a compromise between textural and thermal properties. These mixtures were prepared by weighing p-BN and h-BN accordingly to ratios of 67:33 (wt%) and 33:67 (wt%), and by mixing them manually using a spatula to obtain homogeneous mixtures. Pellets of the four materials introduced above were prepared using a 5-mm diameter pellet die following the preparation described in the Methods chapter (section 4.1.2). The two mixtures in powder or pellet form were named p-BN(67%)/h-BN(33%) and p-BN(33%)/h-BN(67%).

7.2.2. Activated carbon

Activated carbon Norit RB3 rods were used as supplied by the manufacturer (Sigma-Aldrich, CAS 7440-44-0), i.e., in the form of cylindrical rods with variable dimensions (L ~3 mm; Ø ~1 mm). Since the material was already in a shaped form, it was used in its commercial form rather than being ground and re-pelletized. For simplicity, the activated carbon material was referred to as AC in this chapter.

7.2.3. Adsorbates

Three adsorbates were selected: heptane (anhydrous 99%, Sigma-Aldrich, CAS 142-82-5), n-propanol ($\geq$ 99.9%, Sigma-Aldrich, CAS 71-23-8) and distilled water.

7.3. Methods

All materials were characterized using: Fourier transform infrared spectroscopy (FTIR) and X-ray photoelectron spectroscopy (XPS) for chemical features; X-ray diffraction (XRD), N_2 sorption at –196 °C and mercury intrusion porosimetry (MIP) for structural and textural features; differential scanning calorimetry (DSC) for thermal properties. These techniques are detailed in Chapter 4 of this thesis, whereas some specific methods used in the current chapter are explained below.

7.3.1. Bed density measurement

The bed density of a packed column was measured by weighing the amount of a sample that could be added inside the column of a known volume, after tapping gently and adding material to fill to the top. This was done with an adsorption column of dimensions L = 7.03 cm and D = 1.09 cm, hence a volume V = 6.56 cm^3.

7.3.2. Stability testing

To assess the stability of the materials upon exposure to n-propanol, p-BN, h-BN and AC were soaked for 24 h at room temperature in a Petri dish filled with the solvent. After that, materials were filtered with a Büchner funnel and dried in an oven at 150 °C overnight. XRD analyses were carried out to assess potential changes in crystallinity, which would indicate a degradation of the material (see Chapter 6 with water-induced degradation). Porosity analyses were then conducted using N_2 sorption at –196 °C after ex-situ and in-situ degassing.

7.3.3. Heat of adsorption determination for heptane and n-propanol adsorption

To estimate the heat of adsorption with heptane and n-propanol, sorption isotherms were measured at three different temperatures with a 10-degree interval: 15 °C, 25 °C and 35 °C. The recording of these isotherms is described in the Methods chapter of this thesis (section 4.5.3). The heats of adsorption were derived using two approaches: the virial isotherm fitting method and the 'manual' isosteric method.[212]

7.3.3.1. *Virial fitting method*

The adsorption isotherms of a material were fitted to a virial-type equation[213, 214] as shown in equation (33), using the same fitting parameters for each temperature:

$$ln\ P = ln\ n + \frac{1}{T}\sum_{i=0}^{m} a_i n^i + \sum_{i=0}^{m'} b_i n^i \quad (33)$$

with:

P pressure (bar)

n loading (mmol g^{-1})

T temperature (K)

a_i virial coefficients (K mol^{-i})

b_i virial coefficients (mol^{-i})

m, m' number of coefficients for adequate fitting

A fit-for-purpose MATLAB programme created by Hassan Azzan was used to obtain the virial coefficients (with $m = 3$ and $m' = 1$, so four a_i and two b_i coefficients).[215] The heat of adsorption at a given loading n was then derived using formula (34), based on the Clausius-Clapeyron differential equation:

$$\Delta H_{ads}(n) = R \sum_{i=0}^{3} a_i n^i \quad (34)$$

with:

ΔH_{ads} heat of adsorption (J mol^{-1})

R universal gas constant (≈ 8.314 J K^{-1} mol^{-1})

Error bars were added using the errors δa_i provided by MATLAB on each a_i virial coefficient as shown in equation (35):

$$\delta H_{ads}(n) = \pm R \left(\sum_{i=0}^{3} (\delta a_i n^i)^2 \right)^{\frac{1}{2}} \quad (35)$$

with:

δH_{ads} error bar of the heat of adsorption at a loading point n (J mol^{-1})

δa_i error on the virial coefficient a_i (K mol^{-i})

Furthermore, it can be useful to determine the heat of adsorption at zero coverage, which corresponds to the adsorption of the first few molecules onto the adsorbent ($n \rightarrow 0$). This can be evaluated by using the first virial coefficient, as shown in equation (36):

$$\Delta H_{ads}^0 = R\, a_0 \quad (36)$$

with:

ΔH_{ads}^0 heat of adsorption at zero coverage (J mol^{-1})

a_0 first virial coefficient (K)

7.3.3.2.   Manual isosteric method

The adsorption isotherms were fitted to either a shape-preserving interpolant model or a smoothing spline model using the curve fitting tool on MATLAB ('cftool'). This method is helpful in particular for isotherms with uncommon shapes and/or with a limited number of experimental points in some regions of pressure. A unique complex equation is used to predict the shape of any isotherm, and MATLAB does not provide any parameters. A distribution of 300 loading points n was created within a common loading range for all three isotherms (no extrapolation should be done beyond experimental points), and the associated pressure points were calculated using the 'feval' function in MATLAB. $ln(P)$ values were then calculated for each loading n in the common loading range at each temperature, and plots of $ln(P) = f\left(\frac{1}{T}\right)$ were generated for each loading point. A linear regression of these plots provided the slopes s_n for each loading point, so that the heat of adsorption ΔH_{ads} profile could be obtained using the Clausius-Clapeyron differential equation shown in equation (37):

$$\Delta H_{ads}(n) = R\, s_n = R\left[\frac{\partial\, ln(P)}{\partial\left(\frac{1}{T}\right)}\right]_n \quad (37)$$

with:

ΔH_{ads} heat of adsorption (J mol^{-1})

n loading (mmol g^{-1})

s_n slope of a $ln(P) = f\left(\frac{1}{T}\right)$ plot at a loading n (K)

R universal gas constant (≈ 8.314 J K^{-1} mol^{-1})

P pressure (bar)

T temperature (K)

Error bars were added for each point with 95%-confidence intervals.

The heat of adsorption at zero coverage ΔH_{ads}^0 can also be evaluated in the manual isosteric approach, but it must be carefully considered if not enough experimental points were recorded in the isotherms at low loadings. At least three loading points n in the low loading region (< 1 mmol g^{-1}) of each isotherm were plotted against $ln\left(\frac{P}{n}\right)$ and fitted to a straight line. The intercepts at each temperature were then plotted against the inverse of the temperature $\left(\frac{1}{T}\right)$. The slope of this straight line multiplied by the universal gas constant R returned an estimation of the heat of adsorption at zero coverage for each material, and could be compared to the value obtained using the virial fitting method as explained in section 7.3.3.1.

7.3.4. Breakthrough and temperature profiles

7.3.4.1. *Experimental acquisition using a TES set-up (water)*

To directly assess the performance of my materials in TES via adsorption with water, I undertook a research visit in the group of Prof. F. Handan Tezel at the University of Ottawa, Canada. The team had previously devised a TES set-up (**Figure 7.1**) allowing to record breakthrough curves and temperature profiles during water adsorption and desorption in a column submitted to a controlled atmosphere at the inlet.[131] This set-up was similar to another apparatus used in a previous study by Hua et al.[137] The set-up in Ottawa consisted of a stainless-steel adsorption column (L = 7.03 cm; D = 1.09 cm; V = 6.56 cm^3) connected at the inlet to a heater and to an air flow (Q = 4 L min^{-1}) with a controlled relative humidity (RH). The RH level was set using a mixture of dry air flow (0% RH) and wet air flow saturated with water (100% RH), and adjusting their respective flow rates depending on the desired RH at the inlet of the column. The temperatures and pressures at different points in the set-up were recorded using a fit-for-purpose LABVIEW program, allowing to obtain breakthrough behavior and temperature profiles during adsorption/desorption cycles.
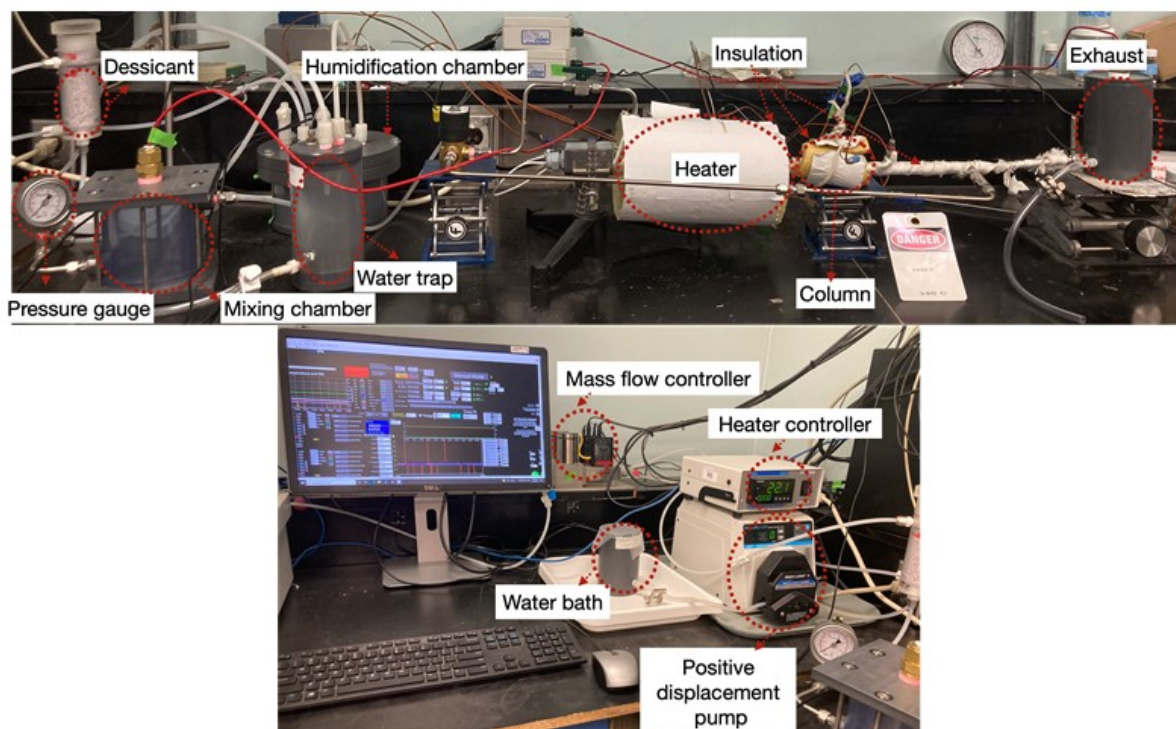
Figure 7.1 Lab-scale TES set-up used for experiments using water vapor as an adsorbate at the University of Ottawa, Canada. Reproduced with permission from reference [131]. Copyright 2022 Elsevier.

Before starting an experiment on the TES set-up, BN-based pellets and AC pellets were gently crushed using a mortar and a pestle. Each adsorbent was then sieved to have particles at least smaller than a tenth of the column diameter (< 1.09 mm) for appropriate packing. To do this, I sieved each sample using a 20 × 60 mesh size (0.25-0.81 mm). The 20-mesh size prevented smaller particles from leaving the column during experiments. Each sample was then packed inside the adsorption column (between 2 and 5 g depending on the material's density), and fiberglass was used at each end to insulate and trap all the particles.

Considering the instability of porous BN with water (see Chapter 6), the RH at the inlet was set to 30% for all experiments. Each sample was tested through three cycles to assess its stability with water and the repeatability of the measurements. Each cycle consisted of the following two steps: 1) activation/regeneration at 180 °C under dry air at 4 L min^{-1}; 2)

adsorption at room temperature with air at 4 L min^{-1} with 30% RH. The first step allowed removing moisture from the sample, and was considered complete when the outlet RH was below 3% for at least 15 min. The second step corresponded to the hydration of the adsorbent, during which the temperatures at the inlet and the outlet were measured to calculate the temperature lift triggered during adsorption, and leading to the amount of energy released as I will explain in section 7.3.5. The recordings of pressure and relative humidity also allowed the obtention of breakthrough curves, which were expressed in terms of absolute humidity to remove any pressure drop effects in the column.[133]

7.3.4.2. Derivation from adsorption isotherms (heptane and n-propanol)

To assess the suitability of heptane and n-propanol as adsorbates for TES, I looked at ways of estimating breakthrough curves and temperature profiles without the need of a tailored TES set-up. To do so, a MATLAB programme developed by Ward and Pini was used.[211] Their model allows the derivation of both breakthrough curves and temperature profiles for an adsorption experiment when providing adsorption isotherms and a range of parameters.

First, heptane and n-propanol adsorption isotherms were fitted to a dual-site Langmuir (DSL) model for BN-based materials, and to a more complex model for activated carbon to account for the multiple steps observed with this adsorbent. This latter model was devised by Ng et al. and will be referred to as the 'NBSI' model, as a reference to the authors.[216] I then provided all the required parameters to Dr. Humera Ansari who ran the model to obtain the breakthrough curves and temperature profiles. These parameters were related to properties of the adsorbent, the adsorbate and the column used. Some parameters were directly measured whereas others had to be estimated based on literature. In the case of the column, we used the parameters for an aluminum column as used in a previous study by Pini et al.[217] The experimental results in

this study were used when developing the model presented in reference [211]. We note that the theory behind the model falls beyond the scope of this thesis but can be found in reference [211].

To model the breakthrough curves and temperature profiles, some assumptions had to be made to obtain the necessary parameters:

• the specific heat capacity of the adsorbed phase was assumed to be that of the vapor of heptane or n-propanol.

• the parameters of the adsorption column were based on standard values for an aluminum column, as reported in the study by Pini et al.[217] that was used for the development of the model presented in reference [211].

• the outer heat transfer coefficient was taken from the study by Ward and Pini considering the aluminum column mentioned previously.[211] We conducted a sensitivity analysis to confirm its minimal impact on the modeled results (section 7.4.4.2).

• the thermo-couple that would measure the temperature lift was placed half-way through the column.

The adsorbate and column parameters used in the mathematical model for heptane and n-propanol sorption are presented in **Table 7.1** below. When relevant, the physical properties were taken at 25 °C in the literature.

Table 7.1 Parameters used for all the materials in the modeling of heptane and n-propanol breakthrough curves and temperature profiles, with the associated references from the literature.

Parameters	Unit	Heptane	Ref.	n-propanol	Ref.
Adsorbate parameters					
Heat capacity of adsorbed phase	J kg^{-1} K^{-1}	1098	[218]	1424	[219]
Effective thermal conductivity	J s^{-1} m^{-1} K^{-1}	0.14	[220]	0.158	[221]
Molecular diffusivity	m^2 s^{-1}	3.12×10^{-9}	[222]	8.00×10^{-6}	[223]
Column parameters					
Wall density	kg m^{-3}	2700	[211, 217]	2700	[211, 217]
Wall specific heat capacity	J kg^{-1} K^{-1}	902	[211, 217]	902	[211, 217]
Wall thermal conductivity	J s^{-1} m^{-1} K^{-1}	205	[211, 217]	205	[211, 217]
Outer heat transfer coefficient h_{out}	W m^{-2} K^{-1}	5.88	[211]	5.88	[211]

One parameter remained to be assessed for the model, which was the inner heat transfer coefficient, h_{in}. This parameter depends on the column, the adsorbate and the adsorbent, and represents how fast the inside of the column would go back to the initial temperature, which is quite crucial for a TES process. A sensitivity analysis was carried out in the case of p-BN with both heptane and n-propanol adsorption to understand the impact of the inner heat transfer coefficient on the breakthrough and temperature profiles, and to decide on a value.

7.3.5. Energy storage density calculation

To estimate the energy storage density of each adsorbent/adsorbate working pair, two different methods were used. In the case of water adsorption, the temperature profiles obtained experimentally were directly used, while for heptane and n-propanol adsorption, the energy density values were estimated from the modeled temperature profiles (**Figure 7.2**).
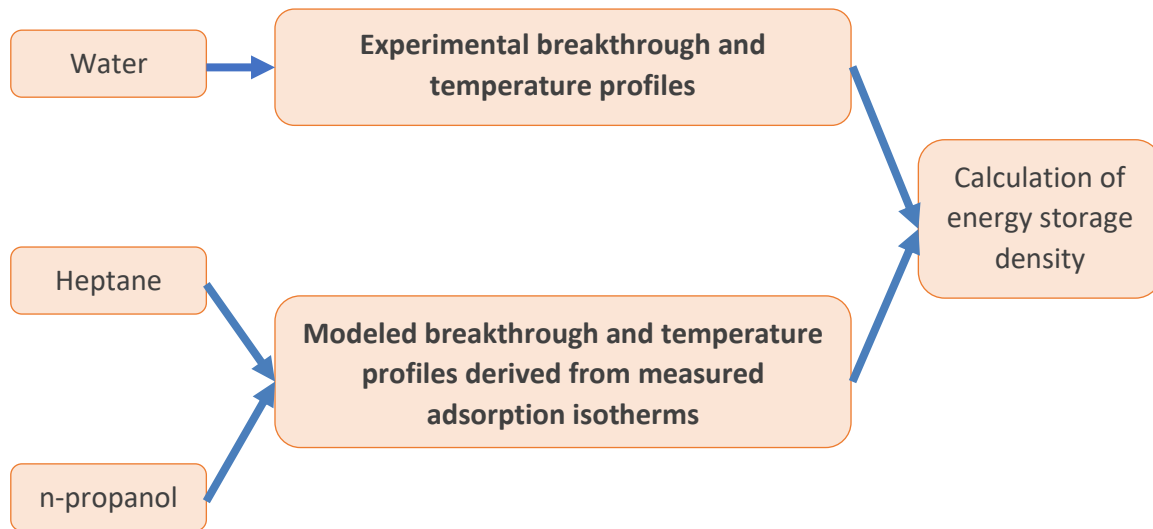
Figure 7.2 Workflow of the determination of energy storage density values for water, heptane and n-propanol adsorption.

The first step was to determine the energy released during adsorption of a given adsorbate. The area under the curve of a given temperature profile (either experimental or modeled) was integrated over the adsorption time, i.e., until the adsorbent was saturated as observed in a breakthrough profile. With a potential delay depending on heat transfer, the end of adsorption would also roughly correspond to the time when the outlet temperature reached the initial temperature after the temperature lift. The obtained area was then multiplied by the mass flow rate of the adsorbate and by the specific heat capacity of the adsorbed phase. This led to equation (8), previously described in Chapter 2:

$$E_{ads} = \int_0^{t_f} \dot{m}\, C_p(T)\, (T_{out} - T_{in})\, dt \qquad (8)$$

with:

E_{ads} energy released during adsorption (J)

t_f time corresponding to the end of adsorption (s)

$\dot{m}$ mass flow rate of the adsorbate (kg min^{-1})

$C_p(T)$ specific heat capacity of the adsorbate (J kg^{-1} K^{-1})

T_{out} temperature at the column outlet (K)

T_{in} temperature at the column inlet (K)

The specific heat capacity of adsorbed water was evaluated using the specific heat capacities of both dry air and water vapor as shown in equation (38):

$$C_{p,ma} = \frac{C_{p,da}}{M_{da}} + \frac{C_{p,H_2O}}{M_{H_2O}} * H \quad (38)$$

with:

$C_{p,ma}$ specific heat capacity of moist air (J kg^{-1} K^{-1})

$C_{p,da}$ specific heat capacity of dry air (J kg^{-1} K^{-1})

C_{p,H_2O} specific heat capacity of water vapor (J kg^{-1} K^{-1})

M_{da} molar mass of air (g mol^{-1})

M_{H_2O} molar mass of water (g mol^{-1})

H absolute humidity (g H$_2$O g^{-1} dry air)

The specific heat capacity of moist air was directly calculated on LabVIEW for each temperature point recorded in the column, using the Shomate equation for both $C_{p,da}$ and C_{p,H_2O},[224] which is described below in equation (39):

$$C_p(T) = \frac{1}{M} * [A + B * \frac{T}{1000} + C * \left(\frac{T}{1000}\right)^2 + D * \left(\frac{T}{1000}\right)^3 + E * \left(\frac{1000}{T}\right)^2] \quad (39)$$

with:

$C_p(T)$ specific heat capacity of a given compound (J mol^{-1} K^{-1})

T temperature in the column (K)

M molar mass of a given compound (g mol^{-1})

A…E   Shomate coefficients for a given compound (J mol^{-1} K^{-1})

In the case of heptane and n-propanol, the specific heat capacities of the adsorbed phases were approximated to those of the respective vapors as found in the literature.

For all the adsorbates, the energy storage density was finally calculated using the energy released during adsorption and the volume of the column considered for the TES process, as shown in equation (40):

$$ESD = \frac{E_{ads}}{V} \quad (40)$$

with:

ESD energy storage density (J m^{-3})

V volume of the adsorption column (m^3)

7.4. Results & discussion

7.4.1. Adsorbents characterization

7.4.1.1. Chemical features

The chemical features of all materials were examined using FTIR and XPS. FTIR was carried out on powder samples, and in the case of AC, the commercial pellets were ground prior to analysis (**Figure 7.3**a). For all BN-based materials, FTIR results showed B-N and B-N-B bands at 1353 cm^{-1} and 801 cm^{-1}, respectively.[206] The shoulder around 1120 cm^{-1} indicated the presence of B-O bonds, which were also observed in XPS as shown by the estimated atomic composition in **Figure 7.3**b, derived from the XPS spectra shown in **Figure A4.1** in Appendix 4. The FTIR band around 2520 cm^{-1} present in h-BN and in p-BN(33%)/h-BN(67%) could correspond to N-C bonds,[206] but this was not certain. The spectrum of AC was harder to obtain due to the dark color of the material, but the characteristic C=C band was visible around 1570 cm^{-1}. As expected, XPS showed that AC was mainly composed of C (~94 at%) with some O-based functional groups (**Figure 7.3**b). Looking at the BN-based samples, they all contained between 51-53 at% of B and 39-41 at% of N. While p-BN contained ~1 at% of C, h-BN contained ~5 at% of C. The two mixtures were estimated to contain ~2 at% of C, which could

be linked to the accuracy of the XPS quantification method. In summary, the chemical analyses confirmed that the chemistry of all BN-based materials was very similar, as expected since two different forms of BN were mixed together.
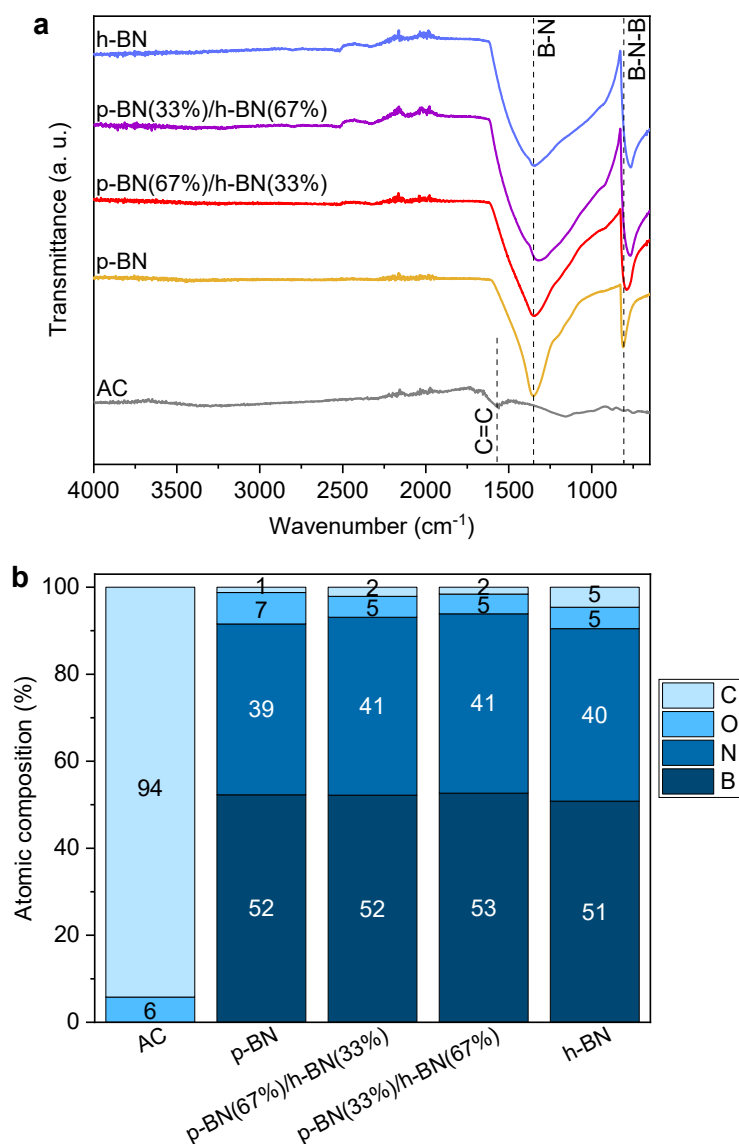
Figure 7.3 Chemical analyses of BN-based materials and activated carbon (AC). (a) FTIR spectra and (b) atomic composition derived from XPS; the XPS spectra can be found in Figure A4.1 in Appendix 4. <u>Note:</u> H atoms are not detected in XPS.

7.4.1.2. *Structural and textural features*

The structural features of the materials were surveyed using powder XRD (**Figure 7.4**). In the case of AC, the commercial pellets were ground prior to analysis. In porous BN and AC, humps

at 24° and 44° were observed, corresponding to the (002) and (100) crystallographic plans, respectively, expected for amorphous BN and AC.[19] h-BN exhibited peaks at 26°, 42°, 44° and 55°, corresponding to (002), (100), (101) and (004) plans, respectively.[225] The two mixtures of p-BN and h-BN exhibited these four peaks, with higher intensity observed in p-BN(33%)/h-BN(67%) since it had a higher content of crystalline h-BN.
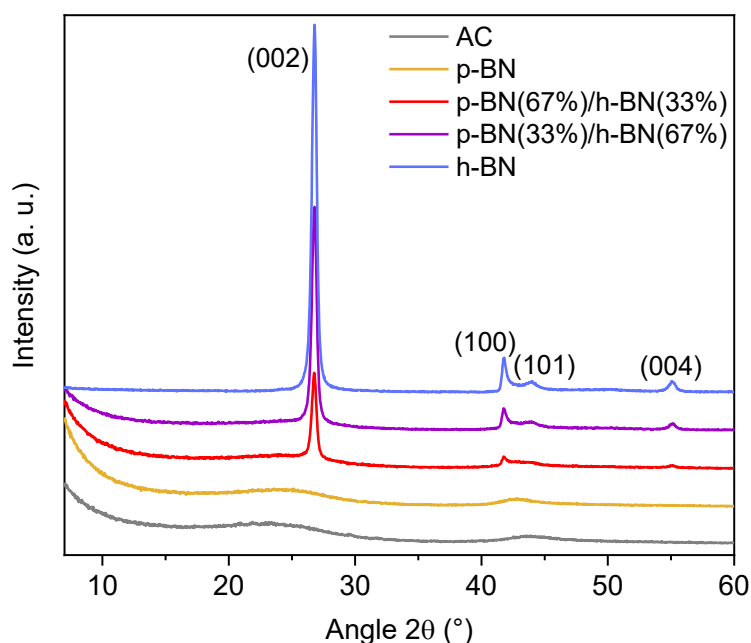
Figure 7.4 XRD patterns of activated carbon (AC) and the BN-based materials.

N_2 sorption at –196 °C and MIP were used to determine textural parameters of the pelletized adsorbents. First, BET areas were obtained through the analysis of the N_2 sorption isotherms (**Figure 7.5**a-b). p-BN and AC both had high BET areas (1297 m^2 g^{-1} and 1068 m^2 g^{-1}, respectively), but their porosities appeared different. The type of commercial AC used in this study was mainly microporous, as shown by the small difference between its micropore volume and its total pore volume obtained via N_2 sorption at –196 °C, whereas p-BN exhibited both micropores and mesopores (**Figure 7.5**b). h-BN hardly exhibited any surface area as it is a non-porous material, and any surface area would be linked to structural defects rather than pores.

Figure 7.5c was produced to check the relationship between BET area and porosity on one hand, and the composition of the p-BN/h-BN mixtures on the other hand. As expected, a linear trend was observed for each parameter as the concentration of p-BN varied, confirming a reliable preparation of the mixtures.
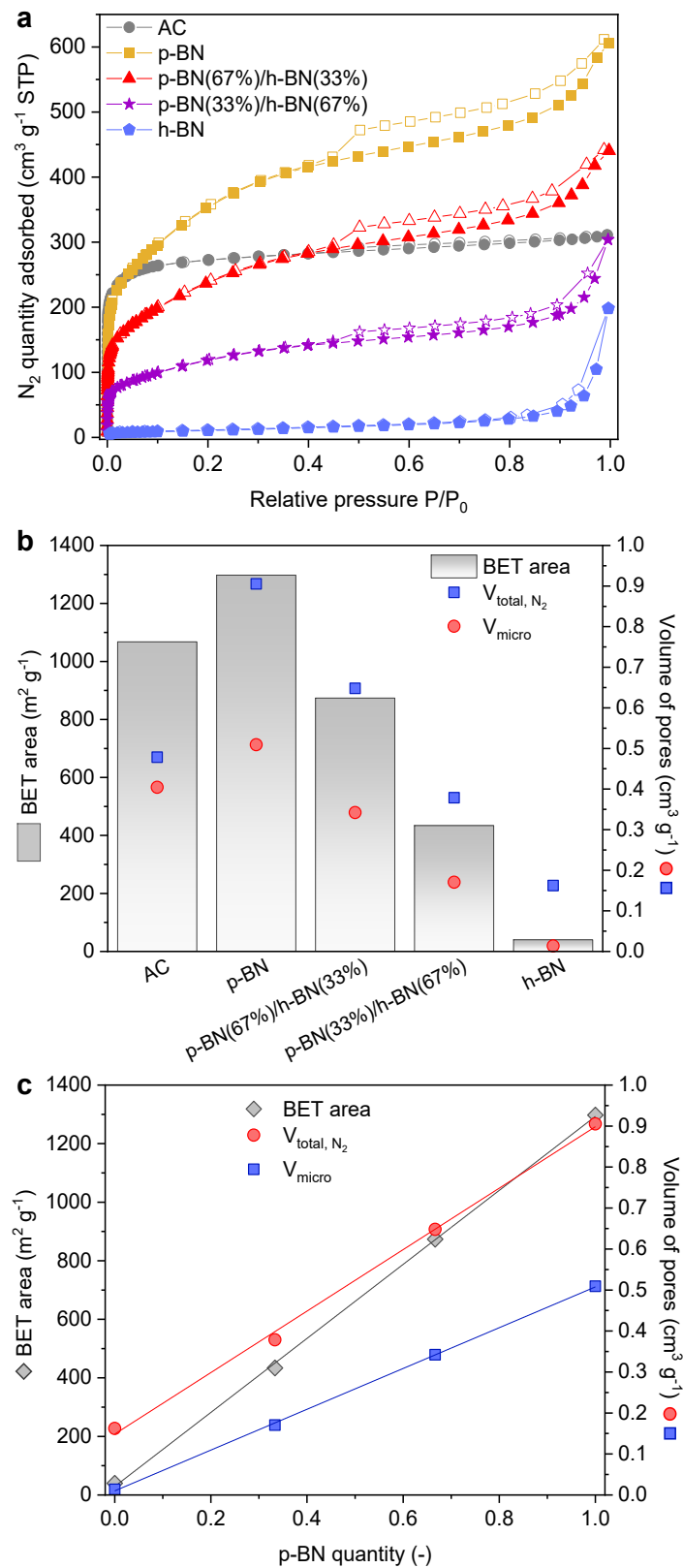
Figure 7.5 (a) N_2 sorption isotherms at –196 °C (full symbols = adsorption; open symbols = desorption) and (b) associated textural parameters for the BN-based materials and activated carbon (AC). (c) Correlation between textural parameters obtained from N_2 sorption isotherms at –196 °C and the composition of p-BN and h-BN in the mixtures.

The pore size distributions obtained from both N_2 sorption at –196 °C and MIP (**Figure A4.2** in Appendix 4) were combined to obtain the overall pore size distribution over the range 0.5 nm - 325 μm,[205] as shown in **Figure 7.6**. As explained in Chapter 6, the total volumes of pores in **Figure 7.5**b and **Figure 7.6** differ since MIP can survey larger pores than N_2 sorption at – 196 °C alone. Both techniques combined allow to get an accurate indication of the total pore volume in samples that have a very wide pore size distribution, such as porous BN. The volumes of micropores (< 2 nm) are identical in both **Figure 7.5**b and **Figure 7.6** as only the contribution from N_2 sorption is considered for this size range. AC appeared to have a certain amount of macropores above 500 nm, which could be linked to its production method forming large pores. Similarly, h-BN exhibited a relatively high volume of pores between 20-30 nm, which were likely linked to interparticle voids generated during pelletization of h-BN powder, considering the material is intrinsically non-porous. As observed in past work, p-BN showed a wide pore size distribution up to 7 μm.[8, 178] The two mixtures showed a fairly wide pore size distribution with lower pore volumes than in p-BN alone due to the presence of non-porous h-BN, and the trend between the two mixtures was consistent based on their respective contents of p-BN and h-BN (**Figure 7.6**).
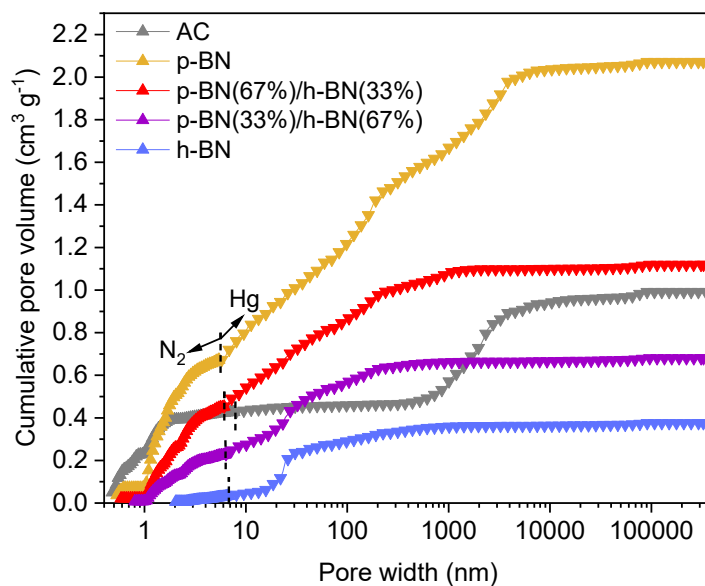
Figure 7.6 Pore size distribution based on the combination of N_2 sorption at -196 °C and mercury intrusion porosimetry. <u>Note 1:</u> the dotted lines represent the cut-off points used to combine the pore size distributions obtained from N_2 sorption isotherms and MIP (see Figure A4.2 in Appendix 4). <u>Note 2:</u> the data for p-BN was already published in our previous publication.[8]

7.4.1.3. Thermal properties

DSC allowed the calculation of the specific heat capacity for each material in a powder form (**Figure 7.7**). Each test (including the baseline and the reference material, i.e., sapphire) was run three times to remove any error and verify the repeatability of the measurements as explained in Chapter 4 (Methods). The specific heat capacity profile of AC was compared to that of another activated carbon (Maxsorb III) found in the literature,[143] which confirmed the reliability of our measurements (**Figure A4.3** in Appendix 4). However, all materials displayed similar profiles, which did not allow to draw trends nor link these results to chemical and structural properties evaluated in the previous sections.
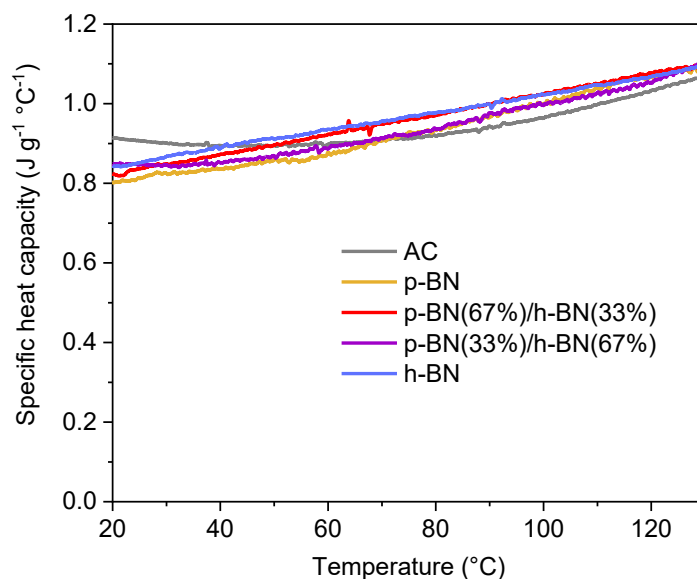
Figure 7.7 Specific heat capacity profiles measured between 20 and 130 °C for all materials.

7.4.2. Stability of adsorbent/adsorbate working pairs

7.4.2.1. *Water stability*

Activated carbon is commonly used for water filtration and exhibits great stability towards water.[226] h-BN has also shown stability in water environments, partly thanks to its high crystallinity and lack of defects. On the other hand, it was shown in Chapter 6 of this thesis that p-BN is unstable with water.[6, 8] Considering its significant hydrolytic instability at 52% relative humidity (RH) shown in Chapter 6, lower RH levels should be used during thermal energy storage testing.

7.4.2.2. *Heptane stability*

The stability of p-BN towards heptane has already been investigated in a previous study in our laboratory.[5, 113] p-BN was soaked in heptane at room temperature overnight, before being filtered, dried and regenerated at 250 °C under vacuum. N_2 sorption isotherms at −196 °C were carried out before and after exposure to heptane, and they showed no differences in BET area

and pore volume, pointing to the stability of the material. These results indicate that h-BN would also be highly stable in the presence of heptane. Finally, considering the organic chemistry of activated carbon, the material should not degrade in the presence of heptane either.

7.4.2.3. *n-propanol stability*

In the same study that looked at the stability of p-BN in heptane in our laboratory and mentioned in section 7.4.2.2, the stability with ethanol was assessed.[5, 113] p-BN was also soaked in ethanol at room temperature overnight, before being filtered, dried and regenerated at 250 °C under vacuum. N_2 sorption isotherms at –196 °C carried out after exposure to ethanol showed that hardly any degradation was observed in p-BN. Since the alcohol used in my thesis is n-propanol, it is worth checking the stability of our materials for this different alcohol.

After soaking AC, p-BN and h-BN in n-propanol, filtering and drying them (see section 7.3.2), XRD analyses and N_2 sorption isotherms at –196 °C were carried out to compare the structural and textural features before and after exposure to n-propanol (**Figure 7.8**). XRD did not show significant change in the structure of the three materials, as p-BN and AC both maintained their highly amorphous character (**Figure 7.8**a). N_2 sorption analyses showed no reduction in BET area and pore volume in h-BN and AC. In p-BN, the BET area decreased from 1297 m^2 g^{-1} to 1113 m^2 g^{-1} (**Figure 7.8**c), which remains reasonable but needs to be remembered later on.
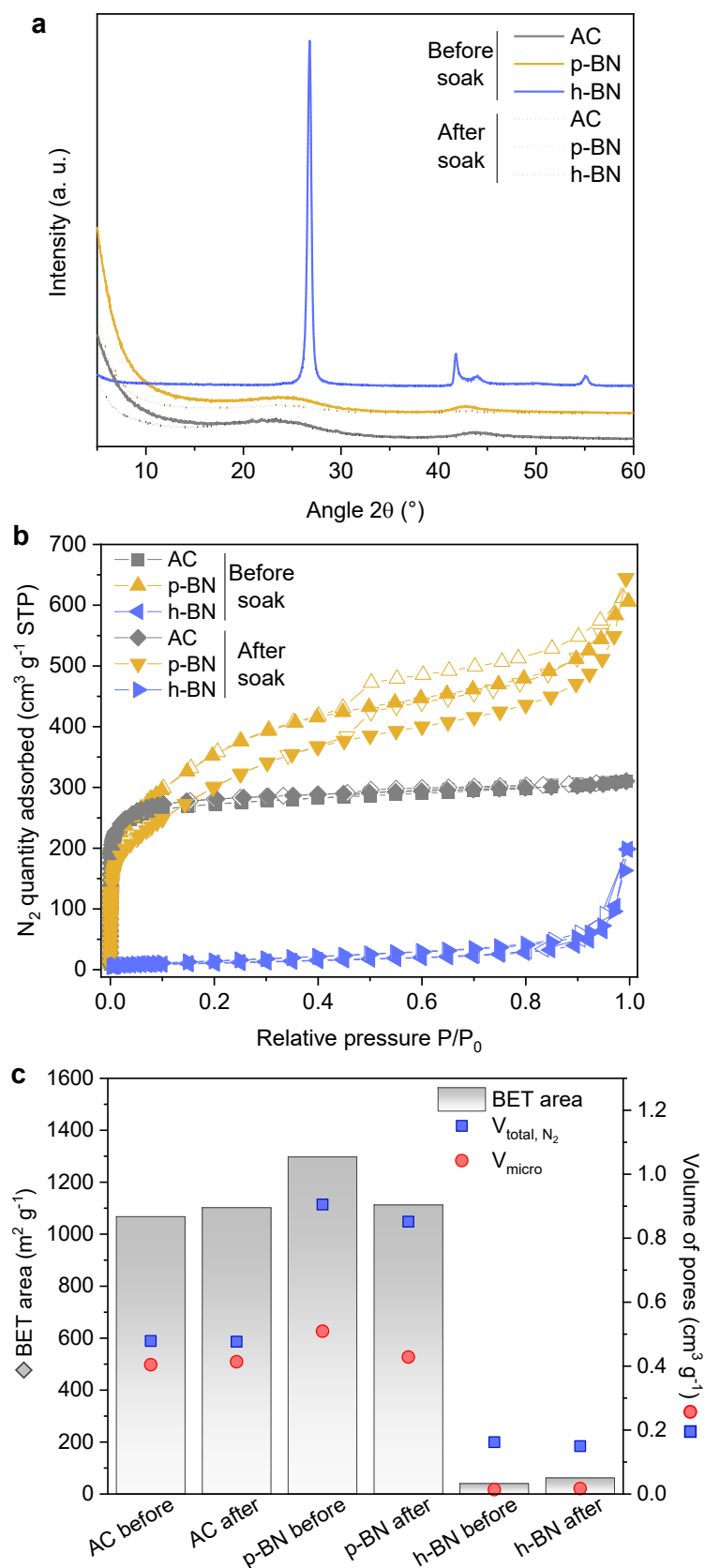
Figure 7.8 (a) XRD analyses, (b) N_2 sorption isotherms at –196 °C, and (c) associated textural parameters for activated carbon (AC), p-BN and h-BN, before and after exposure to n-propanol for 24 h at room temperature.

7.4.3. Heat of adsorption determination

7.4.3.1. Heptane adsorption

Adsorption isotherms

The adsorption isotherms measured with heptane vapor at 15 °C, 25 °C and 35°C °C for all five samples are shown in **Figure 7.9**. To verify the sorption behavior of the physical mixtures of p-BN and h-BN, heptane adsorption isotherms were calculated using the individual isotherms of p-BN and h-BN at each temperature and weighing each of them with the relevant weight percentages (67%:33% and 33%:67%). The results were in very good agreement with the experimental heptane adsorption isotherms of the mixtures and can be found in **Figure A4.4** in Appendix 4.
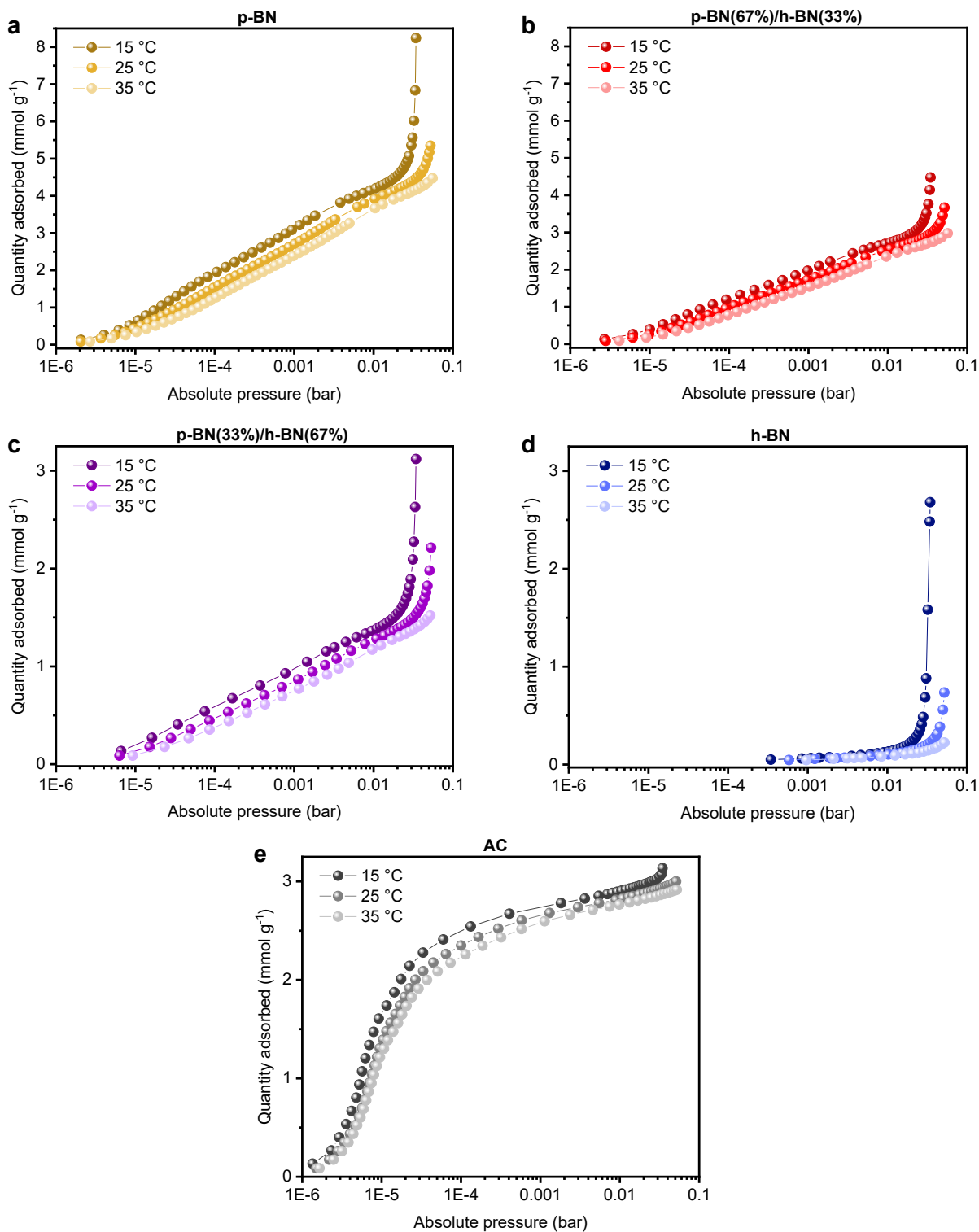
Figure 7.9 Heptane adsorption isotherms measured at 15 °C, 25 °C and 35 °C for: (a) p-BN; (b) p-BN(67%)/h-BN(33%); (c) p-BN(33%)/h-BN(67%); (d) h-BN; (e) activated carbon (AC).

Virial fitting method

Figure 7.10 shows the experimental adsorption isotherms with heptane and their fitting following a virial-type equation, as presented earlier in section 7.3.3.1. In the case of AC and h-BN, no appropriate fitting was obtained using this method, therefore results are not shown here but they can be found in **Figure A4.6** in Appendix 4. In the case of h-BN, the lack of fitting may have been due to a low number of experimental points in the low loading region. **Table 7.2** contains the associated virial coefficients for the fitting of the isotherms of p-BN and the two mixtures of p-BN and h-BN. In this method, some experimental points at higher loadings were omitted as compared to **Figure 7.9** to allow appropriate fitting.
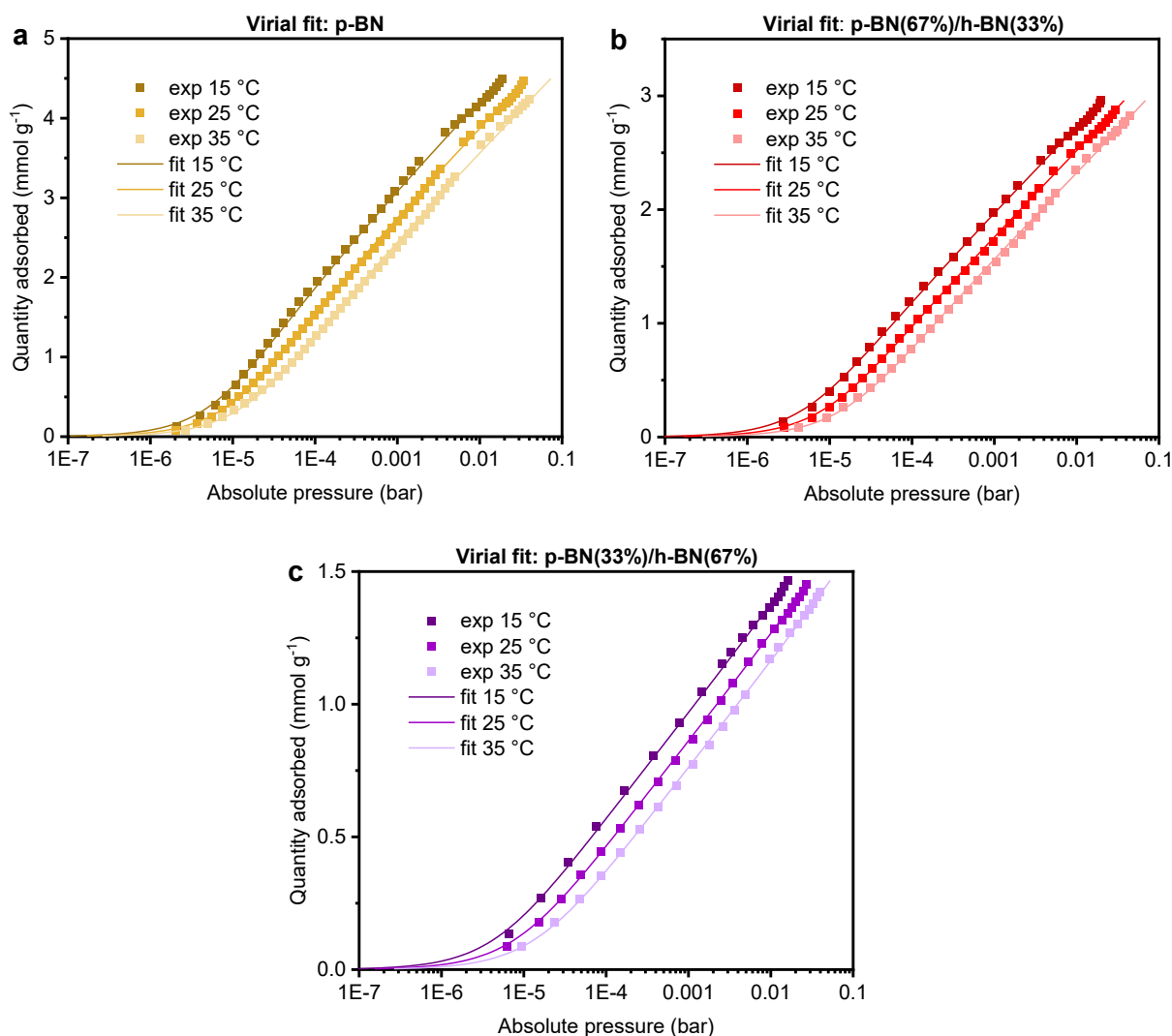
Figure 7.10 Experimental heptane adsorption isotherms (symbols) and their fits (lines) obtained using a virial-type equation for: (a) p-BN; (b) p-BN(67%)/h-BN(33%); (c) p-BN(33%)/h-BN(67%). Note: the fitting for activated carbon (AC) and h-BN was not suitable (see Figure A4.6 in Appendix 4).

Table 7.2 Virial parameters obtained with the virial analysis of heptane adsorption isotherms.

Coefficient	a_0 (K)	a_1 (K mol^{-1})	a_2 (K mol^{-2})	a_3 (K mol^{-3})	b_0 (-)	b_1 (mol^{-1})
p-BN	-3992 ± 7	-802 ± 3	98 ± 0.7	-7 ± 0.2	3 ± 0.02	3 ± 0.009
p-BN(67%)/ h-BN(33%)	-4765 ± 7	-645 ± 3	215 ± 1	-27 ± 0.6	6 ± 0.02	3 ± 0.01
p-BN(33%)/ h-BN(67%)	-4981 ± 8	-797 ± 7	680 ± 6	-193 ± 4	7 ± 0.03	5 ± 0.02

Figure 7.11 shows the experimental adsorption isotherms with heptane and their fitting following a shape-preserving interpolant or smoothing spline model, as presented earlier in section 7.3.3.2. This method generally allows a better fitting of the isotherms, since all types of isotherms could be fitted as opposed to the virial fitting method.
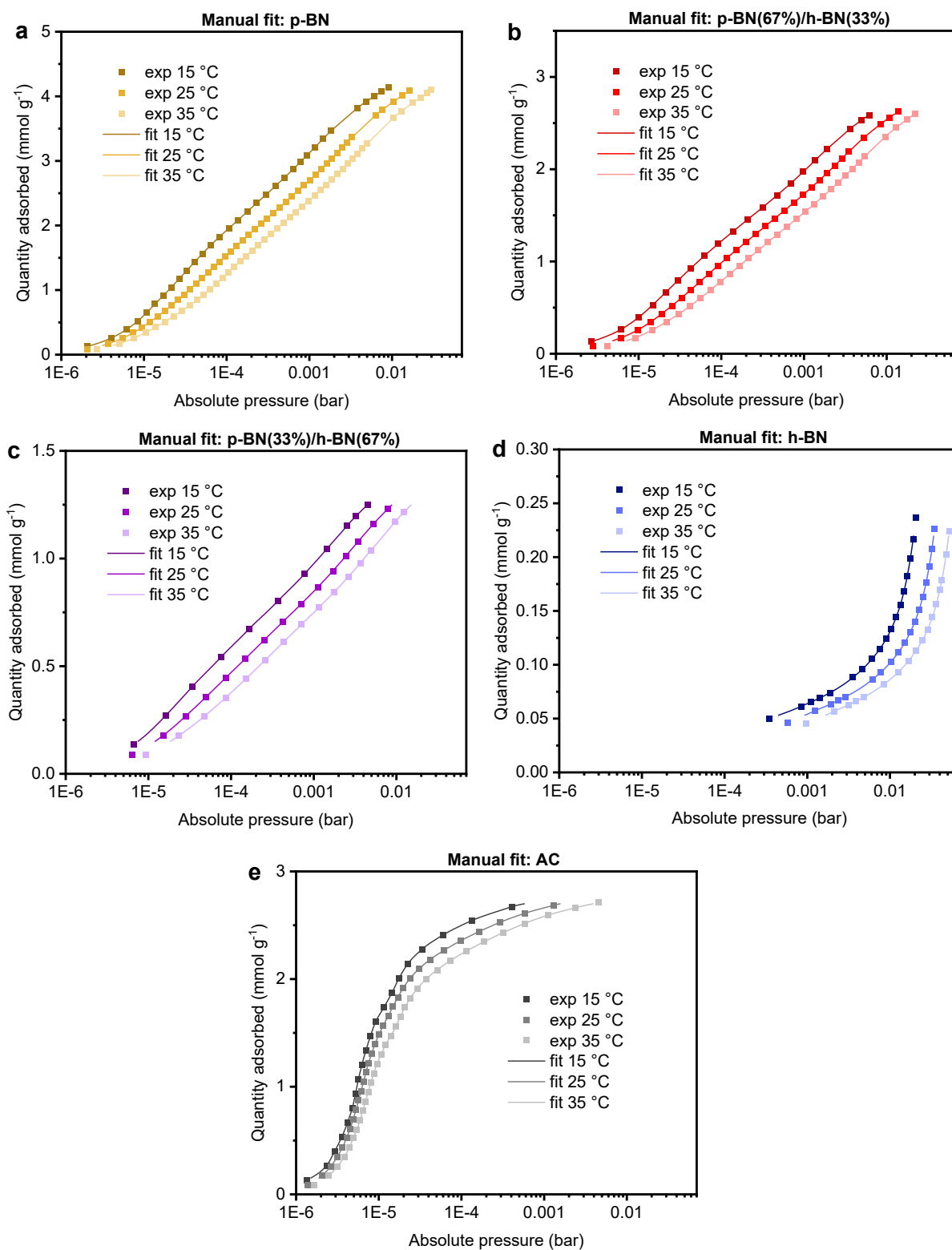
Figure 7.11 Experimental heptane adsorption isotherms and their 'manual' fits for: (a) p-BN; (b) p-BN(67%)/h-BN(33%); (c) p-BN(33%)/h-BN(67%); (d) h-BN; (e) AC.

Heats of adsorption obtained via both methods

The heat of adsorption profiles were derived following both methods (**Figure 7.12**), as explained in section 7.3.3. Discrepancies were found between the two methods when looking at p-BN and the two mixtures (the only samples analyzed via both methods), but the overall trend was similar. At low loading, the higher the content of p-BN, the lower the heat of adsorption. At higher loading, this trend seemed to inverse, and one would expect the profiles to converge towards the enthalpy of vaporization of heptane, i.e., ~35 kJ mol^{-1},[227] when the adsorbate molecules mostly interact with each other and not the adsorbent anymore. It was difficult to draw any conclusion for h-BN as the loading range was very limited for this sample. Finally, AC presented a lower heat of adsorption at low loading than all the other samples, whereas the values significantly increased above 2 mmol g^{-1}. This sharp increase may be due to experimental errors and the relative shapes of the experimental isotherms at 15 °C, 25 °C and 35 °C. Each heat of adsorption profile presented in **Figure 7.12** can be found with its error bars in Appendix 4 (**Figure A4.7**, **Figure A4.8**). Overall, these results suggested a better affinity of heptane with p-BN up to ~2 mmol g^{-1}, after which point the adsorbates molecules may mainly interact with each other. The heat of adsorption is not the only parameter to predict TES performance, and it will be discussed alongside other results.
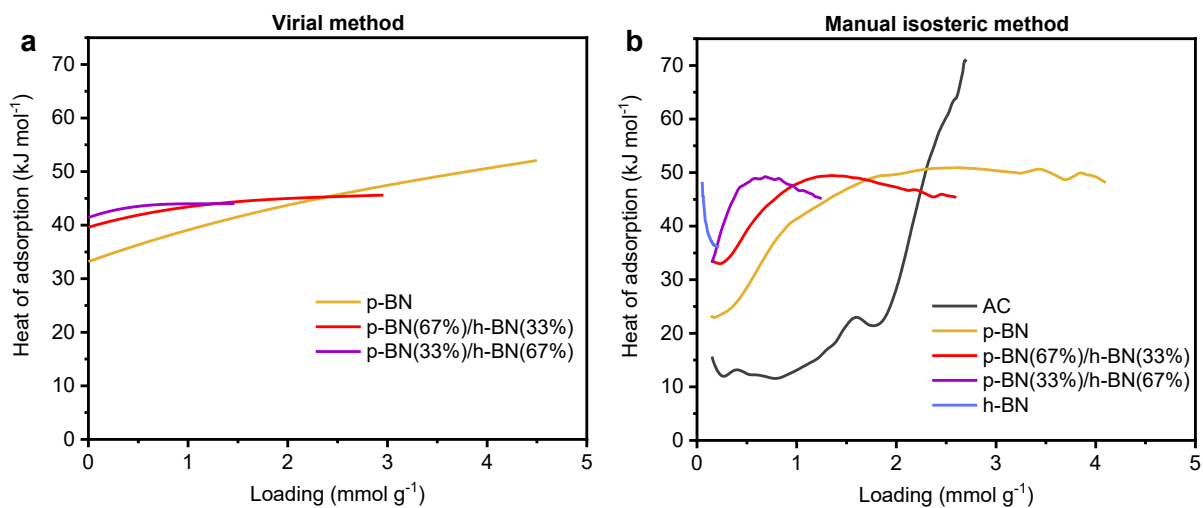
Figure 7.12 Heat of adsorption profiles (absolute values) for heptane adsorption obtained using (a) the virial method and (b) the manual isosteric method.

7.4.3.2. *n-propanol adsorption*

Adsorption isotherms

The adsorption isotherms measured with n-propanol vapor at 15 °C, 25 °C and 35°C °C for all five samples are shown in **Figure 7.13**.
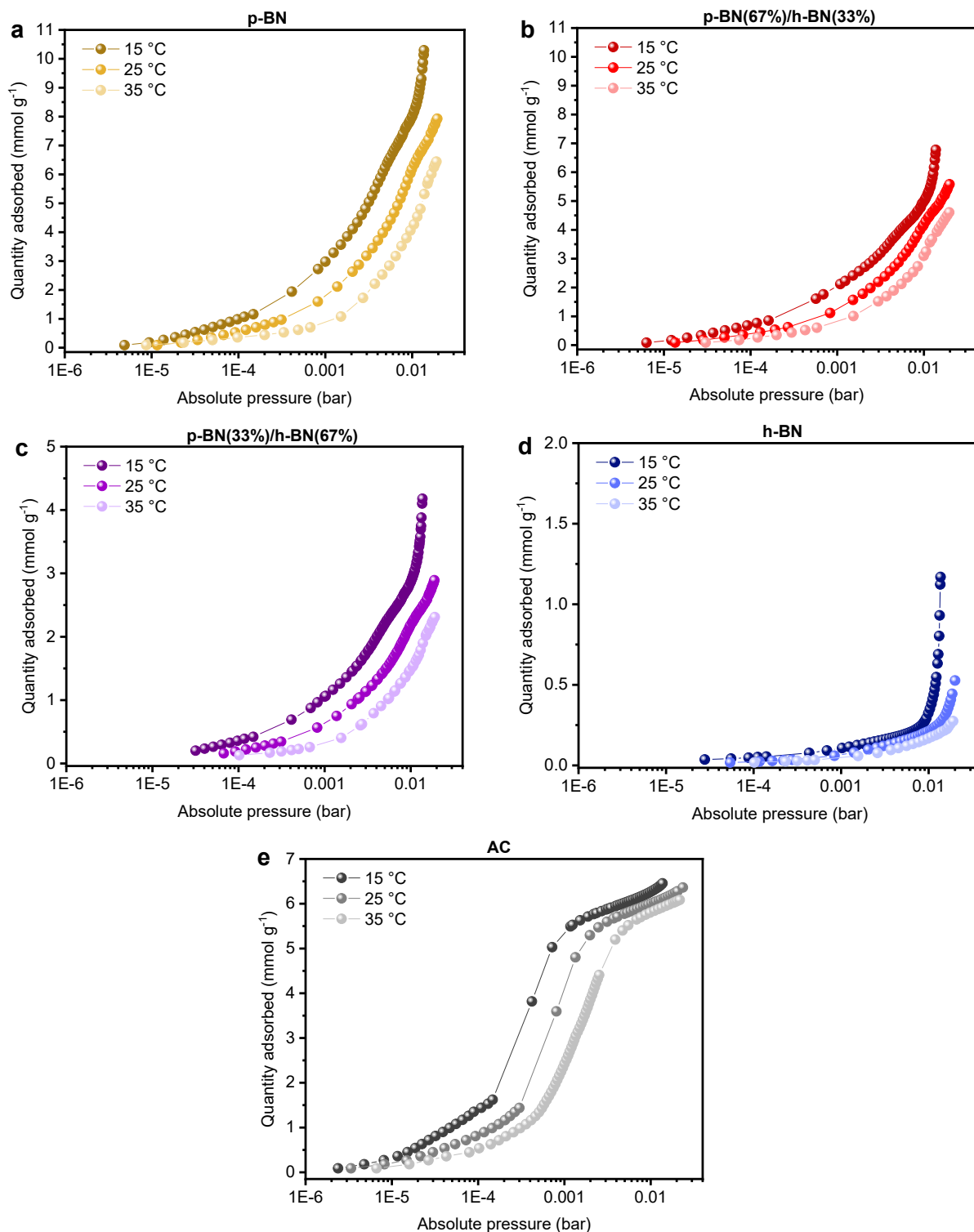
Figure 7.13 n-propanol adsorption isotherms at 15 °C, 25 °C and 35 °C for: (a) p-BN; (b) p-BN(67%)/h-BN(33%); (c) p-BN(33%)/h-BN(67%); (d) h-BN; (e) AC. <u>Note:</u> p-BN(33%) is a calculated isotherm based on the individual isotherms of p-BN and h-BN. This was validated by the comparison of calculated and experimental isotherms for heptane adsorption, as discussed in section 7.4.3.1 and shown in Figure A4.4 in Appendix 4.

Virial fitting method

Figure 7.14 shows the experimental adsorption isotherms with n-propanol and their fitting following a virial-type equation, as presented earlier in section 7.3.3.1. In the case of AC and h-BN, no appropriate fitting was obtained using this method, as observed with heptane adsorption, therefore results are not shown here but they can be found in **Figure A4.9** in Appendix 4. **Table 7.3** contains the associated virial coefficients for the fitting of the isotherms of p-BN and the two mixtures of p-BN and h-BN. In this method, some experimental points at higher loadings were omitted as compared to **Figure 7.13** to allow appropriate fitting.
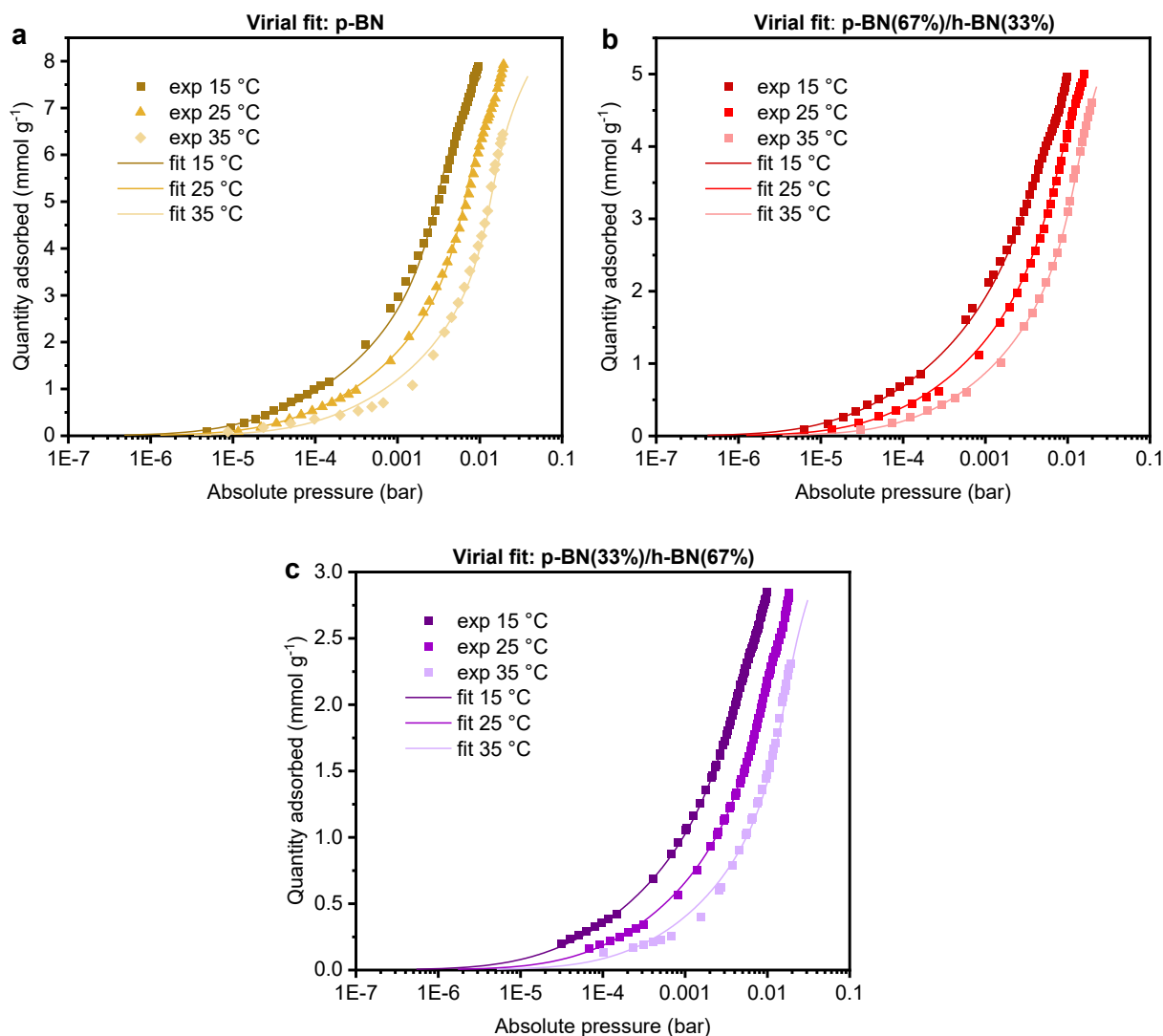
Figure 7.14 Experimental n-propanol adsorption isotherms (symbols) and their fits (lines) obtained using a virial-type equation for: (a) p-BN; (b) p-BN(67%)/h-BN(33%); (c) p-BN(33%)/h-BN(67%). <u>Note:</u> the fitting for activated carbon (AC) and h-BN was not suitable (see Figure A4.9 in Appendix 4).

Table 7.3 Virial parameters obtained with the virial analysis of n-propanol adsorption isotherms.

| Coefficient	a_0 (K)	a_1 (K mol^{-1})	a_2 (K mol^{-2})	a_3 (K mol^{-3})	b_0 (-)	b_1 (mol^{-1})
p-BN	-8656 ± 18	684 ± 4	-88 ± 0.6	6 ± 0.1	20 ± 0.06	-0.8 ± 0.01
p-BN(67%)/ h-BN(33%)	-9312 ± 7	1537 ± 2	-147 ± 0.6	14 ± 0.1	22 ± 0.02	-3 ± 0.008
p-BN(33%)/ h-BN(67%)	-9998 ± 8	2529 ± 4	-469 ± 2	82 ± 0.8	25 ± 0.03	-5 ± 0.01

Manual isosteric method

Figure 7.15 shows the experimental adsorption isotherms with n-propanol and their fitting following a shape-preserving interpolant or smoothing spline model, as presented earlier in section 7.3.3.2. As observed with heptane adsorption, this method allows a better fitting of the isotherms, so all the isotherms could be fitted.
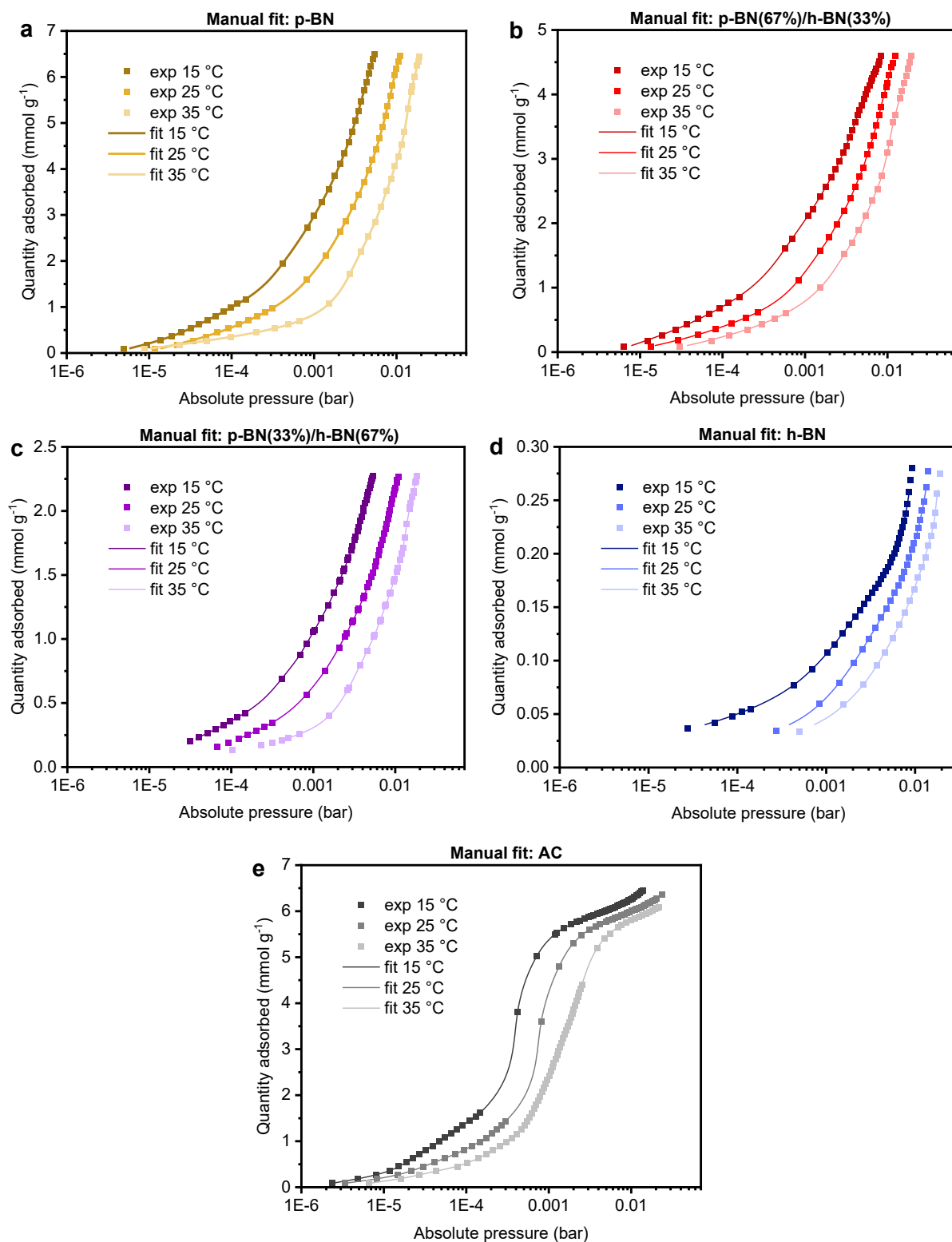
Figure 7.15 Experimental n-propanol adsorption isotherms and their 'manual' fits for: (a) p-BN; (b) p-BN(67%)/h-BN(33%); (c) p-BN(33%)/h-BN(67%); (d) h-BN; (e) AC.

Heats of adsorption obtained via both methods

The heat of adsorption profiles were derived following both methods (**Figure 7.16**), as explained in section 7.3.3. As observed in the case of heptane adsorption, discrepancies were found between the two derivation methods when looking at p-BN and the two mixtures, but the overall trend was similar. At low loading, the higher the content of p-BN, the lower the heat of adsorption. At higher loading (> 1 mmol g^{-1}), this trend seemed to inverse, and one would expect the profiles to converge towards the heat of vaporization of n-propanol, i.e., ~47 kJ mol^{-1},[228] when the adsorbate molecules mostly interact with each other. This was observed in the case of p-BN and AC, but the other materials had lower uptakes, making this observation difficult. In particular, the loading range was very limited for h-BN due its low porosity. Each heat of adsorption profile can be found with its error bars in Appendix 4 (**Figure A4.10** and **Figure A4.11**). As mentioned previously, the heat of adsorption is not the only parameter to predict TES performance, and it will be discussed alongside other results.
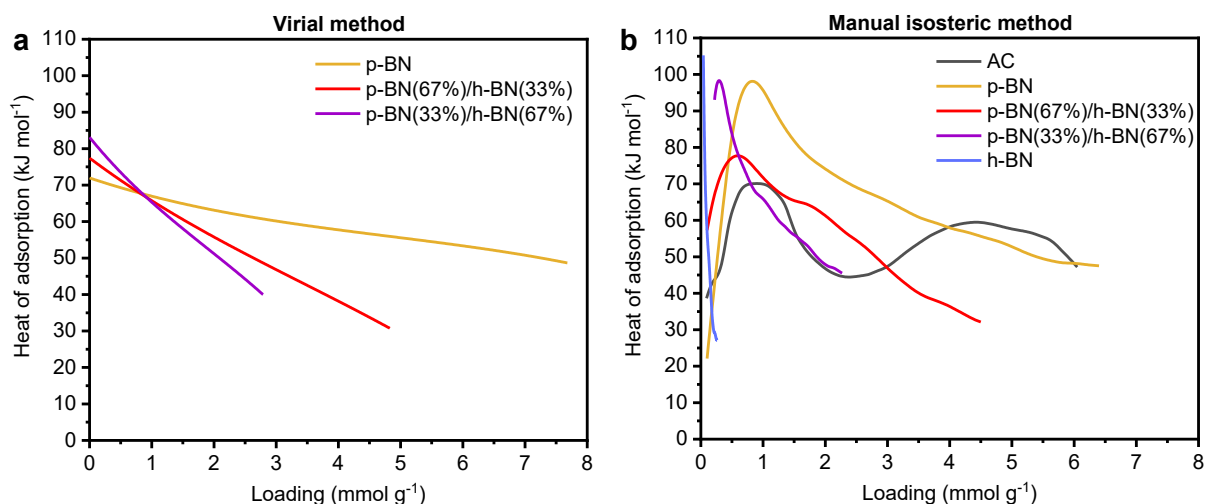

Figure 7.16 Heat of adsorption profiles (absolute values) for n-propanol adsorption obtained using (a) the virial method and (b) the manual isosteric method.

7.4.3.3. *Heat of adsorption at zero loading*

Another parameter worth investigating is the heat of adsorption at zero coverage, which corresponds to the adsorption of the first few molecules onto the adsorbent ($n \to 0$). This is a good indication of the energy exchanged between the adsorbent and the adsorbate, rather than the mutual interactions of the adsorbate molecules at higher loading. **Figure 7.17** shows the heats of adsorption at zero coverage for each material with heptane and n-propanol, following the two derivation methods ('virial' and 'manual', see sections 7.3.3.1 and 7.3.3.2). The plots generated to derive these values can be found in Appendix 4 (heptane: **Figure A4.12** and **Figure A4.13**; n-propanol: **Figure A4.14** and **Figure A4.15**). AC and h-BN only have values obtained from the manual derivation method as no appropriate fits could be obtained using the virial fitting method.
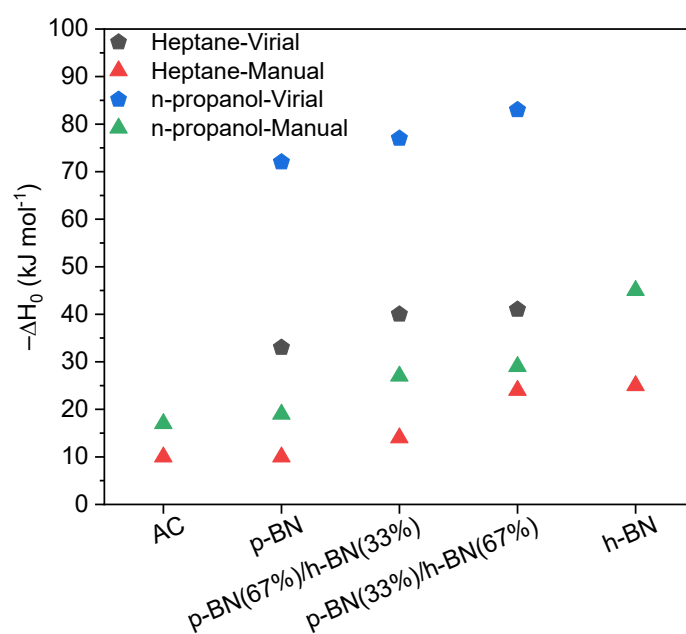
Figure 7.17 Heat of adsorption near zero coverage (loading $n \to 0$) calculated using the virial method and the manual isosteric method for both heptane and n-propanol adsorption.

For both heptane and n-propanol, I observed an overall increase in heat of adsorption at zero coverage as the content of p-BN decreased. AC shared similar values as p-BN with both

adsorbates. Comparing the heptane and n-propanol adsorbates, the latter exhibited higher heats of adsorption at zero coverage for each material, via either derivation method. In the case of BN-based materials, this was likely due to the affinity with OH groups in the alcohol as opposed to purely organic heptane, considering the presence of OH groups in p-BN and h-BN. To explain the higher affinity of AC with n-propanol rather than heptane, which may not seem intuitive, one could assume that the content of oxygen in AC (~6 at% as seen previously in **Figure 7.3**b) enhanced favorable interactions with the alcohol.

7.4.4. Breakthrough and temperature profiles

7.4.4.1. Experimental results: water TES

The experimental TES set-up at the University of Ottawa allowed the obtention of the transient temperature profiles and the breakthrough curves of water vapor during adsorption at 30% RH with an inlet flow of 4 L min^{-1} (**Figure 7.18**). The three repeats of each cycle can be found in **Figure A4.16** and **Figure A4.17** in Appendix 4, whereas only one cycle is shown below for clarity purpose.
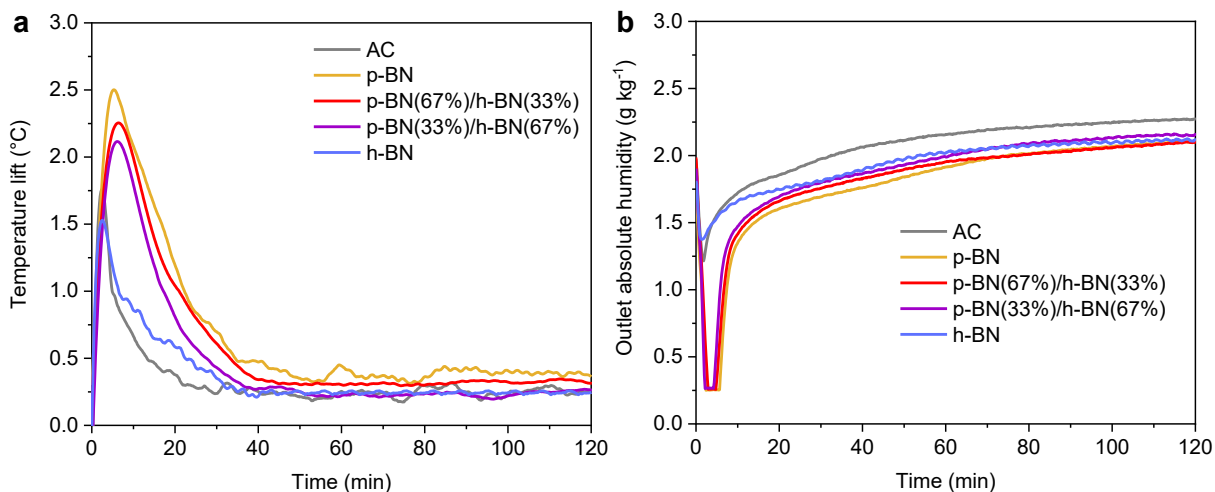
Figure 7.18 (a) Experimental temperature profiles and (b) breakthrough curves recorded for water TES at 30% RH and an inlet flow of moist air $Q = 4$ L min^{-1}.

The maximum temperature lift, which depends on both the temperature increase and the duration of the lift, is key to determine the performance of a TES process.[133] A higher/wider temperature lift implies a higher amount of heat that can be stored in the TES system. In the case of these experiments, the RH level that could be used was limited by the stability of p-BN towards humidity (see Chapter 6). Therefore, the maximum water uptake achievable was limited, leading to low temperature increases during adsorption and relatively fast breakthrough behaviors (**Figure 7.18**). It is worth noting that the flow rate used with the set-up was quite high and likely impacted on the breakthrough results. The AC sample, despite being porous (**Figure 7.5**, **Figure 7.6**), exhibited a similar behavior to non-porous h-BN. This can be explained by the fact that AC is highly hydrophobic since it is mainly composed of carbon (as seen in XPS in **Figure 7.3**b). Looking at the BN mixtures, the trend observed corresponded to the varying quantities of p-BN and h-BN as expected: the higher the content of p-BN, the higher/wider the temperature lift. However, a linear trend did not obviously appear as the content of p-BN decreased in the samples. The calculation of the energy density in section 7.4.5 will provide further information on the relative performance of each material in water TES at 30% RH.

The adsorbent parameters used in the mathematical model for heptane and n-propanol sorption are presented in **Table 7.4** below. The heat capacities were measured using DSC (**Figure 7.7**), the particle voidage values were calculated from the MIP analyses (**Figure 7.6**), and the bed densities were measured as explained in section 7.3.1. As the work in this chapter was a preliminary study, we used a column void fraction of 0.37 describing randomly-packed spheres for simplicity purpose, but this would not perfectly represent our system as my samples were crushed and sieved, thus were not perfectly spherical. The intra-pellet tortuosity was assumed based on reference [211].

Table 7.4 Parameters for each material used as inputs to the model with both adsorbates, heptane and n-propanol.

Adsorbent parameters	Unit	AC	p-BN	p-BN(67%)/ h-BN(33%)	p-BN(33%)/ h-BN(67%)	h-BN
Heat capacity	$J\ kg^{-1}\ K^{-1}$	901	825	849	846	868
Particle voidage	-	0.642	0.856	0.836	0.652	0.443
Bed density of packed column	$kg\ m^{-3}$	356	214	290	456	647
Column void fraction	-	0.37	0.37	0.37	0.37	0.37
Intra-pellet tortuosity	-	3	3	3	3	3

Each set of heptane and n-propanol adsorption isotherms were fitted to a relevant model to input the parameters into the MATLAB model (BN-based materials in **Table 7.5**, AC in **Table 7.6**). As explained in section 7.3.4.2, a dual-site Langmuir (DSL) model was used as a first approximation to describe the isotherms of the BN-based samples (fitted isotherms in **Figure A4.18** and **Figure A4.19** in Appendix 4). For activated carbon (AC), a model introduced by Ng et al.[216] (referred to as 'NBSI' herein) was used to describe the multi-step heptane and n-

propanol adsorption isotherms (fitted isotherms in **Figure A4.20** in Appendix 4). The equations corresponding to the models can also be found in Appendix 4.

Table 7.5 Dual-site Langmuir (DSL) parameters for the heptane and n-propanol adsorption isotherms with the BN-based samples obtained from fitting the relevant isotherm model to the data from Figure 7.9 and Figure 7.13.

Parameters	Unit	p-BN	p-BN(67%)/ h-BN(33%)	p-BN(33%)/ h-BN(67%)	h-BN
DSL model – Heptane					
$q_{s,1}$	mol kg^{-1}	2.265	1.389	0.692	0.058
$b_{0,1}$	bar^{-1}	1.48×10^{-6}	1.00×10^{-5}	1.00×10^{-5}	5.46×10^{-6}
$-\Delta U_1$	kJ mol^{-1}	48.271	53.335	53.143	51.203
$q_{s,2}$	mol kg^{-1}	2.114	1.525	0.804	0.142
$b_{0,2}$	bar^{-1}	1.00×10^{-5}	4.18×10^{-6}	4.61×10^{-6}	2.53×10^{-6}
$-\Delta U_2$	kJ mol^{-1}	53.527	45.198	44.515	41.378
DSL model – n-propanol					
$q_{s,1}$	mol kg^{-1}	10.000	7.574	3.858	0.373
$b_{0,1}$	bar^{-1}	4.0×10^{-8}	9.22×10^{-8}	2.34×10^{-8}	1.00×10^{-5}
$-\Delta U_1$	kJ mol^{-1}	53.989	51.214	54.541	38.755
$q_{s,2}$	mol kg^{-1}	0.778	0.683	0.380	0.068
$b_{0,2}$	bar^{-1}	1.41×10^{-14}	1.85×10^{-14}	3.06×10^{-14}	6.67×10^{-14}
$-\Delta U_2$	kJ mol^{-1}	101.902	99.757	98.439	96.050

Table 7.6 'NBSI' parameters for the heptane and n-propanol adsorption isotherms with activated carbon (AC) obtained from fitting the relevant isotherm model to the data from Figure 7.9 and Figure 7.13.

'NBSI' model parameters	Unit	AC/heptane	AC/n-propanol
n_{sat}	mol kg^{-1}	3.485	6.489
α_1	-	0.211	0.578
$ln(b_{0,1})$	-	–3.552	–1.413
$\varepsilon_{0,1}$	kJ mol^{-1}	25.619	13.061
m_1	kJ mol^{-1}	2.747	3.571
α_2	-	0.553	0.152
$ln(b_{0,2})$	-	20.383	14.061
$\varepsilon_{0,2}$	kJ mol^{-1}	–28.050	–25.480
m_2	kJ mol^{-1}	1.192	0.563
α_3	-	0.236	0.270
$ln(b_{0,3})$	-	–7.886	–5.321
$\varepsilon_{0,3}$	kJ mol^{-1}	18.138	21.827
m_3	kJ mol^{-1}	4.462	0.628

Since the adsorption isotherms of activated carbon were not fitted to a DSL model (i.e., not returning ΔU values), we estimated the heats of adsorption with heptane and n-propanol to input in the model leading to the breakthrough curves and temperature profiles. We used values based on the manual isosteric determination of the heat of adsorption, as values were not obtained using the virial equation for activated carbon. The values used were 70 kJ mol^{-1} for activated carbon/heptane (**Figure 7.12**), and 50 kJ mol^{-1} for activated carbon/n-propanol (**Figure 7.16**).

Two sets of sensitivity analysis were carried out using MATLAB to determine the impact of the outer and inner heat transfer coefficients h_{out} and h_{in} on the modeled results, namely the outlet mole fraction of heptane or n-propanol y_{out}, the internal temperature at the thermocouple (assumed half-way through the column) T_{tc}, and the outlet flow rate of heptane or n-propanol f_{out} (**Figure 7.19** and **Figure 7.20**). To this aim, p-BN/heptane and p-BN/n-propanol were considered as adsorbent/adsorbate working pairs, and all parameters were maintained constant apart from one heat transfer coefficient at a time. A flowrate of 200 mL min^{-1} was considered. Results of the sensitivity analyses showed that the outer heat transfer coefficient hardly had any impact on the outputs (**Figure 7.19**), whereas the inner heat transfer coefficient changed the internal temperature profiles, T_{tc} (**Figure 7.20**). This needs to be considered when examining the modeled results for each working pair, as well as the energy storage density values estimated later on. For each material, a value of 35.23 W m^{-2} K^{-1} was used for the inner heat transfer coefficient as a first estimate, based on the study of Ward and Pini when using a flowrate of 200 mL min^{-1}.[211]
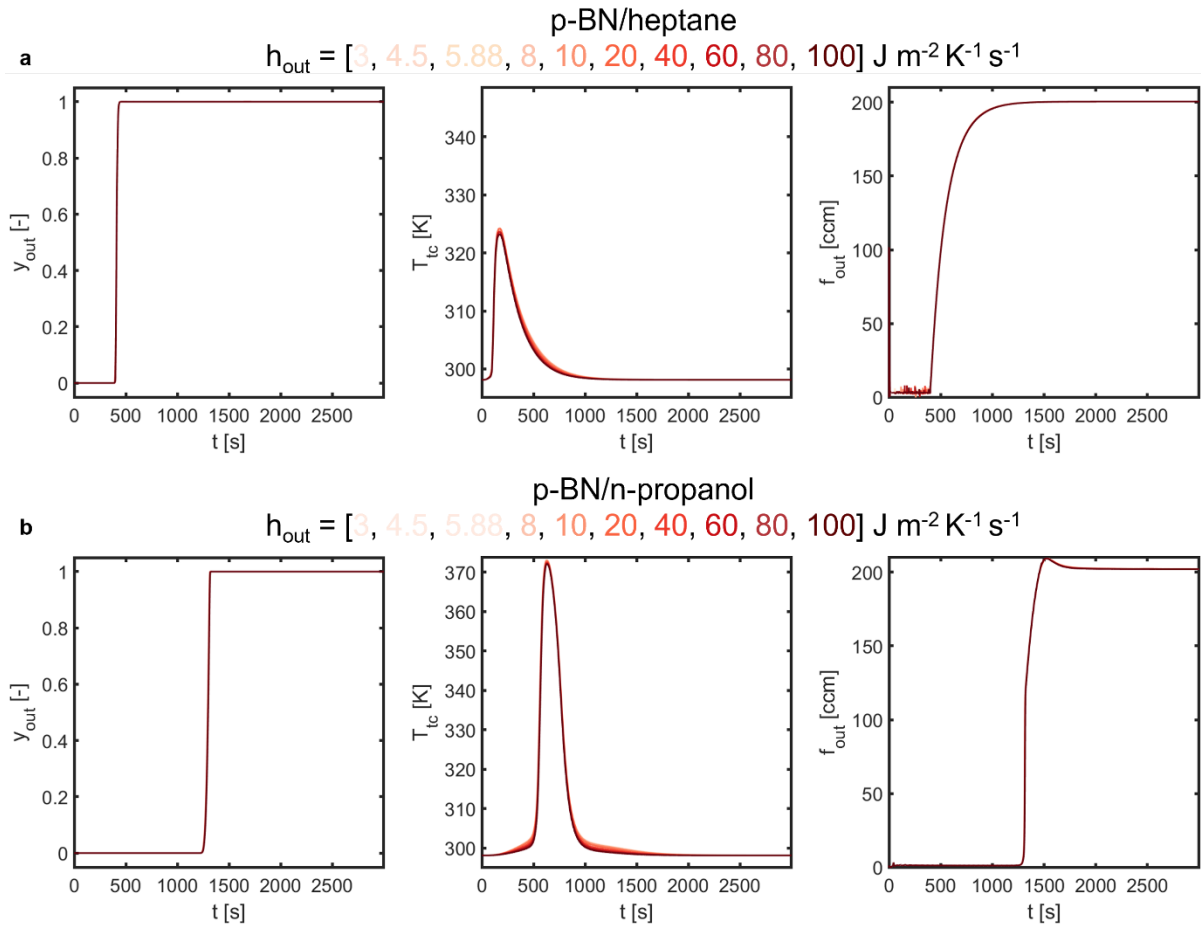
Figure 7.19 Sensitivity analysis for the outer heat transfer coefficient h_{out} in the case of: (a) heptane and (b) n-propanol adsorption on p-BN. The profiles obtained correspond to (from left to right): y_{out}, mole fraction of heptane or n-propanol at the outlet of the column; T_{tc}, internal temperature at the thermocouple (half-way through the column); f_{out}, flow rate of heptane or n-propanol at the outlet.
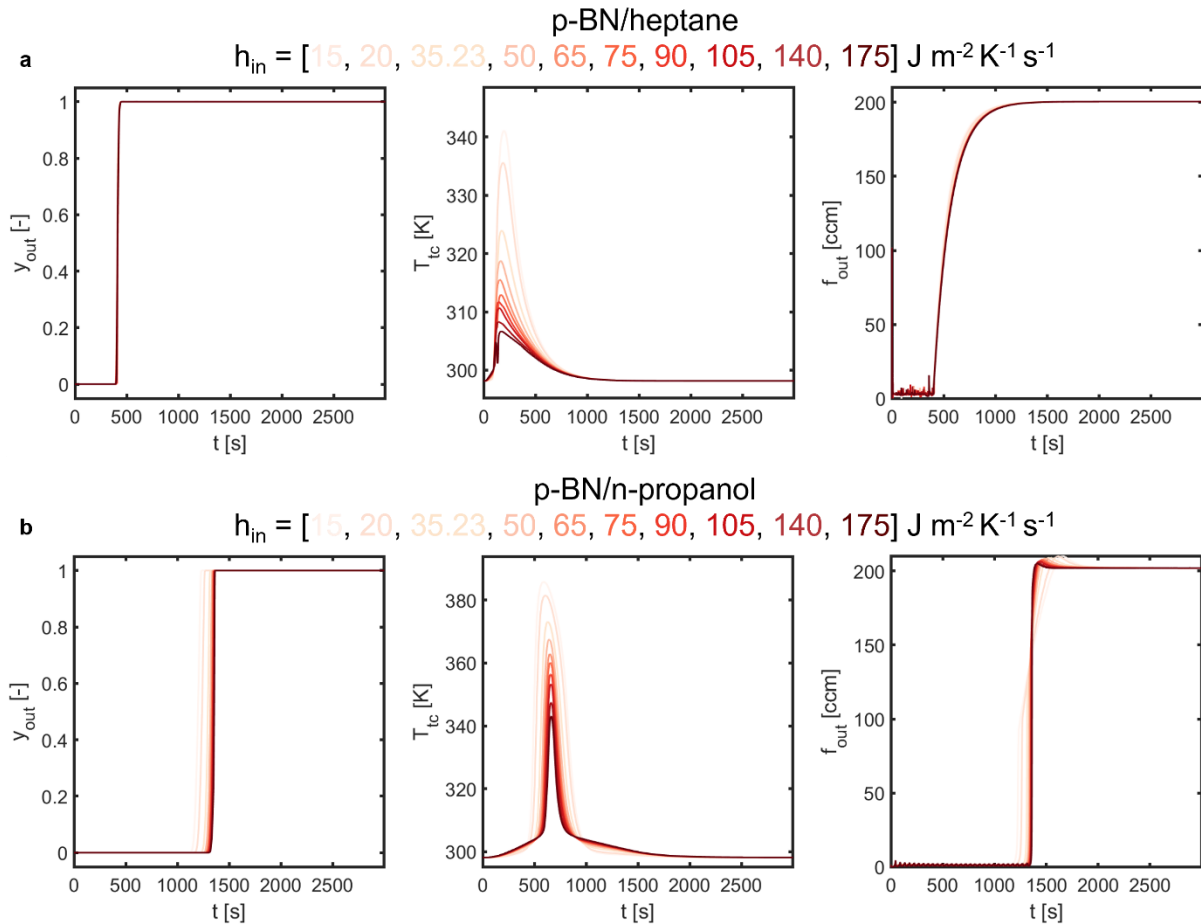
Figure 7.20 Sensitivity analysis for the inner heat transfer coefficient h_{in} in the case of: (a) heptane and (b) n-propanol adsorption on p-BN. The profiles obtained correspond to (from left to right): y_{out}, mole fraction of heptane or n-propanol at the outlet of the column; T_{tc}, internal temperature at the thermocouple (half-way through the column); f_{out}, flow rate of heptane or n-propanol at the outlet.

The outputs of the model are presented below for each material and both adsorbates, heptane (**Figure 7.21**) and n-propanol (**Figure 7.22**). The simulation used an inlet flow rate of heptane/n-propanol of 200 mL min⁻¹ (adsorption) and 200 mL min⁻¹ of helium (desorption), and it considered an outer heat transfer coefficient of 5.88 W m⁻² K⁻¹ (section 7.3.4.2) and an inner heat transfer coefficient of 35.23 W m⁻² K⁻¹. As mentioned previously, one must bear in mind that the inner heat transfer coefficient would impact on the temperature profiles, but it would probably not change the relative order of the temperature lifts observed for each material.
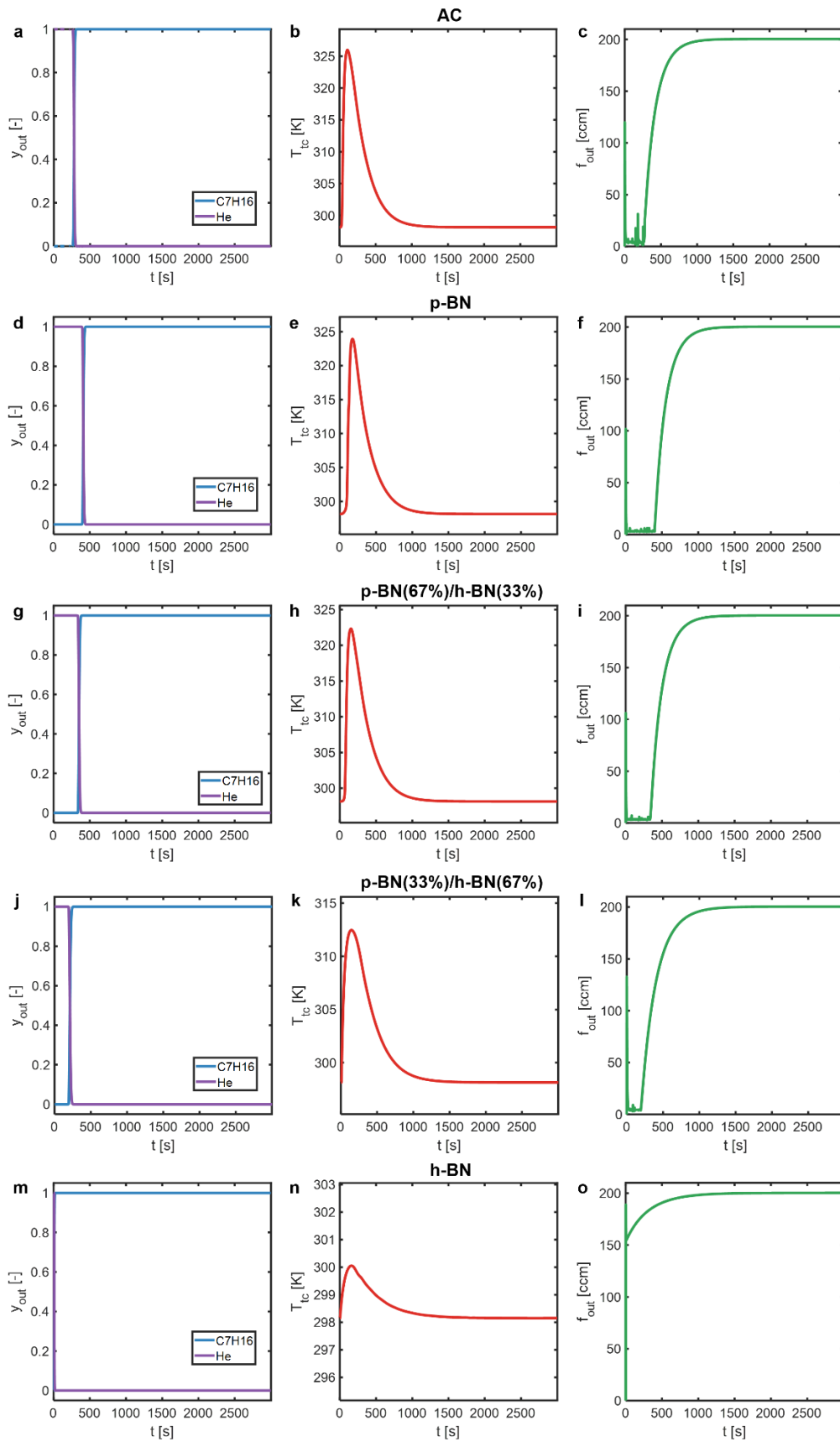
Figure 7.21 Prediction of the outlet mole fraction of heptane and helium, the internal temperature at the thermocouple and the outlet flow rate for: (a) AC, (b) p-BN, (c) p-BN(67%)/h-BN(33%), (d) p-BN(33%)/h-BN(67%) and (e) h-BN.

Looking at heptane adsorption first, I observed that as the content of p-BN decreased in the sample, the breakthrough of heptane took less time (**Figure 7.21**f, i, l, o) as adsorption was shorter, mainly due to the reduction of surface area and porosity in the materials (**Figure 7.5**, **Figure 7.6**). Similarly, the temperature lift decreased as the content of p-BN was lower (**Figure 7.21**e, h, k, n). In the case of h-BN, the temperature lift was very small, likely limited by the non-porous character of the material. When comparing p-BN and AC, both materials displayed fairly similar temperature profiles, though slightly varying in height and width. The breakthrough appeared shorter in the case of AC, which can be linked to the higher pore volume of p-BN compared to AC (**Figure 7.6**) and the higher heptane uptake with p-BN than with AC at a given pressure and temperature (**Figure 7.9**). To visualise this in a clearer way, I plotted the maximum heptane uptake as a function of the 'total' pore volume of the samples (**Figure A4.5**a in Appendix 4). The results showed that as the pore volume increased (considering all the materials), the maximum heptane loading increased. This trend was linear for the BN-based materials, but AC behaved differently, implying an effect of the chemistry of the materials. These observations were reflected in the breakthrough curves, where the least porous materials displayed faster breakthrough behaviors (**Figure 7.21**). However, the energy storage density calculation in section 7.4.5 is still needed to shed light on the relative performances of each material, since it can be difficult to estimate the area under the temperature profile with the naked eye, and the energy storage density also depends on the specific heat capacity of each material.

Now looking at n-propanol adsorption, a similar trend was observed in the temperature profiles with the content of p-BN, with the exception of p-BN and p-BN(67%)/h-BN(33%), which shared similar results (**Figure 7.22** e, h, k, n). The temperature profile of AC exhibited a very high temperature increase, but with a narrow peak compared to p-BN (**Figure 7.22**b, e).
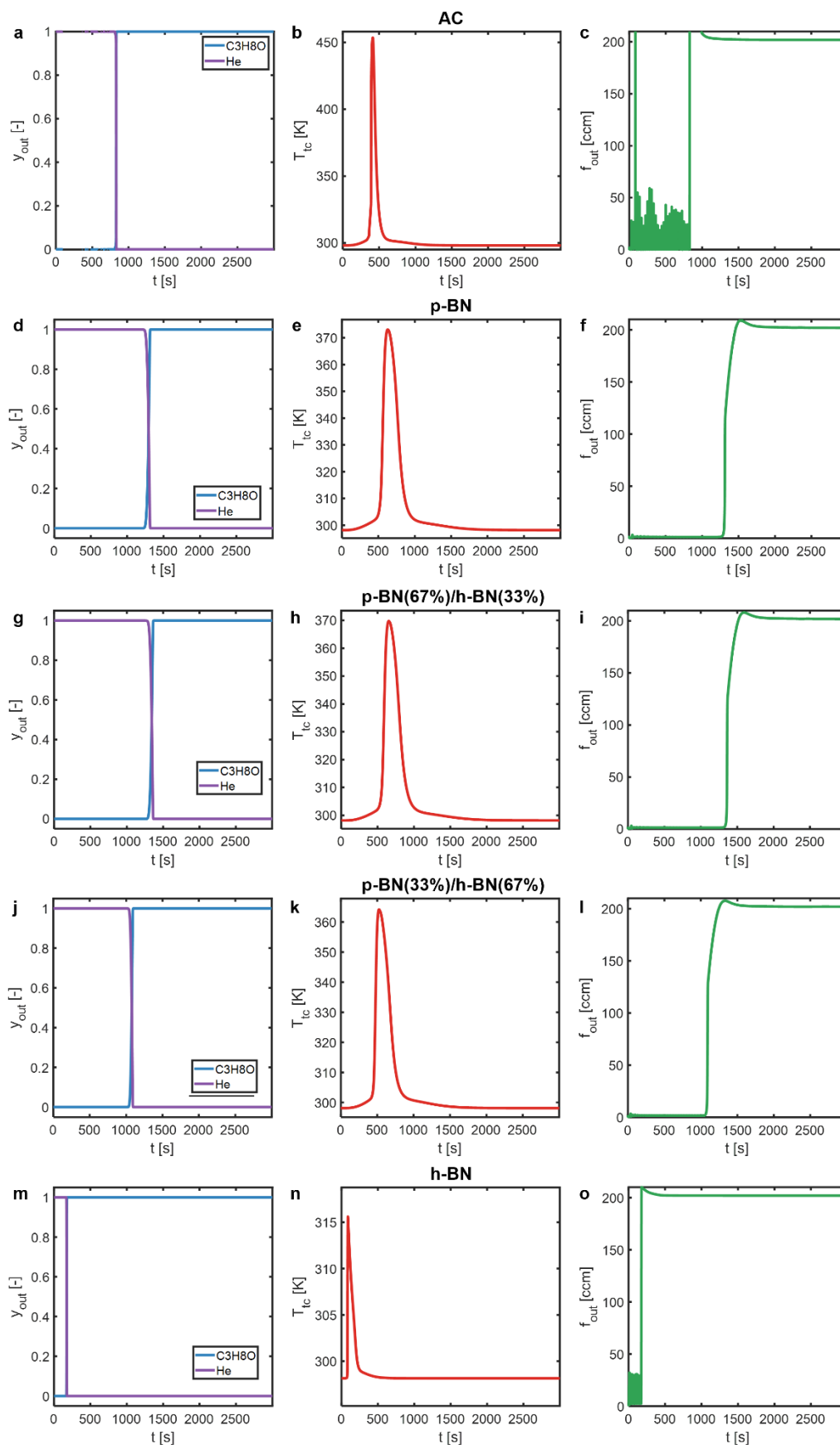
Figure 7.22 Prediction of the outlet mole fraction of n-propanol and helium, the internal temperature at the thermocouple and the outlet flow rate for: (a) AC, (b) p-BN, (c) p-BN(67%)/h-BN(33%), (d) p-BN(33%)/h-BN(67%) and (e) h-BN.

224

As a comparison between the two adsorbates, n-propanol seemed to generate much higher temperature lifts than heptane for a given sample, up to 75 °C with p-BN and 155 °C with AC, which are considered high compared to literature values.[131] This observation can first be linked to the heats of adsorption at zero coverage (**Figure 7.17**): n-propanol exhibited higher heats of adsorption at zero coverage for each material, which was linked to the affinity between BN-based materials and the alcohols via polar OH groups. In the case of AC, I mentioned earlier that the presence of O atoms in AC may also contribute to the slightly higher heat of adsorption at zero loading with n-propanol than with heptane, and thus the higher temperature lift during adsorption. Furthermore, the uptakes of n-propanol were significantly higher than those of heptane for each material (**Figure 7.9** and **Figure 7.13**), which is also key.

The calculation of the energy density in section 7.4.5 will provide further information on the relative performance of each material in water, heptane and n-propanol TES.

7.4.5. Energy storage density

For each adsorbate, the energy storage density values were calculated using formulas (8) and (40) shown in section 7.3.5. **Figure 7.23** shows the results for each experimental cycle in water TES, which allowed to assess a potential degradation of an adsorbent upon contact with water vapor. The low RH level of 30% did not lead to significant degradation of any material, but it also limited the adsorption uptake considering the low content of water available. This led to low energy storage density, even in the case of highly porous p-BN. Despite these small values, a downward trend was observed as the content of p-BN decreased in the samples as one could have expected. The breakthrough and temperature profiles obtained previously (**Figure 7.18**) showed that the materials containing at least 33wt% of p-BN were not performing as differently from one another as expected, whereas h-BN had a very low uptake of water and a very fast

breakthrough behavior. Overall, it is worth noting that such values of energy storage density are considered low and would not be viable in a larger scale TES process.
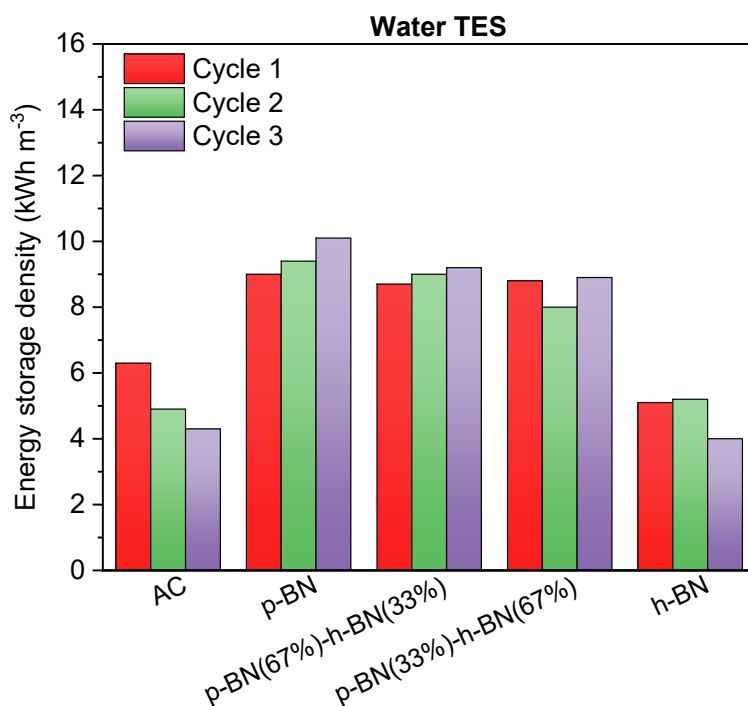
Figure 7.23 Energy storage density values obtained using the experimental temperature profiles recorded during adsorption of water (RH = 30 %; Q = 4 L min^{-1}) on the TES set-up at the University of Ottawa.

Figure 7.24 shows the energy density values estimated for each sample with both heptane and n-propanol, based on the temperature profiles modeled in **Figure 7.21** and **Figure 7.22**. It is worth remembering that results depend on the volume of the column considered and the inlet flow rate. Herein, I considered an aluminum column and a flow rate of 200 mL min^{-1} as used in the study that initially developed the mathematical model.[211]
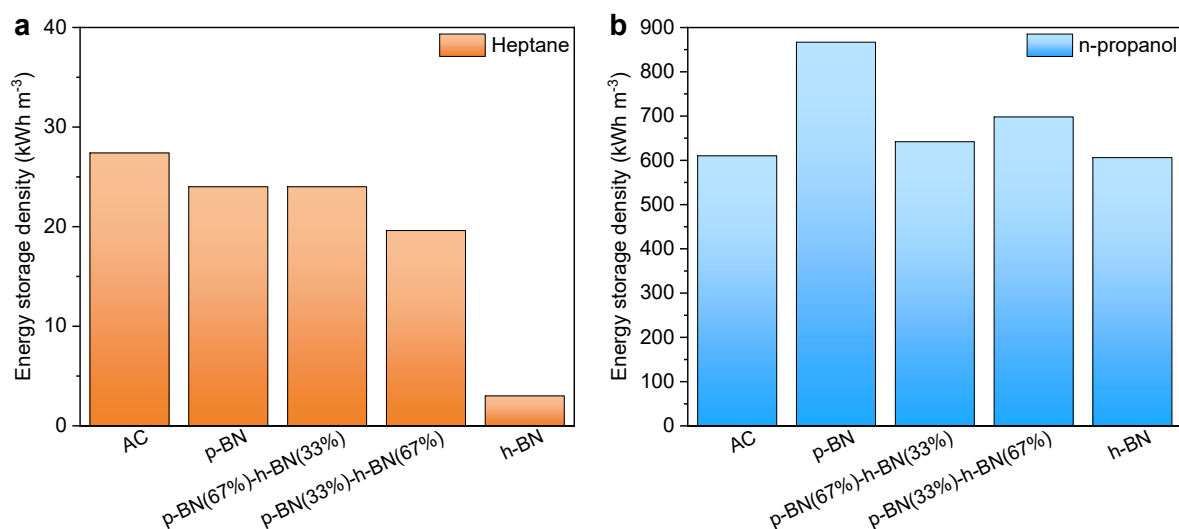
Figure 7.24 Energy storage density values obtained through the modeling of temperature profiles during adsorption of (a) heptane and (b) n-propanol.

A stark difference was observed between heptane and n-propanol TES, with significantly higher theoretical energy storage density obtained in the latter case (**Figure 7.24**). This echoed the previous analysis linking the higher heat of adsorption with n-propanol for each material (**Figure 7.12**, **Figure 7.16**). When comparing AC and p-BN, AC exhibited slightly higher energy storage density with heptane than p-BN, likely due to greater affinity with a purely organic adsorbate. In the case of n-propanol, p-BN performed better, potentially due to the hydrophilicity of p-BN and its affinity with OH groups. These observations can be linked to the heat of adsorption at zero coverage, since it was higher for AC/heptane and p-BN/n-propanol, compared to p-BN/heptane and AC/n-propanol, respectively (**Figure 7.17**). As a comparison with literature values reaching up to 556 kWh m^{-3} experimentally,[135] or ~1250 kWh m^{-3} via predictions,[125] our results seemed promising. However, it is important to remember that some parameters had to be estimated for our model, including the inner heat transfer coefficient, which may vary depending on the sample.

Furthermore, as observed in the experimental water TES results, the mixtures of p-BN and h-BN did not show significantly lower results compared to p-BN. Despite being non-porous (or

more exactly with low porosity), h-BN seems to benefit from good thermal properties, as hypothesized based on literature values of thermal conductivity for the crystalline material. These observations point towards a promising method of mixing two materials combining great chemical, textural and thermal properties, but this would need further investigation.

7.5. Conclusions

In this chapter, I assessed the potential of porous BN and other BN-based materials for thermal energy storage (TES) via adsorption. After selecting three different adsorbates (i.e., water, heptane and n-propanol), an adaptative workflow was designed to estimate the energy storage density achievable for each adsorbent/adsorbate working pair considered. In the case of water TES, experiments could be directly carried out to estimate breakthrough curves and temperature profiles, leading to the derivation of energy storage density values. For both heptane and n-propanol, equipment limitations led me to collaborate with Dr. Humera Ansari to model breakthrough curves and temperature profiles from the adsorption isotherms I had measured at different temperatures for the heat of adsorption determination. Thanks to this versatile study, I was able to provide the following answers to my research questions highlighted in Chapter 3 and related to research objective 3:

• BN-based materials showed potential in TES via adsorption, especially porous BN leading to greater energy storage density.

• Specific heat capacity was measured reliably, although the materials studied did not present significantly different values. Thermal conductivity should now be measured to understand better the performance of each adsorbent, and to estimate the inner heat transfer coefficients with more accuracy as they were shown to have great impact on the temperature lift achievable, and subsequently on the TES performance.

• After testing water, heptane and n-propanol, the alcohol appeared to be the most suitable adsorbate with BN-based materials, in particular due to high uptakes and heats of adsorption.

• The modeling of the temperature profiles appeared as a promising tool if adsorption isotherms at different temperatures (≥ 3) are available. This allows to assess the potential of an adsorbent/adsorbate working pair before testing it on a TES set-up, which may be difficult to access rapidly. Further work would be needed to validate the model in the case of heptane and n-propanol adsorption. Ideally, the model would be used with water adsorption to compare with the TES experiments carried out with water vapor, bearing in mind that this adsorbate is less than ideal given the hydrolytic instability of porous BN (see Chapter 6).

This work has opened the door to a new application using porous BN materials, owing to its tunable properties and rich chemistry. Since this study was preliminary, it would need further work to understand better if this is worth pursuing at larger scale.

CHAPTER 8: CONCLUSIONS

8.1. Summary of findings

In this thesis, I addressed the three research objectives detailed in Chapter 3:

• To investigate the formation mechanism of porous BN, which was tackled in Chapter 5;

• To enhance the hydrolytic stability of porous BN, which was studied in Chapter 6;

• To assess the potential of porous BN for adsorption-based processes, namely CO_2/N_2 separation and thermochemical energy storage, which was investigated in both Chapter 6 and Chapter 7.

In Chapter 5, I investigated the formation mechanism and the porosity development of porous BN using a synthesis parameter space leading to a highly porous material. Thanks to the preparation of various intermediates obtained at different temperatures and their subsequent characterization, I highlighted the most critical stages of this synthesis. In particular, these stages included the formation of non-porous carbon nitride as a reaction intermediate, and the onset of porosity between 700 °C and 800 °C. This work provided a better understanding of how porous BN is formed, and how and when its porosity develops, which are key aspects to consider for industrial scale-up towards adsorption-based applications. The results of this chapter have been published in the Journal of Physical and Chemistry C.[7]

In Chapter 6, I devised two surface functionalization routes for porous BN using a fluoroalkylsilane grafting agent. Both methods partially helped enhance the hydrophobicity of porous BN and improve its resistance against moisture. A decrease in porosity was also observed, meaning that the grafting method must be carefully considered to obtain a balance between hydrophobicity and porosity, depending on the application targeted. The two grafting

methods led to enhanced selectivity towards CO_2 in CO_2/N_2 separation while maintaining reasonable CO_2 uptakes. This was even more pronounced upon exposure to moisture, when the gas uptakes of all the samples decreased, but less so for the functionalized samples owing to their greater structural stability. Finally, a kinetics study highlighted three different mass transfer mechanisms in pristine porous BN and the functionalized samples. The results of this chapter have been published in Microporous and Mesoporous Materials.[8]

In Chapter 7, a different application was investigated for porous BN, namely thermal energy storage (TES) via adsorption. To understand better whether BN-based materials could be suitable adsorbents for this application, different samples were prepared using both porous and hexagonal forms of BN to obtain a range of textural and thermal properties. A selection of adsorbates (i.e., water, heptane and n-propanol) was used and I estimated the heats of adsorption for each adsorbent/adsorbate working pair, as well as energy storage density. Energy storage density was evaluated using either experimental or modeled temperature profiles depending on the adsorbate. While water and heptane did not show great results with BN-based materials, n-propanol appeared to be a highly promising adsorbate, even leading to a greater performance than with activated carbon, in theory. Further work is needed to confirm this experimentally, and a manuscript is currently in preparation to cover the results of this chapter.

Overall, my PhD has provided a greater understanding of porous BN, in particular on its formation mechanism, its hydrolytic stability and its use in adsorption-based applications. With the ultimate aim of scaling-up the synthesis of porous BN, its formation mechanism has been extensively covered and is now well understood to design a synthesis process at larger scale. In terms of hydrolytic stability, the functionalization routes used in this thesis have proven promising to improve the structural stability of porous BN materials. Although not fully satisfying considering the loss of porosity upon functionalization, the comprehensive study on

the impact of functionalization on chemistry, porosity and CO_2 adsorption kinetics constitutes valuable knowledge to pursue the effort of hydrolytic stability enhancement. The optimization of the surface functionalization methods would constitute valuable future work, as explained in section 8.2. Finally, the preliminary work on TES, beyond the traditional gas and liquid separations using porous BN, has shown potential with theoretically high energy storage density with n-propanol. The use of a previously-developed mathematical model has proven interesting and would benefit from further experimental work to validate its application to TES. All the findings contained in this thesis are highly valuable in the context of adsorption-based applications, and some could be relevant to other porous materials, for instance when looking at enhancing their hydrolytic stability or probing their potential for TES via adsorption.

8.2. Future work

While this thesis has provided advanced knowledge on porous BN, its use at larger scale would require further work in some areas that I will explain below.

Regarding the hydrolytic stability of porous BN, one can foresee ways to improve the grafting routes used in this thesis. Firstly, it would be relevant to adjust the initial concentration of alkylsilane so that both functionalization routes would lead to the same loading in the final materials, thus allowing a fairer comparison. In parallel, it may also be worth targeting a smaller concentration of alkylsilane after functionalization to have a smaller impact on the porosity of porous BN. Indeed, looking at the promising functionalization route 2 (i.e., chemical vapor deposition on porous BN pellets), a smaller loading of alkylsilane may reach a better balance between moisture stability and performance in CO_2/N_2 separation. Finally, a different alkylsilane molecule could be trialed with porous BN, but the one used in this thesis (i.e.,

trimethoxy(3,3,3-trifluoropropyl)silane) seemed promising, and I believe the options suggested above should be tested first.

When considering the use of porous BN in CO_2/N_2 separation, with or without surface functionalization, process metrics (i.e., purity and recovery) must be extracted to verify whether porous BN can compete with current benchmark adsorbents for such applications. This will allow to assess the viability of using porous BN depending on the conditions considered (e.g., temperature, pressure).

In terms of TES via adsorption, it would be key to measure the thermal conductivity of my samples to estimate the inner heat transfer coefficients with more accuracy for heptane and n-propanol adsorption. This would then provide a more reliable assessment of the performance of each adsorbent/adsorbate working pair when using the mathematical model, and hint towards a clearer link between thermal properties and energy storage density. Further work would also be needed to validate the mathematical model. For instance, we could use the model with water adsorption to compare with the water TES experiments. Another important aspect to consider is the study of adsorption kinetics, which would bring complementary information on the suitability of a given working pair. Finally, the design of a TES set-up usable with other adsorbates than water would be an interesting development to directly test working pairs, like the ones with heptane and n-propanol, or using other solvents.

REFERENCES

1.   Sholl, D. S.; Lively, R. P., Seven chemical separations to change the world. *Nature* **2016,** *532* (7600), 435-437.

2.   Jiang, X.-F.; Weng, Q.; Wang, X.-B.; Li, X.; Zhang, J.; Golberg, D.; Bando, Y., Recent Progress on Fabrications and Applications of Boron Nitride Nanomaterials: A Review. *Journal of Materials Science & Technology* **2015,** *31* (6), 589-598.

3.   Marchesini, S.; McGilvery, C. M.; Bailey, J.; Petit, C., Template-Free Synthesis of Highly Porous Boron Nitride: Insights into Pore Network Design and Impact on Gas Sorption. *ACS Nano* **2017,** *11* (10), 10003-10011.

4.   Marchesini, S.; Regoutz, A.; Payne, D.; Petit, C., Tunable porous boron nitride: Investigating its formation and its application for gas adsorption. *Microporous and Mesoporous Materials* **2017,** *243*, 154-163.

5.   Marchesini, S.; Wang, X.; Petit, C., Porous Boron Nitride Materials: Influence of Structure, Chemistry and Stability on the Adsorption of Organics. *Frontiers in Chemistry* **2019,** *7*, 160.

6.   Shankar, R.; Marchesini, S.; Petit, C., Enhanced Hydrolytic Stability of Porous Boron Nitride via the Control of Crystallinity, Porosity, and Chemical Composition. *The Journal of Physical Chemistry C* **2019,** *123* (7), 4282-4290.

7.   L'Hermitte, A.; Dawson, D. M.; Ferrer, P.; Roy, K.; Held, G.; Tian, T.; Ashbrook, S. E.; Petit, C., Formation Mechanism and Porosity Development in Porous Boron Nitride. *The Journal of Physical Chemistry C* **2021,** *125* (49), 27429–27439.

8.   L'Hermitte, A.; Azzan, H.; Yio, M. H. N.; Rajagopalan, A. K.; Danaci, D.; Hirosawa, T.; Isobe, T.; Petit, C., Effect of surface functionalization on the moisture stability and sorption properties of porous boron nitride. *Microporous and Mesoporous Materials* **2023,** *352*, 112478.

9.   Itskou, I.; L'Hermitte, A.; Marchesini, S.; Tian, T.; Petit, C., How to tailor porous boron nitride properties for applications in interfacial processes. *Accounts of Materials Research* **2023,** *4*, 143-155.

10.   Shi, Y.; Hamsen, C.; Jia, X.; Kim, K. K.; Reina, A.; Hofmann, M.; Hsu, A. L.; Zhang, K.; Li, H.; Juang, Z.-Y.; Dresselhaus, M. S.; Li, L.-J.; Kong, J., Synthesis of Few-Layer Hexagonal Boron Nitride Thin Film by Chemical Vapor Deposition. *Nano Letters* **2010,** *10* (10), 4134-4139.

11.   Olovsson, W.; Magnuson, M., Rhombohedral and Turbostratic Boron Nitride Polytypes Investigated by X-ray Absorption Spectroscopy. *The Journal of Physical Chemistry C* **2022**.

12.   Golberg, D.; Bando, Y.; Huang, Y.; Terao, T.; Mitome, M.; Tang, C.; Zhi, C., Boron Nitride Nanotubes and Nanosheets. *ACS Nano* **2010,** *4* (6), 2979-2993.

13.   Li, L. H.; Cervenka, J.; Watanabe, K.; Taniguchi, T.; Chen, Y., Strong Oxidation Resistance of Atomically Thin Boron Nitride Nanosheets. *ACS Nano* **2014,** *8* (2), 1457-1462.

14.   Brožek, V.; Hubáček, M., A contribution to the crystallochemistry of boron nitride. *Journal of Solid State Chemistry* **1992,** *100* (1), 120-129.

15.   Cofer, C. G.; Economy, J., Oxidative and hydrolytic stability of boron nitride — A new approach to improving the oxidation resistance of carbonaceous structures. *Carbon* **1995,** *33* (4), 389-395.

16.   Kim, T.-H.; Jeon, E. K.; Ko, Y.; Jang, B. Y.; Kim, B.-S.; Song, H.-K., Enlarging the d-spacing of graphite and polarizing its surface charge for driving lithium ions fast. *Journal of Materials Chemistry A* **2014,** *2* (20), 7600-7605.

17.   Postole, G.; Caldararu, M.; Bonnetot, B.; Auroux, A., Characterization of high surface area hexagonal boron nitride by in situ electrical conductivity. *Diamond and Related Materials* **2009,** *18* (5), 1052-1056.

18.   Thomas, J.; Weston, N. E.; O'Connor, T. E., Turbostratic Boron Nitride, Thermal Transformation to Ordered-layer-lattice Boron Nitride. *Journal of the American Chemical Society* **1962,** *84* (24), 4619-4622.

19.   Alkoy, S.; Toy, C.; Gönül, T.; Tekin, A., Crystallization behavior and characterization of turbostratic boron nitride. *Journal of the European Ceramic Society* **1997,** *17* (12), 1415-1422.

20.   Silva, L. A.; Guerini, S. C.; Lemos, V.; Filho, J. M., Electronic and Structural Properties of Oxygen-Doped BN Nanotubes. *IEEE Transactions on Nanotechnology* **2006,** *5* (5), 517-522.

21.   Florent, M.; Bandosz, T. J., Irreversible water mediated transformation of BCN from a 3D highly porous form to its nonporous hydrolyzed counterpart. *Journal of Materials Chemistry A* **2018,** *6* (8), 3510-3521.

22.   Shankar, R.; Sachs, M.; Francàs, L.; Lubert-Perquel, D.; Kerherve, G.; Regoutz, A.; Petit, C., Porous boron nitride for combined CO_2 capture and photoreduction. *Journal of Materials Chemistry A* **2019,** *7* (41), 23931-23940.

23.   Liang, J.; Song, Q.; Lin, J.; Huang, Y.; Fang, Y.; Yu, C.; Xue, Y.; Liu, Z.; Tang, C., Pore structure regulation and carbon dioxide adsorption capacity improvement on porous BN fibers: Effects of high-temperature treatments in gaseous ambient. *Chemical Engineering Journal* **2019,** *373*, 616-623.

24.   Wang, D.; Xue, Y.; Wang, C.; Ji, J.; Zhou, Z.; Tang, C., Improved capture of carbon dioxide and methane via adding micropores within porous boron nitride fibers. *Journal of Materials Science* **2019,** *54* (14), 10168-10178.

25.   Shankar, R. B.; Mistry, E. D. R.; Lubert-Perquel, D.; Nevjestic, I.; Heutz, S.; Petit, C., A Response Surface Model to Predict and Experimentally Tune the Chemical, Magnetic and Optoelectronic Properties of Oxygen-Doped Boron Nitride**. *ChemPhysChem* **2022,** *23* (13), e202100854.

26.   Nehate, S. D.; Saikumar, A. K.; Prakash, A.; Sundaram, K. B., A review of boron carbon nitride thin films and progress in nanomaterials. *Materials Today Advances* **2020,** *8*, 100106.

27.   Weng, Q.; Kvashnin, D. G.; Wang, X.; Cretu, O.; Yang, Y.; Zhou, M.; Zhang, C.; Tang, D.-M.; Sorokin, P. B.; Bando, Y.; Golberg, D., Tuning of the Optical, Electronic, and Magnetic Properties of Boron Nitride Nanosheets with Oxygen Doping and Functionalization. *Advanced Materials* **2017,** *29* (28), 1700695.

28.   Wang, X.; Pakdel, A.; Zhi, C.; Watanabe, K.; Sekiguchi, T.; Golberg, D.; Bando, Y., High-yield boron nitride nanosheets from 'chemical blowing': towards practical applications in polymer composites. *Journal of Physics: Condensed Matter* **2012,** *24* (31), 314205.

29.   Li, J.; Xiao, X.; Xu, X.; Lin, J.; Huang, Y.; Xue, Y.; Jin, P.; Zou, J.; Tang, C., *Activated boron nitride as an effective adsorbent for metal ions and organic pollutants*. 2013; Vol. 3, p 3208.

30.   Deepika; Li, L. H.; Glushenkov, A. M.; Hait, S. K.; Hodgson, P.; Chen, Y., High-Efficient Production of Boron Nitride Nanosheets via an Optimized Ball Milling Process for Lubrication in Oil. *Scientific Reports* **2014,** *4*, 7288.

31.   Han, W.-Q.; Wu, L.; Zhu, Y.; Watanabe, K.; Taniguchi, T., Structure of chemically derived mono- and few-atomic-layer boron nitride sheets. *Applied Physics Letters* **2008,** *93* (22), 223103.

32.   Warner, J. H.; Rümmeli, M. H.; Bachmatiuk, A.; Büchner, B., Atomic Resolution Imaging and Topography of Boron Nitride Sheets Produced by Chemical Exfoliation. *ACS Nano* **2010,** *4* (3), 1299-1304.

33.   Wang, X.; Zhi, C.; Li, L.; Zeng, H.; Li, C.; Mitome, M.; Golberg, D.; Bando, Y., "Chemical Blowing" of Thin-Walled Bubbles: High-Throughput Fabrication of Large-Area, Few-Layered BN and Cx-BN Nanosheets. *Advanced Materials* **2011,** *23* (35), 4072-4076.

34.   Rand, M. J.; Roberts, J. F., Preparation and Properties of Thin Film Boron Nitride. *Journal of The Electrochemical Society* **1968,** *115*, 423-429.

35.   Uchida, Y.; Kawahara, K.; Fukamachi, S.; Ago, H., Chemical Vapor Deposition Growth of Uniform Multilayer Hexagonal Boron Nitride Driven by Structural Transformation of a Metal Thin Film. *ACS Applied Electronic Materials* **2020,** *2* (10), 3270-3278.

36.   Zhang, X.; Lian, G.; Zhang, S.; Cui, D.; Wang, Q., Boron nitride nanocarpets: controllable synthesis and their adsorption performance to organic pollutants. *CrystEngComm* **2012,** *14* (14), 4670-4676.

37.   Dibandjo, P.; Chassagneux, F.; Bois, L.; Sigala, C.; Miele, P., Comparison between SBA-15 silica and CMK-3 carbon nanocasting for mesoporous boron nitride synthesis. *Journal of Materials Chemistry* **2005,** *15* (19).

38.   Dibandjo, P.; Bois, L.; Chassagneux, F.; Letoffe, J. M.; Miele, P., Influence of the thermal process of carbon template removal in the mesoporous boron nitride synthesis. *Journal of Porous Materials* **2008,** *15* (1), 13-20.

39.   Li, J.; Lin, J.; Xu, X.; Zhang, X.; Xue, Y.; Mi, J.; Mo, Z.; Fan, Y.; Hu, L.; Yang, X.; Zhang, J.; Meng, F.; Yuan, S.; Tang, C., Porous boron nitride with a high surface area: hydrogen storage and water treatment. *Nanotechnology* **2013,** *24* (15), 155603.

40.   Nag, A.; Raidongia, K.; Hembram, K. P. S. S.; Datta, R.; Waghmare, U. V.; Rao, C. N. R., Graphene Analogues of BN: Novel Synthesis and Properties. *ACS Nano* **2010,** *4* (3), 1539-1544.

41.   Wu, P.; Zhu, W.; Chao, Y.; Zhang, J.; Zhang, P.; Zhu, H.; Li, C.; Chen, Z.; Li, H.; Dai, S., A template-free solvent-mediated synthesis of high surface area boron nitride nanosheets for aerobic oxidative desulfurization. *Chemical Communications* **2016,** *52* (1), 144-147.

42.   Tian, T.; Hou, J.; Ansari, H.; Xiong, Y.; L'Hermitte, A.; Danaci, D.; Pini, R.; Petit, C., Mechanically stable structured porous boron nitride with high volumetric adsorption capacity. *Journal of Materials Chemistry A* **2021,** *9* (22), 13366-13373.

43.   Ramirez Leyva, J. H.; Vitale, G.; Hethnawi, A.; Hassan, A.; Perez-Zurita, M. J.; Ruiz-Esparza, G. U.; Nassar, N. N., Mechanism of Hierarchical Porosity Development in Hexagonal Boron Nitride Nanocrystalline Microstructures for Biomedical and Industrial Applications. *ACS Applied Nano Materials* **2018,** *1* (9), 4491-4501.

44.   Wu, C.; Wang, B.; Wu, N.; Han, C.; Zhang, X.; Shen, S.; Tian, Q.; Qin, C.; Li, P.; Wang, Y., Molecular-scale understanding on the structure evolution from melamine diborate supramolecule to boron nitride fibers. *Ceramics International* **2020,** *46* (1), 1083-1090.

45.   Gross, P.; Höppe, H. A., Unravelling the Urea-Route to Boron Nitride: Synthesis and Characterization of the Crucial Reaction Intermediate Ammonium Bis(biureto)borate. *Chemistry of Materials* **2019,** *31* (19), 8052-8061.

46.   Gong, Y.; Shi, G.; Zhang, Z.; Zhou, W.; Jung, J.; Gao, W.; Ma, L.; Yang, Y.; Yang, S.; You, G.; Vajtai, R.; Xu, Q.; MacDonald, A. H.; Yakobson, B. I.; Lou, J.; Liu, Z.; Ajayan, P. M., Direct chemical conversion of graphene to boron- and nitrogen- and carbon-containing atomic layers. *Nature Communications* **2014,** *5*, 3193.

47.   Hoffendahl, C.; Duquesne, S.; Fontaine, G.; Bourbigot, S., Decomposition mechanism of melamine borate in pyrolytic and thermo-oxidative conditions. *Thermochimica Acta* **2014,** *590*, 73-83.

48.   O'Connor, T. E., Synthesis of Boron Nitride. *Journal of the American Chemical Society* **1962,** *84* (9), 1753-1754.

49.   Motojima, S.; Tamura, Y.; Sugiyama, K., Low temperature deposition of hexagonal BN films by chemical vapour deposition. *Thin Solid Films* **1982,** *88* (3), 269-274.

50.   Matsuda, T., Stability to moisture for chemically vapour-deposited boron nitride. *Journal of Materials Science* **1989,** *24* (7), 2353-2357.

51.   Hojak, J.; Jähnichen, T.; Bläker, C.; Pasel, C.; Mauer, V.; Rasmussen, L.; Denecke, R.; Enke, D.; Bathen, D., Mesoporous boron nitride in contact with water - Chemical stability and adsorption properties. *Results in Materials* **2022,** *16*.

52.   Cao, F.; Liu, K.; Fang, Z.; Wang, S., Hydrolysis Mechanism of Borazine-derived Boron Nitride Pyrolysized below 1200 °C. *Journal of Materials Science & Technology* **2012,** *28* (10), 956-960.

53.   Saito, T.; Honda, F., Chemical contribution to friction behavior of sintered hexagonal boron nitride in water. *Wear* **2000,** *237* (2), 253-260.

54.   Streletskii, A. N.; Permenov, D. G.; Bokhonov, B. B.; Kolbanev, I. V.; Leonov, A. V.; Berestetskaya, I. V.; Streletzky, K. A., Destruction, amorphization and reactivity of nano-BN under ball milling. *Journal of Alloys and Compounds* **2009,** *483* (1), 313-316.

55.   Feng, Y.; Zhou, Y.; Lee, P.-H.; Shih, K., Mineralization of perfluorooctanesulfonate (PFOS) and perfluorodecanoate (PFDA) from aqueous solution by porous hexagonal boron nitride: adsorption followed by simultaneous thermal decomposition and regeneration. *RSC Advances* **2016,** *6* (114), 113773-113780.

56.   Lin, Y.; Williams, T. V.; Xu, T.-B.; Cao, W.; Elsayed-Ali, H. E.; Connell, J. W., Aqueous Dispersions of Few-Layered and Monolayered Hexagonal Boron Nitride Nanosheets from Sonication-Assisted Hydrolysis: Critical Role of Water. *The Journal of Physical Chemistry C* **2011,** *115* (6), 2679-2685.

57.   Liu, F.; Li, S.; Yu, D.; Su, Y.; Shao, N.; Zhang, Z., Template-Free Synthesis of Oxygen-Doped Bundlelike Porous Boron Nitride for Highly Efficient Removal of Heavy Metals from Wastewater. *ACS Sustainable Chemistry & Engineering* **2018,** *6* (12), 16011-16020.

58.   Ravenelle, R. M.; Schüßler, F.; D'Amico, A.; Danilina, N.; van Bokhoven, J. A.; Lercher, J. A.; Jones, C. W.; Sievers, C., Stability of Zeolites in Hot Liquid Water. *The Journal of Physical Chemistry C* **2010,** *114* (46), 19582-19595.

59.   Prodinger, S.; Derewinski, M. A., Recent Progress to Understand and Improve Zeolite Stability in the Aqueous Medium. *Petroleum Chemistry* **2020,** *60* (4), 420-436.

60.   Wang, C.; Liu, X.; Keser Demir, N.; Chen, J. P.; Li, K., Applications of water stable metal–organic frameworks. *Chemical Society Reviews* **2016,** *45* (18), 5107-5134.

61.   Ding, M.; Cai, X.; Jiang, H.-L., Improving MOF stability: approaches and applications. *Chemical Science* **2019,** *10* (44), 10209-10230.

62.   McHugh, L. N.; McPherson, M. J.; McCormick, L. J.; Morris, S. A.; Wheatley, P. S.; Teat, S. J.; McKay, D.; Dawson, D. M.; Sansome, C. E. F.; Ashbrook, S. E.; Stone, C. A.; Smith, M. W.; Morris, R. E., Hydrolytic stability in hemilabile metal–organic frameworks. *Nature Chemistry* **2018,** *10* (11), 1096-1102.

63.   Burtch, N. C.; Jasuja, H.; Walton, K. S., Water Stability and Adsorption in Metal–Organic Frameworks. *Chemical Reviews* **2014,** *114* (20), 10575-10612.

64.   Howarth, A. J.; Liu, Y.; Li, P.; Li, Z.; Wang, T. C.; Hupp, J. T.; Farha, O. K., Chemical, thermal and mechanical stabilities of metal–organic frameworks. *Nature Reviews Materials* **2016,** *1* (3), 15018.

65.   Yuan, S.; Feng, L.; Wang, K.; Pang, J.; Bosch, M.; Lollar, C.; Sun, Y.; Qin, J.; Yang, X.; Zhang, P.; Wang, Q.; Zou, L.; Zhang, Y.; Zhang, L.; Fang, Y.; Li, J.; Zhou, H.-

C., Stable Metal–Organic Frameworks: Design, Synthesis, and Applications. *Advanced Materials* **2018,** *30* (37), 1704303.

66. Han, X.; Wang, L.; Li, J.; Zhan, X.; Chen, J.; Yang, J., Tuning the hydrophobicity of ZSM-5 zeolites by surface silanization using alkyltrichlorosilane. *Applied Surface Science* **2011,** *257* (22), 9525-9531.

67. Zapata, P. A.; Faria, J.; Ruiz, M. P.; Jentoft, R. E.; Resasco, D. E., Hydrophobic Zeolites for Biofuel Upgrading Reactions at the Liquid–Liquid Interface in Water/Oil Emulsions. *Journal of the American Chemical Society* **2012,** *134* (20), 8570-8578.

68. Zapata, P. A.; Huang, Y.; Gonzalez-Borja, M. A.; Resasco, D. E., Silylated hydrophobic zeolites with enhanced tolerance to hot liquid water. *Journal of Catalysis* **2013,** *308*, 82-97.

69. Yang, S.; Peng, L.; Sun, D. T.; Asgari, M.; Oveisi, E.; Trukhina, O.; Bulut, S.; Jamali, A.; Queen, W. L., A new post-synthetic polymerization strategy makes metal–organic frameworks more stable. *Chemical Science* **2019,** *10* (17), 4542-4549.

70. Esmaeilirad, A.; Rukosuyev, M. V.; Jun, M. B. G.; van Veggel, F. C. J. M., A cost-effective method to create physically and thermally stable and storable super-hydrophobic aluminum alloy surfaces. *Surface & Coatings Technology* **2016,** *285*, 227-234.

71. Saleema, N.; Sarkar, D. K.; Gallant, D.; Paynter, R. W.; Chen, X. G., Chemical nature of superhydrophobic aluminum alloy surfaces produced via a one-step process using fluoroalkyl-silane in a base medium. *ACS Applied Materials & Interfaces* **2011,** *3* (12), 4775-4781.

72. Sah, A.; Castricum, H. L.; Bliek, A.; Blank, D. H. A.; ten Elshof, J. E., Hydrophobic modification of γ-alumina membranes with organochlorosilanes. *Journal of Membrane Science* **2004,** *243* (1), 125-132.

73. Wei, Q.; Achazi, K.; Liebe, H.; Schulz, A.; Noeske, P.-L. M.; Grunwald, I.; Haag, R., Mussel-Inspired Dendritic Polymers as Universal Multifunctional Coatings. *Angewandte Chemie International Edition* **2014,** *53* (43), 11650-11655.

74. Lee, H.; Dellatore, S. M.; Miller, W. M.; Messersmith, P. B., Mussel-Inspired Surface Chemistry for Multifunctional Coatings. *Science* **2007,** *318* (5849), 426.

75. Rouquerol, F.; Rouquerol, J.; Llewellyn, P.; Maurin, G.; Sing, K. S. W., *Adsorption by powders and porous solids: principles, methodology and applications*. 2nd ed.; Academic Press: Oxford, 2013.

76. Keller, J. U.; Staudt, R., Oscillometry. In *Gas Adsorption Equilibria: Experimental Methods and Adsorptive Isotherms*, Springer US: Boston, MA, 2005; pp 235-285.

77. Wang, J.-Y.; Mangano, E.; Brandani, S.; Ruthven, D. M., A review of common practices in gravimetric and volumetric adsorption kinetic experiments. *Adsorption* **2021,** *27* (3), 295-318.

78. Sing, K. S. W.; Everett, D. H.; Haul, R. A. W.; Moscou, L.; Pierotti, R. A.; Rouquérol, J.; Siemieniewska, T., Reporting physisorption data for gas/solid systems with special reference to the determination of surface area and porosity (Recommendations 1984). *Pure and Applied Chemistry* **1985,** *57* (4), 603-619.

79. Bae, Y. S.; Snurr, R. Q., Development and evaluation of porous materials for carbon dioxide separation and capture. *Angewandte Chemie International Edition* **2011,** *50* (49), 11586-96.

80. Morishige, K., Adsorption and Separation of CO2/CH4 on Amorphous Silica Molecular Sieve. *The Journal of Physical Chemistry C* **2011,** *115* (19), 9713-9718.

81. Grande, C. A.; Morence, D. G. B.; Bouzga, A. M.; Andreassen, K. A., Silica Gel as a Selective Adsorbent for Biogas Drying and Upgrading. *Industrial & Engineering Chemistry Research* **2020,** *59* (21), 10142-10149.

82.   Misaelides, P., Application of natural zeolites in environmental remediation: A short review. *Microporous and Mesoporous Materials* **2011,** *144* (1), 15-18.

83.   Bao, Z.; Yu, L.; Dou, T.; Gong, Y.; Zhang, Q.; Ren, Q.; Lu, X.; Deng, S., Adsorption Equilibria of CO2, CH4, N2, O2, and Ar on High Silica Zeolites. *Journal of Chemical & Engineering Data* **2011,** *56* (11), 4017-4023.

84.   Cecilia, J. A.; Vilarrasa-García, E.; Morales-Ospino, R.; Finocchio, E.; Busca, G.; Sapag, K.; Villarroel-Rocha, J.; Bastos-Neto, M.; Azevedo, D. C. S.; Rodríguez-Castellón, E., Kaolinite-based zeolites synthesis and their application in CO2 capture processes. *Fuel* **2022,** *320*, 123953.

85.   James, S. L., Metal-organic frameworks. *Chemical Society Reviews* **2003,** *32* (5), 276-288.

86.   Mueller, U.; Schubert, M.; Teich, F.; Puetter, H.; Schierle-Arndt, K.; Pastré, J., Metal–organic frameworks—prospective industrial applications. *Journal of Materials Chemistry* **2006,** *16* (7), 626-636.

87.   Wilmer, C. E.; Farha, O. K.; Bae, Y.-S.; Hupp, J. T.; Snurr, R. Q., Structure–property relationships of porous materials for carbon dioxide separation and capture. *Energy & Environmental Science* **2012,** *5* (12).

88.   Côté Adrien, P.; Benin Annabelle, I.; Ockwig Nathan, W.; O'Keeffe, M.; Matzger Adam, J.; Yaghi Omar, M., Porous, Crystalline, Covalent Organic Frameworks. *Science* **2005,** *310* (5751), 1166-1170.

89.   Feng, X.; Ding, X.; Jiang, D., Covalent organic frameworks. *Chemical Society Reviews* **2012,** *41* (18), 6010-6022.

90.   Li, B.; Gong, R.; Wang, W.; Huang, X.; Zhang, W.; Li, H.; Hu, C.; Tan, B., A New Strategy to Microporous Polymers: Knitting Rigid Aromatic Building Blocks by External Cross-Linker. *Macromolecules* **2011,** *44* (8), 2410-2414.

91.   Woodward, R. T., The design of hypercrosslinked polymers from benzyl ether self-condensing compounds and external crosslinkers. *Chemical Communications* **2020,** *56* (36), 4938-4941.

92.   Dawson, R.; Stöckel, E.; Holst, J. R.; Adams, D. J.; Cooper, A. I., Microporous organic polymers for carbon dioxide capture. *Energy & Environmental Science* **2011,** *4* (10), 4239-4245.

93.   Ioannidou, O.; Zabaniotou, A., Agricultural residues as precursors for activated carbon production—A review. *Renewable and Sustainable Energy Reviews* **2007,** *11* (9), 1966-2005.

94.   Otowa, T.; Nojima, Y.; Miyazaki, T., Development of KOH activated high surface area carbon and its application to drinking water purification. *Carbon* **1997,** *35* (9), 1315-1319.

95.   Dias, J. M.; Alvim-Ferraz, M. C. M.; Almeida, M. F.; Rivera-Utrilla, J.; Sánchez-Polo, M., Waste materials for activated carbon preparation and its use in aqueous-phase treatment: A review. *Journal of Environmental Management* **2007,** *85* (4), 833-846.

96.   Silvestre-Albero, J.; Wahby, A.; Sepúlveda-Escribano, A.; Martínez-Escandell, M.; Kaneko, K.; Rodríguez-Reinoso, F., Ultrahigh CO2 adsorption capacity on carbon molecular sieves at room temperature. *Chemical Communications* **2011,** *47* (24), 6840-6842.

97.   Azevedo, D. C. S.; Araújo, J. C. S.; Bastos-Neto, M.; Torres, A. E. B.; Jaguaribe, E. F.; Cavalcante, C. L., Microporous activated carbon prepared from coconut shells using chemical activation with zinc chloride. *Microporous and Mesoporous Materials* **2007,** *100* (1), 361-364.

98.   Evans, A.; Luebke, R.; Petit, C., The use of metal–organic frameworks for CO purification. *Journal of Materials Chemistry A* **2018,** *6* (23), 10570-10594.

99.   Taddei, M.; Petit, C., Engineering metal–organic frameworks for adsorption-based gas separations: from process to atomic scale. *Molecular Systems Design & Engineering* **2021,** *6* (11), 841-875.

100.   Peng, Y.-L.; Wang, T.; Jin, C.; Deng, C.-H.; Zhao, Y.; Liu, W.; Forrest, K. A.; Krishna, R.; Chen, Y.; Pham, T.; Space, B.; Cheng, P.; Zaworotko, M. J.; Zhang, Z., Efficient propyne/propadiene separation by microporous crystalline physiadsorbents. *Nature Communications* **2021,** *12* (1), 5768.

101.   Danaci, D.; Bui, M.; Mac Dowell, N.; Petit, C., Exploring the limits of adsorption-based CO2 capture using MOFs with PVSA – from molecular design to process economics. *Molecular Systems Design & Engineering* **2020,** *5* (1), 212-231.

102.   Rajagopalan, A. K.; Rajendran, A., The effect of nitrogen adsorption on vacuum swing adsorption based post-combustion CO2 capture. *International Journal of Greenhouse Gas Control* **2018,** *78*, 437-447.

103.   Rajagopalan, A. K.; Avila, A. M.; Rajendran, A., Do adsorbent screening metrics predict process performance? A process optimisation based study for post-combustion capture of CO2. *International Journal of Greenhouse Gas Control* **2016,** *46*, 76-85.

104.   Ritter, H. L.; Drake, L. C., Pressure Porosimeter and Determination of Complete Macropore-Size Distributions. Pressure Porosimeter and Determination of Complete Macropore-Size Distributions. *Industrial & Engineering Chemistry Analytical Edition* **1945,** *17* (12), 782-786.

105.   Maring, B. J.; Webley, P. A., A new simplified pressure/vacuum swing adsorption model for rapid adsorbent screening for CO2 capture applications. *International Journal of Greenhouse Gas Control* **2013,** *15*, 16-31.

106.   Xiao, F.; Chen, Z.; Casillas, G.; Richardson, C.; Li, H.; Huang, Z., Controllable synthesis of few-layered and hierarchically porous boron nitride nanosheets. *Chemical Communications* **2016,** *52* (20), 3911-4.

107.   Janik, J. F.; Ackerman, W. C.; Paine, R. T.; Hua, D.-W.; Maskara, A.; Smith, D. M., Boron Nitride as a Selective Gas Adsorbent. *Langmuir* **1994,** *10* (2), 514-518.

108.   Saha, D.; Orkoulas, G.; Yohannan, S.; Ho, H. C.; Cakmak, E.; Chen, J.; Ozcan, S., Nanoporous Boron Nitride as Exceptionally Thermally Stable Adsorbent: Role in Efficient Separation of Light Hydrocarbons. *ACS Applied Materials & Interfaces* **2017,** *9* (16), 14506-14517.

109.   Maleki, M.; Beitollahi, A.; Shokouhimehr, M., Simple Synthesis of Two-Dimensional Micro/Mesoporous Boron Nitride. *European Journal of Inorganic Chemistry* **2015,** *2015* (14), 2478-2485.

110.   Lei, W.; Portehault, D.; Liu, D.; Qin, S.; Chen, Y., Porous boron nitride nanosheets for effective water cleaning. *Nature Communications* **2013,** *4*, 1777.

111.   Li, J.-R.; Kuppler, R. J.; Zhou, H.-C., Selective gas adsorption and separation in metal–organic frameworks. *Chemical Society Reviews* **2009,** *38* (5), 1477-1504.

112.   Buckingham, A. D.; Disch, R. L.; Dunmur, D. A., Quadrupole moments of some simple molecules. *Journal of the American Chemical Society* **1968,** *90* (12), 3104-3107.

113.   Marchesini, S. Design of Porous Boron Nitride Materials for Applications in Adsorption. PhD thesis, Imperial College London, 2018.

114.   Dibandjo, P.; Bois, L.; Chassagneux, F.; Miele, P., Thermal stability of mesoporous boron nitride templated with a cationic surfactant. *Journal of the European Ceramic Society* **2007,** *27* (1), 313-317.

115.   Lavrenko, V. A.; Alexeev, A. F., High-temperature oxidation of boron nitride. *Ceramics International* **1986,** *12* (1), 25-31.

116.   Chen, S.; Li, P.; Xu, S.; Pan, X.; Fu, Q.; Bao, X., Carbon doping of hexagonal boron nitride porous materials toward CO2 capture. *Journal of Materials Chemistry A* **2018,** *6* (4), 1832-1839.

117. Yang, C.; Wang, J.; Chen, Y.; Liu, D.; Huang, S.; Lei, W., One-step template-free synthesis of 3D functionalized flower-like boron nitride nanosheets for NH3 and CO2 adsorption. *Nanoscale* **2018,** *10* (23), 10979-10985.

118. Myers, A. L.; Prausnitz, J. M., Thermodynamics of mixed-gas adsorption. *AIChE Journal* **1965,** *11* (1), 121-127.

119. McEwen, J.; Hayman, J.-D.; Ozgur Yazaydin, A., A comparative study of CO2, CH4 and N2 adsorption in ZIF-8, Zeolite-13X and BPL activated carbon. *Chemical Physics* **2013,** *412*, 72-76.

120. Zhao, H.; Song, X.; Zeng, H., 3D white graphene foam scavengers: vesicant-assisted foaming boosts the gram-level yield and forms hierarchical pores for superstrong pollutant removal applications. *NPG Asia Materials* **2015,** *7* (3), e168-e168.

121. Pham, T.; Goldstein, A. P.; Lewicki, J. P.; Kucheyev, S. O.; Wang, C.; Russell, T. P.; Worsley, M. A.; Woo, L.; Mickelson, W.; Zettl, A., Nanoscale structure and superhydrophobicity of sp2-bonded boron nitride aerogels. *Nanoscale* **2015,** *7* (23), 10449-10458.

122. Vasta, S.; Brancato, V.; La Rosa, D.; Palomba, V.; Restuccia, G.; Sapienza, A.; Frazzica, A., Adsorption Heat Storage: State-of-the-Art and Future Perspectives. *Nanomaterials* **2018,** *8* (7), 522.

123. Pfleger, N.; Bauer, T.; Martin, C.; Eck, M.; Wörner, A., Thermal energy storage – overview and specific insight into nitrate salts for sensible and latent heat storage. *Beilstein Journal of Nanotechnology* **2015,** *6*, 1487-1497.

124. Shigeishi, R. A.; Langford, C. H.; Hollebone, B. R., Solar energy storage using chemical potential changes associated with drying of zeolites. *Solar Energy* **1979,** *23* (6), 489-495.

125. Kiyabu, S.; Lowe, J. S.; Ahmed, A.; Siegel, D. J., Computational Screening of Hydration Reactions for Thermal Energy Storage: New Materials and Design Rules. *Chemistry of Materials* **2018,** *30* (6), 2006-2017.

126. Lefebvre, D.; Tezel, F. H., A review of energy storage technologies with a focus on adsorption thermal energy storage processes for heating applications. *Renewable and Sustainable Energy Reviews* **2017,** *67*, 116-125.

127. Fasano, M.; Bergamasco, L.; Lombardo, A.; Zanini, M.; Chiavazzo, E.; Asinari, P., Water/Ethanol and 13X Zeolite Pairs for Long-Term Thermal Energy Storage at Ambient Pressure. *Frontiers in Energy Research* **2019,** *7*, 148.

128. N'Tsoukpoe, K. E.; Liu, H.; Le Pierrès, N.; Luo, L., A review on long-term sorption solar energy storage. *Renewable and Sustainable Energy Reviews* **2009,** *13* (9), 2385-2396.

129. Stritih, U.; Bombač, A., Description and Analysis of Adsorption Heat Storage Device. *Strojniški vestnik – Journal of Mechanical Engineering* **2014,** *60* (10), 619-628.

130. Tatsidjodoung, P.; Le Pierrès, N.; Luo, L., A review of potential materials for thermal energy storage in building applications. *Renewable and Sustainable Energy Reviews* **2013,** *18*, 327-349.

131. Shervani, S.; Strong, C.; Tezel, F. H., Magnesium sulphate hybrids with silica gel and activated alumina for thermal energy storage. *Journal of Cleaner Production* **2022,** *371*, 133262.

132. Dicaire, D.; Tezel, F. H., Use of adsorbents for thermal energy storage of solar or excess heat: improvement of energy density. *International Journal of Energy Research* **2013,** *37* (9), 1059-1068.

133. Strong, C.; Carrier, Y.; Handan Tezel, F., Experimental optimization of operating conditions for an open bulk-scale silica gel/water vapour adsorption energy storage system. *Applied Energy* **2022,** *312*, 118533.

134.   Aidoun, Z.; Ternan, M., The synthesis reaction in a chemical heat pump reactor filled with chloride salt impregnated carbon fibres: the NH3–CoCl2 system. *Applied Thermal Engineering* **2002,** *22* (17), 1943-1954.

135.   Donkers, P. A. J.; Sögütoglu, L. C.; Huinink, H. P.; Fischer, H. R.; Adan, O. C. G., A review of salt hydrates for seasonal heat storage in domestic applications. *Applied Energy* **2017,** *199*, 45-68.

136.   Lim, K.; Kim, J.; Lee, J., Comparative study on adsorbent characteristics for adsorption thermal energy storage system. *International Journal of Energy Research* **2019,** *43* (9), 4281-4294.

137.   Hua, Y.; Godin, A.; Handan Tezel, F., Water vapor adsorption in silica gel for thermal energy storage application. *Advanced Materials Letters* **2019,** *10* (2), 124-127.

138.   Lefebvre, D.; Amyot, P.; Ugur, B.; Tezel, F. H., Adsorption Prediction and Modeling of Thermal Energy Storage Systems: A Parametric Study. *Industrial & Engineering Chemistry Research* **2016,** *55* (16), 4760-4772.

139.   Demir, H.; Mobedi, M.; Ülkü, S., A review on adsorption heat pump: Problems and solutions. *Renewable and Sustainable Energy Reviews* **2008,** *12* (9), 2381-2403.

140.   Ayaz, H.; Chinnasamy, V.; Yong, J.; Cho, H., Review of Technologies and Recent Advances in Low-Temperature Sorption Thermal Storage Systems. *Energies* **2021,** *14* (19).

141.   Bird, J. E.; Humphries, T. D.; Paskevicius, M.; Poupin, L.; Buckley, C. E., Thermal properties of thermochemical heat storage materials. *Physical Chemistry Chemical Physics* **2020,** *22* (8), 4617-4625.

142.   Parrott, J. E.; Stuckes, A. D., Thermal Conductivity of Solids. *Physics Today* **1977,** *30* (2), 60.

143.   Uddin, K.; Amirul Islam, M.; Mitra, S.; Lee, J.-b.; Thu, K.; Saha, B. B.; Koyama, S., Specific heat capacities of carbon-based adsorbents for adsorption heat pump application. *Applied Thermal Engineering* **2018,** *129*, 117-126.

144.   Querejeta, N.; García, S.; Álvarez-Gutiérrez, N.; Rubiera, F.; Pevida, C., Measuring heat capacity of activated carbons for CO2 capture. *Journal of CO2 Utilization* **2019,** *33*, 148-156.

145.   Anupam, K.; Halder, G. N.; Roy, Z.; Sarkar, S. C.; Yadav, A., A simple calorimeter to measure specific heat of activated carbon prepared for pressure swing adsorption refrigeration system. *The Canadian Journal of Chemical Engineering* **2013,** *91* (4), 751-759.

146.   Menard, D.; Py, X.; Mazet, N., Activated carbon monolith of high thermal conductivity for adsorption processes improvement: Part A: Adsorption step. *Chemical Engineering and Processing: Process Intensification* **2005,** *44* (9), 1029-1038.

147.   Kuwagaki, H.; Meguro, T.; Tatami, J.; Komeya, K.; Tamura, K., An improvement of thermal conduction of activated carbon by adding graphite. *Journal of Materials Science* **2003,** *38* (15), 3279-3284.

148.   Verma, R.; Nagendra, H. N.; Kasthurirengan, S.; Shivaprakash, N. C.; Behera, U., Thermal conductivity studies on activated carbon based cryopanel. *IOP Conference Series: Materials Science and Engineering* **2019,** *502*.

149.   Yuan, C.; Li, J.; Lindsay, L.; Cherns, D.; Pomeroy, J. W.; Liu, S.; Edgar, J. H.; Kuball, M., Modulating the thermal conductivity in hexagonal boron nitride via controlled boron isotope concentration. *Communications Physics* **2019,** *2* (1), 43.

150.   McDonald, R. A.; Stull, D. R., The heat content and heat capacity of boron nitride from 298 to 1689°K. *The Journal of Physical Chemistry* **1961,** *65* (10), 1918.

151.   Vu, M. C.; Tran, T. S.; Bae, Y. H.; Yu, M. J.; Doan, V. C.; Lee, J. H.; An, T. K.; Kim, S.-R., Self-Assembly of Carbon Nanotubes and Boron Nitride via Electrostatic Interaction for Epoxy Composites of High Thermal Conductivity and Electrical Resistivity. *Macromolecular Research* **2018,** *26* (6), 521-528.

152. Srivastava, N. C.; Eames, I. W., A review of adsorbents and adsorbates in solid–vapour adsorption heat pump systems. *Applied Thermal Engineering* **1998,** *18* (9), 707-714.

153. Saha, B. B.; El-Sharkawy, I. I.; Chakraborty, A.; Koyama, S.; Yoon, S.-H.; Ng, K. C., Adsorption Rate of Ethanol on Activated Carbon Fiber. *Journal of Chemical & Engineering Data* **2006,** *51* (5), 1587-1592.

154. Saha, B. B.; Chakraborty, A.; Koyama, S.; Yoon, S.-H.; Mochida, I.; Kumja, M.; Yap, C.; Ng, K. C., Isotherms and thermodynamics for the adsorption of n-butane on pitch based activated carbon. *International Journal of Heat and Mass Transfer* **2008,** *51* (7), 1582-1589.

155. Madero-Castro, R. M.; Vicent-Luna, J. M.; Peng, X.; Calero, S., Adsorption of Linear Alcohols in Amorphous Activated Carbons: Implications for Energy Storage Applications. *ACS Sustainable Chemistry & Engineering* **2022,** *10* (20), 6509-6520.

156. Kohler, T.; Müller, K., Influence of different adsorbates on the efficiency of thermochemical energy storage. *Energy Science & Engineering* **2017,** *5* (1), 21-29.

157. Sigma-Aldrich Activated Charcoal Norit®. https://www.sigmaaldrich.com/GB/en/product/sigald/29204 (accessed 01/03/2023).

158. Wu, J. W.; Madani, S. H.; Biggs, M. J.; Phillip, P.; Lei, C.; Hu, E. J., Characterizations of Activated Carbon–Methanol Adsorption Pair Including the Heat of Adsorptions. *Journal of Chemical & Engineering Data* **2015,** *60* (6), 1727-1731.

159. Chairunnisa, C. Z.; Mikšík, F.; Miyazaki, T.; Thu, K.; Miyawaki, J.; Nakabayashi, K.; Wijayanta, A. T.; Rahmawati, F., Enhancing water adsorption capacity of acorn nutshell based activated carbon for adsorption thermal energy storage application. *Energy Reports* **2020,** *6*, 255-263.

160. Curthoys, G.; Elkington, P. A., Heats of adsorption on boron nitride. *The Journal of Physical Chemistry* **1967,** *71* (5), 1477-1483.

161. Smith, B. C., *Fundamentals of Fourier Transform Infrared Spectroscopy*. Second ed.; CRC Press: 2011; p 207.

162. Van Grieken, R. E.; Markowicz, A. A., *Handbook of X-Ray Spectrometry*. CRC Press: 2001.

163. NIST NIST X-ray Photoelectron Spectroscopy (XPS) Database. https://srdata.nist.gov/xps/main_search_menu.aspx (accessed 05/09/2019).

164. Duer, M. J., *Introduction to Solid-State NMR Spectroscopy*. Wiley-Blackwell: 2005.

165. Ashbrook, S. E.; Griffin, J. M.; Johnston, K. E., Recent Advances in Solid-State Nuclear Magnetic Resonance Spectroscopy. *Annual Review of Analytical Chemistry* **2018,** *11* (1), 485-508.

166. Yio, M. H. N.; Ho, Y. W.; Abdul Wahid, F.; Wong, H. S.; Buenfeld, N. R., Analysis of cement paste and aggregate content of concrete using micro X-ray fluorescence. *Magazine of Concrete Research* **2022,** *74* (17), 889-904.

167. Stöhr, J., Theory of Inner Shell Excitation Spectra. In *NEXAFS Spectroscopy*, Stöhr, J., Ed. Springer Berlin Heidelberg: Berlin, Heidelberg, 1992; pp 8-47.

168. Diller, K.; Maurer, R. J.; Muller, M.; Reuter, K., Interpretation of X-ray absorption spectroscopy in the presence of surface hybridization. *The Journal of Chemical Physics* **2017,** *146* (21), 214701.

169. Held, G.; Venturini, F.; Grinter, D.; Ferrer, P.; Arrigo, R.; Deacon, L.; Garzon, W.; Roy, K.; Large, A.; Stephens, C.; Watts, A.; Larkin, P.; Hand, M.; Wang, H.; Pratt, L.; Mudd, J.; Richardson, T.; Patel, S.; Hillman, M.; Scott, S., Ambient-pressure endstation of the Versatile Soft X-ray (VerSoX) beamline at Diamond Light Source. *Journal of Synchrotron Radiation* **2020,** *27*.

170.   Bunaciu, A. A. U., Elena Gabriela; Aboul-Enein, H. Y., X-Ray Diffraction: Instrumentation and Applications. *Critical Reviews in Analytical Chemistry* **2015,** *45* (5), 289-299.

171.   Brunauer, S.; Emmett, P. H.; Teller, E., Adsorption of Gases in Multimolecular Layers. *Journal of the American Chemical Society* **1938,** *60* (2), 309-319.

172.   Langmuir, I., The adsorption of gases on plane surfaces of glass, mica and platinum. *Journal of the American Chemical Society* **1918,** *40* (9), 1361-1403.

173.   Rouquerol, J.; Llewellyn, P.; Rouquerol, F., Is the bet equation applicable to microporous adsorbents? In *Studies in Surface Science and Catalysis*, Llewellyn, P. L.; Rodriquez-Reinoso, F.; Rouqerol, J.; Seaton, N., Eds. Elsevier: 2007; Vol. 160, pp 49-56.

174.   Walton, K. S.; Snurr, R. Q., Applicability of the BET Method for Determining Surface Areas of Microporous Metal−Organic Frameworks. *Journal of the American Chemical Society* **2007,** *129* (27), 8552-8556.

175.   Osterrieth, J. W. M.; Rampersad, J.; Madden, D.; Rampal, N.; Skoric, L.; Connolly, B.; Allendorf, M. D.; Stavila, V.; Snider, J. L.; Ameloot, R.; Marreiros, J.; Ania, C.; Azevedo, D.; Vilarrasa-Garcia, E.; Santos, B. F.; Bu, X. H.; Chang, Z.; Bunzen, H.; Champness, N. R.; Griffin, S. L.; Chen, B.; Lin, R. B.; Coasne, B.; Cohen, S.; Moreton, J. C.; Colón, Y. J.; Chen, L.; Clowes, R.; Coudert, F. X.; Cui, Y.; Hou, B.; D'Alessandro, D. M.; Doheny, P. W.; Dincă, M.; Sun, C.; Doonan, C.; Huxley, M. T.; Evans, J. D.; Falcaro, P.; Ricco, R.; Farha, O.; Idrees, K. B.; Islamoglu, T.; Feng, P.; Yang, H.; Forgan, R. S.; Bara, D.; Furukawa, S.; Sanchez, E.; Gascon, J.; Telalović, S.; Ghosh, S. K.; Mukherjee, S.; Hill, M. R.; Sadiq, M. M.; Horcajada, P.; Salcedo-Abraira, P.; Kaneko, K.; Kukobat, R.; Kenvin, J.; Keskin, S.; Kitagawa, S.; Otake, K. i.; Lively, R. P.; DeWitt, S. J. A.; Llewellyn, P.; Lotsch, B. V.; Emmerling, S. T.; Pütz, A. M.; Martí-Gastaldo, C.; Padial, N. M.; García-Martínez, J.; Linares, N.; Maspoch, D.; Suárez del Pino, J. A.; Moghadam, P.; Oktavian, R.; Morris, R. E.; Wheatley, P. S.; Navarro, J.; Petit, C.; Danaci, D.; Rosseinsky, M. J.; Katsoulidis, A. P.; Schröder, M.; Han, X.; Yang, S.; Serre, C.; Mouchaham, G.; Sholl, D. S.; Thyagarajan, R.; Siderius, D.; Snurr, R. Q.; Goncalves, R. B.; Telfer, S.; Lee, S. J.; Ting, V. P.; Rowlandson, J. L.; Uemura, T.; Iiyuka, T.; van der Veen, M. A.; Rega, D.; Van Speybroeck, V.; Rogge, S. M. J.; Lamaire, A.; Walton, K. S.; Bingel, L. W.; Wuttke, S.; Andreo, J.; Yaghi, O.; Zhang, B.; Yavuz, C. T.; Nguyen, T. S.; Zamora, F.; Montoro, C.; Zhou, H.; Kirchon, A.; Fairen-Jimenez, D., How Reproducible are Surface Areas Calculated from the BET Equation? *Advanced Materials* **2022,** *34* (27).

176.   Chen, S. G.; Yang, R. T., Theoretical Basis for the Potential Theory Adsorption Isotherms. The Dubinin-Radushkevich and Dubinin-Astakhov Equations. *Langmuir* **1994,** *10* (11), 4244-4249.

177.   Lowell, S.; Shields, J. E.; Thomas, M. A.; Thommes, M., *Characterization of Porous Solids and Powders: Surface Area, Pore Size and Density*. Springer Netherlands: Dordrecht, 2004.

178.   Azzan, H.; Rajagopalan, A. K.; L'Hermitte, A.; Pini, R.; Petit, C., Simultaneous Estimation of Gas Adsorption Equilibria and Kinetics of Individual Shaped Adsorbents. *Chemistry of Materials* **2022,** *34* (15), 6671–6686.

179.   Jahnichen, T.; Hojak, J.; Blaker, C.; Pasel, C.; Mauer, V.; Zittel, V.; Denecke, R.; Bathen, D.; Enke, D., Synthesis of Turbostratic Boron Nitride: Effect of Urea Decomposition. *ACS Omega* **2022,** *7* (37), 33375-33384.

180.   Geick, R.; Perry, C. H.; Rupprecht, G., Normal Modes in Hexagonal Boron Nitride. *Physical Review* **1966,** *146* (2), 543-547.

181.   Wei, X.; Qiu, Y.; Duan, W.; Liu, Z., Cathodic and anodic photocurrents generation from melem and its derivatives. *RSC Advances* **2015,** *5* (34), 26675-26679.

182.   Xiong, Q.; Yuan, Y.; Zhang, L.; Xing, J.; Utama, M.; Lu, X.; Du, K.; Li, Y.; Hu, X.; Wang, S.; Genç, A.; Dunin-Borkowski, R.; Arbiol, J., High-yield Synthesis and Optical Properties of g-C3N4. *Nanoscale* **2015,** *7.*

183.   Liu, J.; Zhang, T.; Wang, Z.; Dawson, G.; Chen, W., Simple pyrolysis of urea into graphitic carbon nitride with recyclable adsorption and photocatalytic activity. *Journal of Materials Chemistry* **2011,** *21* (38), 14398-14401.

184.   Liu, X.; Ye, S.; Qiao, Y.; Dong, G.; Zhang, Q.; Qiu, J., Facile synthetic strategy for efficient and multi-color fluorescent BCNO nanocrystals. *Chemical Communications* **2009,** (27), 4073-4075.

185.   Wang, C.; Fan, H.; Ren, X.; Fang, J.; Ma, J.; Zhao, N., Porous graphitic carbon nitride nanosheets by pre-polymerization for enhanced photocatalysis. *Materials Characterization* **2018,** *139*, 89-99.

186.   Panicker, C. Y.; Varghese, H. T.; John, A.; Philip, D.; Nogueira, H. I. S., Vibrational spectra of melamine diborate, C3N6H62H3BO3. *Spectrochimica Acta Part A: Molecular and Biomolecular Spectroscopy* **2002,** *58* (8), 1545-1551.

187.   Roy, A.; Choudhury, A.; Rao, C. N. R., Supramolecular hydrogen-bonded structure of a 1:2 adduct of melamine with boric acid. *Journal of Molecular Structure* **2002,** *613* (1), 61-66.

188.   Randall, S. P.; Margrave, J. L., Vapour equilibria in the B2O3-H2O system at elevated temperatures. *Journal of Inorganic and Nuclear Chemistry* **1960,** *16* (1), 29-35.

189.   Kinoshita, H., Synthesis of Melamine from Urea. *The Review of Physical Chemistry of Japan* **1955,** *24* (1), 19-27.

190.   Schaber, P. M.; Colson, J.; Higgins, S.; Thielen, D.; Anspach, B.; Brauer, J., Thermal decomposition (pyrolysis) of urea in an open reaction vessel. *Thermochimica Acta* **2004,** *424* (1-2), 131-142.

191.   Wirnhier, E.; Mesch, M. B.; Senker, J.; Schnick, W., Formation and Characterization of Melam, Melam Hydrate, and a Melam–Melem Adduct. *Chemistry – A European Journal* **2013,** *19* (6), 2041-2049.

192.   Jürgens, B.; Irran, E.; Senker, J.; Kroll, P.; Müller, H.; Schnick, W., Melem (2,5,8-Triamino-tri-s-triazine), an Important Intermediate during Condensation of Melamine Rings to Graphitic Carbon Nitride: Synthesis, Structure Determination by X-ray Powder Diffractometry, Solid-State NMR, and Theoretical Studies. *Journal of the American Chemical Society* **2003,** *125* (34), 10288-10300.

193.   Finkel'shtein, A. I.; Spiridonova, N. V., Chemical Properties and Molecular Structure of Derivatives of Sym-Heptazine[1,3,4,6,7,9,9b-Heptaazaphenalene, Tri-1,3,5-Triazine]. *Russian Chemical Reviews* **1964,** *33* (7), 400-405.

194.   Thomas, A.; Fischer, A.; Goettmann, F.; Antonietti, M.; Müller, J.-O.; Schlögl, R.; Carlsson, J., Graphitic Carbon Nitride Materials: Variation of Structure and Morphology and Their Use as Metal-Free Catalysts. *Journal of Materials Chemistry* **2008,** *18* (41), 4893-4908.

195.   Cholet, V.; Vandenbulcke, L.; Rouan, J. P.; Baillif, P.; Erre, R., Characterization of boron nitride films deposited from BCl3-NH3-H2 mixtures in chemical vapour infiltration conditions. *Journal of Materials Science* **1994,** *29* (6), 1417-1435.

196.   Jiménez, I.; Jankowski, A. F.; Terminello, L. J.; Sutherland, D. G. J.; Carlisle, J. A.; Doll, G. L.; Tong, W. M.; Shuh, D. K.; Himpsel, F. J., Core-level photoabsorption study of defects and metastable bonding configurations in boron nitride. *Physical Review B* **1997,** *55* (18), 12025-12037.

197.   Liu, L.; Sham, T.-K.; Han, W.; Zhi, C.; Bando, Y., X-ray Excited Optical Luminescence from Hexagonal Boron Nitride Nanotubes: Electronic Structures and the Role of Oxygen Impurities. *ACS Nano* **2011,** *5* (1), 631-639.

198.   Zhou, X. T.; Sham, T. K.; Chan, C. Y.; Zhang, W. J.; Bello, I.; Lee, S. T.; Heigl, F.; Jürgenen, A.; Hofsäss, H., Preferable orientation of turbostatic BN basal planes from an x-ray absorption study. *Journal of Materials Research* **2006,** *21* (1), 147-152.

199.   Itskou, I.; L'Hermitte, A.; Marchesini, S.; Tian, T.; Petit, C., How to Tailor Porous Boron Nitride Properties for Applications in Interfacial Processes. *Accounts of Materials Research* **2023**.

200.   Takada, Y.; Sakai, M.; Isobe, T.; Matsushita, S.; Nakajima, A., Preparation and hydrophobicity of solid–liquid bulk composite using porous glass and fluorinated oil. *Journal of Materials Science* **2015,** *50* (23), 7760-7769.

201.   Takahashi, T.; Tanimoto, R.; Isobe, T.; Matsushita, S.; Nakajima, A., Surface modification of porous alumina filters for CO2 separation using silane coupling agents. *Journal of Membrane Science* **2016,** *497*, 216-220.

202.   Furuta, T.; Sakai, M.; Isobe, T.; Nakajima, A., Negative Line Tension for an Ionic Liquid on a Hydrophobic Fluoroalkylsilane Coating. *Chemistry Letters* **2009,** *38* (11), 1092-1093.

203.   Greenspan, L., Humidity fixed points of binary saturated aqueous solutions. *Journal of Research of the National Bureau of Standards Section A: Physics and Chemistry* **1977**, 89-96.

204.   Bahamon, D.; Vega, L. F., Systematic evaluation of materials for post-combustion CO2 capture in a Temperature Swing Adsorption process. *Chemical Engineering Journal* **2016,** *284*, 438-447.

205.   Pini, R., Interpretation of net and excess adsorption isotherms in microporous adsorbents. *Microporous and Mesoporous Materials* **2014,** *187*, 40-52.

206.   Socrates, G., *Infrared and Raman characteristic group frequencies: tables and charts*. Third ed.; Chichester, Wiley: 2001.

207.   Harlick, P. J. E.; Sayari, A., Applications of Pore-Expanded Mesoporous Silicas. 3. Triamine Silane Grafting for Enhanced CO2 Adsorption. *Industrial & Engineering Chemistry Research* **2006,** *45* (9), 3248-3255.

208.   Ulman, A., Formation and Structure of Self-Assembled Monolayers. *Chemical Reviews* **1996,** *96* (4), 1533-1554.

209.   Kurakevych, O. O.; Solozhenko, V. L., Rhombohedral boron subnitride, B13N2, by X-ray powder diffraction. *Acta Crystallographica Section C* **2007,** *63* (Pt 9), i80-2.

210.   Glueckauf, E., Theory of chromatography. Part 10.—Formulæ for diffusion into spheres and their application to chromatography. *Transactions of the Faraday Society* **1955,** *51* (0), 1540-1551.

211.   Ward, A.; Pini, R., Integrated uncertainty quantification and sensitivity analysis of single-component dynamic column breakthrough experiments. *Adsorption* **2022,** *28* (3), 161-183.

212.   Nuhnen, A.; Janiak, C., A practical guide to calculate the isosteric heat/enthalpy of adsorption via adsorption isotherms in metal–organic frameworks, MOFs. *Dalton Transactions* **2020,** *49* (30), 10295-10307.

213.   Bezus, A. G.; Kiselev, A. V.; Sedlaček, Z.; Du, P. Q., Adsorption of ethane and ethylene on X-zeolites containing Li+, Na+, K+, Rb+ and Cs+ cations. *Transactions of the Faraday Society* **1971,** *67* (0), 468-482.

214.   Jaroniec, M.; Jaroniec, J. A., On the characterization of microporous adsorbents. *Carbon* **1977,** *15* (2), 107-111.

215.   Azzan,   H.   *https://github.com/ImperialCollegeLondon/IsothermFittingTool*, isothermFitting, Accessed: 2023/03/15.

216.   Ng, K. C.; Burhan, M.; Shahzad, M. W.; Ismail, A. B., A Universal Isotherm Model to Capture Adsorption Uptake and Energy Distribution of Porous Heterogeneous Surface. *Scientific Reports* **2017,** *7* (1), 10634.

217.   Pini, R.; Joss, L.; Hosseinzadeh Hejazi, S. A., Quantitative imaging of gas adsorption equilibrium and dynamics by X-ray computed tomography. *Adsorption* **2021,** *27* (5), 801-818.
218.   Mewes, D., Physical Property Data for the Design Engineer. *Chemie Ingenieur Technik* **1989,** *61* (10), 774.
219.   Zwolinki, B. J. In *Selected values of properties of chemical compounds : Thermodynamics Research Center data project*, 1969.
220.   Assael, M. J.; Bogdanou, I.; Mylona, S. K.; Huber, M. L.; Perkins, R. A.; Vesovic, V., Reference Correlation of the Thermal Conductivity ofn-Heptane from the Triple Point to 600 K and up to 250 MPa. *Journal of Physical and Chemical Reference Data* **2013,** *42* (2).
221.   Wang, C. Y.; Yang, M. L., A new calorimeter for measuring rapidly the thermal conductivity of liquids. *Thermochimica Acta* **1995,** *255*, 365-370.
222.   Moore, J. W.; Wellek, R. M., Diffusion coefficients of n-heptane and n-decane in n-alkanes and n-alcohols at several temperatures. *Journal of Chemical & Engineering Data* **1974,** *19* (2), 136-140.
223.   Lapuerta, M.; Hernández, J. P.; Agudelo, J. R., An equation for the estimation of alcohol-air diffusion coefficients for modelling evaporation losses in fuel systems. *Applied Thermal Engineering* **2014,** *73* (1), 539-548.
224.   NIST, Water, NIST Chemistry Webbook. Accessed: 23/03/2023. https://webbook.nist.gov/cgi/cbook.cgi?ID=C7732185&Units=SI&Mask=7&Type=JANAFG &Table=on#ref-1 ed.; 2021.
225.   Li, S.; Lu, X.; Lou, Y.; Liu, K.; Zou, B., The Synthesis and Characterization of h-BN Nanosheets with High Yield and Crystallinity. *ACS Omega* **2021,** *6* (42), 27814-27822.
226.   Djilani, C.; Zaghdoudi, R.; Djazi, F.; Bouchekima, B.; Lallam, A.; Modarressi, A.; Rogalski, M., Adsorption of dyes on activated carbon prepared from apricot stones and commercial activated carbon. *Journal of the Taiwan Institute of Chemical Engineers* **2015,** *53*, 112-121.
227.   Thomson, G. W., The Antoine Equation for Vapor-pressure Data. *Chemical Reviews* **1946,** *38* (1), 1-39.
228.   Majer, V.; Svoboda, V., *Enthalpies of vaporization of organic compounds: a critical review and data compilation*. Blackwell Scientific Publications,Oxford, England: United Kingdom, 1986.
229.   Brunauer, S.; Deming, L. S.; Deming, W. E.; Teller, E., On a Theory of the van der Waals Adsorption of Gases. *Journal of the American Chemical Society* **1940,** *62* (7), 1723-1732.
230.   Ballou, E. V., Discontinuities in the adsorption isotherm of n-heptane on molybdenum disulfide. *Journal of the American Chemical Society* **1954,** *76* (4), 1199-1200.
231.   Singleton, J. H.; Halsey, G. D., Jr., The Solution of Argon in Layers of Krypton. *The Journal of Physical Chemistry* **1954,** *58* (11), 1011-1017.
232.   Corrin, M. L.; Rutkowski, C. P., Discontinuities in Adsorption Isotherms. *The Journal of Physical Chemistry* **1954,** *58* (12), 1089-1090.
233.   Clark, H., Vertical Discontinuities in the Adsorption Isotherm of Krypton on Graphitized Carbon Black. *The Journal of Physical Chemistry* **1955,** *59* (10), 1068-1069.

APPENDICES

Appendix 1

There were originally five types of isotherms, from I to V, as introduced by Brunauer et al. in 1940.[229] A sixth type of isotherm, referred to as VI, was added later on after reports of stepped isotherms by Ballou,[230] Singleton and Halsey[231], and Corrin and Rutkowski[232] in 1954, followed by a thorough discussion by Clark in 1955.[233] Herein, I will describe the different types of isotherms and their main characteristics (**Figure A1.1**).[75]
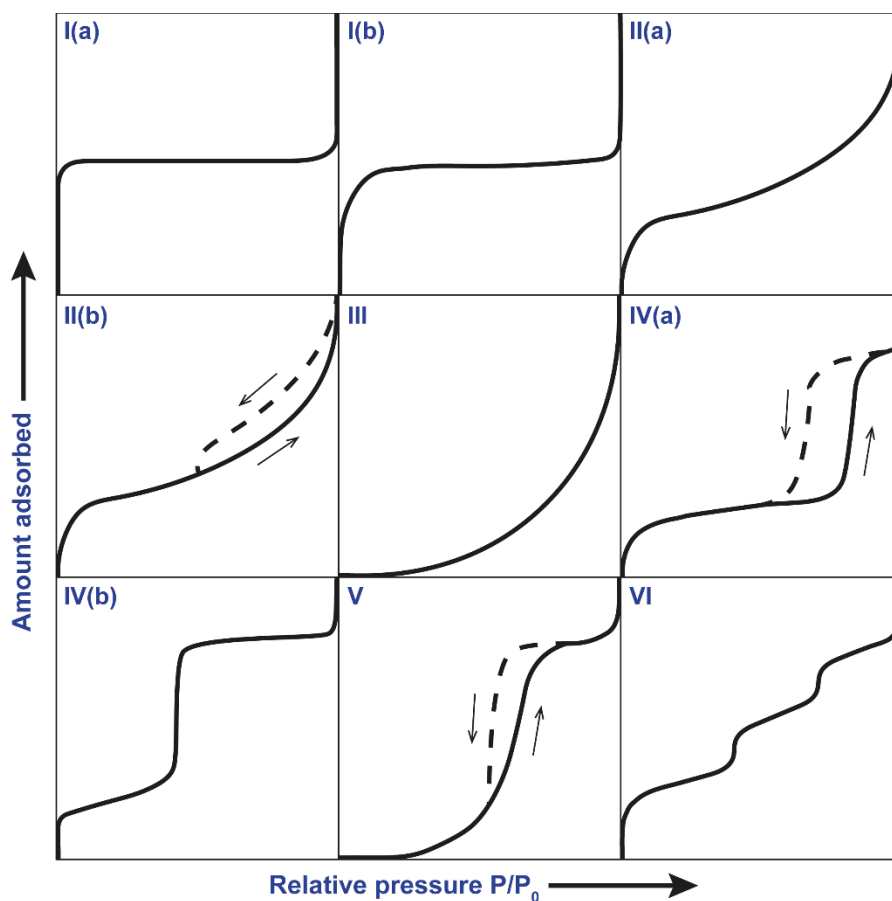
Figure A1.1 Adsorption isotherm types as defined by the International Union of Pure and Applied Chemistry (IUPAC).

Type I isotherms are reversible and correspond to microporous adsorbents. A plateau is reached at low relative pressure, indicating a narrow pore size distribution and a small external surface area. Type I(a) isotherms exhibit very steep uptake and correspond to the filling of narrower micropores than in type I(b) isotherms. Type II isotherms correspond to non-porous or macroporous adsorbents. The first part of the isotherm, prior to the middle quasi-linear section, represents the monomolecular coverage of the surface, called the monolayer. After that, a multimolecular layer starts forming, called the multilayer. Type II(a) isotherms are reversible, whereas type II(b) exhibit some hysteresis between adsorption and desorption, due to inter-particle capillary condensation. Type III isotherms correspond to non-porous or macroporous adsorbents with low adsorbent-adsorbate interactions. Type IV isotherms are similar to type II isotherms in the lower relative pressure region, but they show a saturation plateau at higher relative pressure before levelling off. Type IV isotherms are typical of mesoporous adsorbents. Type IV(a) isotherms display some hysteresis due to capillary condensation, whereas type IV(b) isotherms are reversible. Type V isotherms are close to type III isotherms until reaching a plateau and then levelling off. They correspond to microporous or mesoporous adsorbents with low adsorbent-adsorbate interactions. Type VI isotherms represent layer-by-layer adsorption with several steps observed and are quite rare.

At pressures small enough, most isotherms simplify to a linear form, which assumes that there are negligible interactions between the adsorbed molecules.[75] In this linear region, one can apply Henry's law shown in the equation below:

$$q^* = k_H P$$

with:

q^* adsorbed amount per unit weight of adsorbent ($cm^3 \ g^{-1}$)

k_H Henry's law constant ($cm^3 \ g^{-1} \ torr^{-1}$)

P Pressure (torr)

Appendix 2

Chemical aspects of the pilot-plant samples
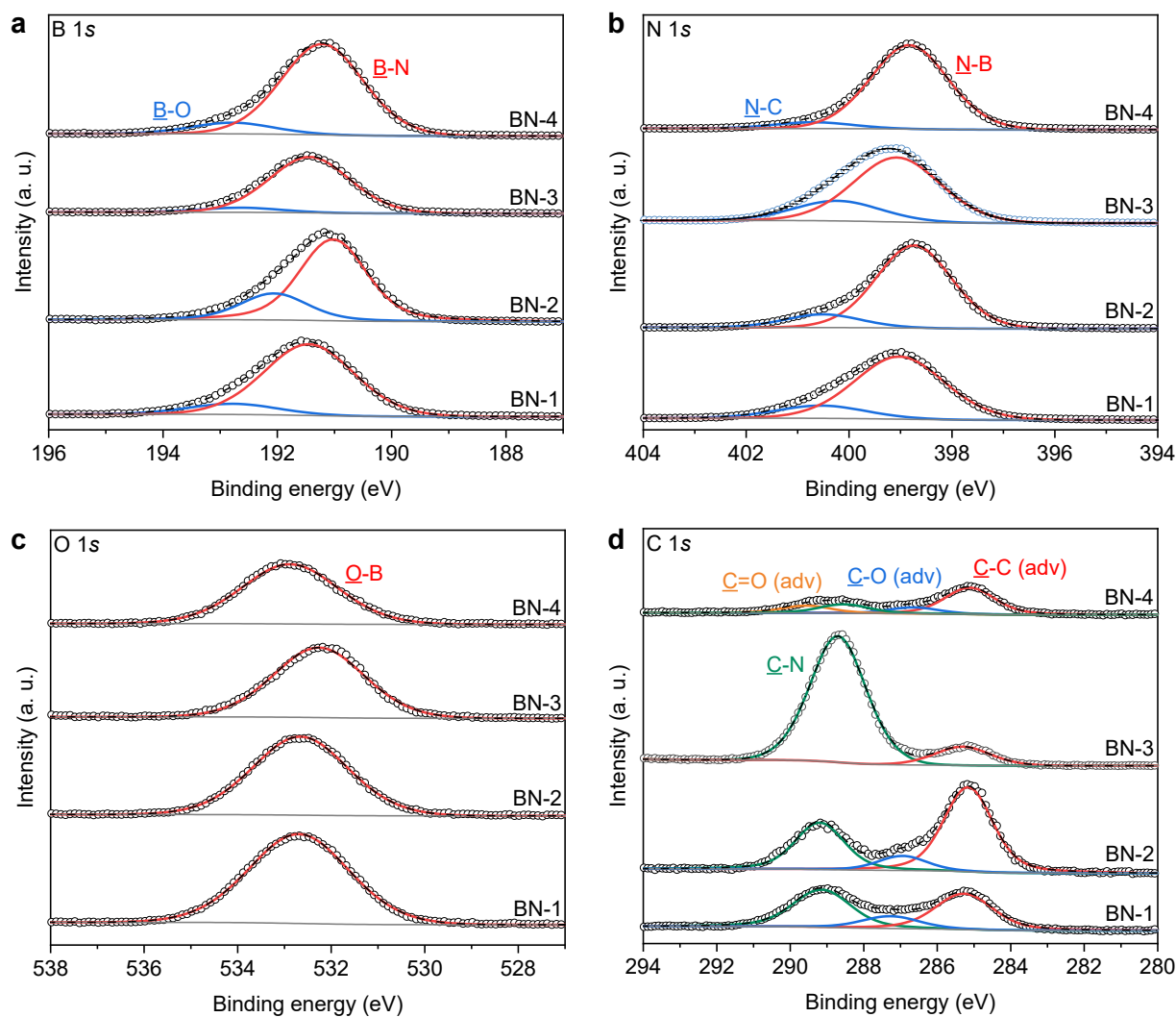
Figure A2.1 High-resolution XPS and peak fitting of the (a) B 1*s* (b) N 1*s* (c) O 1*s* and (d) C 1*s* core levels for all the pilot-plant samples BN-1 to BN-4 introduced in Chapter 5. Note: 'adv' = adventitious.
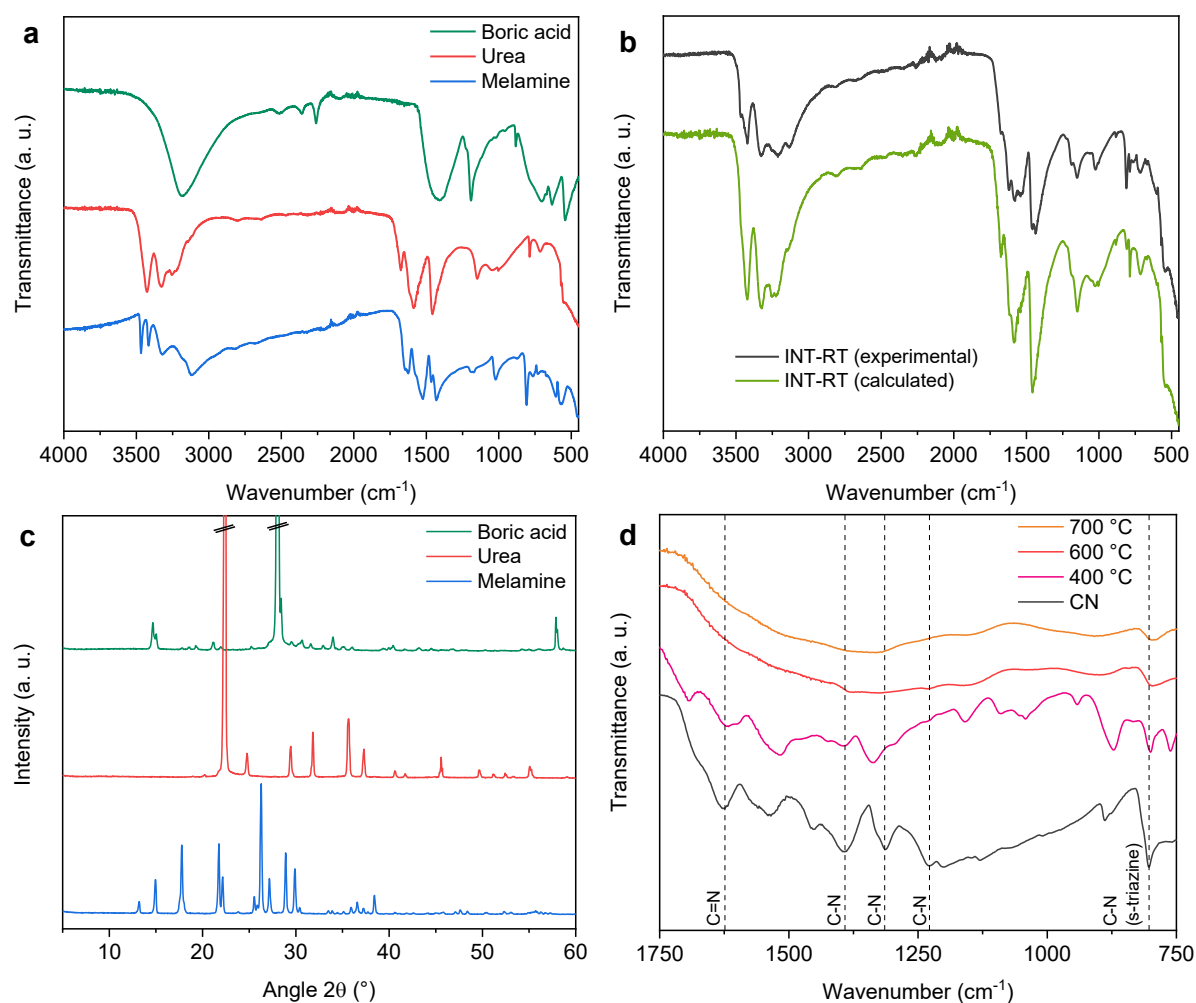
Figure A2.2 (a) FTIR spectra for each individual precursor. (b) FTIR spectra for INT-RT based on measurement ('experimental') and calculation ('calculated'). (c) XRD patterns for each individual precursor. (d) FTIR spectra for carbon nitride (CN) in comparison with INT-400, INT-600 and INT-700.

Table A2.1 Atomic composition derived from XPS analysis and calculated atomic composition for sample INT-RT corresponding to the initial mixture of reagents (BA:M:U = 1:1:5). <u>Note:</u> H atoms are not detected in XPS.

Atom	Calculated quantity (%at)	Measured quantity (%at)
B	3	14
N	49	37
O	24	28
C	24	22

Figure A2.3 shows the calculated ^{11}B δ_{iso} for the various models of N and O arrangements around B (see structures in the insets). Note that for the tetrahedral B species, simple clusters of the formula $[B(NH_2)_n(OH)_{4-n}]^-$ were used, whereas for trigonal B, a slightly larger model, approximating the structure of BN was used. However, these models tended to distort significantly on optimization (the under-bonded N atoms favoring sp^3 rather than sp^2 hybridization), and it was not possible to embed a tetrahedral B species in these small models.

The computed δ_{iso} values allow assignment of the NMR resonances from trigonal B species as discussed in the main text. However, for the tetrahedral B species, while δ_{iso} varies systematically with the number of bonded N and O, this is over a much smaller shift range and definitive assignment of the various tetrahedral B species observed in this study was not possible.
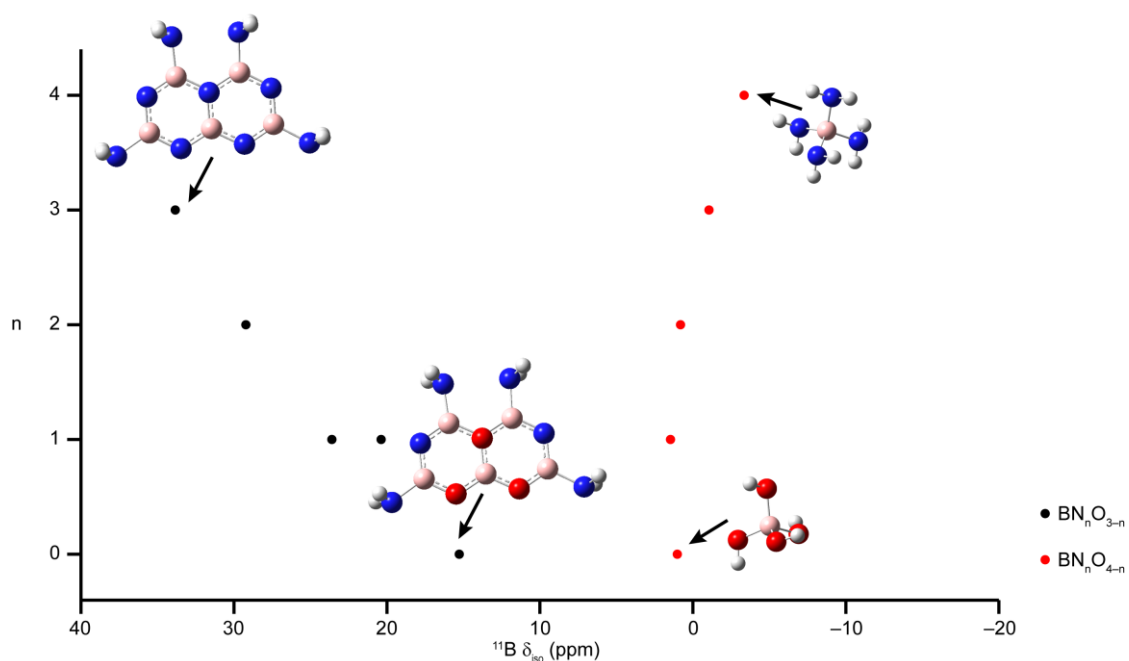
Figure A2.3 Plot of calculated ^{11}B δ_{iso} as a function of number of bonded nitrogen atoms (n) for tetrahedral BN$_n$O$_{4-n}$ (red points, $0 \leq n \leq 4$) and trigonal BN$_n$O$_{3-n}$ (black points, $0 \leq n \leq 3$)

species. Examples for n = 0 and n = 3 or 4 input structures are shown, with atoms colored B = pink, N = blue, O = red and H = white.
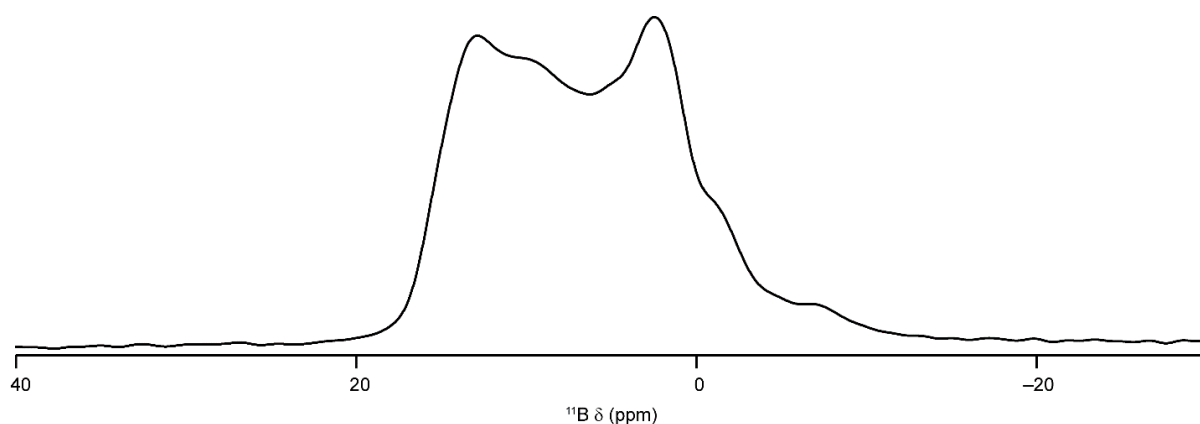
Figure A2.4 ^{11}B MAS NMR spectrum of B_2O_3, showing that the material is predominantly trigonal B. The spectrum was recorded using a Bruker Avance III spectrometer equipped with a wide-bore 9.4 T superconducting magnet (^{11}B Larmor frequency of 128.4 MHz) and a standard Bruker 4-mm MAS probe head. The sample was ground and packed into a zirconia rotor, and rotated about an axis inclined at the magic angle at a rate of 14 kHz. Spectra were acquired using a single soft pulse (ν_1 ~20 kHz) of short flip angle (β ~7°). Signal averaging was carried out for 32 transients with a recycle interval of 60 s. Chemical shifts are shown relative to $BF_3.Et_2O$ using BPO_4 ($\delta = -3.3$ ppm) as a secondary solid reference.
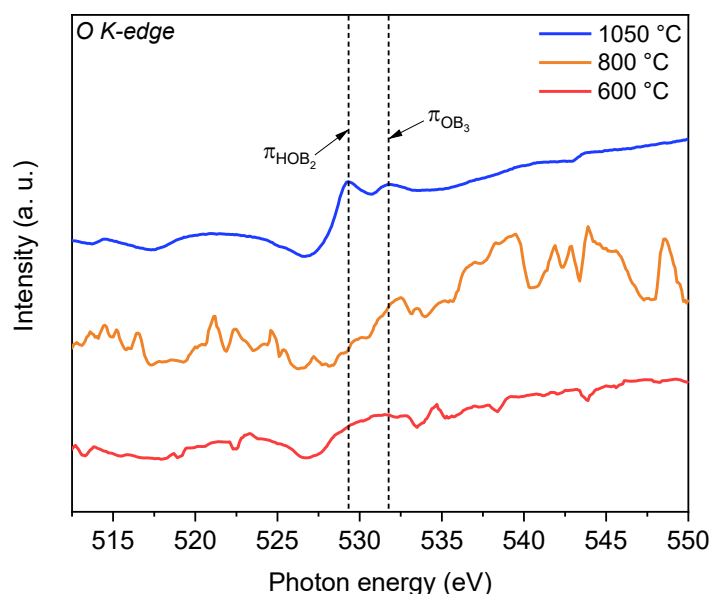
Figure A2.5 NEXAFS O K-edge spectra for the intermediates at 600 °C, 800 °C and the final product BN-1050-t$_{3.5}$.

Functionalization with PTS and OTS grafting agents
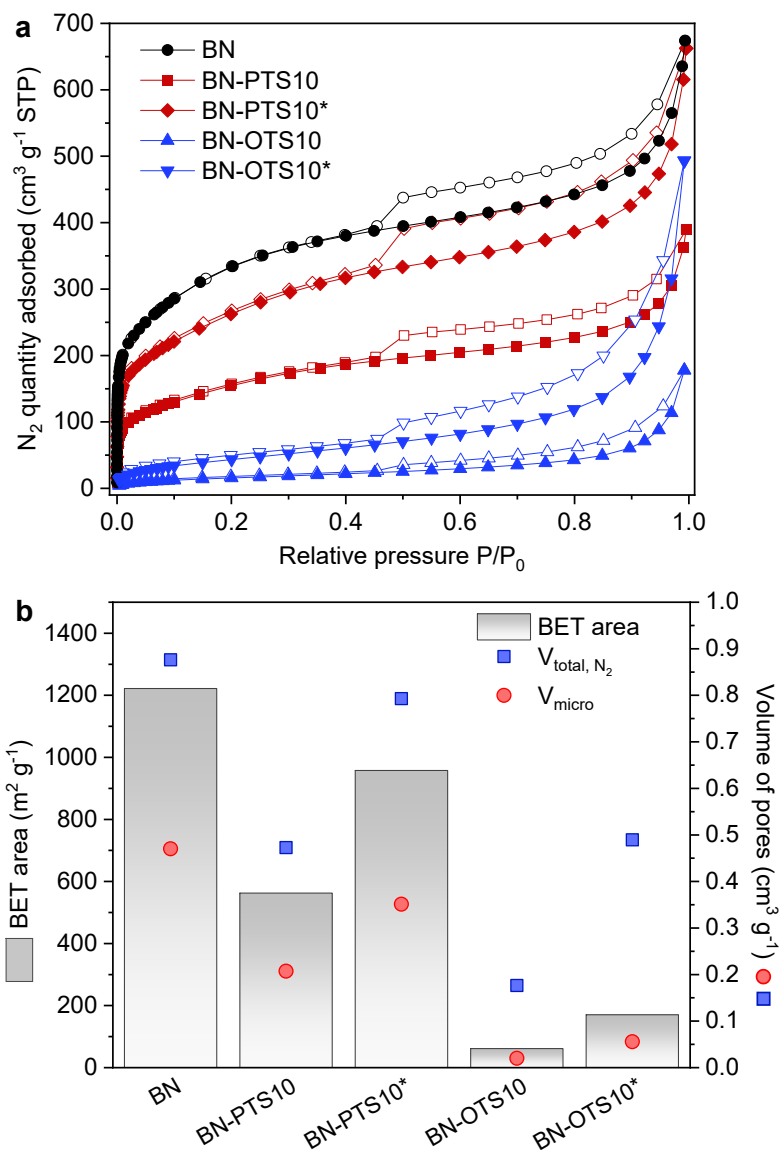
Figure A3.1 (a) N_2 sorption isotherms at $-196\,°C$ for unmodified porous BN and functionalized porous BN with n-propyltrichlorosilane (PTS) and n-octadecyltrichlorosilane (OTS) silane agents (10 mmol per g of BN for each). (b) Associated textural parameters extracted from N_2 sorption measurements. <u>Note 1:</u> total pore volumes $V_{tot,\,N_2}$ correspond to pore sizes up to 12 nm as obtained from N_2 sorption. <u>Note 2:</u> '*' indicates results after weight adjustment, based on the atomic composition derived from XPS measurements.
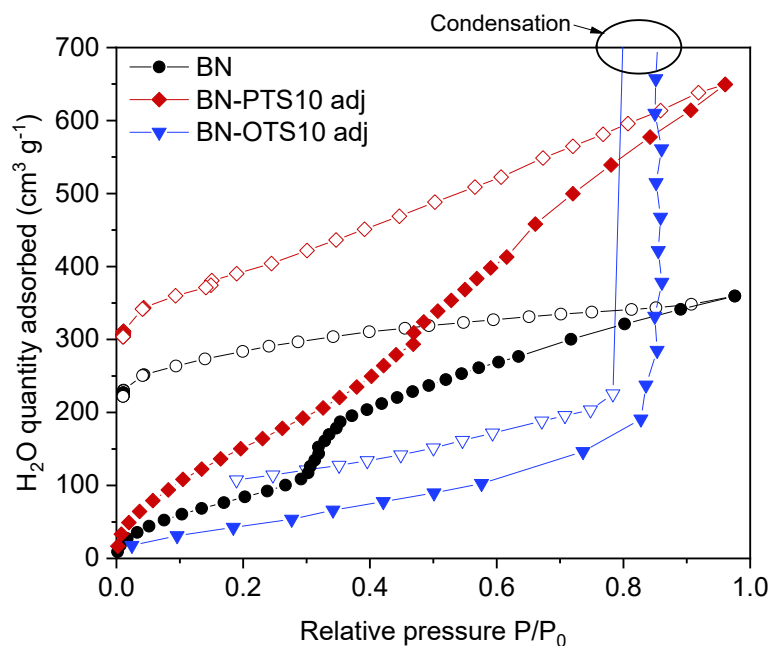
Figure A3.2 Water vapor sorption isotherms at 22 °C for pristine porous BN, and functionalized porous BN with 10 mmol per g of BN of PTS or OTS (after weight adjustment based on XPS measurements).

Additional characterization results to confirm functionalization

A zoomed-in FTIR spectrum in the range 500-1500 cm^{-1} is presented to better observe bonds involving silicon and fluorine in the functionalized sample BN-FAS (**Figure A3.3**a). XRD patterns were collected for all samples, which appeared all highly amorphous (**Figure A3.3**b).
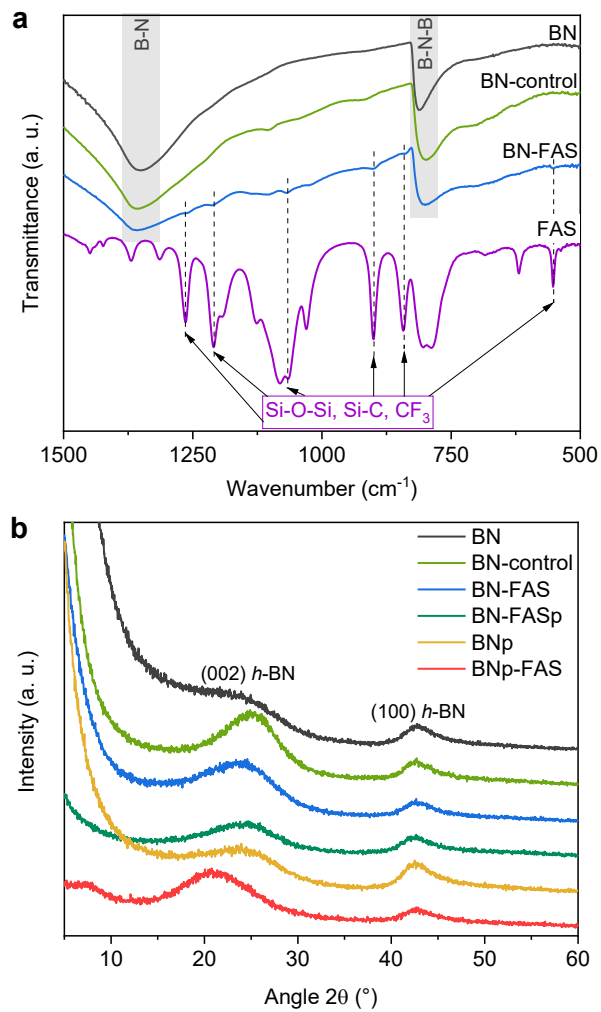
Figure A3.3 (a) FTIR spectra in the range 500-1500 cm^{-1}. (b) XRD profiles for all samples.

The F 1*s* spectrum of unmodified porous BN is shown to confirm that no fluorine atoms were detected before functionalization (**Figure A3.4**).
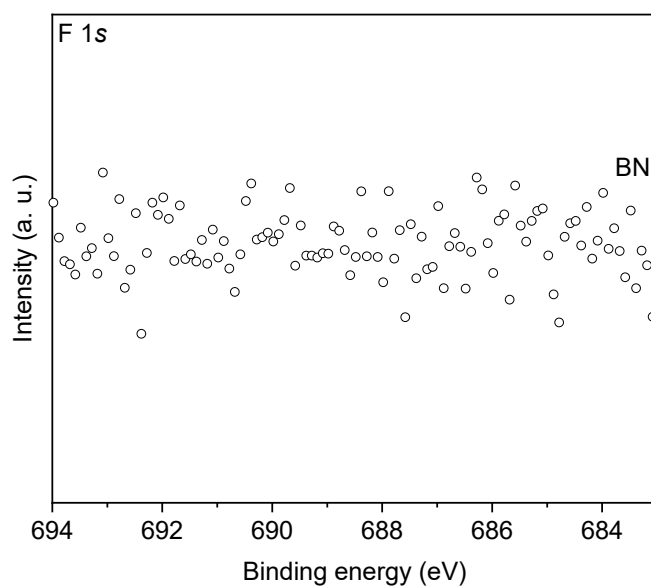
Figure A3.4 High-resolution XPS of the F 1*s* core level of unmodified porous BN (only noise observed).

Control sample for route 1

A control sample (BN-control) was synthesized via the route 1 method, without using FAS to check the potential impact of the silylation method itself. We observed a decrease in both surface area and porosity in BN-control (**Figure A3.5**), implying an impact from the solvents involved in route 1, i.e., toluene and ethanol. This would explain the decreased surface area seen in BN-FAS obtained via route 1.
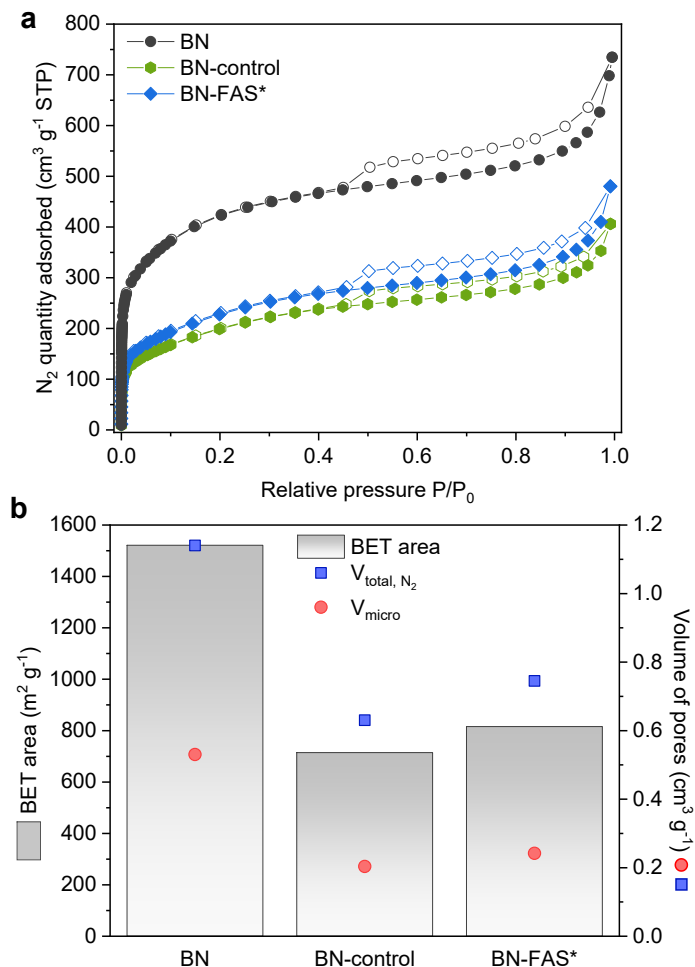
Figure A3.5 (a) N_2 sorption isotherms at -196 °C and (b) Derived textural parameters for porous BN powder, BN-control and BN-FAS* (after weight adjustment, see paragraph 5 in SI) obtained via route 1. <u>Note:</u> total pore volumes V_{tot, N_2} correspond to pore sizes up to 12 nm as obtained from N_2 sorption.

SEM images of the pellets

SEM was used to compare the structure of unmodified and functionalized porous BN pellets, looking both at the external surface and at a cross-section. SEM images were obtained with the lead of Dr. Marcus H. N. Yio at Imperial College London.

Pelletized samples were directly mounted onto carbon tape to observe the top surface in SEM (**Figure A3.6**), whereas the samples prepared for μXRF (see section 6.4.3) were directly used to look at their cross-sections (**Figure A3.7**). The samples were not coated for these SEM measurements. SEM was carried out with a Hitachi TM4000 tabletop microscope in

backscattered electron (BSE) mode at 10 kV. Magnifications of x100, x500 and x1500 were used for each sample.

	BNp	BN-FASp	BNp-FAS
x100			
x500			
x1500			
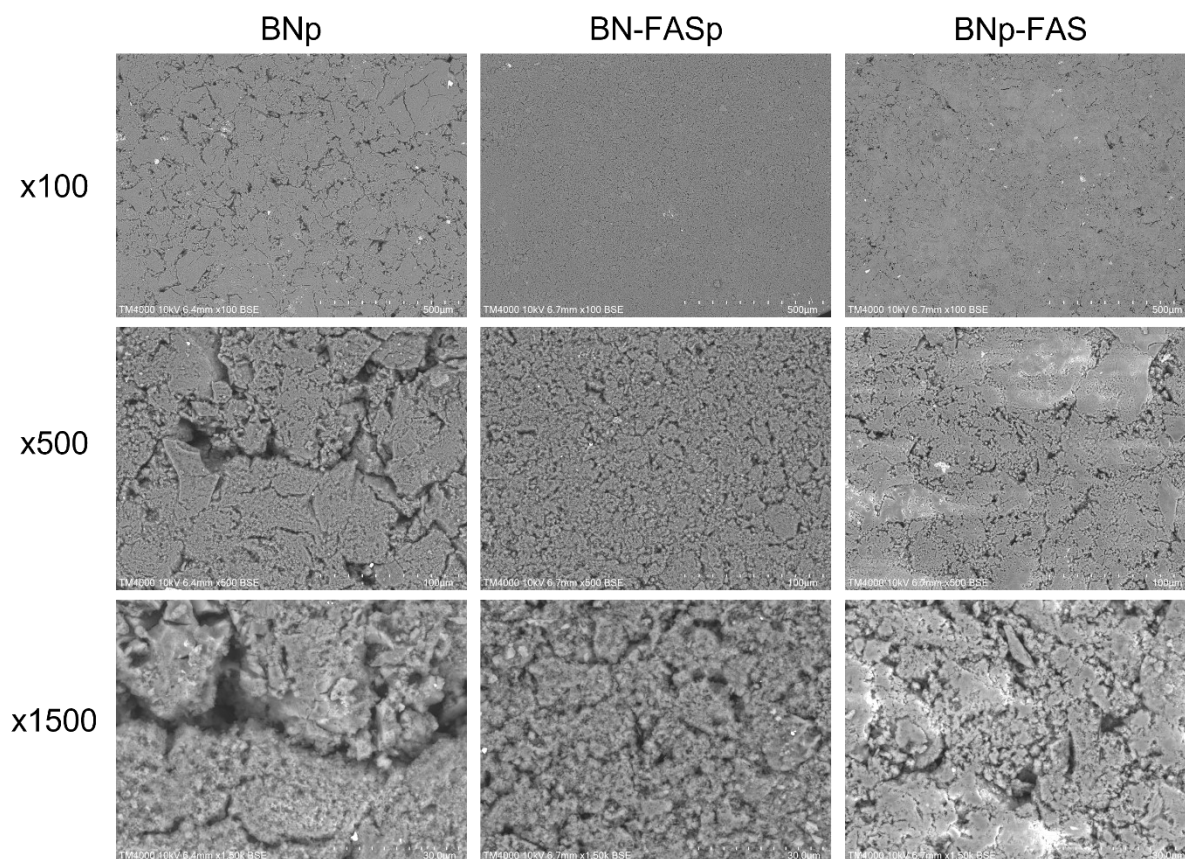
Figure A3.6 SEM images of the top surface of unmodified and functionalized porous BN pellets at magnifications 100, 500 and 1500.
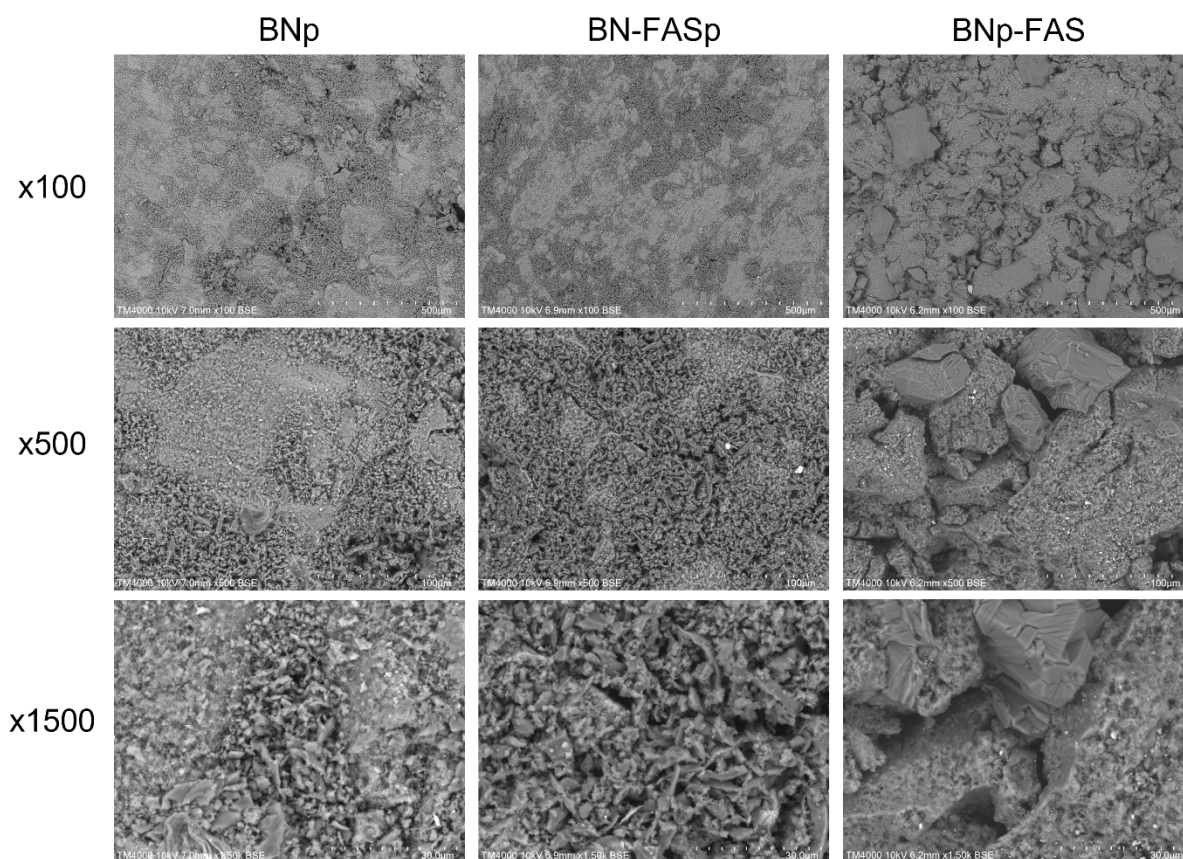
Figure A3.7 SEM images of the cross-section of unmodified and functionalized porous BN pellets at magnifications 100, 500 and 1500.

Additional characterization results to probe moisture impact

XPS was used on all pelletized samples prior to and after moisture exposure to understand the impact of moisture on their chemistry. Herein, we reported the Si $2s$ spectra for the functionalized pellets, BN-FASp and BNp-FAS (**Figure A3.8**).
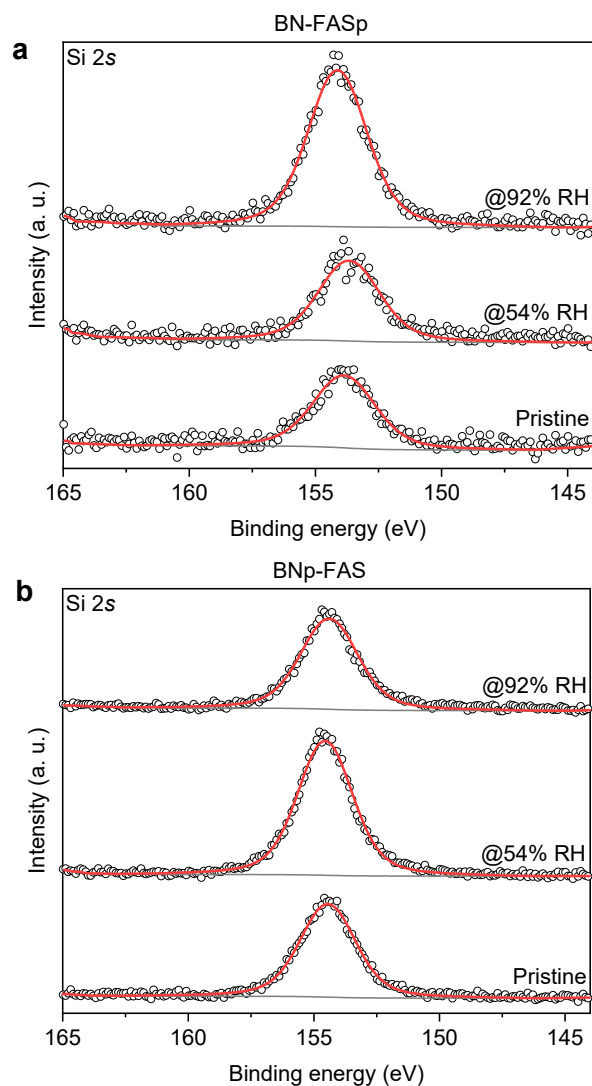
Figure A3.8 High-resolution XPS and peak fitting of the Si 2*s* core level before and after humidity testing for: (a) BN-FASp and (b) BNp-FASp.

In Chapter 6, we measured XRD and N_2 sorption isotherms at -196 °C before and after humidity exposure at 52% and 92% relative humidity levels for the pelletized samples. **Figure A3.9** shows these results for all powder and pelletized samples, including the textural parameters obtained from these isotherms.
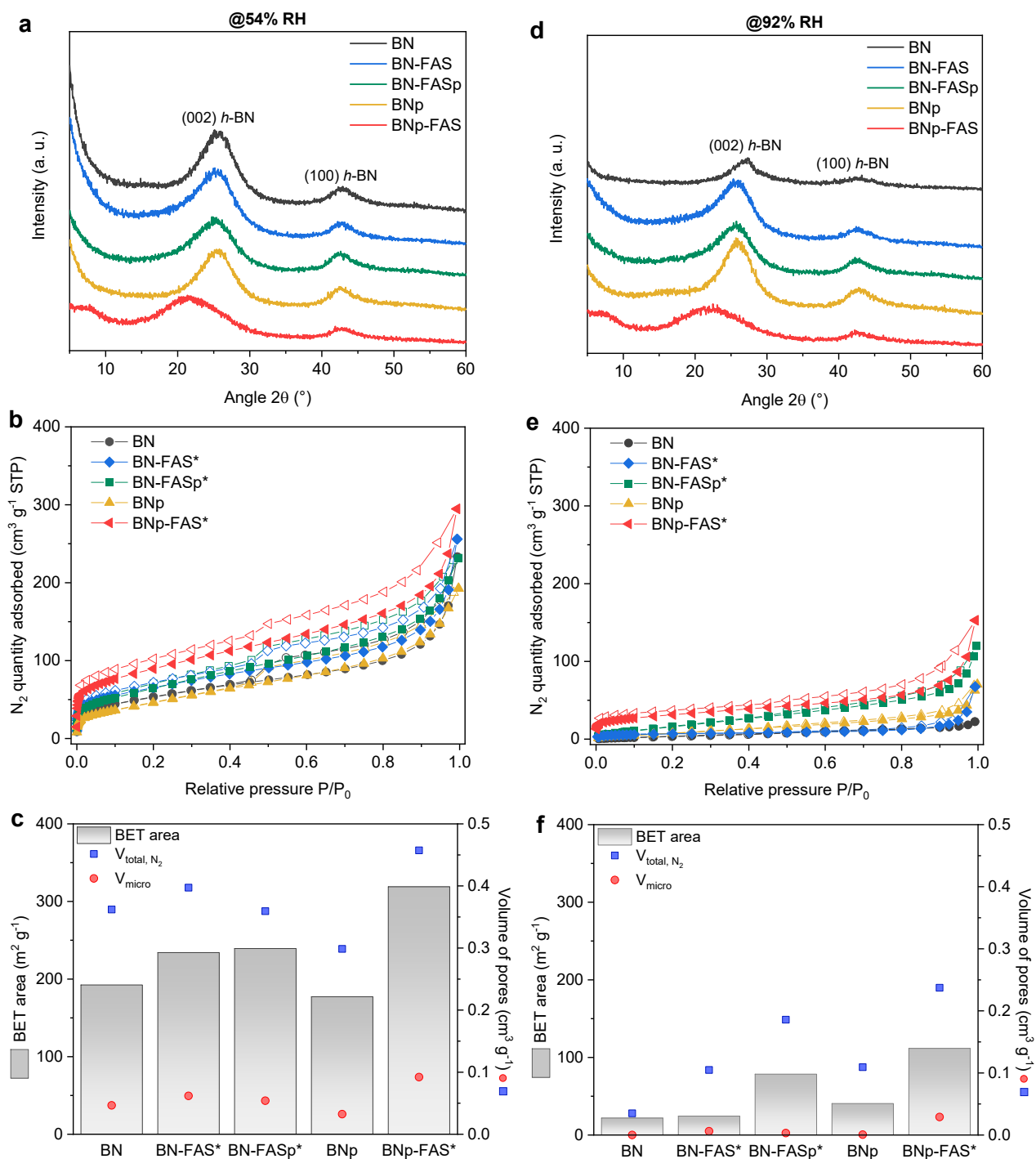
Figure A3.9 XRD patterns for all powder and pelletized samples after humidity exposure at: (a) 54% RH and (d) 92% RH. N_2 sorption isotherms at –196 °C for all powder and pelletized samples after exposure at: (b) 54% RH and (e) 92% RH. Derived textural parameters after exposure at: (c) 54% RH and (f) 92% RH.

Kinetics sorption study – Validation of experimental desorption curves

The experimental desorption curves shown later (**Figure A3.12**) used for the kinetic sorption study were validated by carrying out a mass balance on the CO_2 exiting the adsorption cell (following a blank volume correction of the set-up), and comparing the resulting CO_2 desorbed from the sorbent with the isotherm models obtained by fitting the volumetrically-obtained CO_2 isotherms to a relevant adsorption model. The amount of desorbed CO_2 from a given desorption curve was calculated using the following equation:

$$q^*_{CO_2,des} = \frac{P}{RTm_{ads}} \int_0^{t_{des}} \left(F_{des}(t) y_{CO_2,des}(t) - F_{blank}(t) y_{CO_2,blank}(t) + V_{ads} \right) dt$$

where $q^*_{CO_2,des}$ [mol kg^{-1}] is the predicted CO_2 loading at the temperature and the initial partial pressure of CO_2 in the system, P is the total pressure [bar], R is the universal gas constant [J mol^{-1} K^{-1}], T is the absolute temperature [K], m_{ads} is the mass of adsorbent [kg], F is the total flowrate out of the adsorption cell [m^3 s^{-1}], y_{CO_2} is the mole fraction of CO_2 at the mass spectrometer (which can be measured in the range of 0.01 to 1), V_{ads} is the volume of the adsorbent [m^3], and t_{des} is the duration of the experimental desorption experiment [s]. The subscript 'des' corresponds to the desorption experiment, and 'blank' corresponds to the blank model obtained by fitting a transport model to blank experiments. The result of this comparison is shown in **Figure A3.10**. The results show good agreement between the two methods with a difference less than 10%, particularly when accounting for the low adsorption capacity in the functionalized BN pellets. It should also be noted that the CO_2 loading obtained by integrating the desorption curves will be expected to be lower than the true value, since the mole fraction of CO_2 (y_{CO_2}) can only be accurately measured down to 0.01 using the mass spectrometer. Therefore, the amount of CO_2 desorbed below this range will not be included in the mass balance.
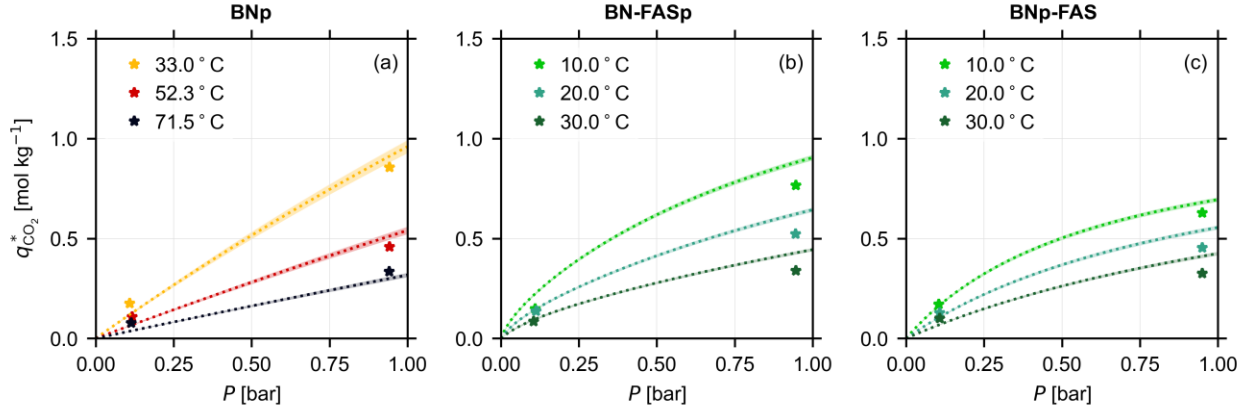
Figure A3.10 Comparison of CO_2 adsorption equilibrium ($q^*_{CO_2}$) prediction between model fits to volumetric data (dashed lines) and equilibrium loading obtained by carrying out a mass balance on the experimental desorption curves obtained at high and low feed compositions of CO_2 (stars).

Kinetics sorption study – Equilibrium isotherm models and kinetic rate model

The experimental CO_2 equilibrium isotherms obtained volumetrically (shown in **Figure 6.21**a-c Chapter 6) were fitted to a single-site Langmuir (SSL) model for CO_2 on BNp and BNp-FAS, and a dual-site Langmuir (DSL) model was used for BN-FASp. The DSL model is given by:

$$q^*_{CO_2} = \frac{q_{sb,CO_2} b_{CO_2} c_{CO_2}}{1 + b_{CO_2} c_{CO_2}} + \frac{q_{sd,CO_2} d_{CO_2} c_{CO_2}}{1 + d_{CO_2} c_{CO_2}}$$

$$b_{CO_2} = b_{0,CO_2} \exp(\frac{-\Delta U_{b,CO_2}}{RT})$$

$$d_{CO_2} = d_{0,CO_2} \exp(\frac{-\Delta U_{d,CO_2}}{RT})$$

$$c_{CO_2} = \frac{P y_{CO_2}}{RT}$$

where $q^*_{CO_2}$ [mol kg^{-1}] is the absolute amount of CO_2 adsorbed on the adsorbent; c_{CO_2} [mol m^{-3}] is the bulk phase gas concentration calculated using the ideal gas law at a given gas mole fraction c_{CO_2} [−], an absolute pressure P [Pa], and an absolute temperature T [K]; R [J mol^{-1} K^{-1}] is the universal gas constant; q_{sb,CO_2} [mol kg^{-1}] and q_{sd,CO_2} [mol kg^{-1}] are the saturation

capacities for the two energetically different adsorption sites; b_{CO_2} [m^3 mol^{-1}] and d_{CO_2} [m^3 mol^{-1}] are the temperature-dependent adsorption coefficients for the corresponding sites, each described by an Arrhenius expression with two constants, b_{0,CO_2} [m^3 mol^{-1}] and $-\Delta U_{b,CO_2}$ [J mol^{-1}] for the first site, and d_{0,CO_2} [m^3 mol^{-1}] and $-\Delta U_{d,CO_2}$ [J mol^{-1}] for the second site, respectively. For a single-site Langmuir model, we neglect the second site in the DSL model, which reduces the DSL model to an SSL model.

The lumped kinetic rate constant k_{CO_2} is given by the following expression:

$$\frac{1}{k_{CO_2}} = \frac{1}{k_{1,CO_2}} + \frac{\left(\dfrac{dq^*_{CO_2}}{dc_{CO_2}}\right)}{k_{2,CO_2}}$$

Kinetics sorption study – Modifications to experimental set-up
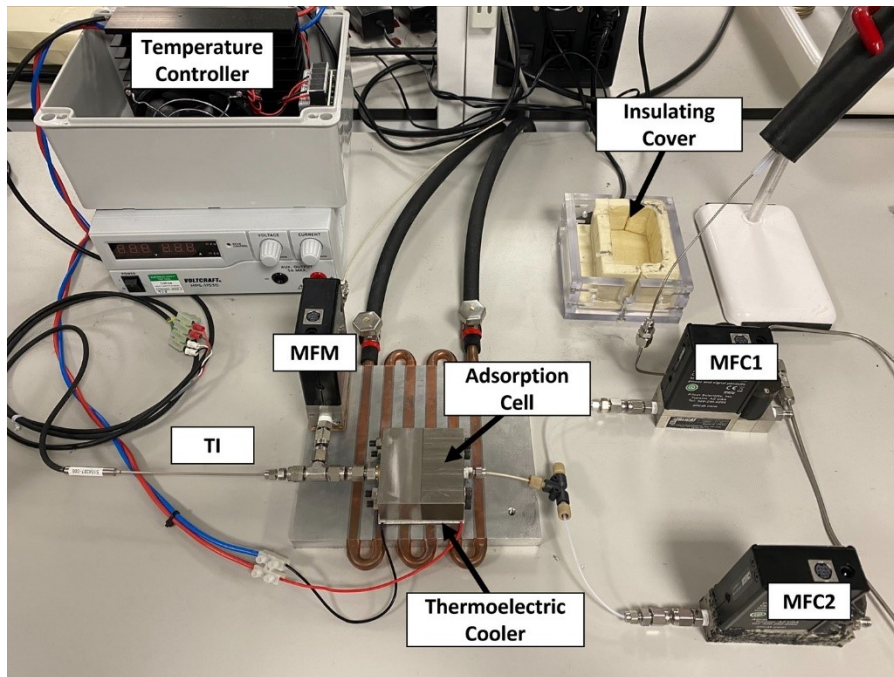
Figure A3.11 Modified experimental set-up from Azzan et al.[178] showing the modifications to the temperature control system and the modified adsorption cell.
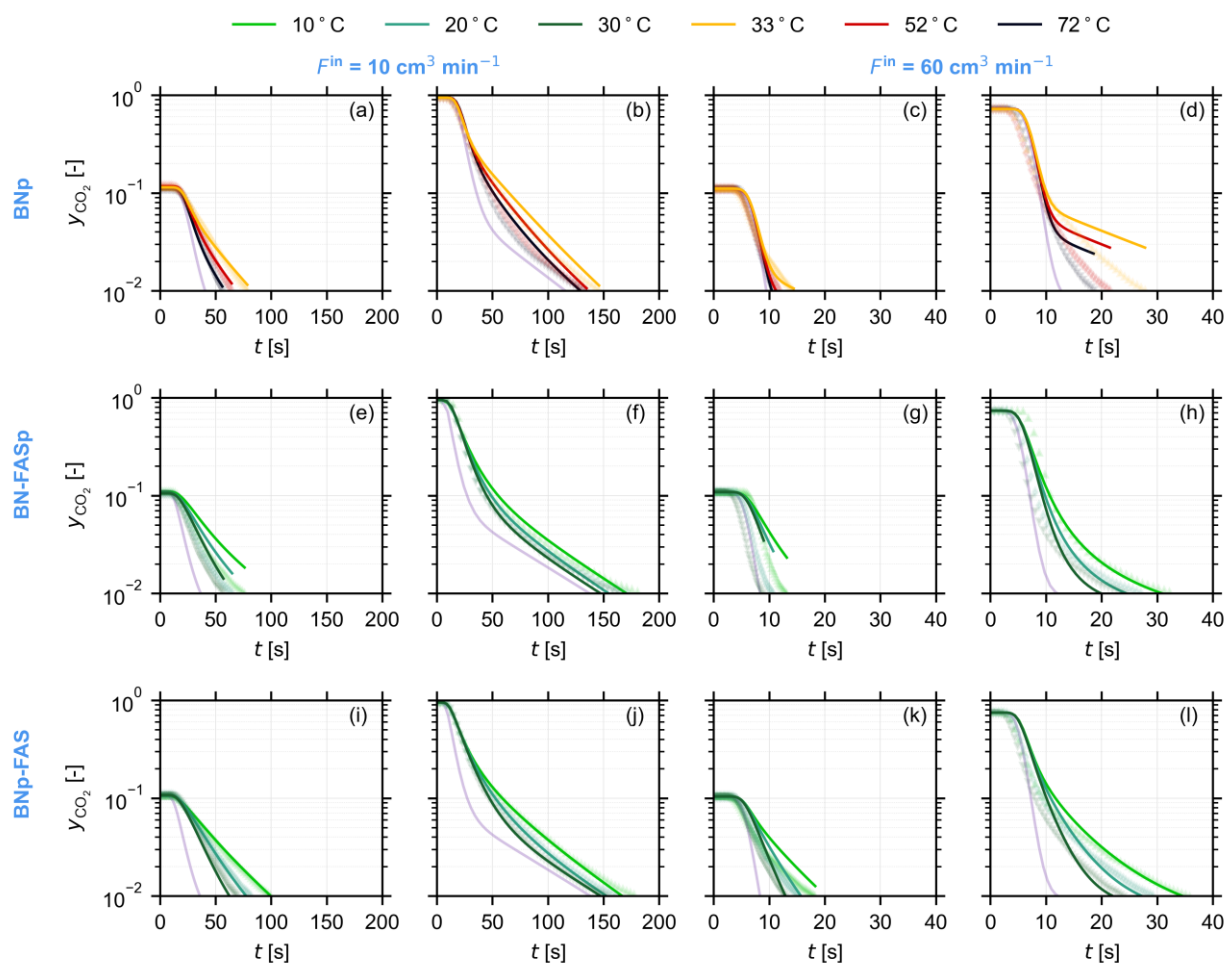
Figure A3.12 Experimental and simulated desorption responses for: (a-d) BNp, at 33, 52 and 72 °C; (e-h) BN-FASp, at 10, 20 and 30 °C; (i-l) BNp-FAS, at 10, 20 and 30 °C. The markers show the time evolution of the CO_2 composition y_{CO_2}, and the solid lines show the corresponding simulated response obtained using the optimal kinetic parameters and equilibrium model fits shown in Table 6.4. The light purple curve in each panel represents the blank response of the set-up at the given flowrate and initial composition of CO_2.

Appendix 4

Additional characterization results
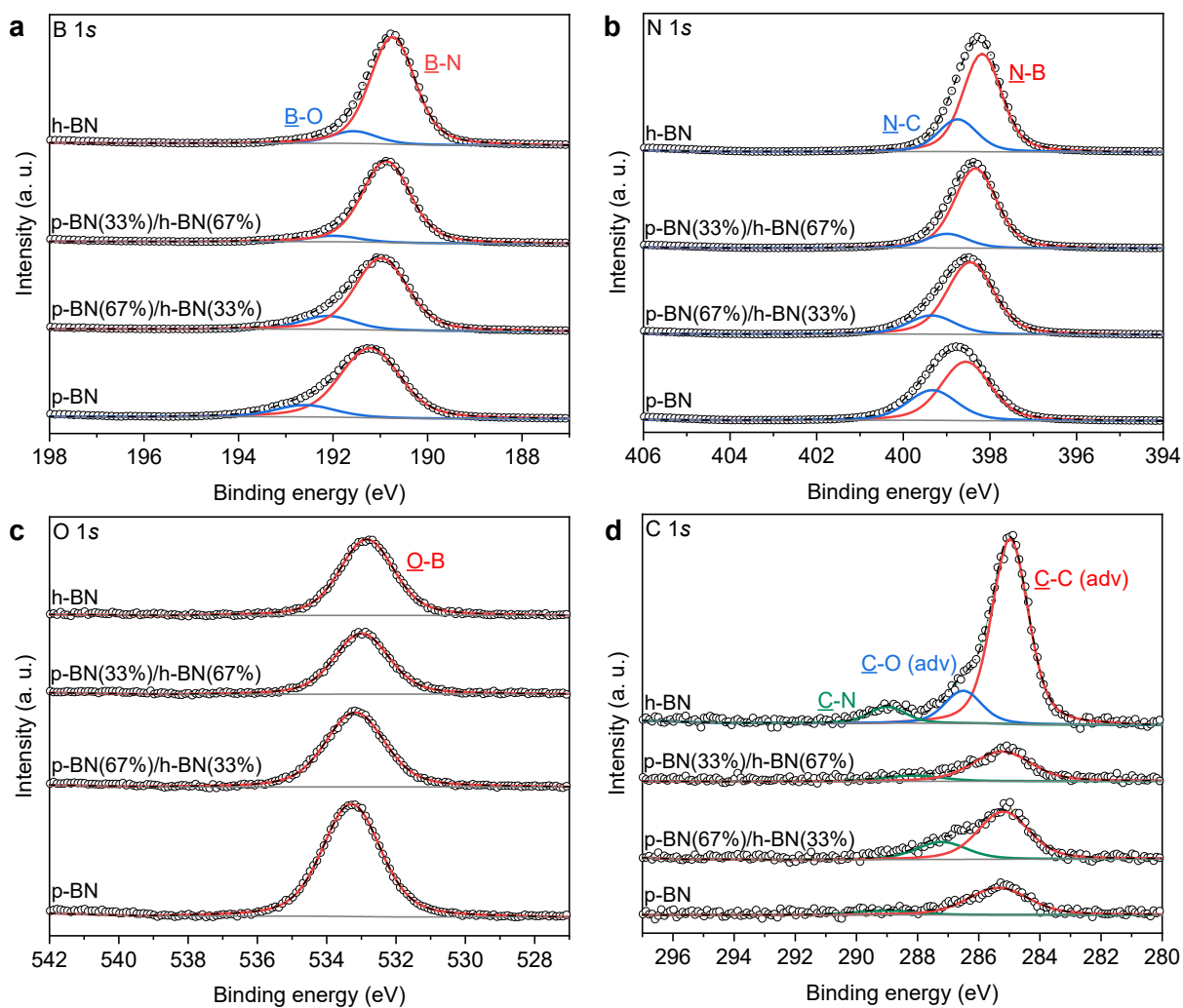
Figure A4.1 High-resolution XPS and peak fitting of the (a) B 1*s*, (b) N 1*s*, (c) O 1*s* and (d) C 1*s* core levels of the BN-based materials: p-BN, p-BN(67%)/h-BN(33%), p-BN(33%)/h-BN(67%) and h-BN. <u>Note:</u> 'adv' = adventitious.
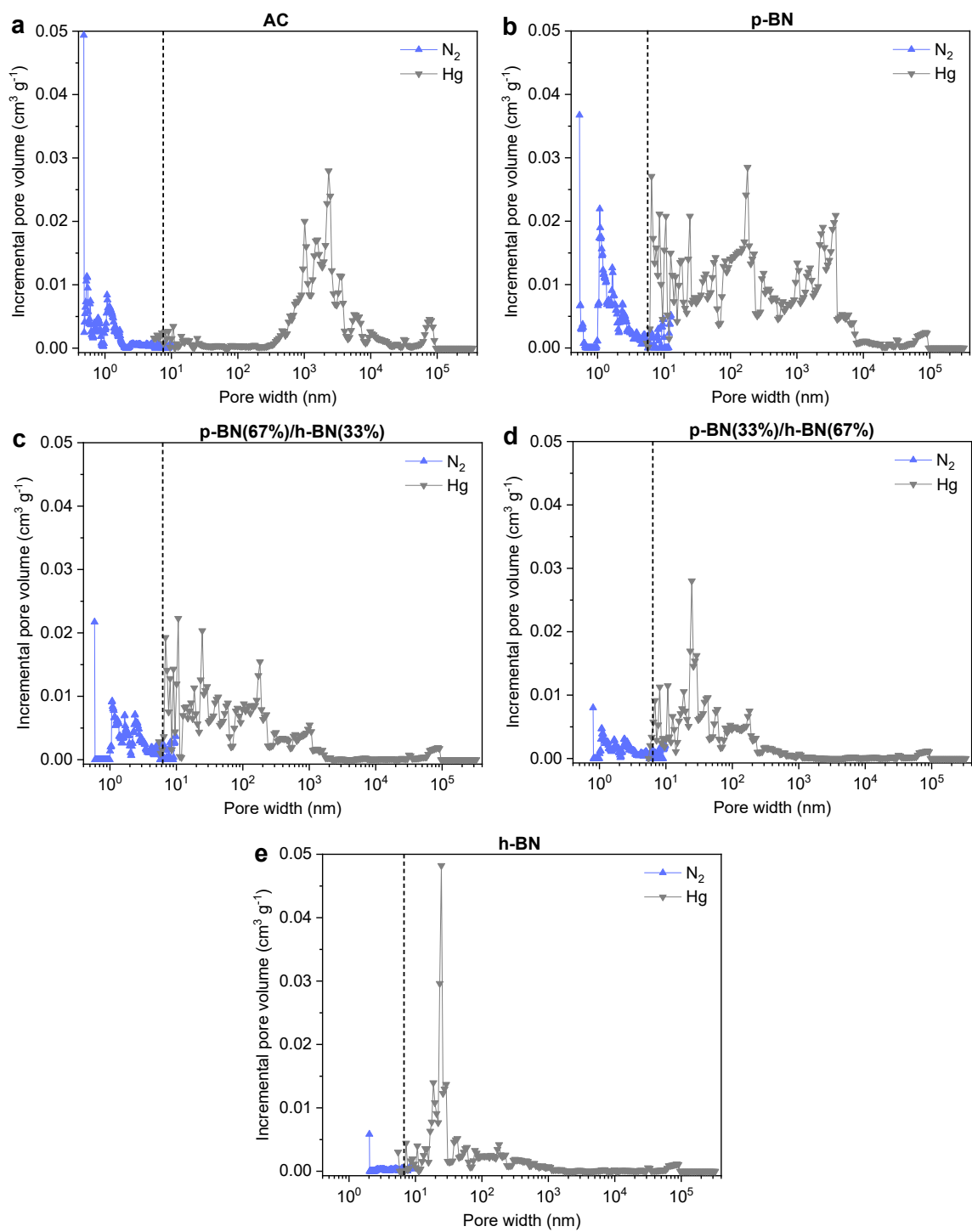
Figure A4.2 Pore size distributions derived from N_2 sorption isotherms at –196 °C and mercury intrusion porosimetry for: a) AC, (b) p-BN, (c) p-BN(67%)/h-BN(33%), (d) p-BN(33%)/h-

BN(67%), and (e) h-BN. <u>Note</u>: the dotted lines represent the cut-off points used to combine the two pore size distributions.
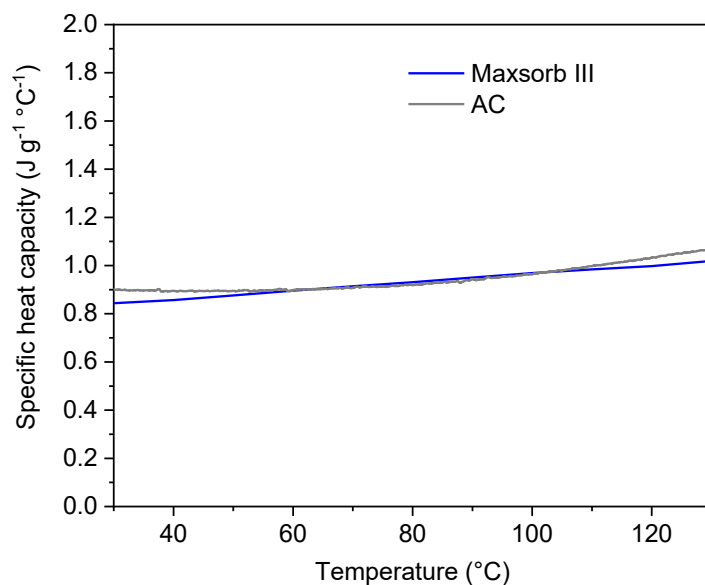
Figure A4.3 Specific heat capacity profile between 30 and 130 °C for AC and Maxsorb III. Data for Maxsorb III was reproduced from reference [143]. Copyright 2018 Elsevier.

Calculated vs. experimental heptane adsorption isotherms for the mixtures of p-BN and h-BN
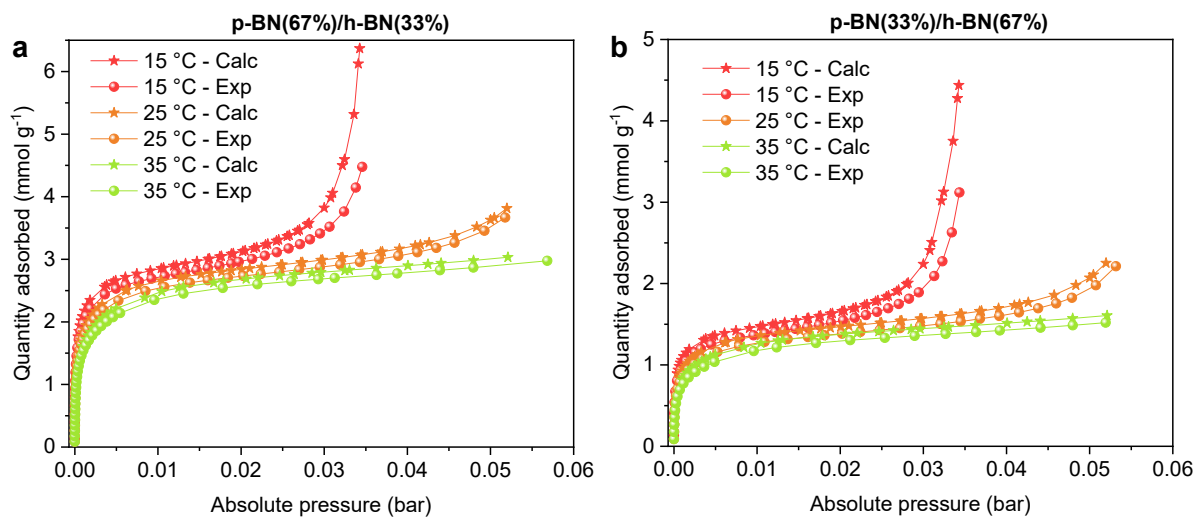
Figure A4.4 Calculated and experimental heptane adsorption isotherms for: (a) p-BN(67%)/h-BN(33%) and (b) p-BN(33%)/h-BN(67%).

Uptake vs. pore volume for heptane and n-propanol adsorption
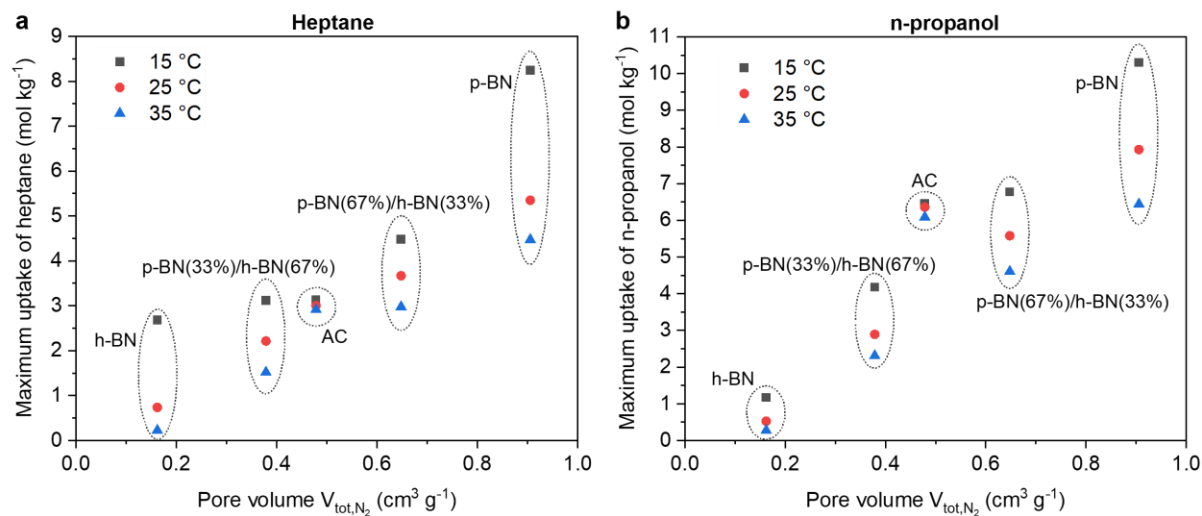
Figure A4.5 Maximum uptake of (a) heptane and (b) n-propanol at 15 °C, 25 °C and 35 °C represented as a function of the 'total' pore volume (as obtained using N_2 sorption at –196 °C) for each sample.

Heat of adsorption determination – Heptane
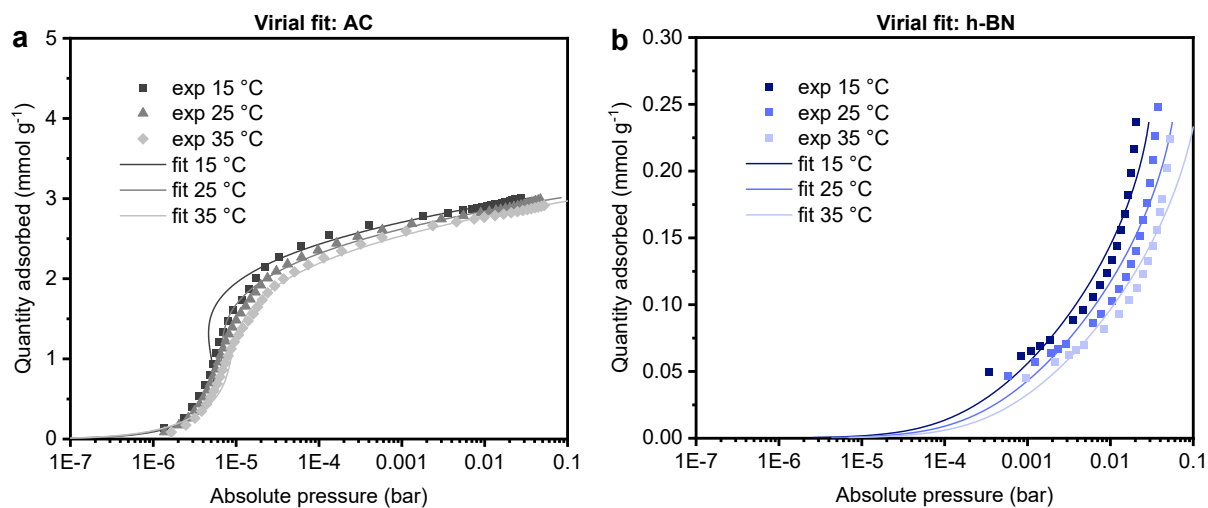
Figure A4.6 Experimental heptane sorption isotherms (symbols) and their inadequate fits (lines) obtained using a virial-type equation for activated carbon (AC) and h-BN were not suitable.
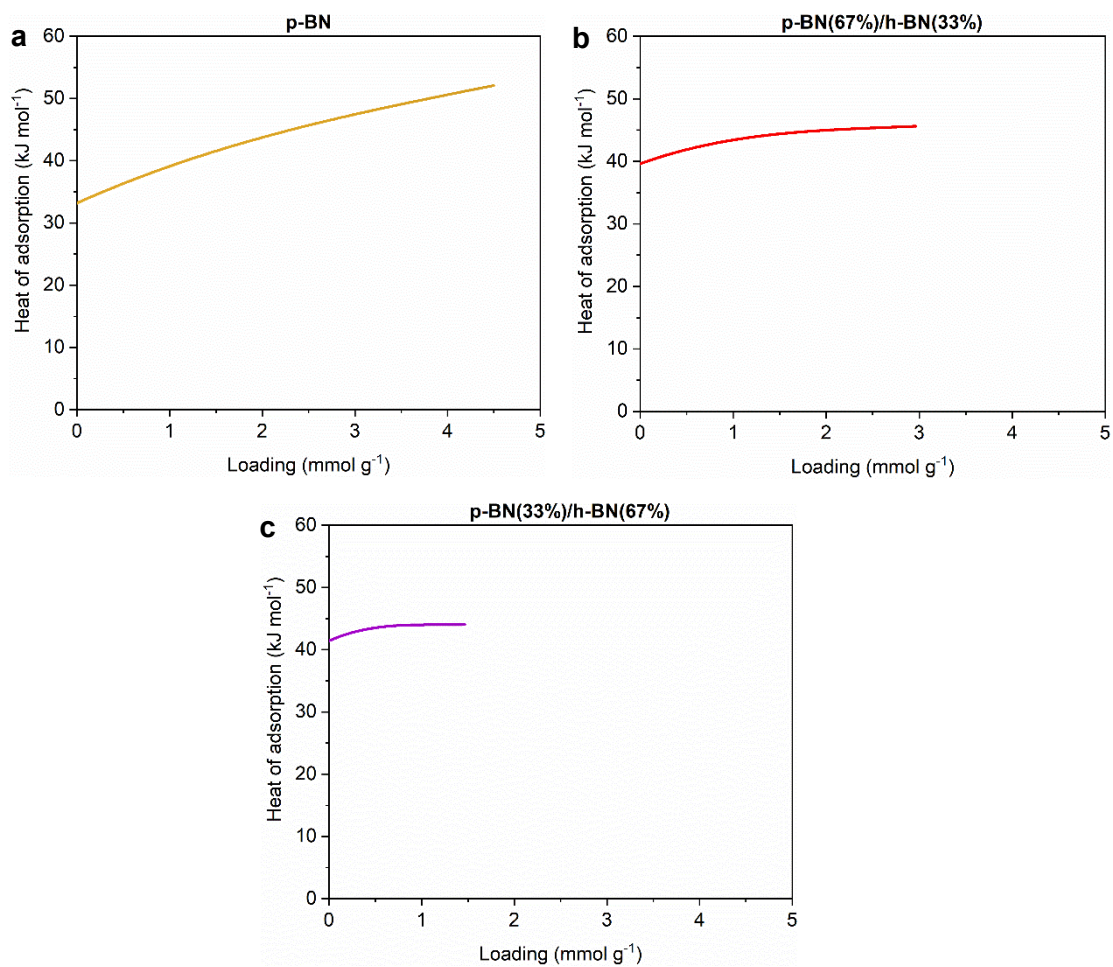
Figure A4.7 Heat of adsorption profiles for heptane adsorption obtained using the virial fitting method, with error bars (very narrow) represented as shaded regions for each sample.
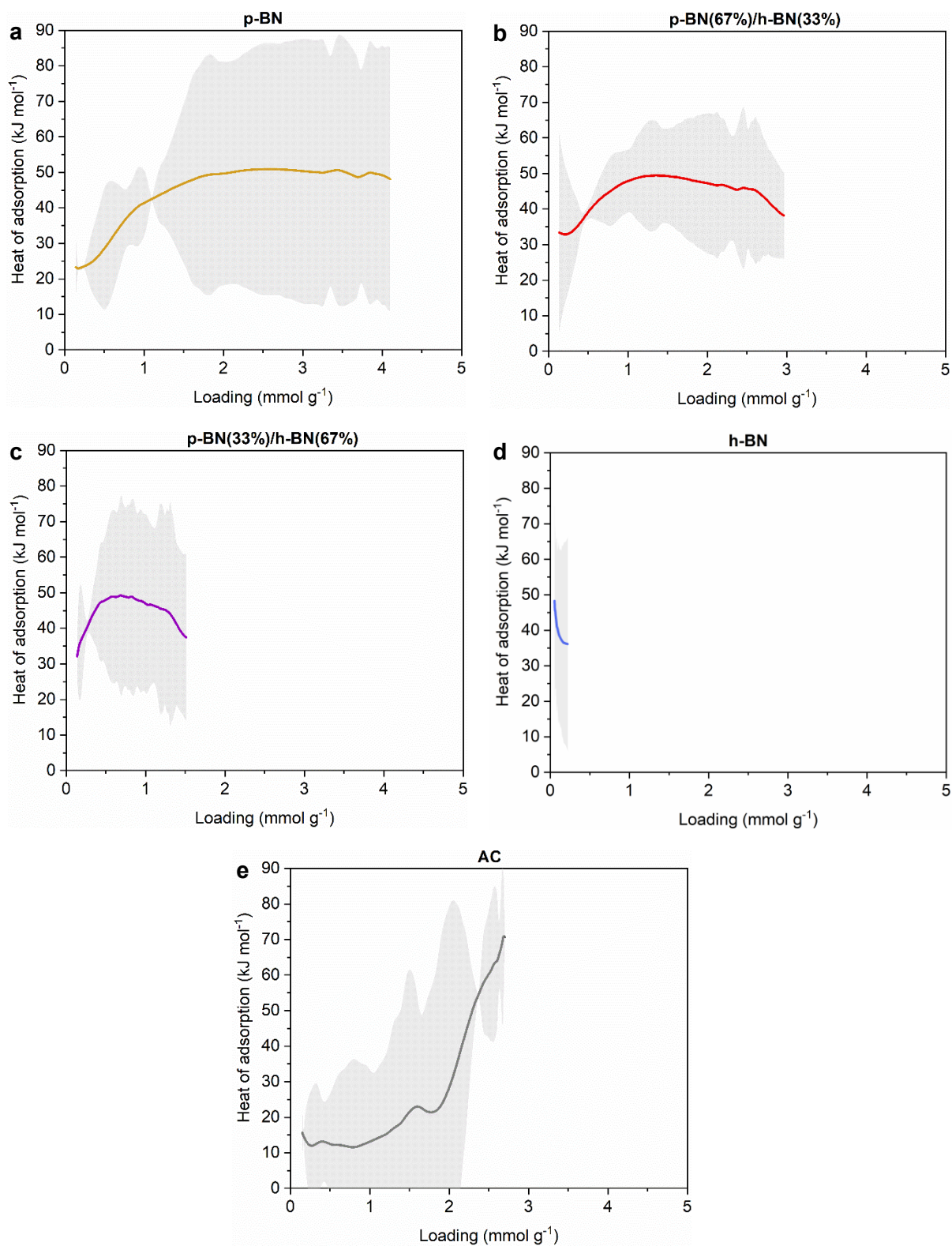
Figure A4.8 Heat of adsorption profiles for heptane adsorption obtained using the manual isosteric method, with error bars represented as shaded regions for each sample.

Figure A4.9 Experimental n-propanol sorption isotherms (symbols) and their inadequate fits (lines) obtained using a virial-type equation for activated carbon (AC) and h-BN were not suitable.
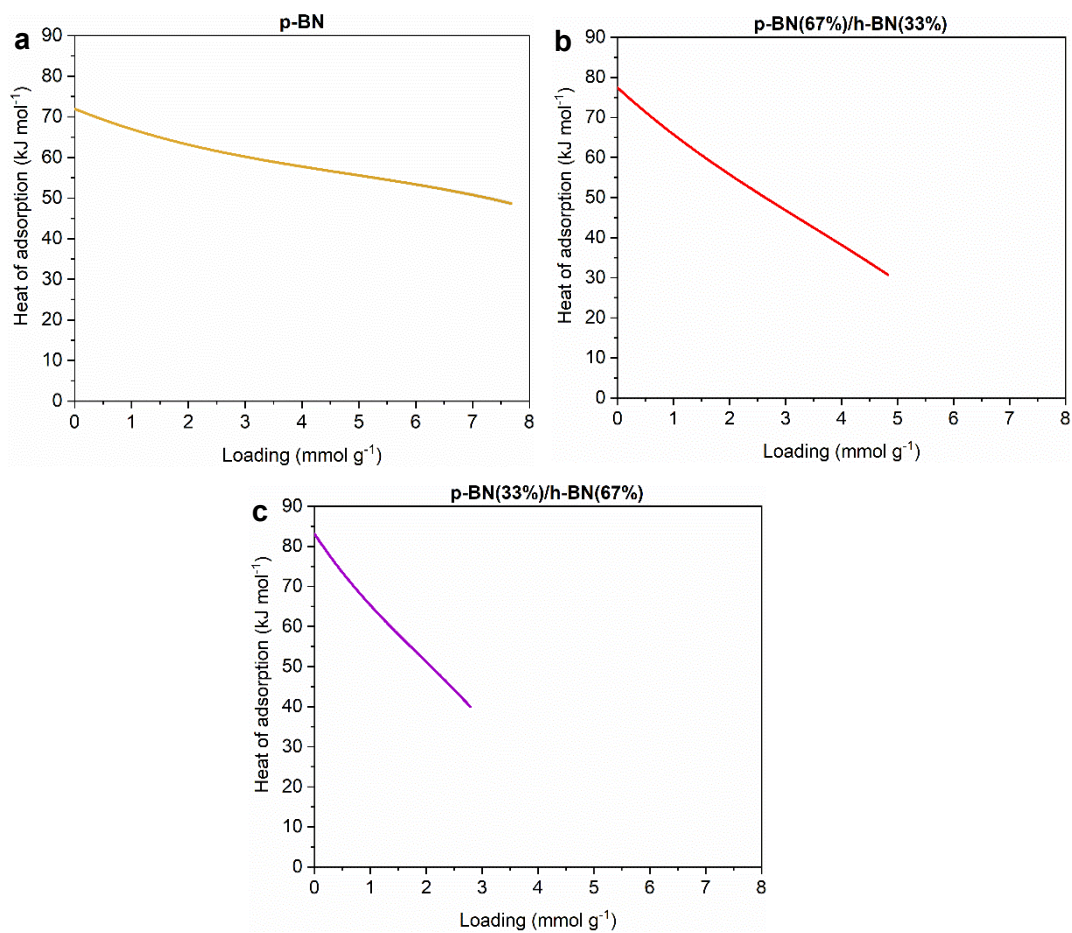
Figure A4.10 Heat of adsorption profiles for n-propanol adsorption obtained using the virial fitting method, with error bars (very narrow) represented as shaded regions for each sample.
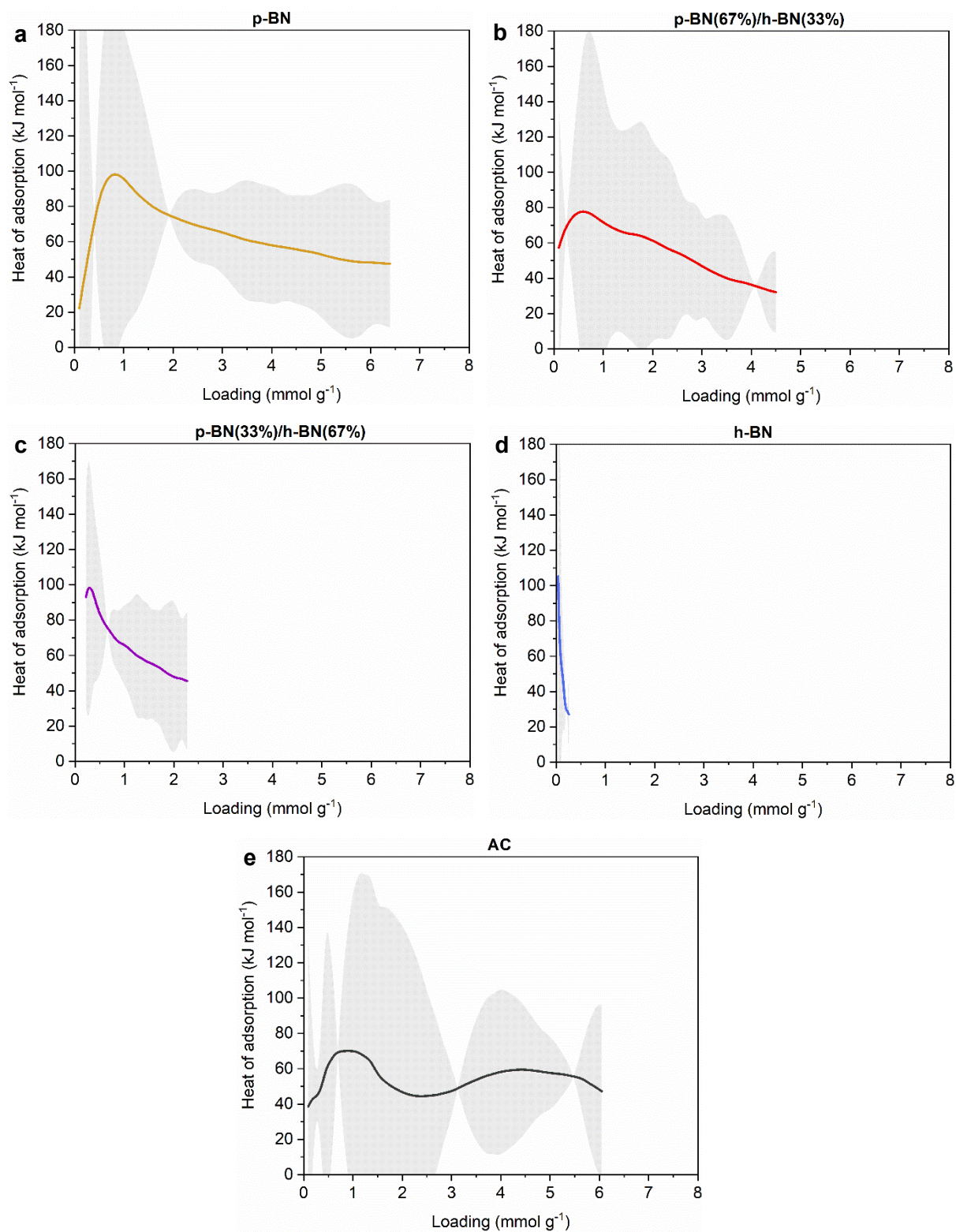
Figure A4.11 Heat of adsorption profiles for n-propanol adsorption obtained using the manual isosteric method, with error bars represented as shaded regions for each sample.

Figure A4.12 Plots of $ln\left(\frac{P}{n}\right)$ versus n at low loading for heptane adsorption on: (a) AC, (b) p-BN, (c) p-BN(67%)/h-BN(33%), (d) p-BN(33%)/h-BN(67%) and (e) h-BN.
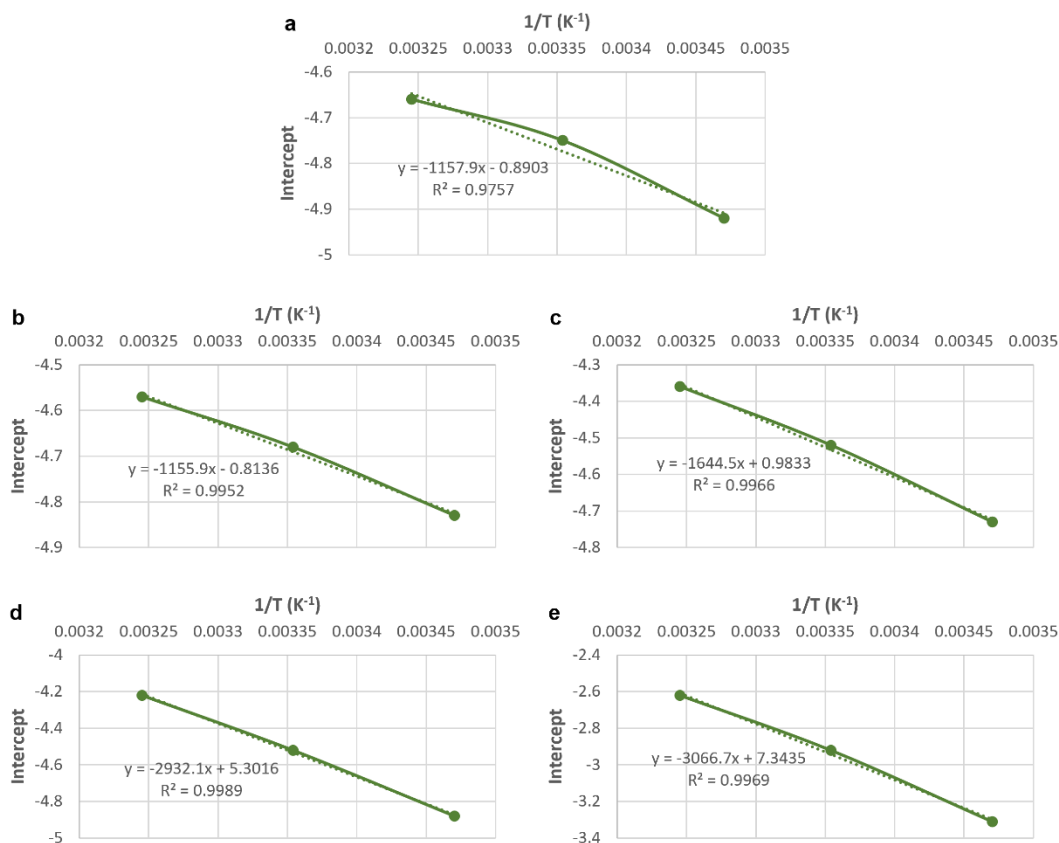
Figure A4.13 Plots of the intercepts from the linear regressions in Figure A4.12 versus $\frac{1}{T}$ for heptane adsorption on: (a) AC, (b) p-BN, (c) p-BN(67%)/h-BN(33%), (d) p-BN(33%)/h-BN(67%) and (e) h-BN. Each slope multiplied by the universal gas constant (≈ 8.314 J K^{-1} mol^{-1}) returns an estimate of the heat of adsorption at zero loading for the working pair considered.
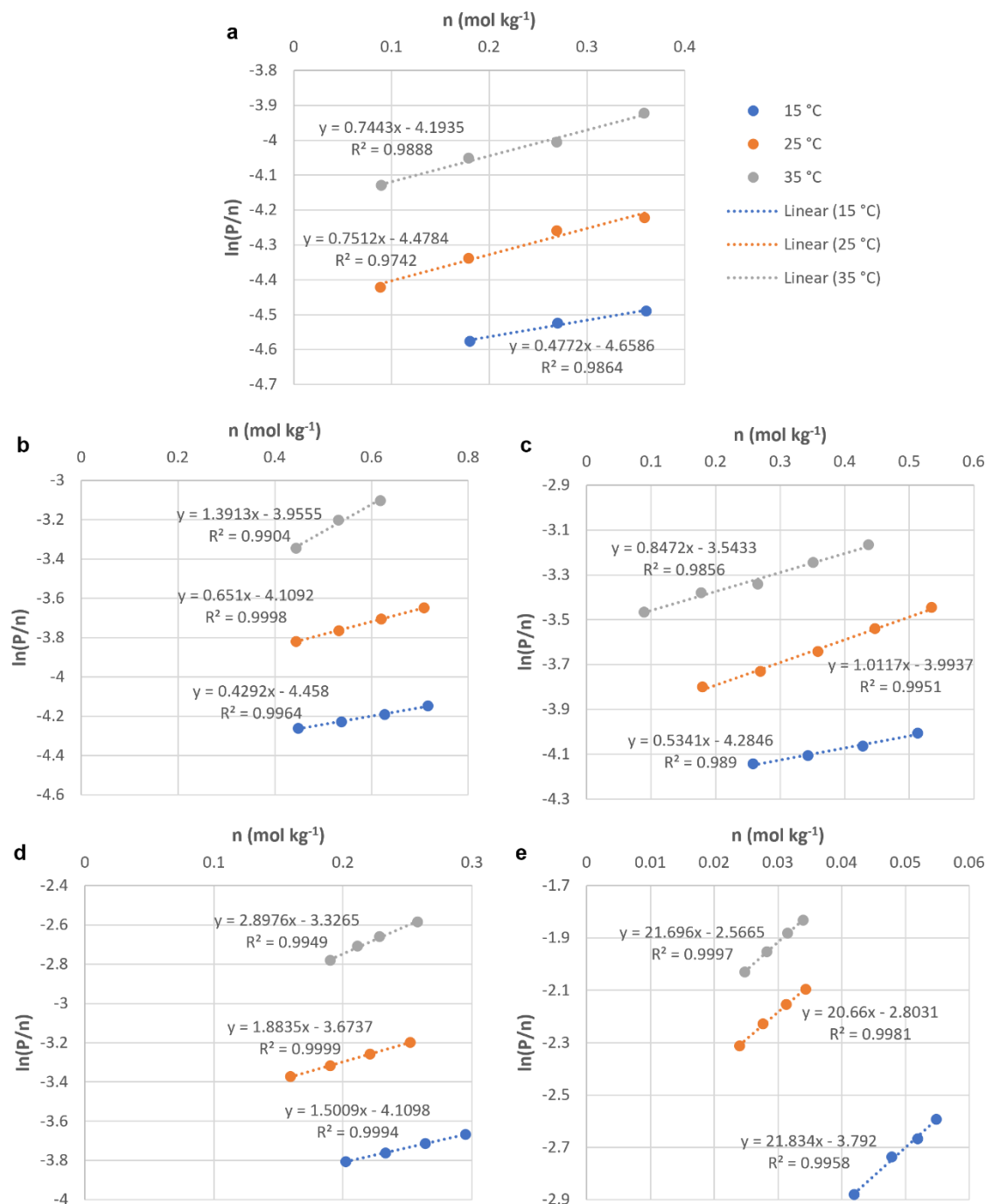
Figure A4.14 Plots of $ln\left(\frac{P}{n}\right)$ versus n at low loading for n-propanol adsorption on: (a) AC, (b) p-BN, (c) p-BN(67%)/h-BN(33%), (d) p-BN(33%)/h-BN(67%) and (e) h-BN.
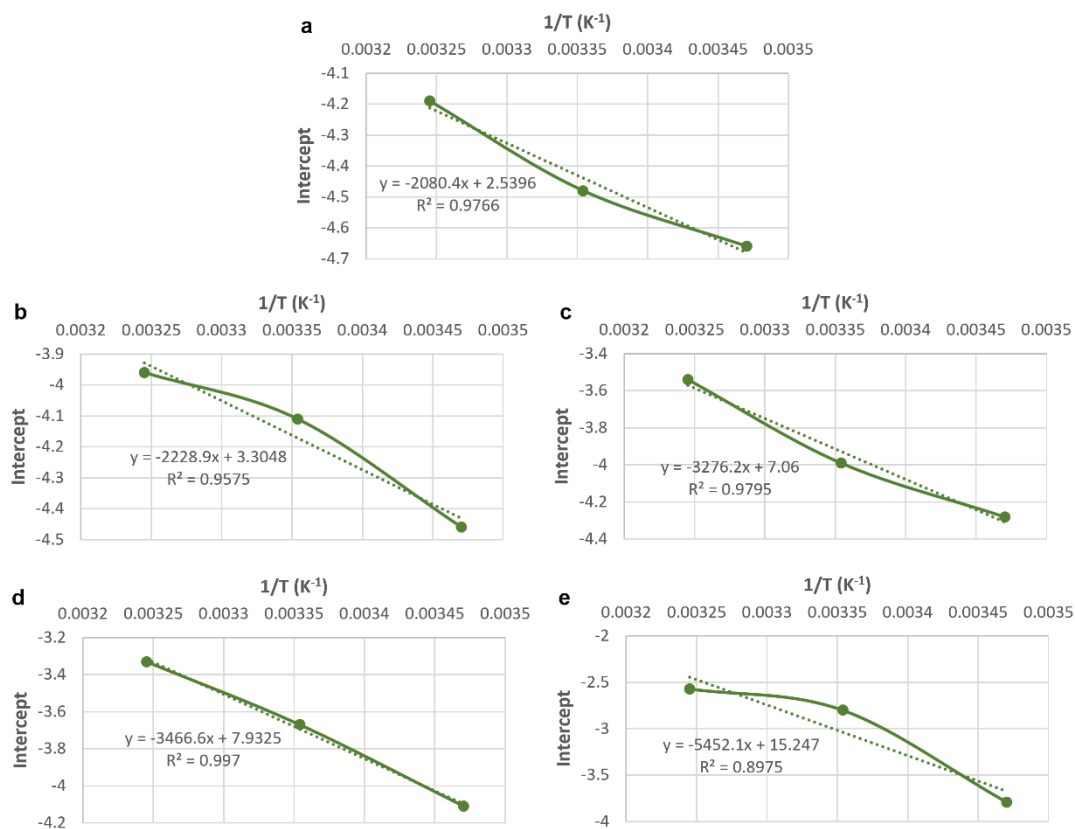
Figure A4.15 Plots of the intercepts from the linear regressions in Figure A4.14 versus $\frac{1}{T}$ for heptane adsorption on: (a) AC, (b) p-BN, (c) p-BN(67%)/h-BN(33%), (d) p-BN(33%)/h-BN(67%) and (e) h-BN. Each slope multiplied by the universal gas constant (≈ 8.314 J K^{-1} mol^{-1}) returns an estimate of the heat of adsorption at zero loading for the working pair considered.
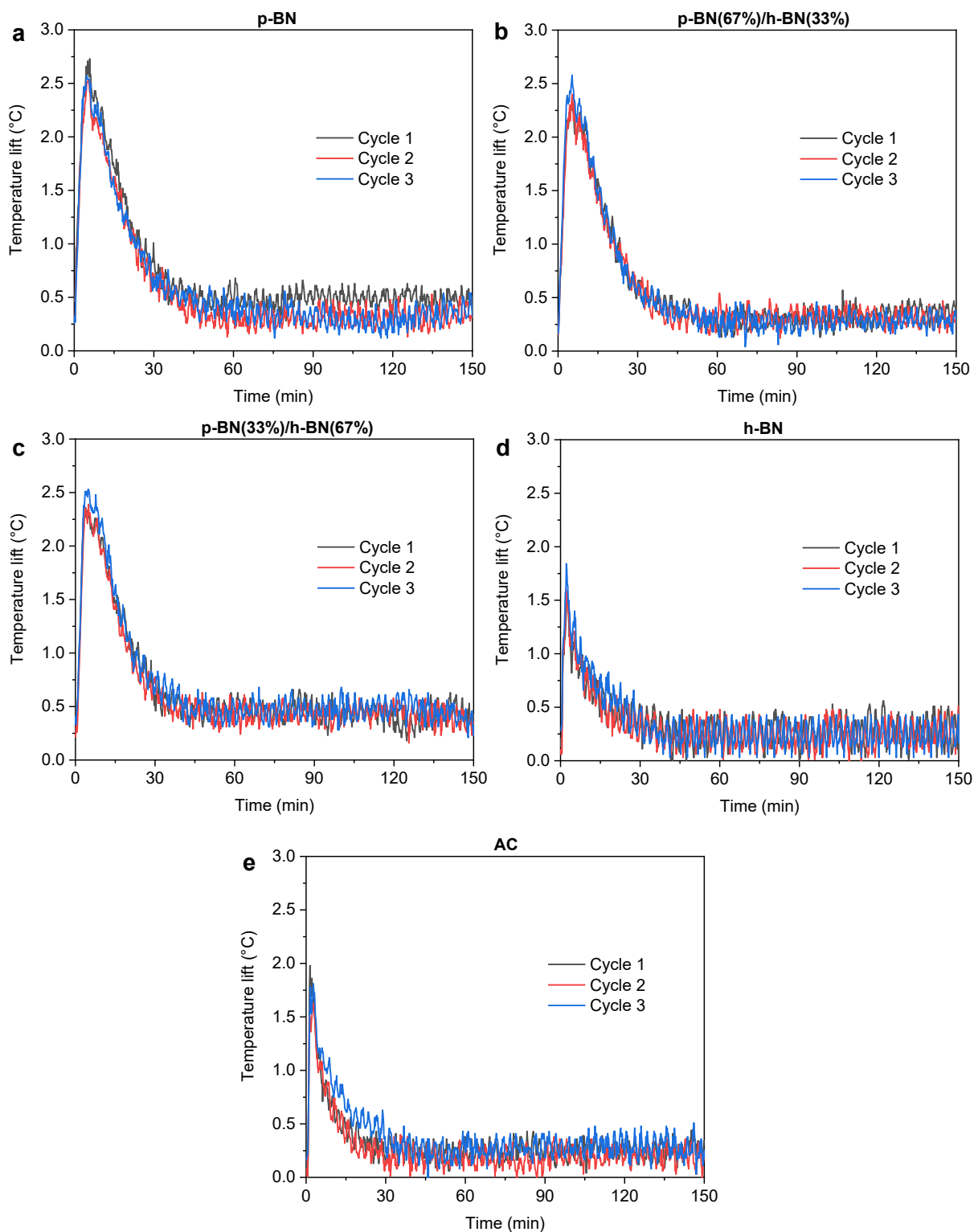
Figure A4.16 All temperature profiles measured during water TES for (a) p-BN, (b) p-BN(67%)/h-BN(33%), (c) p-BN(33%)/h-BN(67%), (d) h-BN and (e) AC.
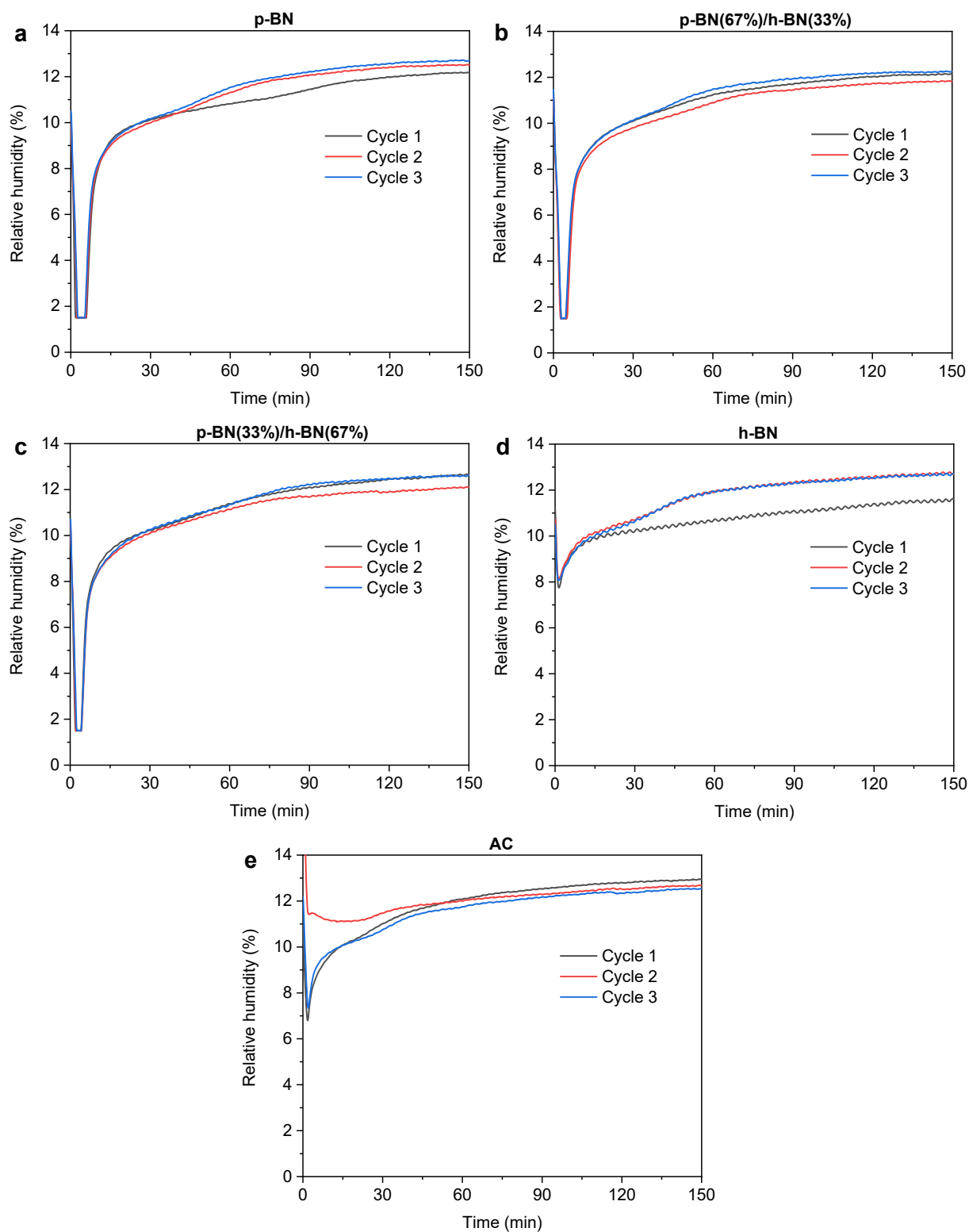
Figure A4.17 All breakthrough curves measured during water TES, before adjustment to absolute humidity, for (a) p-BN, (b) p-BN(67%)/h-BN(33%), (c) p-BN(33%)/h-BN(67%), (d) h-BN (measurement error during cycle 1), and (e) AC (measurement error during cycle 2).

Fitting of the adsorption isotherms for the modeling of breakthrough curves and temperature profiles

The dual-site Langmuir (DSL) equations can be found in Appendix 3.

The 'NBSI' model is given as:

$$n = n_{sat} * \sum_{i=1}^{j} \alpha_i \left(\left(\frac{P}{P_0} \right) * e^{\frac{\varepsilon_{0,i}}{RT}} \right)^{\frac{RT}{m_i}}$$

with:

n loading (mmol g^{-1})

n_{sat} saturation loading (mmol g^{-1})

α_i probability factor of adsorption site i with $\sum \alpha_i = 1$

$\frac{P}{P_0}$ relative pressure

$\varepsilon_{0,i}$ energy of adsorption site i (J mol^{-i})

R universal gas constant ($\approx$8.314 J K^{-1} mol^{-1})

T temperature (K)

m_i standard deviation of adsorption site i (J mol^{-i})

j coefficient (≤ 4)

In Chapter 7, this equation was used with $j = 3$, and we added a temperature-dependent factor b_0, i in each exponential term to improve the fitting, so that each exponential term became $e^{\frac{\varepsilon_{0,i}}{RT} + \ln (b_0, i)}$.
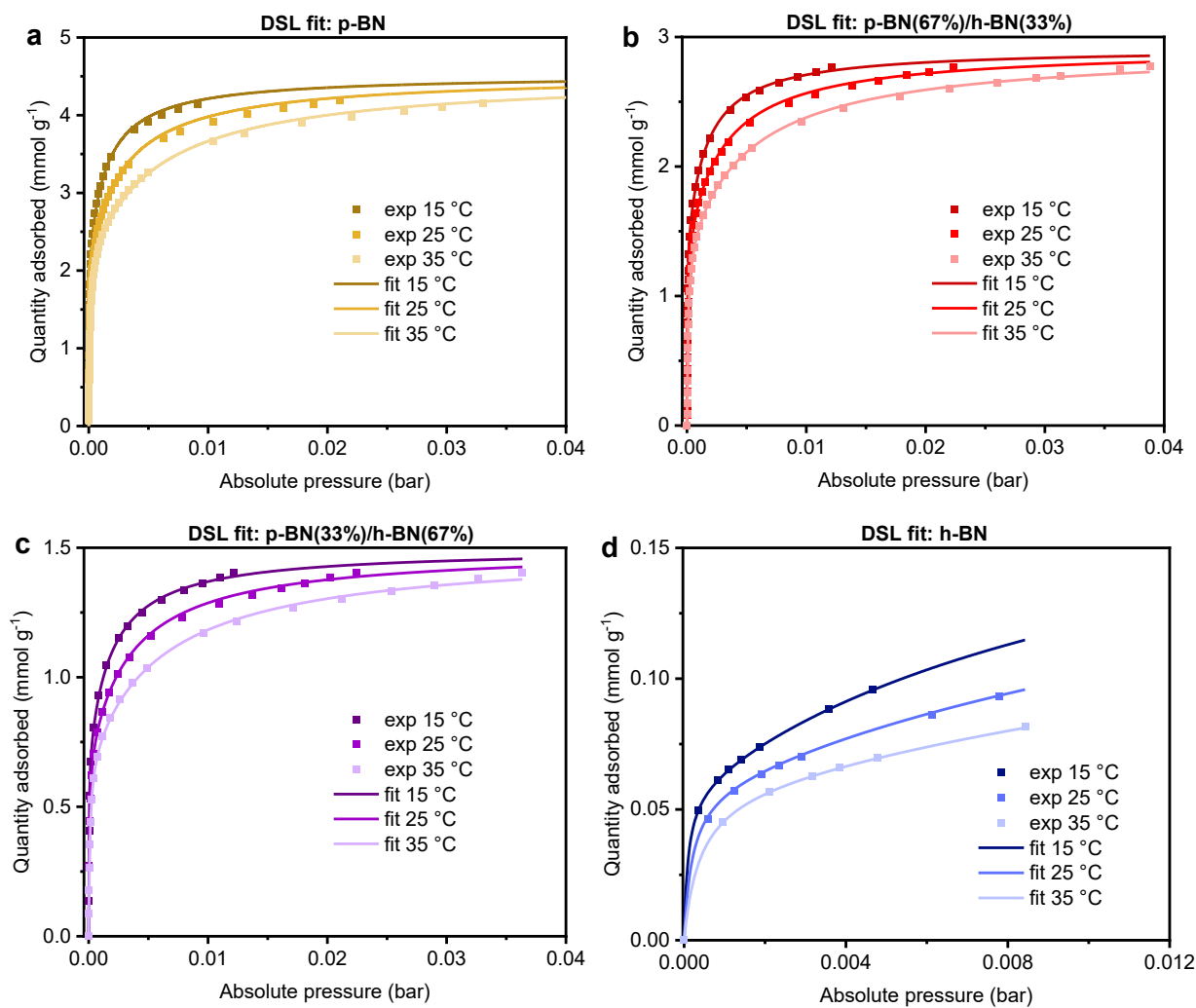
Figure A4.18 Experimental heptane sorption isotherms (symbols) and their fits (lines) obtained using a dual-site Langmuir (DSL model) for the BN-based samples.
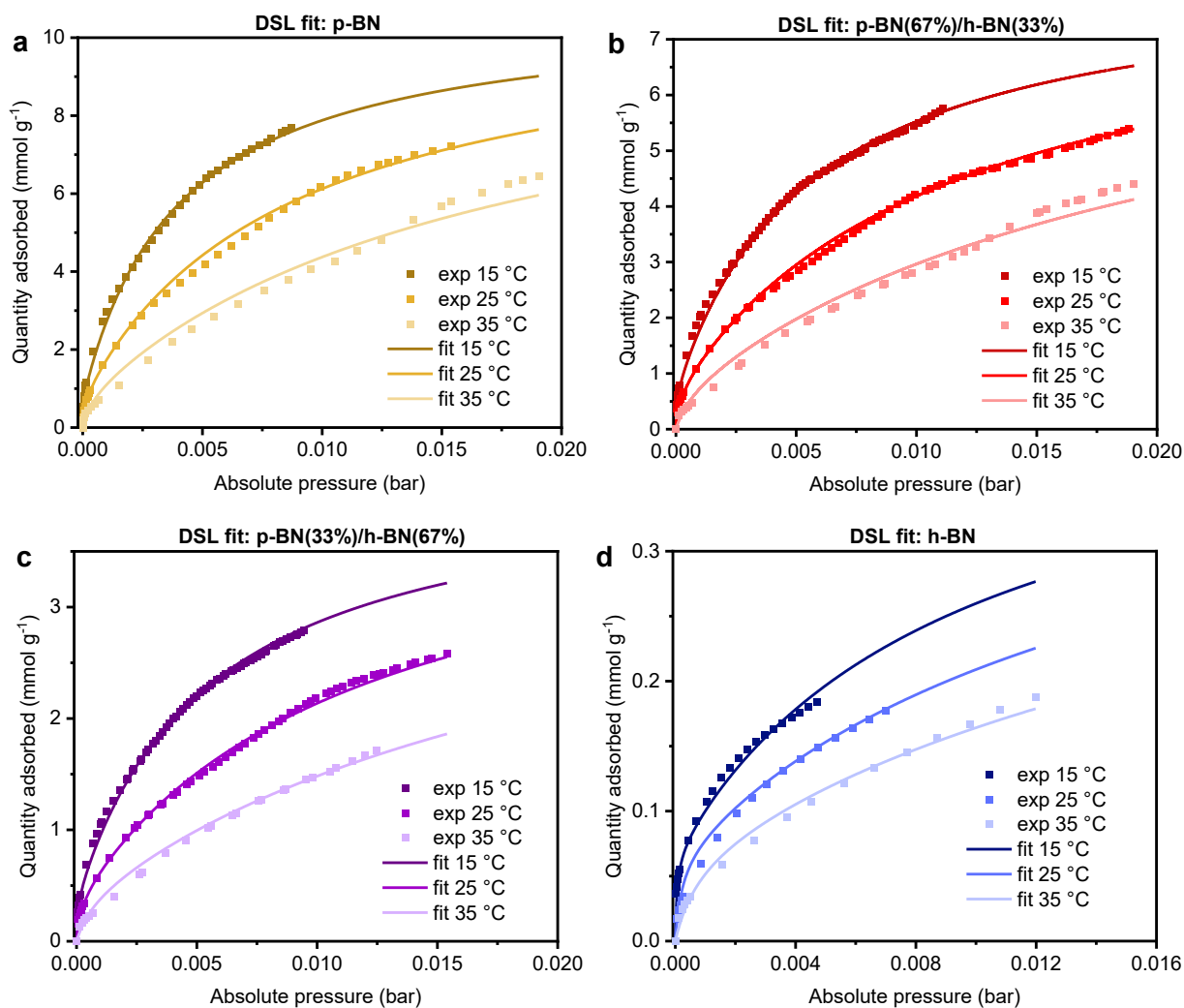
Figure A4.19 Experimental n-propanol sorption isotherms (symbols) and their fits (lines) obtained using a dual-site Langmuir (DSL model) for the BN-based samples, and the 'NBSI' model for activated carbon (AC).
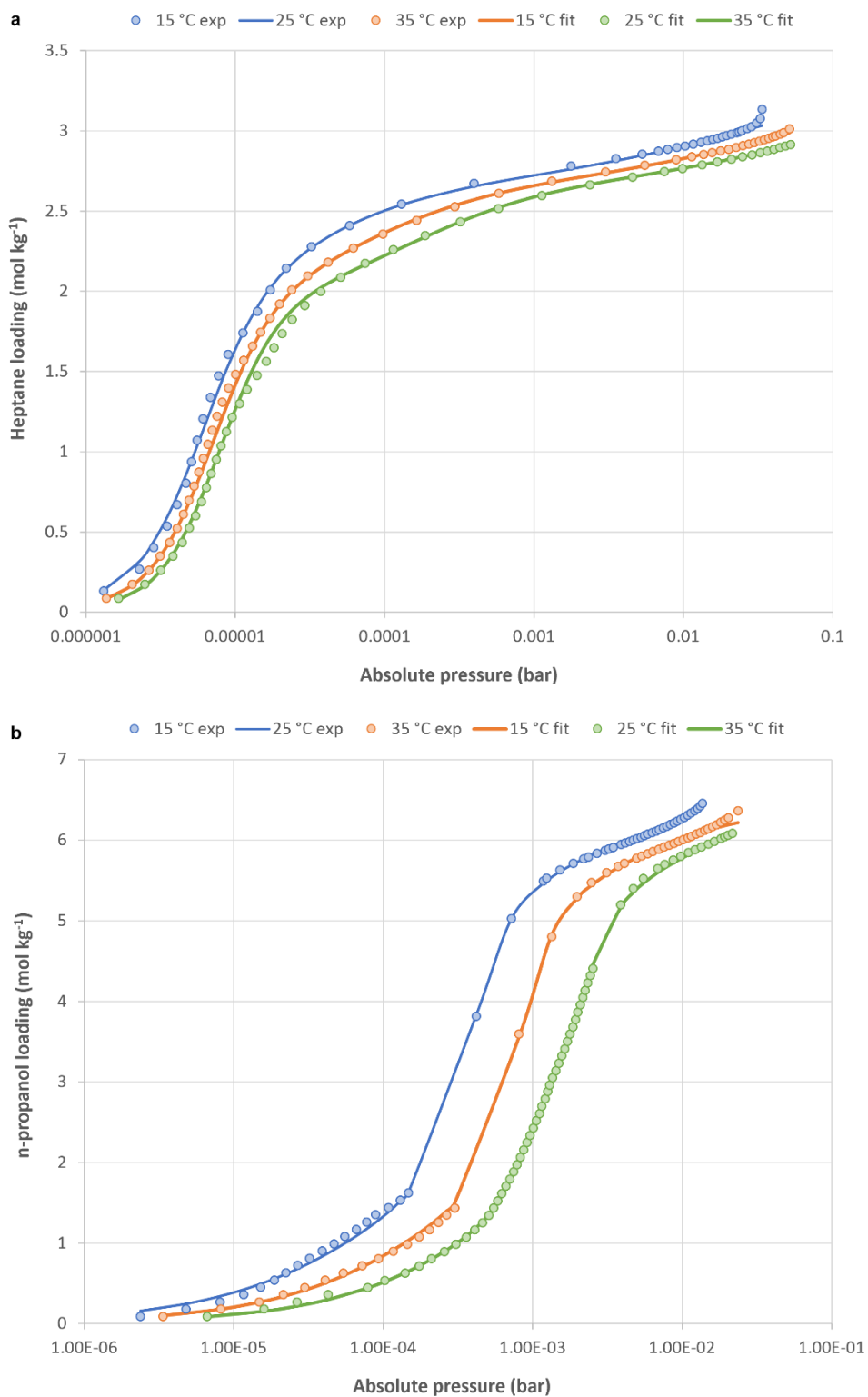
Figure A4.20 Experimental heptane sorption isotherms (symbols) and their fits (lines) obtained using the 'NBSI' model for activated carbon (AC).

Rights and permissions

1) L'Hermitte, A.; Dawson, D. M.; Ferrer, P.; Roy, K.; Held, G.; Tian, T.; Ashbrook, S. E.; Petit, C., Formation Mechanism and Porosity Development in Porous Boron Nitride. *J. Phys. Chem. C* **2021,** *125* (49), 27429–27439.

2) L'Hermitte, A.; Azzan, H.; Yio, M. H. N.; Rajagopalan, A. K.; Danaci, D.; Hirosawa, T.; Isobe, T.; Petit, C., Effect of surface functionalization on the moisture stability and sorption properties of porous boron nitride. *Microporous Mesoporous Mater.* **2023,** *352,* 112478.

3) Itskou, I.; L'Hermitte, A.; Marchesini, S.; Tian, T.; Petit, C., How to tailor porous boron nitride properties for applications in interfacial processes. *Accounts of Materials Research* **2023,** *4*, 143-155.

How to Tailor Porous Boron Nitride Properties for Applications in Interfacial Processes

Ioanna Itskou, Anouk L'Hermitte, Sofia Marchesini, Tian Tian, and Camille Petit*

4) Marchesini, S.; McGilvery, C. M.; Bailey, J.; Petit, C., Template-Free Synthesis of Highly Porous Boron Nitride: Insights into Pore Network Design and Impact on Gas Sorption. *ACS Nano* **2017,** *11* (10), 10003-10011.

5) Brožek, V.; Hubáček, M., A contribution to the crystallochemistry of boron nitride. *Journal of Solid State Chemistry* **1992,** *100* (1), 120-129.

A contribution to the crystallochemistry of boron nitride

Author: Vlastimil Brožek, Milan Hubáček
Publication: Journal of Solid State Chemistry
Publisher: Elsevier
Date: September 1992

Copyright © 1992 Published by Elsevier Inc.

Order Completed

Thank you for your order.

This Agreement between Anouk L'Hermitte ("You") and Elsevier ("Elsevier") consists of your license details and the terms and conditions provided by Elsevier and Copyright Clearance Center.

Your confirmation email will contain your order number for future reference.

License Number	5513340169888
License date	Mar 20, 2023

Licensed Content

Licensed Content Publisher	Elsevier
Licensed Content Publication	Journal of Solid State Chemistry
Licensed Content Title	A contribution to the crystallochemistry of boron nitride
Licensed Content Author	Vlastimil Brožek, Milan Hubáček
Licensed Content Date	Sep 1, 1992
Licensed Content Volume	100
Licensed Content Issue	1
Licensed Content Pages	10

Order Details

Type of Use	reuse in a thesis/dissertation
Portion	figures/tables/illustrations
Number of figures/tables/illustrations	1
Format	electronic
Are you the author of this Elsevier article?	No
Will you be translating?	No

About Your Work

Title	Using porous boron nitride in adsorption-based processes: investigation of material challenges and opportunities
Institution name	Imperial College London
Expected presentation date	Apr 2023

Additional Data

Portions	Figures 3, 4 and 5

6) Shankar, R.; Marchesini, S.; Petit, C., Enhanced Hydrolytic Stability of Porous Boron Nitride via the Control of Crystallinity, Porosity, and Chemical Composition. *J. Phys. Chem. C* **2019,** *123* (7), 4282-4290.
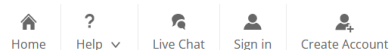
CCC RightsLink

Home · Help · Live Chat · Sign in · Create Account

Enhanced Hydrolytic Stability of Porous Boron Nitride via the Control of Crystallinity, Porosity, and Chemical Composition

Author: Ravi Shankar, Sofia Marchesini, Camille Petit
Publication: The Journal of Physical Chemistry C
Publisher: American Chemical Society
Date: Feb 1, 2019

Copyright © 2019, American Chemical Society

PERMISSION/LICENSE IS GRANTED FOR YOUR ORDER AT NO CHARGE

This type of permission/license, instead of the standard Terms and Conditions, is sent to you because no fee is being charged for your order. Please note the following:

- Permission is granted for your request in both print and electronic formats, and translations.
- If figures and/or tables were requested, they may be adapted or used in part.
- Please print this page for your records and send a copy of it to your publisher/graduate school.
- Appropriate credit for the requested material should be given as follows: "Reprinted (adapted) with permission from {COMPLETE REFERENCE CITATION}. Copyright {YEAR} American Chemical Society." Insert appropriate information in place of the capitalized words.
- One-time permission is granted only for the use specified in your RightsLink request. No additional uses are granted (such as derivative works or other editions). For any uses, please submit a new request.

If credit is given to another source for the material you requested from RightsLink, permission must be obtained from that source.

BACK | CLOSE WINDOW

7) Sah, A.; Castricum, H. L.; Bliek, A.; Blank, D. H. A.; ten Elshof, J. E., Hydrophobic modification of γ-alumina membranes with organochlorosilanes. *Journal of Membrane Science* **2004**, *243* (1), 125-132.

8) Yang, S.; Peng, L.; Sun, D. T.; Asgari, M.; Oveisi, E.; Trukhina, O.; Bulut, S.; Jamali, A.; Queen, W. L., A new post-synthetic polymerization strategy makes metal–organic frameworks more stable. *Chem. Sci.* **2019**.
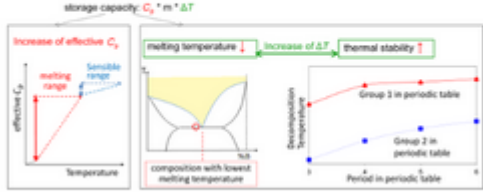
9) Pfleger, N.; Bauer, T.; Martin, C.; Eck, M.; Wörner, A., Thermal energy storage – overview and specific insight into nitrate salts for sensible and latent heat storage. *Beilstein Journal of Nanotechnology* **2015,** *6*, 1487-1497.

BEILSTEIN JOURNAL OF NANOTECHNOLOGY

**Thermal energy storage – overview and specific insight into nitrate salts for sensible and latent heat storage**

Nicole Pfleger, Thomas Bauer, Claudia Martin et al.

Beilstein J. Nanotechnol. **2015,** *6*, 1487–1497.

doi:10.3762/bjnano.6.154
CC BY 2.0

10) Lim, K.; Kim, J.; Lee, J., Comparative study on adsorbent characteristics for adsorption thermal energy storage system. *International Journal of Energy Research* **2019,** *43* (9), 4281-4294.
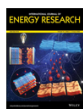
Comparative study on adsorbent characteristics for adsorption thermal energy storage system

Author: Jaeseon Lee, Jongkyu Kim, Kihoon Lim
Publication: International Journal of Energy Research
Publisher: John Wiley and Sons
Date: Apr 24, 2019

© 2019 John Wiley & Sons, Ltd.

11) Shervani, S.; Strong, C.; Tezel, F. H., Magnesium sulphate hybrids with silica gel and activated alumina for thermal energy storage. *Journal of Cleaner Production* **2022**, *371*, 133262.

Magnesium sulphate hybrids with silica gel and activated alumina for thermal energy storage
Author: Suboohi Shervani,Curtis Strong,F. Handan Tezel
Publication: Journal of Cleaner Production
Publisher: Elsevier
Date: 15 October 2022

Order Completed

Thank you for your order.

This Agreement between Anouk L'Hermitte ("You") and Elsevier ("Elsevier") consists of your license details and the terms and conditions provided by Elsevier and Copyright Clearance Center.

Your confirmation email will contain your order number for future reference.

License Number	5513340871029
License date	Mar 20, 2023

☑ **Licensed Content**

Licensed Content Publisher	Elsevier
Licensed Content Publication	Journal of Cleaner Production
Licensed Content Title	Magnesium sulphate hybrids with silica gel and activated alumina for thermal energy storage
Licensed Content Author	Suboohi Shervani,Curtis Strong,F. Handan Tezel
Licensed Content Date	Oct 15, 2022
Licensed Content Volume	371
Licensed Content Issue	n/a
Licensed Content Pages	1

📋 **Order Details**

Type of Use	reuse in a thesis/dissertation
Portion	figures/tables/illustrations
Number of figures/tables/illustrations	1
Format	electronic
Are you the author of this Elsevier article?	No
Will you be translating?	No

📄 **About Your Work**

|	
Title	Using porous boron nitride in adsorption-based processes: investigation of material challenges and opportunities
Institution name	Imperial College London
Expected presentation date	Apr 2023

📁 **Additional Data**

Portions	Figure 2

12) Uddin, K.; Amirul Islam, M.; Mitra, S.; Lee, J.-b.; Thu, K.; Saha, B. B.; Koyama, S., Specific heat capacities of carbon-based adsorbents for adsorption heat pump application. *Applied Thermal Engineering* **2018,** *129*, 117-126.
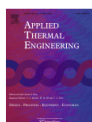
Specific heat capacities of carbon-based adsorbents for adsorption heat pump application
Author: Kutub Uddin,Md. Amirul Islam,Sourav Mitra,Jong-boong Lee,Kyaw Thu,Bidyut Baran Saha,Shigeru Koyama
Publication: Applied Thermal Engineering
Publisher: Elsevier
Date: 25 January 2018

Order Completed

Thank you for your order.

This Agreement between Anouk L'Hermitte ("You") and Elsevier ("Elsevier") consists of your license details and the terms and conditions provided by Elsevier and Copyright Clearance Center.

Your confirmation email will contain your order number for future reference.

License Number	5513350033592
License date	Mar 20, 2023

☑ **Licensed Content**

Licensed Content Publisher	Elsevier
Licensed Content Publication	Applied Thermal Engineering
Licensed Content Title	Specific heat capacities of carbon-based adsorbents for adsorption heat pump application
Licensed Content Author	Kutub Uddin,Md. Amirul Islam,Sourav Mitra,Jong-boong Lee,Kyaw Thu,Bidyut Baran Saha,Shigeru Koyama
Licensed Content Date	Jan 25, 2018
Licensed Content Volume	129
Licensed Content Issue	n/a
Licensed Content Pages	10

📋 **Order Details**

Type of Use	reuse in a thesis/dissertation
Portion	figures/tables/illustrations
Number of figures/tables/illustrations	1
Format	electronic
Are you the author of this Elsevier article?	No
Will you be translating?	No

📄 **About Your Work**

Title	Using porous boron nitride in adsorption-based processes: investigation of material challenges and opportunities
Institution name	Imperial College London
Expected presentation date	Apr 2023

📁 **Additional Data**

Portions	Heat capacity data of Maxsorb III